Aus dem Adolf-Butenandt-Institut im Biomedizinischen Centrum
der Ludwig-Maximilians-Universität München
Lehrstuhl für Molekularbiologie
Vorstand: Prof. Dr. rer. nat. Peter B. Becker

Probing the conformation of ISWI-type chromatin remodeling enzymes by an integrative structural approach

Dissertation
zum Erwerb des Doktorgrades der Naturwissenschaften
an der Medizinischen Fakultät der
Ludwig-Maximilians-Universität München

vorgelegt von
Harrer Nadine
aus Neumarkt i.d.OPf.
2018

Mit Genehmigung der Medizinischen Fakultät
der Ludwig-Maximilians-Universität München

Betreuer:	Prof. Dr. rer. nat. Peter B. Becker
Zweitgutachterin:	Prof. Michaela Smolle, PhD

Dekan:	Prof. Dr. med. dent. Reinhard Hickel
Tag der mündlichen Prüfung:	11.04.2019

Eidesstattliche Versicherung

Harrer, Nadine

Ich erkläre hiermit an Eides statt,
dass ich die vorliegende Dissertation mit dem Thema

„Probing the conformation of ISWI-type chromatin remodeling enzymes by an integrative structural approach“

selbständig verfasst, mich außer der angegebenen keiner weiteren Hilfsmittel bedient und alle Erkenntnisse, die aus dem Schrifttum ganz oder annähernd übernommen sind, als solche kenntlich gemacht und nach ihrer Herkunft unter Bezeichnung der Fundstelle einzeln nachgewiesen habe.

Ich erkläre des Weiteren, dass die hier vorgelegte Dissertation nicht in gleicher oder in ähnlicher Form bei einer anderen Stelle zur Erlangung eines akademischen Grades eingereicht wurde.

Sengenthal, den 16.04.2019

Nadine Harrer

Table of contents

I. Abbreviations

A	Å	Ångström
	ACF	ATP-utilizing chromatin assembly and remodeling factor
	Acidic N	Acidic region in the N-terminus of ISWI
	ACN	Acetonitrile
	ADP-BeF_x	Adenosine-diphosphate beryllium-fluoride
	ATP	Adenosine-triphosphate
	AutoN	N-terminal autoinhibitory region in ISWI
B	B or Bpa	p-benzoyl- p- phenylalanine
	BAZ2B	Bromodomain adjacent to zing finger domain 2B
	bp	Base pair(s)
	BPTF	Bromodomain PHD finger transcription factor
	BRF	BAZ2*B*- containing remodeling factor
	BS^2G	Bissulfosuccinimidyl glutarate
	BS^3	Bissulfosuccinimidyl suberate
	BSA	Bovine serum albumin
C	CECR2	Cat eye syndrome critical region protein 2
	CERF	CECR2-containing remodeling factor
	Chd1	Chromodomain helicase DNA-binding protein 1
	CHRAC	Chromatin accessibility complex
	CID	Collision-induced dissociation
	CtBP	COOH-terminal-binding protein
	CV(s)	Column volume(s)
D	Da	Dalton
	Dm	*Drosophila melanogaster*
	DMSO	Dimethylsulfoxide
	DNA	Desoxyribonucleic acid
	dNTP	Desoxyribonucleotidetriphosphate
	Dr	*Danio rerio*
	DTT	Dithiothreitol
E	*E. coli*	*Escherichia coli*
	EDC	1-ethyl-3-(3-dimethylaminopropyl)carbodiimide
	EDTA	Ethylenediaminetetraacetic acid
	EM	Electron microscopy
	EMSA	Electrophoretic mobility shift assay
	EPR	Electron paramagnetic resonance
	EtBr	Ethidiumbromide
	ETD	Electron transfer dissociation
F	FDR	False discovery rate
	FL	Full-length
	FPLC	Fast protein liquid chromatography

** continues next page **

	FRET	Fluorescence resonance energy transfer
H	HAT	Histone acetyltransferases
	HDX-MS	Hydrogen/deuterium exchange mass spectrometry
	HP1	Heterochromatin binding protein 1
	HSS	HAND-SANT-SLIDE
I	IAA	Iodoacetamide
	INO80	Inositol auxotroph mutant 80
	IPTG	Isopropyl-β-D-thiogalactopyranoside
	ISWI	Imitation switch
K	K	Lysine
L	LC-MS/MS	Liquid chromatography-tandem mass spectrometry
M	m/z	Mass-to-charge
	MS	Mass spectrometry
	Mt	*Myceliophthora thermophila*
	MW	Molecular weight
N	NADH	Reduced nicotinamide adenine dinucleotide
	NCP	Nucleosome core particle
	NegC	C-terminal autoinhibitory motif in ISWI
	NHS	N-hydroxysuccinimide
	NMR	Nuclear magnetic resonance
	NoRC	Nucleolar remodeling complex
	NTR	N-terminal region
	NuRD	Nucleosome Remodeling and Deacetylase
	NURF	Nucleosome remodeling factor
O	OD	Optical density
P	PAGE	Polyacrylamide gel electrophoresis
	PCR	Polymerase chain reaction
	PHD	Plant homeodomain
	PMSF	Phenylmethylsulfonyl fluoride
	ppm	Parts per million
	PTM	Posttranslational modification
R	R_g	Radius of gyration
	RHP	Rapid Histone Purification
	RMSD	Root-mean-square deviation
	RSF	Remodeling and spacing factor
S	SAXS	Small angle X-ray scattering
	Sc	*Saccharomyces cerevisiae*
	SDS	Sodium dodecyl sulfate
	SEC	Size-exclusion chromatography
	SF	Superfamily

** continues next page **

	SHL	Superhelical location
	SLIDE	SANT-like ISWI domain
	Snf2H	Sucrose non-fermenting protein 2 homolog
	Snf2L	Sucrose non-fermenting 2 like
	SPE	Solid-phase extraction
	Sso	*Sulfolobus solfataricus*
	SWI/SNF	SWItch/Sucrose Non-Fermentable
T	TCA	Trichloroacetic acid
	TEV	Tobacco etch virus
	TFA	Trifluoroacetic acid
	Tip5	TTF-I interacting protein 5
	TLC	Thin-layer chromatography
	ToRC	Toutatis-containing chromatin remodeling complex
	TTF-I	Transcription termination factor I
U	UV	Ultraviolet
V	v/v	Volume per volume
W	w/v	Weight per volume
	WICH	WSTF-ISWI chromatin remodeling complex
	WSTF	Williams Syndrome transcription factor
	WT	Wild type
	wwPDB	Worldwide Protein Data Bank
X	XL-MS	Cross-linking coupled to mass spectrometry
--	χ	Chi

II. Summary

The eukaryotic genome is compacted into a higher-order chromatin structure to facilitate the packaging of DNA into the cell’s nucleus and to allow for controlled accessibility of genetic information at any given time. The chromatin landscape is dynamic and changes in response to endogenous and exogenous stimuli such that essential nuclear processes (e.g., DNA transcription and replication) can be carried out. The fundamental units of chromatin are nucleosomes, which are composed of DNA wrapped around an octamer of histone proteins. ATP-dependent chromatin remodeling enzymes play a key role in the modulation of chromatin structure by catalyzing various reactions such as the repositioning of nucleosomes along DNA. Despite the importance of ATP-dependent chromatin remodeling enzymes in regulating chromatin structure, however, the structure and function of these proteins have largely remained elusive.

In this PhD project, the structural architectures of prototypical imitation switch (ISWI)-type chromatin remodeling enzymes from *Drosophila melanogaster* (DmISWI) and humans (Snf2H) were probed across different functional states of the catalytic cycle using an integrative structural approach. The approach combines experimental data from protein cross-linking coupled to high-resolution mass spectrometry and small angle X-ray scattering in order to guide computational modeling of three-dimensional enzyme structures.

The findings of the present study are consistent with the notion that the full-length DmISWI and Snf2H enzymes assume an overall compact resting state in the absence of ligands in solution. While the C-terminal HAND-SANT-SLIDE domain packs against the ATPase module, the autoregulatory NTR and NegC domains bridge the ATPase lobe-lobe interface and keep the remodeling enzymes in a catalytically incompetent conformation. The findings thus provide a structure-based explanation for the repressed basal ATPase activity of ISWI-type proteins in the absence of substrate. In addition, the respective structural model of the DmISWI ATPase domain provides support for the recently captured X-ray crystal structure of an ISWI-type remodeling enzyme from the thermophilic yeast *Myceliophthora thermophilia*. In order to leave the identified resting state, ISWI-type remodeling enzymes presumably undergo a series of conformational changes in the presence of ligands and/or substrate. These conformational changes may comprise a rotation of the two ATPase lobes relative to each other such that residues involved in ATP binding and hydrolysis are in close spatial proximity. Interestingly, the Snf2H enzyme appears to interact *via* the HAND-SANT-SLIDE domain with a highly acidic region on the nucleosome core in the presence of both the non-hydrolysable nucleotide analog ADP-BeF$_x$ and nucleosomes. Our structural data of the substrate-bound Snf2H enzyme thus substantiate the recent notion that this acidic patch represents an important nucleosomal epitope, which could play an important mechanistic role during ATP-dependent chromatin remodeling by ISWI-type enzymes.

III. Zusammenfassung

Das eukaryotische Genom wird in höher geordneten Chromatinstrukturen organisiert, um die kompakte Verpackung von DNA innerhalb des Zellkerns zu ermöglichen und um die Zugänglichkeit zur genetischen Information zu kontrollieren. Die Chromatinstruktur ist dynamisch und ändert sich in Abhängigkeit von endogenen und exogenen Stimuli, sodass essentielle Zellkern-Prozesse (z. B. DNA-Transkription und -Replikation) durchgeführt werden können. Die grundlegenden Strukturelemente des Chromatins sind Nukleosomen, in denen DNA um ein Oktamer aus Histonen gewickelt ist. ATP-abhängige Chromatin-*Remodeling*-Enzyme nehmen eine Schlüsselrolle bei der Veränderung der Chromatinstruktur ein, indem sie verschiedene Reaktionen, wie beispielsweise die Repositionierung von Nukleosomen entlang der DNA, katalysieren. Trotz der Wichtigkeit von ATP-abhängigen Chromatin-*Remodeling*-Enzymen bei der Regulation der Chromatinstruktur blieben die Struktur und Funktionsweise dieser Proteine weitgehend ungeklärt.

In der vorliegenden Dissertation wurde der Aufbau von prototypischen *Imitation Switch* (ISWI)-Chromatin-*Remodeling*-Enzymen der Fruchtfliege *Drosophila melanogaster* (DmISWI) und des Menschen (Snf2H) mithilfe von integrativen Strukturmethoden untersucht. Die experimentellen Daten aus Protein-*Crosslinking* gekoppelt an hochauflösende Massenspektrometrie und Kleinwinkel-Röntgenstreuung wurden verwendet um computergestützte Modelle der dreidimensionalen Enzymstruktur für verschiedene funktionelle Zustände des Katalysezyklus zu erstellen.

Die Ergebnisse der vorliegenden Arbeit stimmen mit der Vorstellung überein, dass sowohl DmISWI als auch Snf2H in ungebundener Form einen kompakten Ruhezustand in Lösung annehmen. Während die C-terminale *HAND-SAND-SLIDE* Enzymdomäne gegen das ATPase Modul packt, überbrücken die autoregulatorischen NTR und NegC Domänen das Interface beider ATPase Untereinheiten, um die *Remodeling*-Enzyme in einer katalytisch inkompetenten Konformation zu halten. Die Ergebnisse erklären auf struktureller Ebene die gehemmte ATPase-Aktivität von ISWI-Proteinen in Abwesenheit von Substrat. Des Weiteren stützt unser Strukturmodell der DmISWI ATPase Domäne die erst kürzlich mittels Röntgenkristallographie identifizierte ATPase-Konformation der thermophilen Hefe *Myceliophthora thermophila*. Es ist davon auszugehen, dass ISWI-Enzyme in Abhängigkeit von Liganden und/oder Substrat eine Serie von Konformationsänderungen durchlaufen um den Ruhezustand zu verlassen. Die zwei Untereinheiten der ATPase Domäne drehen sich vermutlich relativ zueinander, sodass Aminosäureseitenketten, die an der ATP-Bindung und -Hydrolyse beteiligt sind, sich räumlich nahe anordnen. In Gegenwart des nicht-hydrolysierbaren Nukleotidanalogs ADP-BeF$_x$ und Nukleosomen interagiert das Snf2H-Enzym wahrscheinlich über die *HAND-SANT-SLIDE* Domäne mit der negativ geladenen Region des Nukleosoms. Folglich stützen unsere Strukturdaten des substratgebundenen Snf2H-Enzyms neuste Forschungsergebnisse, dass diese negativ geladene Region des Nukleosoms ein wichtiges Erkennungsmerkmal darstellt und somit eine wichtige mechanistische Rolle bei der ATP-abhängigen Umstrukturierung des Chromatins durch ISWI-Enzyme spielen könnte.

1. Introduction

1.1. Chromatin organization and dynamics

The genetic information of eukaryotic organisms is organized into a compact chromatin structure, which comprises DNA and chromatin-associated proteins. Efficient DNA compaction is essential to pack the DNA into the dimensions of a cell's nucleus and allows for controlled accessibility of genetic information at any given time. The molecular mechanisms that ensure access to the correct DNA sequence are essential for all fundamental nuclear processes such as DNA replication, gene expression, and DNA repair. Despite the groundbreaking achievements in sequencing the entire human genome (2), however, the central principles underlying the regulation of genetic information on a molecular level have remained elusive. A complex network of various factors and mechanisms control the accessibility of genetic information as well as prompt alterations in chromatin structure in response to endogenous and exogenous stimuli (3-7).

The following sections outline the different hierarchical levels of the chromatin structure and delineate the dynamics of this supramolecular assembly.

1.1.1. Nucleosome and chromatin structure

The first level of eukaryotic DNA compaction is achieved by the formation of nucleosomes, the fundamental units of chromatin, which repeat every 160 to 240 base pairs (bp) across the genome depending on the cell type and species (8, 9). Each nucleosome core particle (NCP) consists of approximately 145−147 bp DNA, which is wrapped in roughly 1.65 left-handed, superhelical turns around an octamer of core histone proteins (Figure 1A) (10, 11).

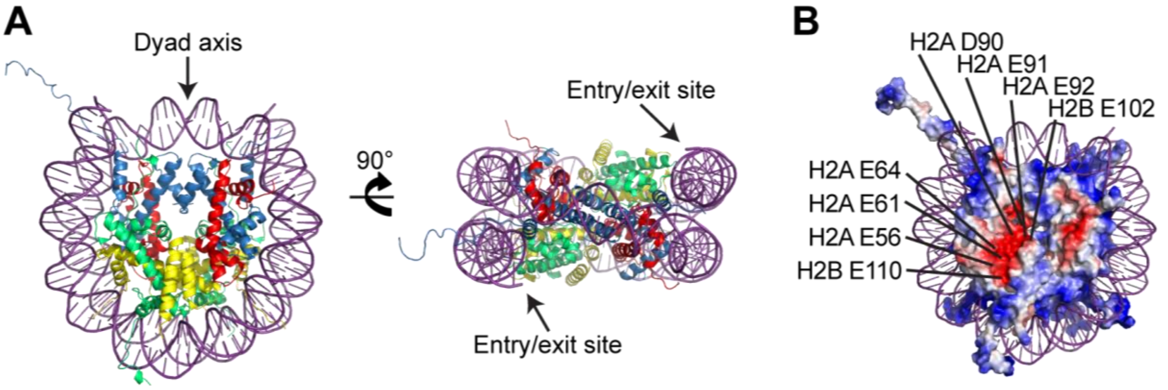

Figure 1: Structure of the nucleosome. (A) The crystal structure (pdb 1AOI) of a nucleosome core particle in top and side view is shown (10). Human alpha-satellite DNA comprising 146 bp (purple) is wrapped around an octamer of *Xenopus laevis* histone proteins (H2A, green; H2B, yellow; H3, blue; H4, red). Histone tails protrude from the surface of the nucleosome and are only partially crystallized. **(B)** Electrostatic surface potential of the nucleosome highlights the acidic patch formed by H2A and H2B residues. The view is identical to (A, left). Negative and positive electrostatic potentials are shown in red and blue, respectively.

The octamer comprises two copies of each of the evolutionarily conserved H2A, H2B, H3, and H4 histone proteins (12-14). Each of these histones has a structured core that includes a characteristic three-dimensional ‘histone fold’ motif. This motif consists of three α-helices being interconnected by two unstructured loops and facilitates the dimerization of histones (15). That is, histones H2A and H2B as well as histones H3 and H4 form heterodimers, which are predominantly stabilized through hydrophobic interactions (15). The H3/H4 dimers arrange in a tetramer and assemble with two H2A/H2B dimers to form the octamer (10, 13). The dynamic N-terminal tail of each core histone and the C-terminal tails of H2A subunits protrude from the NCP. Individual histone tails represent important interaction surfaces for cellular factors and contribute to the formation of higher-order chromatin structures (16, 17).

The disk-shaped histone octamer carries a net positive charge under physiological conditions with basic residues being in particular concentrated along the outer curved edge to form a path for DNA wrapping (Figure 1B). The DNA contacts the histone octamer at regular intervals *via* direct DNA-protein and water-mediated interactions (18). The association of DNA with the histone octamer is described in the DNA superhelix relative to the central bp at the nucleosomal dyad axis as superhelical location (SHL) 0. Alternating regions of the DNA, where the major and minor grooves face the histone octamer, are defined in either direction from SHL 0 as SHL ±1 to ±7 and SHL ±0.5 to ±6.5, respectively. The DNA-histone interactions at these sites are energetically not equivalent (19). Interactions at DNA entry/exit regions are typically weak to facilitate for instance unwrapping of the outer nucleosomal DNA, which might be initiated asymmetrically from one side as suggested recently (20). In contrast, the strongest interaction between the octamer and DNA occurs at the dyad. Notably, energetically weaker contacts are also formed at SHL ±2.5 (19), in close proximity to the SHL 2 region, which acts as binding site for several chromatin remodeling enzymes (21-25).

The complex electrostatic surface of the NCP (Figure 1B) also arises from conserved residues on the H2A/H2B dimer surface. These residues form a negatively charged surface area, termed ‘acidic patch’, which represents an interaction platform for numerous proteins, including the histone H4 tail (26). Recent data also suggest that the acid patch plays an important role during the catalytic cycle of imitation switch (ISWI)-type remodeling enzymes (27, 28). The stability and electrostatic characteristics of NCPs can be affected by the incorporation of histone variants as well as posttranslational modifications (PTMs) of histones (cf. section 1.1.2.1).

Individual NCPs are connected by stretches of linker DNA of varying length (approximately 20–90 bp) in nucleosomal arrays. This primary structure of chromatin, which appeared as ‘beads-on-a-string’ in early electron microscopy studies (29, 30), generates a fiber with a width of 11 nm. Nucleosomal arrays represent fundamental structural entities of chromosomal superstructures and play an important role during the transcription of genetic information (31).

Further compaction of DNA is achieved by the association of linker histones. This class of histones bind proximal to DNA entry/exit sites of NCPs and influence the orientation of linker DNA of adjacent nucleosomes. Multiple isoforms of the mammalian linker histone H1 family have been identified, which differ in their binding affinities to chromatin (32). Linker histones are assumed to stabilize nucleosomes as well as higher-order chromatin structures such as the ‘30 nm fiber’ (32, 33).

The local packing of a nucleosomal array into a coil-like structure of approximately 30 nm in diameter, which was observed under distinct experimental conditions (34, 35), has been defined as the secondary level of DNA compaction. Experimental *in vitr*o data have given rise to various models for the structural arrangement of the ’30 nm fiber’ including the solenoid and zigzag models (36-39). However, conclusive evidence for the existence of the ’30 nm fiber’ *in vivo* is still lacking and the subject of controversial debate (40-44). Recent models of chromatin organization suggest a rather dynamic and irregularly folded chromatin structure composed of 10 nm fibers (45), which challenges previous static models such as the folding into ‘30 nm fibers’. That is, nucleosomal arrays are assumed to interact interdigitated through histone tail and inter-fiber interactions (46). Such folded nucleosome fibers might give rise to higher-order chromatin structures present in interphase chromatin and mitotic chromosomes.

1.1.2. Dynamic regulation of chromatin

The packing of DNA into chromatin clearly restricts the access to genetic information. To assure controlled accessibility in DNA-mediated processes, several strategies have evolved to modulate structural properties of individual nucleosomes and of the higher-order chromatin organization. That is, individual nucleosomes are not static assemblies but were found to exhibit a pronounced dynamic behavior and to be capable of extensive crosstalk with various cellular factors such as chromatin remodeling enzymes (47). For instance, the nucleosome conformation can vary due to the breathing, unwrapping, and opening of DNA (48). The structural properties of nucleosomes depend on various factors including the incorporation of histone variants and/or a large variety of PTMs, which will be described in the following section.

1.1.2.1. Histone variants and of posttranslational modifications

Apart from canonical histones, numerous histone variants have been identified *in vivo*. These histone variants differ in the primary protein sequence from the canonical counterparts and some are expressed throughout the cell cycle. Whereas canonical histones are expressed during S-phase and are deposited in a replication-coupled manner, histone variants are incorporated into nucleosomes in a spatiotemporally uncoupled manner (49, 50). In general, the incorporation of histone variants changes intra-nucleosomal contacts, which in turn can affect the stability of nucleosomes (51, 52). Furthermore, variant nucleosomes exhibit differences in surface-exposed residues, which potentially impact various protein-nucleosome interactions as well as chromatin folding. For instance, nucleosomes comprising the H2A.Z histone variant have an expanded acidic patch region (53), which represents an important interaction platform for many proteins including the ISWI-type remodelers (26-28). Apart from H2A.Z, a multitude of other histone variants is known, in particular for H3 and H2A histones. The enrichment of individual histone variants is frequently associated with distinct functional chromatin states. For example, the H3.3 and H2A.Z variants have been observed to be enriched at transcriptionally active loci (54). Lastly, histone variants have been shown to facilitate the recruitment of cellular components. For instance, the phosphorylated form of H2AX is a key player in the DNA damage response by promoting the recruitment of many additional factors (e.g., Mediator of DNA Damage Checkpoint 1 protein, Mdc1) to the damaged DNA sites (55). New histone variants are still being discovered and their functions in remodeling the chromatin landscape has been a topic of intense research.

Diverse PTMs add an additional level of complexity to the observed nucleosome diversity and potentially affect the function of histone proteins to modulate chromatin structure. Acetylation, methylation, phosphorylation, ubiquitylation, and ADP-ribosylation belong to the better studied

PTMs of histone proteins (56, 57), whereas additional modifications of lysine residues such as crotonylation, succinylation, and malonylation have been characterized more recently (58, 59). Notably, also histone variants represent profound targets for modifications.

Histone PTMs can affect chromatin structure in different ways. That is, PTMs may directly alter histone-DNA or histone-histone interactions giving rise to changes in intrinsic nucleosome dynamics. The modifications predominantly occur at the flexible histone tails, whereas histone cores are less frequent targets for PTMs (57). PTMs on histones are dynamically set and removed by specific enzymes called ‘writers’ and ‘erasers’, respectively. For instance, the acetylation of lysine residues is catalyzed by histone acetyltransferases (HAT) and removes a positive charge, which causes a reduction in the electrostatic interaction with DNA (57). Historically, histone acetylation was described in connection with transcriptional activity as one of the first PTMs (60, 61) and decades later, the development of inhibitors targeting the dynamics of histone acetylation represents a promising avenue for cancer therapy (62).

A PTM of particular interest is H4K16ac. That is, deacetylation of K16 in the basic patch of the H4 tail has been shown to be of functional relevance for heterochromatin formation in both *in vivo* and *in vitro* experiments (63-67). Furthermore, this modification may contribute to the regulation of nucleosome remodeling by ISWI-type enzymes, although the impact of histone acetylation on enzyme activity has been controversially discussed (65, 68-71).

Histone PTMs can also affect chromatin structure in an indirect manner as they are sensed by molecular ‘readers’. Such ‘readers’ are often chromatin remodeling enzymes that harbor specific domains adjacent to the catalytic motor domain or as part of associated subunits. For instance, bromodomains, which are found in numerous subunits of the mating type switching/sucrose non-fermenting (SWI/SNF) family of remodeling complexes (72), are able to bind to acetylated lysine residues (73). Intriguingly, a single nucleosome can exhibit a combination of histone modifications. Thus, PTM patterns on histone proteins may represent a “molecular code”, which can be recognized by chromatin-associated proteins. The presence of combinatorial marks on histone proteins has resulted in the postulation of the ‘histone code’ hypothesis (17, 74), which links histone PTMs to gene regulation. Understanding the seemingly complex nature of modifications of histone proteins and their diverse potential to regulate and fine-tune chromatin organization have been investigated intensely (75, 76).

Aside from the described histone-based mechanisms, additional strategies such as DNA methylation, association of small and long non-coding RNAs, as well as the binding of architectural proteins, such as the non-histone protein heterochromatin protein-1 (HP1), have evolved to modulate the chromatin state and to regulate chromatin-related processes (77-80). Furthermore, chromatin remodeling enzymes play a pivotal role in chromatin dynamics and will thus be further introduced in the subsequent section.

1.1.2.2. ATP-dependent chromatin remodeling

Chromatin remodeling enzymes are generally involved in changing the molecular contacts between nucleosomal DNA and the histone octamer in an ATP-dependent manner (81, 82). These enzymes typically comprise a catalytic core and additional accessory subunit(s). The catalytic core is composed of a central bilobal ATPase domain that shares sequence homology with the superfamily (SF) 2 of helicases. Individual remodeling enzymes are classified into the SWI/SNF, ISWI, INO80 (inositol auxotroph mutant 80), or CHD (chromodomain helicase DNA-binding) families on the basis of unique domains that flank the ATPase lobes (83).

Remodeling enzymes catalyze a diverse set of reactions on their nucleosomal substrate as schematically illustrated in Figure 2. That is, these enzymes facilitate (i) the reposition of nucleosomes along DNA without disrupting the histone octamers (generally referred to as ’sliding’), (ii) the eviction of octamers or histone dimers, (iii) the *de novo* assembly of nucleosomes, (iv) the local unwrapping of nucleosomal DNA, and (v) the exchange/integration of histone variants. Importantly, distinct remodeling enzymes differ in their functionality. For example, members of the ISWI family are known to slide nucleosomes along the DNA strand, sometimes giving rise to evenly spaced nucleosomal arrays as in the case of the ACF complex (84, 85), yet they are not capable of ejecting histone octamers. On the contrary, members of the SWI/SNF family are capable of ejecting histone octamers as well as displacing H2A/H2B dimers (83, 86, 87), but they lack the competency to evenly space nucleosomes (83, 86-88). Notably, chromatin remodeling enzymes represent functionally important components of multi-protein chromatin remodeling factors (cf. section 1.2.1) and are thus found in complex with various accessory proteins *in vivo*.

Given the broad range of catalyzed reactions on nucleosomes, these highly abundant chromatin remodeling enzymes play an essential role in chromatin-related processes ranging from the regulation of transcription activity and DNA repair to more global phenomena such as embryonic development. For instance, the ATP-dependent sliding of nucleosomes allows access to the underlying nucleosomal DNA sequences to initiate critical cellular processes such as gene expression. Consequently, perturbations to this finely balanced system in terms of mutations and misregulation of chromatin remodeling enzymes have been associated with carcinogenesis and other diseases (89, 90). However, inhibition of the remodeling activity also represents a potentially promising strategy in cancer treatment (90, 91).

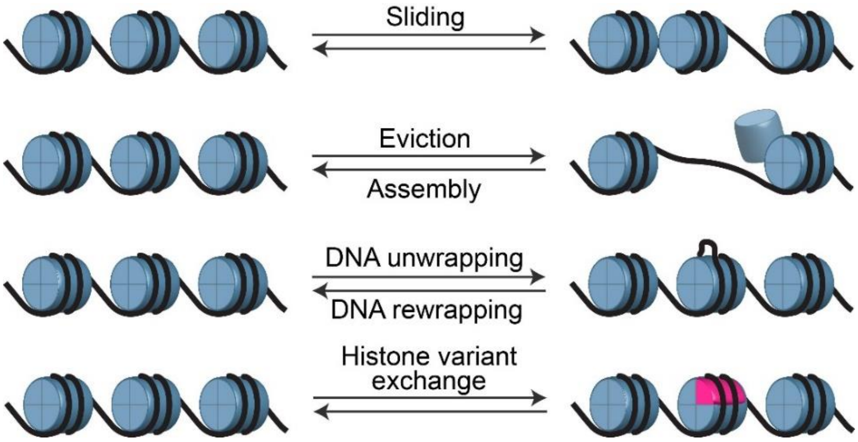

Figure 2: ATP-dependent chromatin remodeling. A schematic illustration of distinct remodeling activities is shown. The reposition (‘sliding’), eviction, and assembly of histone octamers (blue) along DNA (black) results in accessible and/or occluded DNA sites upon remodeling. Similarly, local DNA unwrapping enables the transient access to nucleosomal DNA. Individual remodeling enzymes are also associated with the exchange of canonical histones with histone variants (pink) and *vice versa*.

1.2. ISWI-type chromatin remodelers

1.2.1. Organization of ISWI-type remodelers

The ISWI remodeling enzyme was first purified from *Drosophila melanogaster* (Dm) as the catalytic subunit of the nucleosome remodeling factor (NURF) complex (92, 93). Mammals have two homologs of the catalytic ISWI protein, which are termed sucrose non-fermenting 2 homolog (Snf2H) and sucrose non-fermenting 2 like (Snf2L). Both mammalian enzymes not only share high sequence identity to each other (~ 86%) but they are also highly similar to their *Drosophila* (~ 75%) and yeast counterparts (i.e., Isw1 and Isw2, ~ 65%) (94, 95).

As schematically illustrated in Figure 3A, the DmISWI enzyme assembles with different subunits into distinct multi-protein complexes *in vivo.* Apart from NURF, the DmISWI enzyme was also found to be an essential component in the ACF (ATP-utilizing chromatin assembly and remodeling factor) (85) and CHRAC (chromatin assembly complex) (96, 97) remodeling factors, for which the subunit composition has been evolutionarily conserved between *Drosophila* and mammals. A total of six additional multi-protein remodeling complexes have been identified in humans that comprise either the ISWI-type Snf2H or Snf2L enzyme: RSF (remodeling and spacing factor) (98, 99), NoRC (nucleolar remodeling complex) (100), WICH (WSTF-ISWI chromatin remodeling complex) (101), CERF (CECR2-containing remodeling factor) (102), BRF (BAZ2B- containing remodeling factor) (103), and SNF2H-cohesin (104). The notion that known accessory proteins can interact with both Snf2H and Snf2L has evolved recently in conjunction with the identification of the bromodomain adjacent to zinc finger domain 2B (BAZ2B) protein as seventh accessory factor for both ATPases (103) (Figure 3A).

Individual accessory proteins of remodeling factors may also contribute to the restructuring of chromatin. For instance, the Acf1 protein of the ACF and CHRAC remodeling factors comprises two plant homeodomain (PHD) zinc fingers, which are suggested to improve the efficiency of nucleosome sliding through interactions with the histone octamer (105). The bromodomain PHD finger transcription factor (BPTF) subunit of the human NURF complex represents another example of an accessory protein that comprises PHD fingers. The BPTF subunit furthermore harbors a bromodomain, which plays an important role in anchoring the remodeling factor to nucleosomes by binding to H4K16ac as well as H3K4me3 (106).

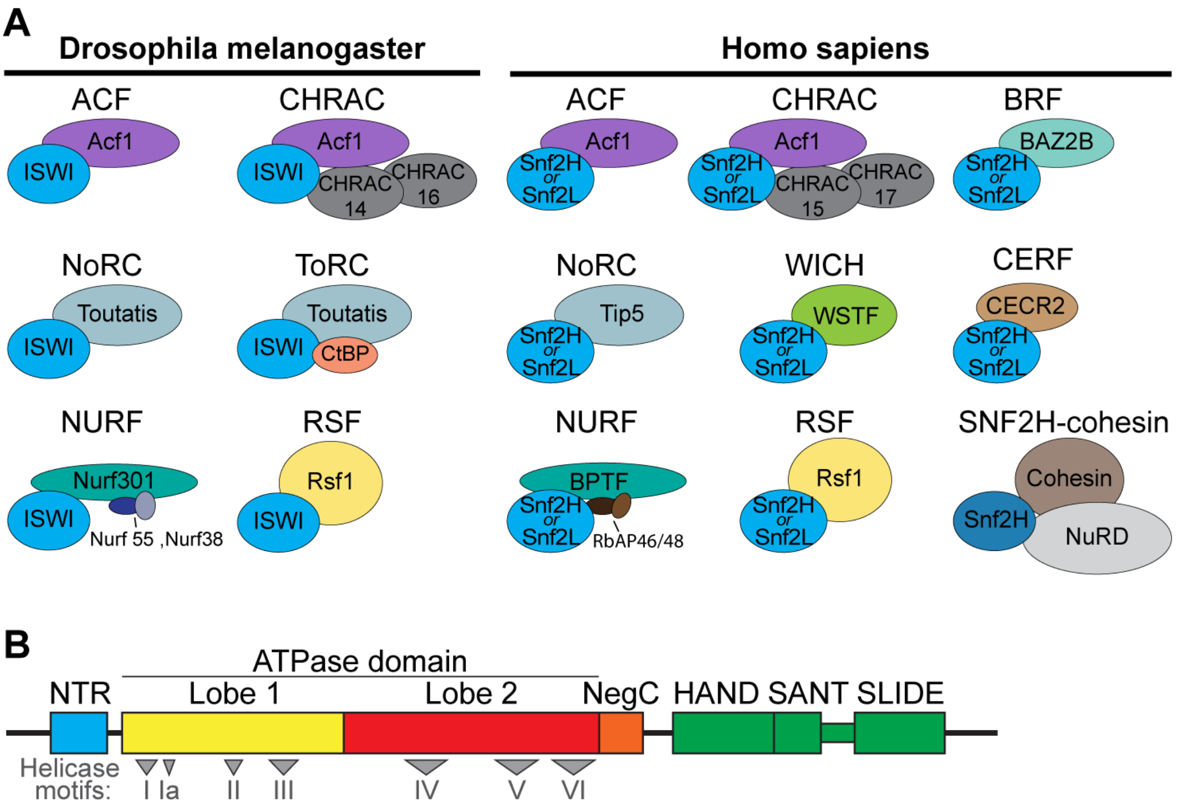

Figure 3: Remodeling factors that comprise ISWI-type enzymes. (A) A schematic representation of the *Drosophila* and human ISWI complexes is shown. The drawing is not to scale. An explanation for each abbreviation can be found in section I. **(B)** Schematic representation of the domain architecture of the *Drosophila* and human ISWI enzyme. The ATPase domain consists of two lobes (yellow and red) and comprises seven sequence motifs (I–VI) typically found in helicase-like enzymes. The ATPase domain is flanked by the N-terminal region (NTR, light blue) and the NegC motif (orange). The NTR and NegC region are implicated in the regulation of the catalytic activity. The DNA-binding HAND-SANT-SLIDE (HSS) domain (green) is located near the C-terminus of the enzyme.

The ISWI-type remodeling enzymes share an overall conserved domain organization (Figure 3B). The ATPase domain is composed of two lobes (i.e., ATPase lobe 1 and ATPase lobe 2), both of which comprise conserved sequence motifs that play an important role during catalysis. Seven sequence motifs are characteristic of SF2 helicases (cf. roman numerals in Figure 3B) and additional conserved sequence blocks have been identified that are typically not found in helicases (107-109). The helicase sequence motif I (i.e., “ILADEMGLGKT”, residues 202−212 and 150−160 in the Snf2H and DmISWI enzymes, respectively) comprises a conserved lysine residue, which is essential for ATP binding (109, 110). Another important motif, named according to the conserved sequence of ATPase lobe 1, is the “DEAH” box (also known as motif II, residues 308−311 and 256−259 in the Snf2H and DmISWI enzymes, respectively). The respective aspartate and glutamate residues have been suggested to be involved in binding of the Mg^{2+} ion and ATP hydrolysis, respectively (111). Two arginine residues in motif VI of ATPase lobe 2 (i.e., “QAMDRAHR”, residues 588−595 and 536−543 in the Snf2H and DmISWI enzymes, respectively) constitute an ‘arginine finger’, which interacts with the ATP γ-phosphate and may stabilizes the transition state during the ATP hydrolysis reaction (112, 113). Importantly, taking into account that these individual motifs facilitate the hydrolysis of ATP in a cooperative manner, it is assumed that the ATPase domain has to adopt a specific conformation with structural motifs being oriented towards each other in order to become catalytically competent.

ATPase lobe 1 and ATPase lobe 2 are adjacent to regulatory domains termed N-terminal region (NTR) and NegC, respectively (114). The NTR exhibits partially conserved motifs (115) such as the N-terminal autoinhibitory region (AutoN), which has been proposed to negatively regulate the ATPase activity of ISWI-type remodeling enzymes (114).

At the C-terminal region, ISWI-type enzymes typically comprise a domain, which is rich in α-helical segments and that can be divided into three characteristic motifs referred to as HAND, SANT, and SLIDE (HSS) as well as a spacer region. The HAND module was characterized by X-ray crystallography and displays four α-helices connected by loop regions in an unique structural arrangement (116). On the contrary, the SANT domain is structurally related to the DNA-binding domain of the transcription factor c-Myb (116, 117) and is furthermore sequence-wise related to the SLIDE (SANT-like ISWI domain) module. The SANT and SLIDE domains contain three α-helices each and harbor a basic and acidic surface patch that are involved in mediating DNA and octamer interactions, respectively (116). In the DmISWI enzyme, the SANT domain is connected to the SLIDE module through a continuous spacer helix of approximately 50 Å in length. The length of the spacer helix varies among related chromatin remodeling enzymes. For instance, the SANT and SLIDE domains are approximately 15 Å closer to each other in the chromodomain-helicase-DNA-binding protein 1 from *Saccharomyces cerevisiae* (ScChd1), relative to the DmISWI enzyme, due to a shorter spacer helix (116, 118).

1.2.2. Mechanism and regulation of ISWI-mediated nucleosome sliding

In order to reposition nucleosomes along DNA, the ATP-dependent chromatin remodeling enzymes have to disrupt DNA-histone interactions without causing the dissociation of the histone octamer. The molecular mechanisms underlying the nucleosome sliding function have remained poorly understood. One experimental challenge in exploring nucleosome sliding relies on the complex series of events that take place during the catalytic cycle. An improved mechanistic understanding for this important class of enzymes may pave the way towards the development of therapeutic strategies to specifically target and regulate ISWI-comprising remodeling factors, which enjoy widespread interest in the scientific community. This section thus aims at describing the interactions between ISWI-type remodeling enzymes and nucleosomes and briefly summarizing current models for nucleosome sliding and the regulation of ISWI-type enzymes.

The ATPase and HSS domains of ISWI-type remodeling enzymes have been demonstrated to directly interact with nucleosomes and DNA. That is, early experiments on ISW2 using site-directed cross-linking suggested that the catalytic ATPase domain engages the nucleosome about two helical turns off the dyad axis at the SHL +2 position (22, 23). In line with this observation, DNA gaps or nicks at different positions in the nucleosome had no major effects on nucleosome sliding by ISWI-type enzymes, only when the gaps or nicks were located near the SHL +2 site (25, 119). The binding mode of the catalytic core of ISWI-type enzymes may represents a common strategy to approach the nucleosomal substrate. The catalytic core of other chromatin remodeling proteins belonging to the SWI/SNF (21, 25, 120, 121), RSC (122), and Chd1 (24, 123) families were also found to interact with the nucleosome at the SHL 2 position. Notably, the region around SHL 2 typically exhibits energetically weak histone-DNA interactions (19) with the mechanistically important H4 tail being in close spatial proximity (10, 115, 124, 125). The remodeling enzyme of the INO80 complex appears to represent an exception considering that the Ino80 protein was found to contact the nucleosome exclusively at SHL –6 (126).

Another functionally important set of intermolecular interactions is formed between the C-terminal HSS domain and DNA (23, 116, 127). The HSS domain of the ScIsw2 enzyme has been observed to contact approximately 30 bp of DNA. That is, while the SLIDE module binds to extranucleosomal DNA 19 bp away from the entry site, the HAND region contacts between 11–13 bp of nucleosomal DNA (22, 23). Interestingly, the structurally related SANT-SLIDE (SS) domain of the ScChd1 enzyme has also been identified to interact with extranucleosomal DNA at a similar position (24, 118, 123, 128). However, the interaction interface is presumably not static during the catalytic reaction. Recent studies on the Snf2H enzyme suggest that the HSS domain is not permanently bound to flanking DNA during the catalytic cycle (28, 129).

Instead, the experimental findings imply that the HSS domain is released from the flanking DNA stretch prior to the DNA translocation event and may interact with the nucleosome core.

A critical question that remains to be answered in chromatin research is how ATP hydrolysis is mechanistically coupled to nucleosome sliding. Several distinct models for the molecular mechanism of the ATP-dependent repositioning of nucleosomes have been proposed, which are the subject of controversial debate. For instance, in the ‘twist diffusion’ model the remodeling enzyme introduces a twist defect in the DNA such that the DNA then propagates around the octamer shifting the nucleosome by 1 bp at the time (130, 131). On the contrary, in the ‘loop propagation’ model, individual remodelers are thought to initiate the sliding reaction by detaching DNA from the octamer at the entry site giving rise to the formation of a DNA loop, which then propagates around the octamer and resolves at the DNA exit site of the nucleosome (132, 133). Notably, the twist diffusion and loop propagation models may not be mutually exclusive and perhaps both mechanisms occur in nucleosomes depending on other factors such as the underlying DNA sequence (134, 135). However, several single-molecule studies have pointed towards a sliding mechanism, which cannot be explained by the above mentioned models. For instance, it was shown that ACF and RSC reposition nucleosomes in a step size > 1 bp (i.e., nearly 7 or 3-4 bp and 2 bp, respectively) as suggested by the ‘twist diffusion’ model (136, 137). In addition, it was demonstrated that the ISWI enzyme repositions nucleosomes such that a stretch of DNA is first translocated to the exit site (138), which stands in contrast to the formation of a DNA loop, but might be explained by local under-twisting of DNA (139). Consequently, the combination of complementary biochemical, biophysical, and computational approaches might pave the way towards the definition of a common nucleosome sliding mechanism and/or the identification of mechanistic differences between remodeling enzymes of distinct families.

The molecular regulation of the ATPase activity represents another important aspect of the chromatin remodeling mechanism. It is remarkable that the DmISWI ATPase module on its own is capable of carrying out fundamental aspects of the nucleosome remodeling reaction (140). That is, ISWI lacking its HSS domain exhibits an intrinsic ability to bind and move nucleosomes along DNA. The HSS domain potentially plays an important role in increasing the affinity and specificity of the remodeling enzyme for its nucleosomal substrate. Consequently, accessory domains of chromatin remodeling enzymes may have evolved to modulate the catalytic activity. This notion is furthermore supported by the identification of the autoregulatory NTR and NegC domains (114), which flank the catalytic core.

The structure and function of the NTR region have not been completely characterized. As outlined in the previous sections, the NTR domain comprises several motifs such as AutoN, for which the primary sequence shares similarities with the basic patch of the histone H4 tail (114). Sequence-related changes to the AutoN motif, i.e. substitution of two arginines to alanines, generate an enzyme that no longer requires the H4 tail for high levels of ATPase activity and nucleosome sliding and even allows the ISWI enzyme to more effectively use free DNA to stimulate ATPase activity (114). Based on the identification of the AutoN region, it was inferred that this motif may inhibit enzyme activity by binding to the ATPase domain in the absence of the nucleosomal substrate. The H4 tail was proposed to compete with the AutoN region for the interaction site on the ATPase domain and to displace the inhibitory NTR motif in the presence of substrate. However, this model of activity regulation by the NTR region has recently been challenged by experimental data that pointed towards a more sophisticated, non-competitive mechanism (115). That is, the binding sites for AutoN and the histone H4 tail were shown to be adjacent to each other but did not overlap on ATPase lobe 2 of the DmISWI enzyme. Furthermore, the study revealed that in the absence of nucleosomes, the AutoN region cooperates with the AcidicN motif of the NTR domain in order to retain an inactive conformation of the DmISWI protein.

Apart from the NTR domain, the NegC region has been shown to negatively influence the activity of chromatin remodeling enzymes. In the crystal structure of the ScChd1 protein (pdb 3MWY), the NegC region bridges both ATPase lobes thereby locking the ATPase module in a catalytically incompetent conformation (141). Consequently, the NegC region has been suggested to prevent the efficient coupling of ATP hydrolysis to nucleosome sliding in the absence of nucleic acids. Consistent with the proposed mechanism of inhibition, deletion of the NegC region has been found to enable nucleosome sliding in an ISWI construct lacking its DNA-binding domain (114).

The activity of the DmISWI enzyme is positively regulated by two nucleosomal features. As mentioned above, the ATPase domain of DmISWI generally engages the nucleosome at the SHL +2 position, which is in close spatial proximity to the protruding N-terminal H4 histone tail. Interestingly, the ATPase activity of the DmISWI enzyme has been shown to rely on the interaction with the H4 tail (124). In particular residues $R_{17}H_{18}R_{19}$ of the basic patch of the H4 tail appeared to be crucial to enhance chromatin remodeling activity (71, 142, 143).

Flanking DNA represents the second nucleosomal feature that impacts the remodeling activity of the ISWI protein. That is, flanking DNA above a certain length threshold is associated with a stimulated remodeling activity (84, 129, 144). For instance, mononucleosomes with 20 bp of flanking DNA were remodeled at a slower rate by the Snf2H enzyme than mononucleosomes comprising > 40 bp of flanking DNA. Furthermore, the ACF complex has been shown to be able to distinguish linker lengths of up to 60 bp (84). In the context of nucleosome arrays, the ability to sense the length of DNA flanking either side of a nucleosome preferentially results in nucleosome sliding towards the longer DNA stretch and may enable evenly spaced NCPs (22, 84). The flanking DNA length sensitivity of ISWI-type remodeling enzymes has predominantly been attributed to the HSS domain (89). Consistent with this notion, ISWI lacking its HSS domain slides mononucleosomes and remodels nucleosome arrays at a decreased rate with similar results being reported for the ScChd1 protein (140, 145). However, the underlying mechanisms of DNA sensing by the HSS domain and molecular details how the information is propagated to the catalytic core have remained elusive. A potential role of the regulatory NegC region in the DNA sensing mechanism has been controversially discussed. That is, the NegC domain has been observed to affect the DNA sensitivity of distinct remodeling enzymes (e.g., Snf2H and MtISWI) (129, 146), whereas the sensitivity of the ACF complex does not appear to rely on the regulatory domain (147).

An additional regulatory potential is offered by the way how individual remodeling enzymes engage the nucleosomal substrate. Whereas the ScChd1 enzyme slides nucleosomes as a monomer (148, 149), the Snf2H protein was shown to act as a dimer on the nucleosome (150). The dimeric architecture of the Snf2H enzyme is associated with an enhanced remodeling activity and bidirectional movement (129, 150). The related ScISW1a protein in turn has been proposed to interact simultaneously with two nucleosomes (151).

Taken together, the activity of ISWI-type enzymes is regulated in a highly complex manner involving inhibitory accessory domains and the structural interplay with the nucleosomal substrate. One may speculate that the regulation is even more complex *in vivo* considering that chromatin remodeling enzymes are essential components of the much larger, multi-protein remodeling factors. That is, the accessory proteins of such remodeling complexes may hold the potential to additionally modulate the ATPase activity of remodeling enzymes. Furthermore, the incorporation of histone variants and/or PTMs in the nucleosomal substrate may fine-tune the activity of remodeling enzymes *in vivo*. However, the fundamental mechanisms underlying nucleosome sliding by ISWI-type enzymes are still not fully understood.

1.2.3. Structural information about remodeling enzymes

The establishment of detailed structure-function relationships for individual remodeling enzymes is believed to pave the way towards an improved mechanistic understanding of how chromatin remodeling is performed on a molecular level. However, high-resolution structural information about remodeling enzymes in terms of X-ray crystallographic data have proven difficult to obtain and are thus sparse and in most cases limited to isolated domains of the studied enzyme. The following section aims at summarizing available high-resolution structural data for remodeling enzymes that are relevant to this study.

As of today, a full-length high-resolution structure of an ISWI-type enzyme is lacking. Attempts to crystalize the full-length DmISWI enzyme have remained unsuccessful. However, limited proteolysis analysis of the DmISWI enzyme suggested compact protein segments with one fragment being suitable for crystallization and X-ray diffraction (116). The fragment turned out to correspond to the HSS domain comprising residues 691–991 of the DmISWI enzyme. The structure (pdb 1OFC) revealed four modules that are rich in α-helical regions (cf. section 1.2.1.). In addition, the structure of the HSS domain of the ScIsw1 enzyme ($\mathrm{HSS}_{\mathrm{ScIsw1}}$) has been solved (pdb 2Y9Y), which displays identical secondary structural elements as indicated by a root-mean-square deviation (RMSD) of 2.8 Å (151). In the same study, the structure of the $\mathrm{HSS}_{\mathrm{ScIsw1}}$ in complex with a 31 bp DNA fragment (pdb 2Y9Z) was determined, which shows that the SANT and SLIDE modules bind to DNA minor grooves. The observed binding mode of the $\mathrm{HSS}_{\mathrm{ScIsw1}}$ thus slightly differs from the structurally related DNA-binding domain of the cMyb protein. The comparison of the $\mathrm{HSS}_{\mathrm{ScIsw1}}$ structures, in the absence and presence of DNA, suggests that the DNA-binding module is rigid, a feature which may be shared across individual members of the ISWI family (116, 151).

The catalytic cores of several chromatin remodeling enzymes have been successfully crystallized depicting a vast diversity in the relative orientation of both ATPase lobes to each other (Figure 4). In the case of the ScChd1 structure (pdb 3MWY), which represented the most closely related enzyme with available structure in the beginning of the PhD project, both ATPase lobes are held apart in a presumably inactive, open conformation (141). The ATPase activity of the ScChd1 protein appears to be regulated by N-terminal chromodomains, which mask the catalytically important motifs (141). In contrast, ATPase lobes and conserved structural motifs of the Rad54 protein have been captured in much closer spatial proximity to each other in the respective structure (pdb 1Z3I) (109). This arrangement of the two ATPase lobes in Rad54 may reflect structural characteristics that are compatible with ATP hydrolysis activity (152). Crystallographic efforts on enzymes from the yeast *Myceliophthora thermophila* (MtSnf2 and MtISWI) have resulted in two structures (pdb 5HZR and 5JXR), which depict the catalytic domain in a presumably inactive conformation with conserved structural motifs pointing towards opposite directions (146, 153). Importantly, the MtISWI structure (pdb 5JXR) revealed a novel orientation of both ATPase lobes and comprised atomic coordinates for large parts of the flanking NTR and NegC domains (146). Notably, the NegC module of the MtISWI enzyme protrudes from the otherwise compact ATPase domain to interact with an adjacent protomer in the crystal. The orientation of the NegC region in the MtISWI structure is thus substantially different to the one observed for the ScChd1 enzyme (pdb 3MWY), in which the corresponding 'brace-bridge' segment (also referred to as 'NegC' hereafter) bridges both ATPase lobes of the same molecule (141). These pronounced differences in the arrangement of both ATPase lobes among Snf2-related enzymes raise the question whether the static snapshots reflect physiologically relevant conformations. It has furthermore remained unclear how the orientation of helicase-related motifs cooperatively function to couple DNA binding and ATP hydrolysis to chromatin remodeling.

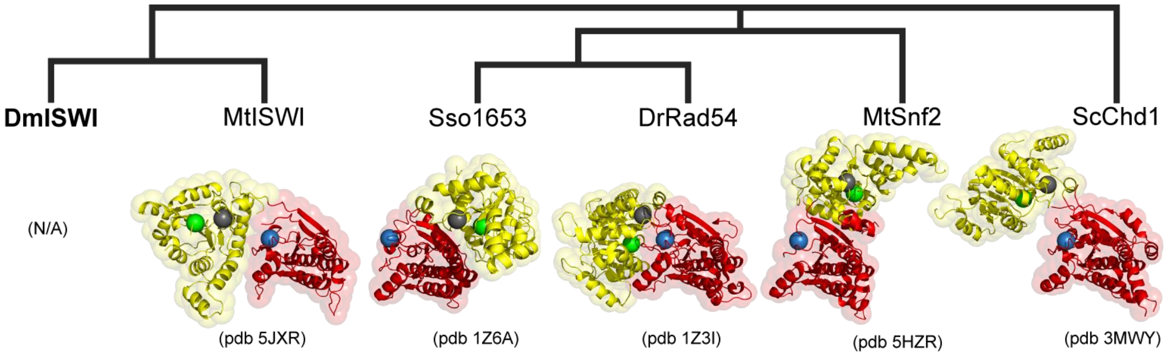

Figure 4: Available apo crystal structures of Snf2-type ATPases differ in the relative orientation of both ATPase lobes. A phylogenetic tree depicts the evolutionary relationship of the DmISWI enzyme to Snf2 ATPase domains, for which crystal structures are available (109, 141, 146, 153, 154). The crystal structures are all aligned to ATPase lobe 2 (red). The relative orientation of ATPase lobe 1 (yellow) to lobe 2 varies drastically among the presented structures. Spheres indicate the position of motifs implicated in ATP hydrolysis (grey, motif I; green, motif II; blue, motif VI). The crystal structure of MtSnf2 lacks electron density for motif VI and thus the position of the closest neighboring amino acid is indicated instead. N/A: not available. Dm: *Drosophila melanogaster*; Mt: *Myceliophthora thermophila*; Sso: *Sulfolobus solfataricus*; Dr: *Dario renio*; Sc: *Saccharomyces cerevisiae*. The figure was adapted from (1) in accordance with Elsevier's policies.

Very recently, the high-resolution cryo-EM structure of the ScChd1 enzyme in complex with its nucleosomal substrate (pdb 5O9G) represented a groundbreaking achievement in chromatin research (24). The corresponding structure provides molecular cues for the binding mode between the monomeric ScChd1 enzyme and its nucleosomal substrate while showing consistency with previous low-resolution structural data for the protein (155). The ATPase domain adopts a closed, presumably active conformation and interacts with nucleosomal DNA at the SHL +2 position. The ATPase module is furthermore anchored to the N-terminal histone

H4 tail in a similar manner as observed in the MtSnf2 ATPase-nucleosome complex (pdb 5JXR) (21) and in agreement with structural data for the DmISWI enzyme (115). The SS domain of the ScChd1 enzyme formed interactions with detached DNA, in close spatial proximity to the SHL –7 position and the N-terminal chromodomains. As such, the crystallographic results by Farnung and co-workers differ from the low-resolution structural data for the Snf2H enzyme, which suggest that a dimer of ATPases interacts with the nucleosome in a coordinated manner (150).

1.3. Structural techniques to study chromatin remodeling enzymes

X-ray crystallography represents a powerful approach to elucidate the structural architecture of chromatin remodeling enzymes, and thus has significantly contributed to our understanding of this important class of proteins. Individual crystal structures have established a structural and functional framework and given rise to mechanistic models for chromatin remodeling. However, these X-ray structures represent static snapshots of presumably highly dynamic remodeling enzymes and they have often been obtained using non-native conditions during the sample preparation procedure. Consequently, complementary biophysical and computational approaches are needed to study the higher-order structure and dynamics of individual remodelers in a more native-like environment in solution in order to comprehensively understand the molecular mechanisms underlying the chromatin remodeling activity. A variety of biophysical approaches including electron microscopy (EM) (21, 24, 123, 126, 150, 155, 156), small angle X-ray scattering (SAXS) (148, 155), protein-protein and protein-DNA cross-linking (22, 23, 28, 115, 123, 155-157), fluorescence resonance energy transfer (FRET) spectroscopy (28, 129, 138, 148, 150, 155, 158, 159), and electron paramagnetic resonance (EPR) spectroscopy (150, 159) have been applied to chromatin remodeling enzymes. The results from these biophysical measurements have substantially contributed to our understanding of chromatin remodeling by highlighting for instance the dynamic nature of chromatin remodeling enzymes in solution and providing insights into the interaction with the nucleosomal substrate.

1.3.1. Small angle X-ray scattering

As of today, SAXS represents a powerful and popular approach to characterize the higher-order structure and interactions of proteins under close-to-physiological conditions in solution (160, 161). The fundamental principles of SAXS were developed in the late 1930s.

In a conventional SAXS experiment, the sample solution containing macromolecules is exposed to high-energy X-rays of a specific wavelength, which scatter elastically dependent on the size and shape of the studied macromolecules, giving rise to a spatially averaged intensity distribution (161-163). The scattering intensity ($I(q)$) is detected as a function of scattering vector length (q), which is defined as

$$q = \frac{4\pi\, sin\theta}{\lambda}$$

, where θ corresponds to half the scattering angle and λ signifies the radiation wavelength. Structural information about the macromolecules present in the sample solution can be derived from the scattering profile. That is, the radius of gyration (R_g), which is an important parameter for describing the size of the macromolecule, can be extracted by the Guinier approximation (valid in the low q-range) according to the following equation

$$lnI(q) = lnI(0) - \frac{{R_g}^2\, q^2}{3}$$

, where $I(0)$ signifies the zero angle scattering intensity (164). A monodisperse sample results in a linear Guinier plot, whereas aggregation is seen as a non-linear dependence (165).

SAXS analysis furthermore allows for the assessment of the folding state of the target macromolecule based on Kratky plots. That is, in the Kratky representation, where (q) is plotted against ($I(q)q^2$), one observes a bell-shaped curve for globular, folded macromolecules, whereas extended and/or unfolded particles exhibit a plateau or a slight increase in the larger q-range (166). Notably, the comparison of SAXS-derived structural parameters for the target protein across distinct steady-state conditions sometimes point towards conformational differences between studied states. For instance, the comparison of SAXS data may reveal a ligand-induced compaction of the overall protein shape if the R_g value is decreased in the ligand-bound state relative to apo state conditions (167-169).

Lastly, SAXS data can be used for *ab-initio* shape reconstruction giving rise to three-dimensional, low-resolution (i.e., 10–30 Å) models of biomolecules in solution (170). To evaluate the quality of the computationally generated *ab-initio* models with respect to experimental SAXS data, the χ-value (or alternatively χ^2) is commonly used (171). This value reports on the goodness of the fit as discrepancy between the calculated, theoretical scattering intensity of the model and the experimental scattering data. Consequently, the χ-value is 0 for two identical scattering profiles and increases for dissimilar profiles. Notably, the χ-acceptance criterion for computed models differs among individual SAXS studies with upper limits being reported ranging from 2 to 5 (172, 173).

Numerous structural studies on chromatin remodeling enzymes, including human CHD4 (174), ScChd1 (155), and MtSnf2 (153), have substantially benefited from SAXS analysis. Furthermore, integrative modeling strategies haven recently proven valuable to translate the SAXS-derived scattering data into high-quality models of protein-protein complexes (175).

1.3.2. Protein cross-linking coupled to mass spectrometry

Protein cross-linking coupled to mass spectrometry (XL-MS) was introduced more than 15 years ago (176) and represents a valuable approach in structural biology to gain structural insights on biomacromolecules in solution. Ongoing developments in MS instrumentation and cross-linking agents, as well as advances in bioinformatics have substantially improved the XL-MS technique to provide important structural information about individual proteins and protein complexes, for which no higher-resolution data (e.g., X-ray crystallography and NMR) can be obtained (177). Protein cross-linking generally involves the reaction of a cross-linking agent with functional groups of the target molecule(s) resulting in the formation of a covalent bond. These reactive residues have to be in spatial proximity in order for a cross-link to be formed. Notably, the maximal spanned distance between two reactive residues differs for individual cross-linking agents and typically ranges from 0 Å to more than 35 Å (178). This distance dependency of cross-linking reactions in turn allows the cross-linking agent to act as a molecular ruler (179) providing information about the higher-order structure (e.g., orientation of individual domains and protein-protein interfaces) of the target protein(s) in solution.

The conventional XL-MS workflow can be divided into distinct steps including (i) the cross-linking reaction, (ii) the enzymatic digestion of the target protein, (iii) LC-MS/MS analysis, and (iv) the identification of cross-linked products. Each of these steps is important for the success of the XL-MS experiment and will thus be further introduced in the subsequent paragraphs.

Different strategies for protein cross-linking have been described, which can be classified as targeted and untargeted approaches (180). Notably, both cross-linking strategies have experimental advantages and can complement each other.

In a targeted cross-linking approach, an unnatural, photo-crosslinkable amino acid (e.g., *p*-benzoyl-L-phenylalanine, Bpa) is genetically engineered at a desired position into the target protein. The Bpa amino acid (Figure 5A) can be site-specifically incorporated into the polypeptide chain in response to an amber stop codon (TAG) using an orthogonal tRNA/aminoacyl-tRNA synthetase pair (181). UV irradiation of the Bpa amino acid induces oxidative radicals, which facilitate the formation of a covalent cross-link. The Bpa residue exhibits a broad reactivity towards different amino acids, even though the benzophenone moiety has been observed to preferentially react with surrounding methionine side chains (182).

In an untargeted cross-linking approach, a chemical cross-linking agent is added to the sample solution. Chemical cross-linkers comprise reactive groups that are capable of covalently binding to specific functional groups. In the present study, the chemical cross-linkers BS^3 and BS^2G were employed, which comprise two reactive N-hydroxysuccinimide (NHS) ester groups on each end of a spacer arm of defined length (Figure 5A). The NHS esters are designed to form a covalent adduct with primary amines, which are present at the N-terminus of each polypeptide chain and in the side chain of lysine residues (Figure 5B). However, these cross-linking reagents are susceptible to hydrolysis and have been observed to sometimes react with serine, threonine, and tyrosine residues (183, 184). Furthermore, isotope-labeled cross-linking agents have become commercially available, in which certain atoms are substituted with heavy stable isotopes (185). For instance, a total of four hydrogens are replaced with deuterium atoms in the “heavy” form of the BS^3 cross-linker (BS^3-D_4, Figure 5A). Some studies rely on the simultaneous use of heavy and light cross-linking reagents to enhance the identification success of chemically cross-linked peptides (186, 187), which in mass spectra appear as two peptide envelopes that are separated on the mass-to-charge (m/z) scale with a mass shift according to the isotope label. In addition, isotope-labeled cross-linkers enable the relative quantification of cross-linking candidates to investigate the dynamics of the target protein(s) (188). That is, the probability of a cross-linking reaction and thus the yield of a cross-linked product is tightly coupled to the conformation of the target protein(s). Consequently, conformational differences in the target protein(s) in response to changed steady-state conditions can be revealed by calculating the extracted ratios between heavy- and light-labeled cross-linking candidates (189).

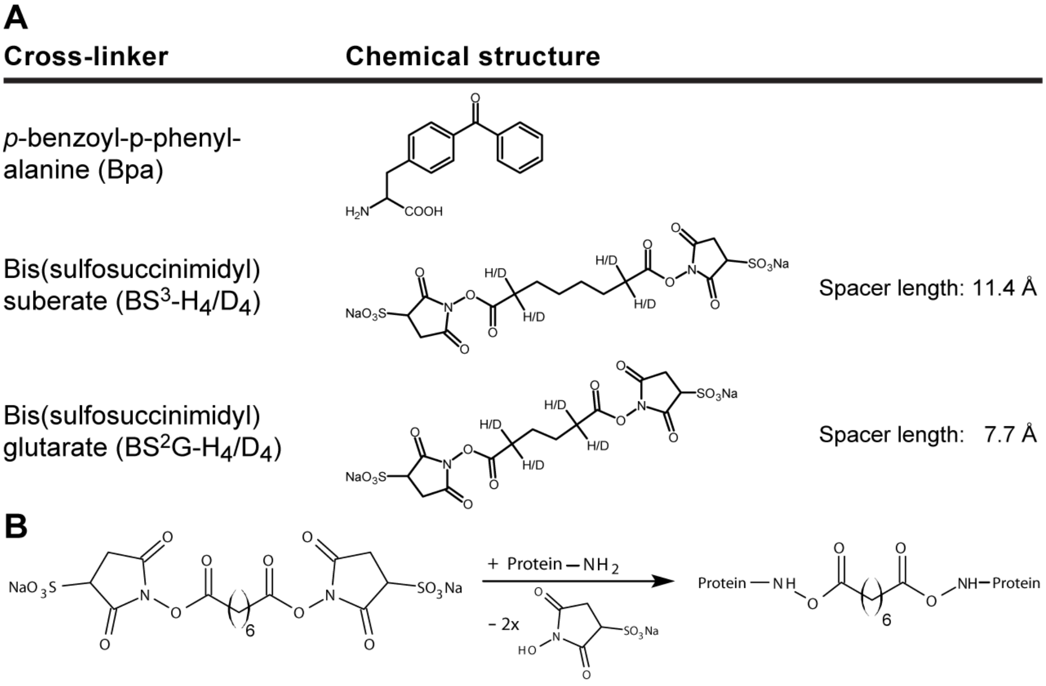

Figure 5: Cross-linking agents. (A) The chemical structures for the BS^3 and BS^2G cross-linking agents as well as the photo-reactive amino acid Bpa are shown. The chemical BS^3 and BS^2G cross-linkers comprise identical Sulfo-NHS ester groups at either end of a spacer arm of defined length. **(B)** An exemplary reaction scheme for protein cross-linking by NHS-esters is shown. The NHS esters of the cross-linking agent BS^3 predominantly react with primary amines (-NH_2) of the target protein(s).

Following UV-induced or chemical cross-linking, protein samples are subjected to enzymatic proteolysis. In most XL-MS studies, trypsin is employed to cleave the target protein into smaller peptides due to its high proteolytic activity, robustness, and substrate specificity (180, 190). Trypsin cleaves the polypeptide chain C-terminally to arginine and lysine residues giving rise to a mixture of peptides with often favorable properties in terms of length, charge, and fragmentation behavior during MS/MS analysis (191). For instance, tryptic peptides typically comprise at least two positively charged residues located at the N- and C-terminus, which is beneficial for MS analysis in positive ionization mode. Consequently, the tryptic sample mixture comprises unmodified linear peptides and the desired inter-peptide cross-linking products, but it also includes so called “loop-links” (i.e., two reactive groups cross-linked within a single peptide) and “mono-links” (i.e., a single peptide modified with a hydrolyzed cross-linker) (Figure 6A) (192). Although mono-links generally do not provide distance information, they report on solvent accessibility and the relative reactivity of individual residues of the target protein(s) in solution (193). In the case of a targeted cross-linking approach using the unnatural Bpa amino acid, UV irradiation occasionally results in the unwanted elimination of hydrogen atoms from nearby amino acids without formation of a cross-linked product (157, 194).

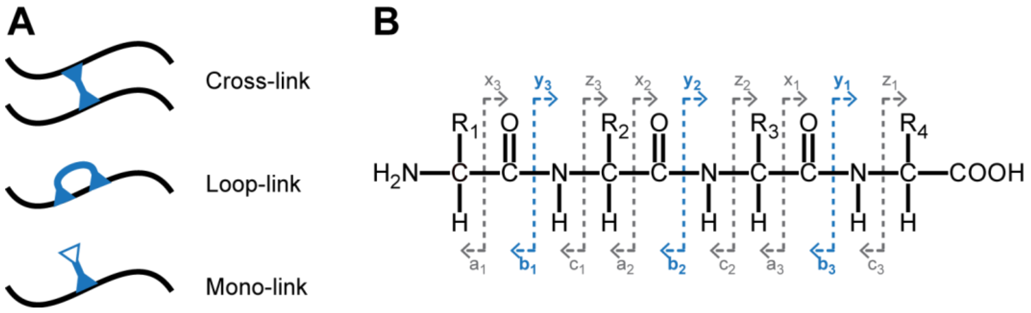

Figure 6: Cross-linking products and the Roepstorff and Fohlman nomenclature. (A) A schematic illustration of cross-links, loop-links, and mono-links is shown. The cross-linking agent and individual peptides are colored in blue and black, respectively. **(B)** Roepstorff and Fohlman nomenclature (195) for fragment ions observed in an MS/MS spectrum. The dashed lines indicate the site at which the peptide backbone is cleaved with arrows pointing towards the product ion. Fragment ions are labeled as a, b, c, x, y, and z depending on the cleavage site and which side retains the charge. Fragmentation by CID predominantly results in the cleavage of the peptide bond giving rise to b- and y-ions (blue). The fragment ions are furthermore labeled with a subscript number corresponding to the residue count and a superscript number (not indicated) specifying the charge state. R, amino acid side chain.

The complex sample mixture is usually desalted and separated by reversed-phase liquid chromatography (LC) and peptides gradually eluted into a high-resolution mass spectrometer for mass analysis. That is, peptides are transferred from solution into the gas-phase using electrospray ionization (196, 197) and analyzed in MS1 mode to deduce the m/z ratio of the precursor ions. Alternatively, analyte molecules are selectively filtered based on their m/z value and subjected to collision-induced dissociation (CID) to produce a set of fragment ions that allow sequence assignments (i.e., MS/MS analysis or MS2 mode). The precursor ions are thereby accelerated into a gas-filled collision chamber. Upon collision with inert gas molecules, the high kinetic energy is converted into vibrational energy, which causes the breakage of peptide bonds in the analyte molecules (198). Consequently, fragmentation of peptides by CID predominantly results in the generation of N-terminal “b-ions” and C-terminal “y-ions” (195) (Figure 6B), which can be used to deduce the sequence of the analyte molecules during MS/MS analysis (199).

In a final step, the LC-MS/MS data is analyzed using specialized software such as ‘Crossfinder’ (200), which matches the observed precursor masses and fragment ions of identified cross-link candidates with the sequence of the target protein(s). Given the complexity and diversity of cross-linking products, in particular in chemical cross-linking experiments, the analysis of LC-MS/MS data is primarily a computational challenge (201). Individual sequence assignments for cross-linked products are primarily validated by three distinct approaches (186). These include a score-based evaluation of the quality of the match between experimental and predicted fragmentation data of a given cross-link candidate as well as the implementation of false discovery rates (FDRs) to minimize the number of false positive identifications (186). Furthermore, individual sequence assignments should ideally be verified by manually inspecting the fragmentation spectra for a given cross-link candidate.

Despite being straightforward in theory, XL-MS analysis of proteins and protein complexes is often challenging due to various technical and biological reasons, which will be described in the following paragraphs.

Cross-linked peptides are typically of low abundance in the proteolytic reaction mixture resulting in suboptimal signal intensities during MS and MS/MS analysis. A possibility to overcome this technical challenge is to selectively enrich the cross-linked peptides prior to LC-MS/MS analysis, for example by size-exclusion chromatography, cation exchange chromatography or purification through an affinity tag (202). However, even in enriched samples only a subset of all cross-linked peptides is typically detected during MS analysis due to either unfavorable ionization properties of the analyte molecules and/or ion suppression by interfering ion species. Thus, even though a particular cross-link is present in the sample solution, it is sometimes difficult to obtain fragmentation data of sufficient quality that allows an unambiguous identification of the candidate and/or the localization of cross-linking sites. Ion suppression is an inherent problem in LC-MS analysis, which in some instances may be counteracted by sophisticated chromatographic separation strategies and extensive sample cleanup (e.g., enrichment of cross-linked products) (203).

To be a proper target for the chemical cross-linking agent, reactive residues are ideally well distributed across the target protein(s) with corresponding side chains being accessible to the cross-linking agent. Accessibility is in most instances warranted if the reactive residue is located on the protein surface and/or occupies solvent-exposed regions. The formation of a cross-link between two distant sites furthermore requires that the bridged path lead through solvent-occupied space such that there are no steric clashes between the cross-linking agent and individual segments of the target protein(s). Consequently, one may observe substantially different experimental outcomes for individual cross-linking agents that differ in their functional groups and/or the length of the spacer arm. The formation of a cross-link generally implies that the corresponding residues were in sufficiently close proximity to each other and were accessible to the cross-linking agent. Consequently, the comparison of cross-linking data sometimes allows for the identification of conformational differences in the target protein(s) across different steady-state conditions. That is, conformational rearrangements in the target protein(s) can give rise to changes in the relative distance between two reactive residues, sometimes resulting in the loss and gain of established and novel cross-linked products during LC-MS/MS analysis, respectively. However, slight conformational differences often remain undetected, if the changes in the distance between reactive residues are beyond the resolution limit of the XL-MS approach. Considering that proteins are inherently dynamic, XL-MS data report on the sum of cross-links that can be formed from an ensemble of distinct structures present in solution (179). The assignment of identified cross-links to distinct, often unknown protein states of a conformational ensemble is currently not feasible. Thus, the target protein is ideally trapped in a desired, physiologically relevant conformation prior to the cross-linking reaction in order to ease the interpretation of XL-MS results.

In principle, any biophysical technique that relies on the covalent modification of the target protein could give rise to structural artefacts in the studied molecule. For instance, the covalent binding of the cross-linking agent may bias the conformational ensemble of the target protein towards infrequent or even physiologically irrelevant solution-phase states. Several studies, in which XL-MS data are compared to high-resolution structures, have not provided experimental evidence for such cross-linking-induced structural artefacts in the investigated proteins (204-206). However, in a recent study by Rozbesky *et al.* (207), it appears that chemical cross-linking may cause local structural perturbations to the target protein, whereas the overall protein fold is well preserved even at an elevated cross-linker to protein ratio.

Despite the above mentioned methodological challenges, the rapidly increasing number of studies, in which XL-MS is applied to probe the conformation and structural architecture of proteins and protein complexes in solution, underscores the usefulness of the approach in protein science. The XL-MS technique has proven to be in particularly powerful in combination with complementary biophysical methods (e.g., SAXS) and computational modeling (cf. section 1.3.3). For instance, XL-MS-derived distance restraints are often used during computational docking of protein complexes. Selected scientific achievements that underline the power of XL-MS analysis include the chromatin remodeling complexes INO80 (156) and SWR1 (208), transcription- and translation-related protein complexes (e.g., RNA polymerase and the translation initiation complex) (209-213), ribosomes (214), chaperons (215-217), and complexes involved in exchange and trafficking of molecules (e.g., nuclear pore complex and the exocyst complex) (218, 219).

1.3.3. An integrative structural approach to study the topology of ISWI-type remodeling enzymes

Given the importance of ISWI-type chromatin remodeling enzymes in the regulation of fundamental nuclear processes, we set out to study the structural architecture of two of these proteins, DmISWI and human Snf2H, by means of an integrative structural approach (Figure 7). The approach combines experimental data from XL-MS and SAXS analysis to guide the computational modeling of the higher-order structure of the remodeling enzymes. The combination of biophysical methods and computational modeling has previously proven useful for the structural characterization of proteins and/or protein complexes, for which no higher-resolution data (e.g., X-ray crystallography) could be obtained (162, 220).

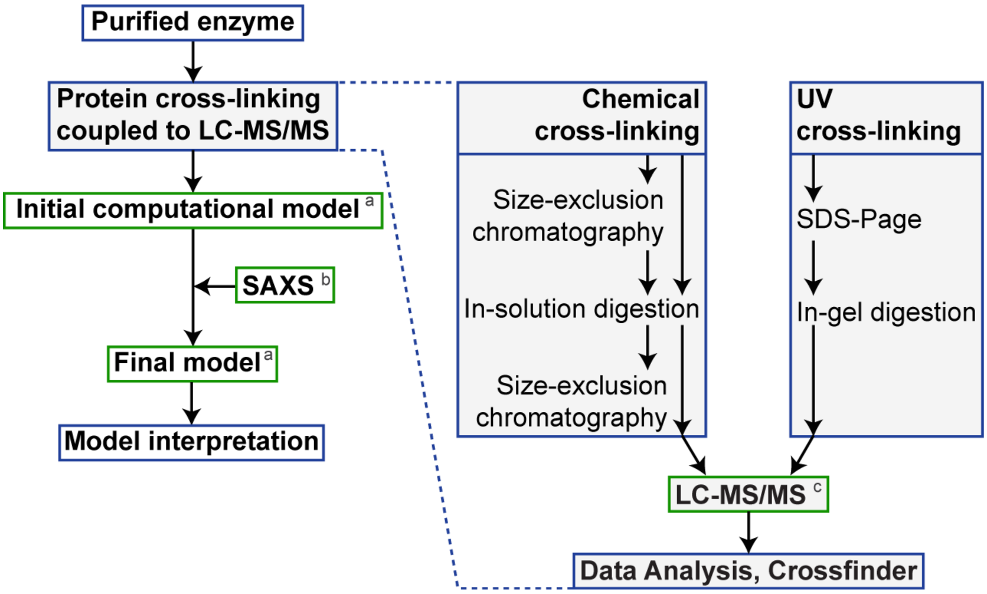

Figure 7: Workflow of the integrative approach for the structural characterization of ISWI-type remodeling enzymes. Collaborative work is indicated by green boxes. [a], Dr. Christina Schindler and Prof. Dr. Martin Zacharias (TUM, Munich); [b], Dr. Linda Brützel and Prof. Dr. Jan Lipfert (LMU, Munich); [c], Dr. Ignasi Forné and Prof. Dr. Axel Imhof (LMU, Munich).

As illustrated in Figure 7, the general workflow for the structural characterization of ISWI-type remodeling enzymes comprised several distinct experimental steps. First, the DmISWI and Snf2H enzymes were purified from bacterial cell extracts to near homogeneity using different chromatographic separation techniques. Subsequently, samples were subjected to either XL-MS or SAXS analysis.

Two complementary XL-MS strategies, UV and chemical cross-linking, were applied in the course of this project in order to obtain intra- and inter-domain distance restraints for each remodeling enzyme. The sample preparation procedures for UV- and chemical cross-linking differed and relied on in-gel and in-solution tryptic digestion, respectively. In the case of the DmISWI enzyme, we used the photo-reactive Bpa residue ($\mathrm{ISWI}_{\mathrm{M578B}}$) as well as chemically cross-linked the enzyme with either the $\mathrm{BS^2G}$ or $\mathrm{BS^3}$ cross-linking agent. The Snf2H protein was chemically cross-linked across distinct steady-state conditions (i.e., ± nucleotide analog, ± substrate) using the $\mathrm{BS^3}$ cross-linker. For selected DmISWI and Snf2H samples, I performed size-exclusion chromatography subsequent to protein proteolysis in order to enrich the cross-linked products in a similar manner as demonstrated previously (177). The tryptic peptide mixture was then subjected to LC-MS/MS analysis using a high-resolution mass spectrometer and XL-MS data analyzed with the Crossfinder software.

Given the XL-MS data, our collaboration partner Dr. C. Schindler (TUM, Munich) performed computational modeling to reconstruct the structural architecture of the full-length DmISWI and Snf2H enzymes. Individual DmISWI and Snf2H domains (e.g., ATPase module) were homology modeled according to corresponding high-resolution structures of related remodeling enzymes. These homology models were subjected to rigid body docking, which was guided by XL-MS-derived upper distance restraints. The upper distance thresholds for individual restraints were set to 25 Å and 29 Å for the chemical $\mathrm{BS^2G}$ and $\mathrm{BS^3}$ cross-linking agents, respectively. The employed threshold values are in agreement with previous XL-MS studies (180, 188, 221, 222) and account for the length of lysine side chains (approximately 6.5 Å), the length of the spacer (7.7 Å for $\mathrm{BS^2G}$ and 11.4 Å for $\mathrm{BS^3}$; cf. Figure 5A), and some degree of protein flexibility (223). Likewise, the distance threshold for Bpa-derived restraints was set to 20 Å, which is comparable to previously published XL-MS studies (182, 224). The docking procedure typically resulted in a multitude of potential enzyme structures, from which the top-ranked 200 models were further considered. These structural models for the DmISWI and Snf2H enzymes were validated with respect to experimental XL-MS data as well as screened against collected SAXS profiles. Generally, the structural model with the lowest discrepancy between theoretical and experimental SAXS data (i.e., the model with the lowest χ-value) was selected as the representative final model.

1.4. Aims of this study

The lack of high-resolution structural information for chromatin remodeling enzymes has been limiting our mechanistic understanding of how the chromatin landscape is regulated on a molecular level. We thus aimed at characterizing the structural architecture of the full-length DmISWI enzyme and the human Snf2H homolog in solution. As outlined in the above section, we used an integrative structural approach that combines the solution-based, biophysical techniques XL-MS and SAXS with computational modeling. We were in particularly interested in elucidating structural characteristics of the catalytic core of both studied enzymes and to better understand how enzyme activity is regulated in a nucleotide- and substrate-dependent manner. We therefore applied our integrative structural approach to both enzymes under apo state conditions and when bound to the nucleotide analog adenosine-5′-diphosphate beryllium-fluoride (ADP-BeF_x). We reasoned that we could detect and visualize the conformational impact of ADP-BeF_x binding on the full-length DmISWI and Snf2H enzymes using our integrative structural approach. In a subsequent step, we aimed at exploring the binding mode of the Snf2H protein to its nucleosomal substrate. The characterization of the interaction between chromatin remodeling enzymes and nucleosomes has proven to be very challenging by traditional structural techniques (e.g., X-ray crystallography), yet it will contribute to our mechanistic understanding of the remodeling activity by ISWI-type enzymes.

2. Results

2.1. Purification of proteins

2.1.1. An improved purification procedure for recombinant histone proteins

In-vitro reconstitution of nucleosomes has become an indispensable part in chromatin research and relies on the time-consuming and labor-intensive expression and purification of recombinant histone proteins. In the conventional workflow (i.e., Inclusion Body Purification, IBP), individual core histones are expressed in bacteria cells and the proteins are solubilized from purified inclusion bodies (225, 226) (Figure 8A). An optimized protocol for the purification of histones (i.e., Rapid Histone Purification, RHP) has recently been developed in our research institute (Division of Molecular Biology, Biomedical Center, LMU Munich) (Figure 8B). My contribution in this project was to directly compare the IBP and RHP strategies for the purification of the four canonical histones from *Drosophila melanogaster*. My results have been published in the PLOS ONE journal (i.e., Fig. 4, Fig. S1 and Fig. S2 in (227)) and detailed purification protocols of both approaches are provided in the method section (cf. section 4.2.2.4).

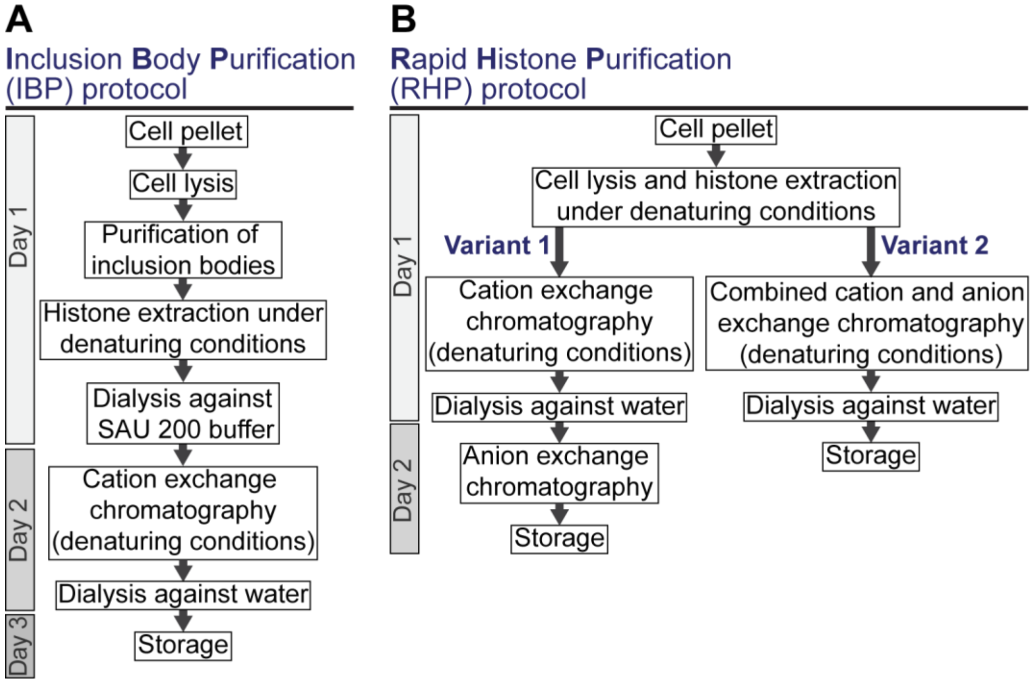

Figure 8: Schematic illustration of distinct purification strategies for recombinant histone proteins. The schematic workflows for **(A)** the conventional IBP and **(B)** the refined RHP approaches are shown. Notably, canonical histones can be purified in a time-saving manner using the RHP strategy. SAU 200, sodium-acetate-urea buffer supplemented with 200 mM NaCl.

To compare the IBP and RHP methods side-by-side, I recombinantly expressed the four canonical *Drosophila* histones in *E. coli* and split the cell pellets into two equal parts. As illustrated in Figure 8, the IBP and RHP protocols already differ at an early stage of the purification procedure. The IBP approach relies on the partition of the histones into inclusion bodies, which then have to undergo a time-consuming washing procedure before the proteins are solubilized under denaturing solution condition. In contrast, the cell lysis step is already conducted under denaturing conditions in the RHP protocol. Notably, we observed that a substantial fraction of the H2B protein (i.e., approximately 50%) did not partition into inclusion bodies in the conventional workflow and remained soluble in the supernatant (Figure 9A). Processing the same cell extract under denaturing conditions resulted in a more efficient extraction of the H2B histone (i.e., approximately 80%, Figure 9B). In line with this observation, we obtained higher yields for the H2B histone using the RHP approach (Figure 9E).

The *Drosophila* core histones are highly basic proteins (228) (i.e., isoelectric points $\geq$ 10.2) and thus carry a net positive charge under slightly acidic solution conditions. Consequently, in both IBP and RHP protocols, cation exchange chromatography provides an excellent opportunity to purify the recombinant histone proteins at pH 5.2 and denaturing conditions. In addition to the conventional workflow, we included anion exchange chromatography in the RHP protocol in order to minimize residual DNA and to remove contaminating protein species. This additional purification step can be performed independently (“Variant 1” in Figure 8B) or in tandem with cation exchange chromatography (“Variant 2” in Figure 8B). In the latter approach, the anion exchange column is placed upstream of the cation exchange column and has to be detached from the FPLC system prior to the salt gradient elution of the histones. The two presented RHP protocols resulted, as demonstrated for the H3 histone in Figure 9D and E, in comparable yields (i.e., 4.5 and 6.6 mg per liter bacteria culture for Variant 1 and 2, respectively) and equivalent sample purity. A direct comparison between the IBP and RHP approach revealed comparable purification parameters in terms of yields (2−11 mg per liter cell culture) and sample purity (Figure 9C, E) for all investigated canonical histones.

In conclusion, we find that the RHP strategy represents a convenient alternative to the conventional purification workflow. That is, the RHP protocol requires less hands-on working time, while sample purity and purification yields are comparable to the inclusion body-based approach. Consequently, canonical histones can be prepared in a time-saving manner, which is an important factor for subsequent downstream applications in chromatin research such as *in-vitro* reconstitution of nucleosomes.

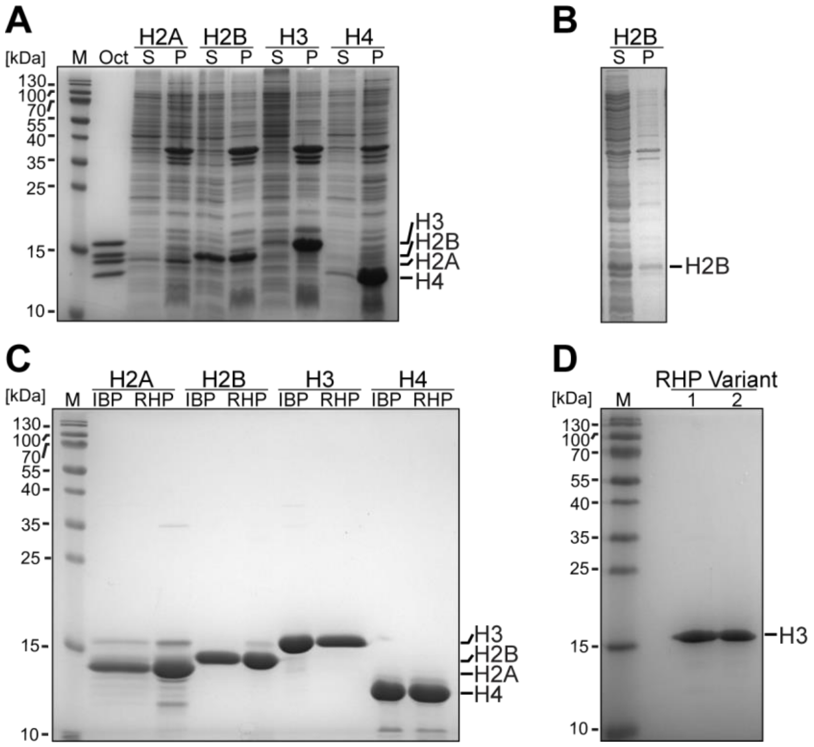

E

	IBP				RHP				RHP Variant 1	RHP Variant 2
	H2A	**H2B**	**H3**	**H4**	**H2A**	**H2B**	**H3**	**H4**	**H3**	**H3**
A260/A280	0.80	0.70	0.99	0.68	0.88	0.71	0.79	0.63	0.90	0.86
DNA contamination [%]	1.9	1.0	4.0	0.8	2.7	1.1	1.8	0.4	<3	<3
Yields [mg/l culture]	2.5	2.1	10.6	10.3	5.3	7.4	3.1	7.3	4.5	6.6

Figure 9: Comparison of purification strategies for canonical histone proteins by SDS-PAGE analysis. (A) For the conventional IBP approach, equivalent amounts of the soluble (S) and pelleted (P) fractions of the whole cell extracts were analyzed for each histone by SDS-PAGE analysis and Coomassie staining. Notably, a substantial fraction of the expressed H2B protein did not partition into inclusion bodies and was lost at an early stage of the IBP purification procedure. **(B)** In the RHP approach, the majority of H2B proteins are extracted under denaturing conditions during the cell lysis step. Similar results were obtained for the other investigated histones. **(C)** Comparison of sample purities obtained for the IBP and RHP (Variant 1) protocol. The SDS-PAGE analysis reveals comparable purities for all four canonical histones. **(D)** SDS-PAGE analysis for the H3 protein, which was either purified by Variant 1 or Variant 2 of the RHP approach (cf. Figure 8B). The two RHP protocols resulted in comparable sample purity and protein yields. **(E)** Comparison of DNA contamination and protein yields (n = 1). Protein concentrations were obtained from UV A_{280nm} absorption measurements. Histone extinction coefficients are provided in Table 13 in Material and Methods. DNA contamination was calculated from the UV absorption ratio A_{260nm}:A_{280nm} as described in (229). M, protein marker; Oct, histone octamer. The panels (A) and (C)–(E) were adapted from (227) in accordance with the Creative Commons Attribution (CC BY) license applied by the Public Library of Science.

2.1.2. Purification of remodeling enzymes

Expression and purification strategies for the full-length DmISWI remodeling enzyme (ISWI_{WT}, Figure 10A), its catalytic core ($\text{ISWI}_{\Delta\text{HSS}}$, Figure 10D), and several point mutant constructs (i.e., $\text{ISWI}_{\text{M578B}}$, Figure 10B) have already been well established prior to the beginning of the PhD project. However, corresponding procedures for the full-length Snf2H protein and the HSS domain of DmISWI (HSS_{ISWI}) were lacking and thus had to be established in the course of the project. The purification strategy for HSS_{ISWI} (Figure 10C) was set up on the basis of published work by Grüne and co-workers (116) and the procedure for the Snf2H enzyme (Figure 10E) was adapted from a protocol kindly provided by Prof. G. Narlikar and Dr. J. Leonard (UCSF, San Francisco, California).

This section aims at describing the key steps of the purification procedures for the above-mentioned remodeling enzymes and their variants with detailed protocols being provided in the method section (cf. chapters 4.2.2.2 and 4.2.2.3).

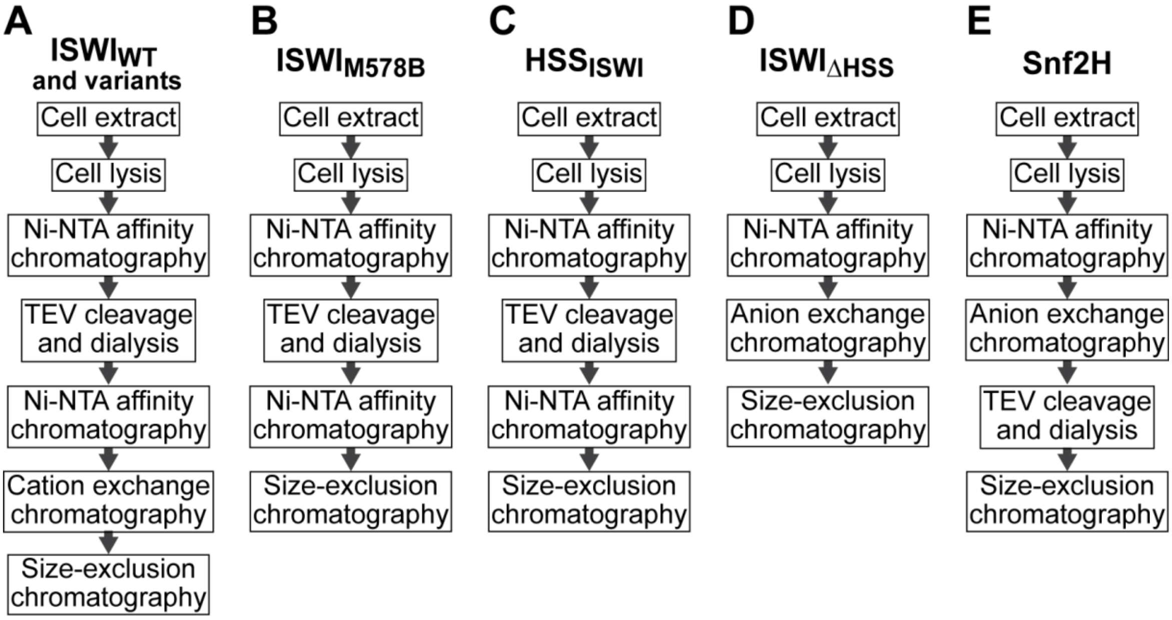

Figure 10: Purification strategies for full-length and variant remodeling enzymes. Schematic illustration of the purification procedures for the following His_6-tagged proteins: **(A)** full-length ISWI_{WT} (157) and additional point mutation constructs (i.e., $\text{ISWI}_{\text{K337D}}$, $\text{ISWI}_{\text{D485K}}$, and $\text{ISWI}_{\text{K337D D485K}}$), **(B)** $\text{ISWI}_{\text{M578B}}$ comprising the UV-inducible cross-linking amino acid Bpa at position 578 (157), **(C)** HSS_{ISWI} (i.e., residues 691–1027 in the full-length ISWI enzyme) (116), **(D)** $\text{ISWI}_{\Delta\text{HSS}}$ (i.e., residues 26–648 in the ISWI enzyme) (140), and **(E)** wild-type Snf2H.

The target proteins were all recombinantly expressed in *E. coli* and purified as schematically illustrated in Figure 10. The full-length and variant remodeling enzymes were expressed with an N-terminal His_6-tag that allows for the purification by Ni-NTA affinity chromatography, as representatively shown in the purification progress for HSS_{ISWI} and Snf2H in Figure 11A and B, respectively. With the exception of the $ISWI_{\Delta HSS}$ variant, the His_6-tag was subsequently cleaved off using tobacco etch virus (TEV) protease and most samples were again subjected to Ni-NTA affinity chromatography to remove unwanted protein species (i.e., the cleaved off His_6-tag, uncleaved target protein, and His_6-tagged TEV protease). The full-length enzymes were further purified by ion exchange chromatography in order to minimize sample impurities including nucleic acids and *E. coli* proteins. In a final step, we performed size-exclusion chromatography on all constructs to enhance sample purity to near homogeneity (Figure 11C). We observed that the sample purity was generally better for the ISWI constructs. However, the Snf2H enzyme was the most abundant protein in the respective samples such that the detected impurities likely did not interfere with XL-MS analysis (230). Furthermore, I did not observe protein species of higher molecular weight than the Snf2H enzyme during SDS-PAGE analysis, which is important for the analysis of SAXS data (231). The yield was on average 3.7 mg and 1.4 mg per liter *E. coli* cell culture for purified full-length Snf2H and $ISWI_{WT}$ proteins, respectively. The yields ranged from 0.2 ($ISWI_{K337D\ D485K}$) to 6.3 mg per liter cell culture ($ISWI_{\Delta HSS}$) for the investigated ISWI variants.

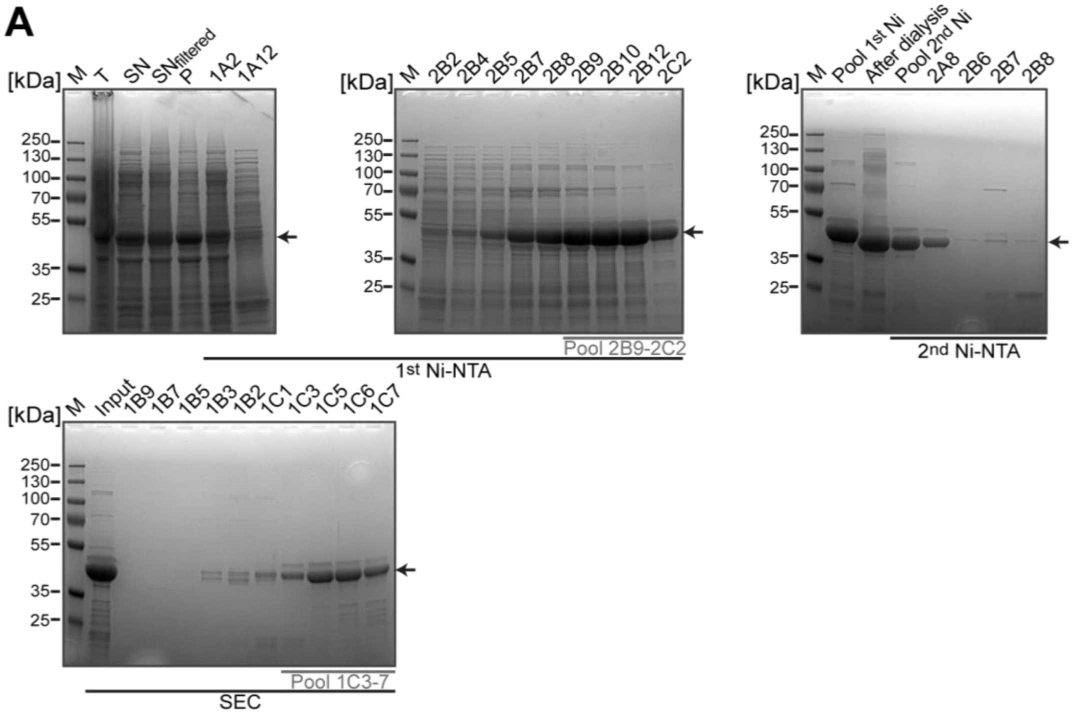

* continues next page *

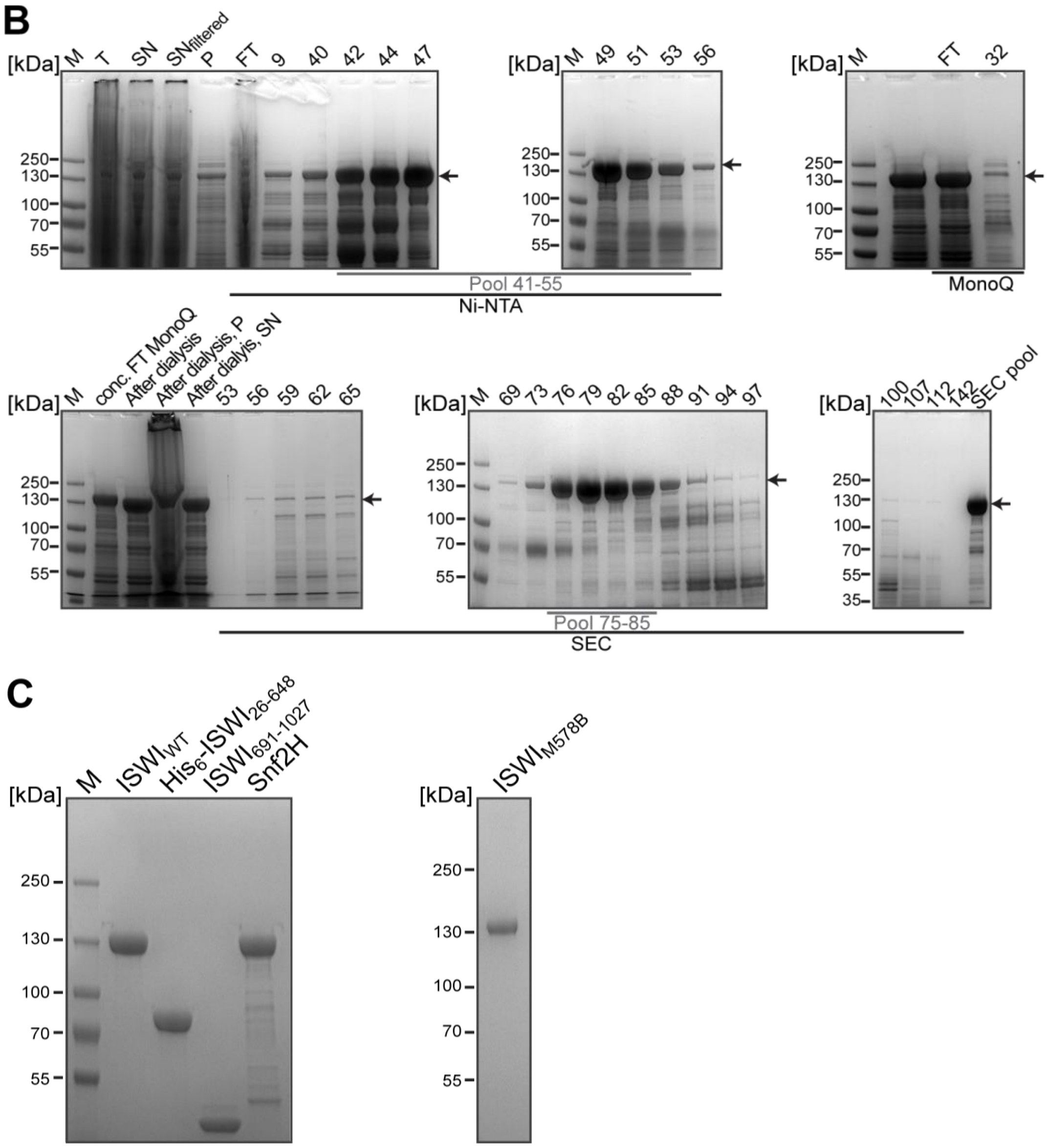

Figure 11: Monitoring the purification progress for remodeling enzymes by SDS-PAGE analysis. I monitored the purification progress for individual remodeling enzymes and variants thereof by SDS-PAGE analysis and Coomassie staining. **(A)** Representative purification progress for the His$_6$-tagged HSS$_{ISWI}$ variant. The lysed whole cell extract ('T') containing soluble HSS$_{ISWI}$ ('SN') was filtered ('SN$_{filtered}$') and subjected to a first Ni-NTA affinity purification ('1st Ni-NTA') in order to remove most bacterial contaminations. Following TEV protease cleavage and dialysis, the target protein was subjected to a second Ni-NTA affinity purification ('2nd Ni-NTA'). In a last step, size-exclusion chromatography ('SEC') ensured near homogeneity of the final sample. Arrows mark the protein of interest. The three letter designations (e.g., 1A2, 2B2, etc.) refer to individual FPLC-separated fractions. M, protein marker; P, pellet; FT, flow through. **(B)** Representative purification progress for the His$_6$-tagged Snf2H enzyme. Ni-NTA affinity purification removed most soluble, contaminating protein species of the pre-cleared whole cell extract. The Snf2H enzyme was further separated from contaminating protein species and DNA fragments by MonoQ anion exchange chromatography and the concentrated flow-through ('conc. FT MonoQ') was subjected to TEV protease cleavage and dialysis. In a final step, the sample ('After dialysis, SN') was further processed using size-exclusion chromatography. **(C)** SDS-PAGE analysis for purified full-length and variant remodeling enzymes. Notably, individual target proteins were purified to near homogeneity.

2.2. Solution structure of the DmISWI enzyme under apo state conditions

As of today, high-resolution structural evidence for the full-length DmISWI remodeling enzyme is lacking and only the respective HSS module has been successfully crystalized (116). As outlined in section 1.3.3, we developed an integrative structural approach (cf. Figure 7), which combines XL-MS and SAXS analyses as well as computational modeling, to probe the relative orientation of individual domains and thus the overall structural architecture of the full-length DmISWI protein in solution.

Briefly, following UV and chemical cross-linking of the full-length target protein under apo state conditions, MS analysis of tryptic DmISWI digests resulted in the identification of 94 cross-linked peptides providing a total of 61 unique cross-linked residue pairs (cf. STable 1, STable 2). I thereby included published cross-links from Forné *et al.* (157) (i.e., XL_{ISWI} 1, 2, 24, 25) and Ludwigsen *et al.* (115) (i.e., XL_{ISWI} 3) and took advantage of an unpublished data set (i.e., XL_{ISWI} 6, 9–13, 16–18, 31–35, 39, 46, 47, 52, 53, 59–61), which was kindly provided by Dr. F. Müller-Planitz. Notably, 43 of all identified cross-linked residue pairs (including ten cross-links used for docking) were reproducible as further specified in STable 1 and STable 2.

In collaboration with Dr. C. Schindler (TUM, Munich), we subsequently implemented a subset of the identified inter-domain cross-links as distance restraints to guide the computational modeling of potential solution structures for the DmISWI ATPase module and the full-length enzyme. Finally, candidate ATPase and full-length DmISWI structures were compared to the molecular shape information gathered from SAXS measurements, which were kindly performed by Dr. L. Brützel (LMU, Munich).

The following sections describe the key findings from XL-MS analysis, SAXS measurements, and computational modeling for each functional domain of the DmISWI enzyme under apo state conditions in a step-by-step manner.

2.2.1. Conformation of the DmISWI ATPase domain

2.2.1.1. The orientation of both ATPase lobes

XL-MS analysis revealed 30 cross-linked residue pairs (cf. STable 1) within the ATPase module, which is defined in the following to include the NTR, ATPase lobe 1, ATPase lobe 2, and the NegC domain. Seven out of these 30 cross-linking positions (XL_{ISWI} 1–7) connected both ATPase lobes (Figure 12) and thus restricted the relative orientation of both ATPase lobes to each other in the full-length DmISWI enzyme. One UV and two chemical cross-links (XL_{ISWI} 3–5) connected the C-terminal region of ATPase lobe 1 with the C-terminal half of ATPase lobe 2. Moreover, three UV cross-links (XL_{ISWI} 1, 2, 7) bridged the N- and the C-terminus of ATPase lobes 1 and 2, respectively, suggesting that these particular regions are in close spatial proximity to each other under apo state conditions.

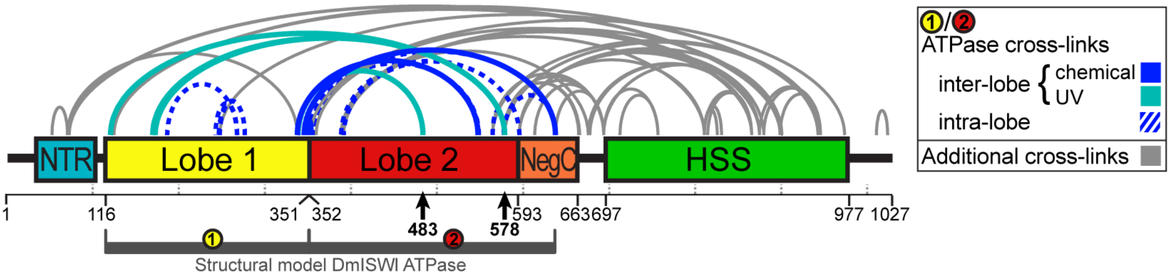

Figure 12: Identified cross-links for the full-length DmISWI protein. Identified cross-links for the DmISWI enzyme under apo state conditions are schematically illustrated in an arc plot. The UV and chemical cross-links that connect the homology models for region "①" (residues 116−351) and region "②" (residues 352−637) are highlighted in blue and cyan color, respectively. Residue numbering is denoted below each DmISWI domain. Arrows indicate the positions of Bpa-substituted amino acids. STable 1 provides further details for each presented cross-link. NTR, N-terminal region; HSS, HAND-SANT-SLIDE. The figure was adapted from (1) in accordance with Elsevier's policies.

Dr. I. Forné (LMU, Munich) performed the MS analysis.

As a complementary approach to XL-MS analysis, we investigated the molecular shape of the ATPase module of the DmISWI protein in solution by means of SAXS. I therefore expressed and purified a truncated variant of the remodeling enzyme (i.e., residues 26−648), which lacks its HSS domain ($ISWI_{\Delta HSS}$) and comprises an N-terminal His_6-tag. Our collaboration partner Dr. L. Brützel (LMU, Munich) conducted the SAXS measurements and analyzed the data for the $ISWI_{\Delta HSS}$ variant at different protein concentrations ranging from 1.5 to 7.0 mg/mL. The experimental scattering curves were well superimposable after data normalization against intensity (Figure 13A) indicating that protein aggregation was minimal and that obtained data were of good quality. The Kratky representation of the scattering data furthermore suggested that the $ISWI_{\Delta HSS}$ enzyme was folded (Figure 13B). The reconstructed molecular envelope

(Figure 13C) visualizes that the ATPase module adopted a globular conformation under apo state conditions.

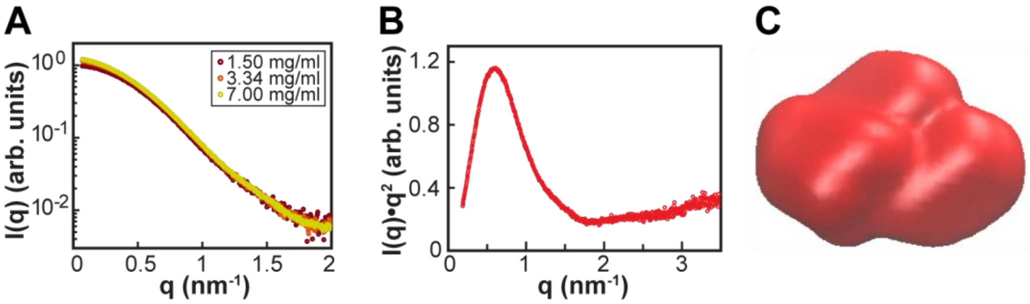

Figure 13: SAXS data and scattering-derived parameters for the ISWI$_{\Delta HSS}$ variant. (A) Extrapolated scattering curves obtained at different ISWI$_{\Delta HSS}$ concentrations are shown. Notably, these curves are well superimposable indicating good data quality, because sample aggregation was negligible. **(B)** Kratky representation of merged SAXS scattering data. **(C)** The *ab-initio* determined molecular envelope of the ISWI$_{\Delta HSS}$ variant is depicted. The panels (A) and (B) were adapted from (1) in accordance with Elsevier's policies.

Dr. L. Brützel (LMU, Munich) conducted the SAXS measurements and analyzed the respective data shown in panels (A)–(C).

In order to resolve and visualize potential orientations of both ATPase lobes in the DmISWI enzyme and thus generate a structural model of the ATPase module, we integrated the experimental XL-MS and SAXS data into a refined docking protocol for the ATTRACT software.

In a first step, our collaboration partner Dr. C. Schindler (TUM, Munich) homology modeled the DmISWI ATPase domain according to the Chd1 structure from *Saccharomyces cerevisiae* (pdb 3MWY), the most closely related remodeler with an available high-resolution structure at this time. In order to model potential orientations of both ATPase lobes to each other in a rigid two-body docking approach, the generated homology model of the ATPase module was cut into two parts at a predicted hinge region that connects both ATPase lobes yielding two structural bodies ("①": residues 116–351; "②": 352–637 residues; cf. Figure 12). To validate the structural bodies with respect to experimental XL-MS data, I measured the Cα-Cα distance of identified intra-domain cross-links (i.e., XL$_{ISWI}$ 13–30) in the computed structures. Importantly, all accessible intra-domain cross-links (XL$_{ISWI}$ 15–22) were consistent with the computational models for the ATPase domain. Some cross-links (i.e., XL$_{ISWI}$ 13, 14, and 23–30), however, mapped to DmISWI regions, for which our structural models lack atomic coordinates.

In a second step, Dr. C. Schindler performed XL-MS-guided docking of the two structural bodies. The docking procedure was initiated by computing one million starting models with random ATPase lobe 1 and ATPase lobe 2 orientations, solely preventing direct steric clashes between the two rigid bodies. Subsequently, the distance between selected cross-linked residue pairs was restrained by implementing an upper harmonic restraint between the respective Cα atoms. That is, we employed inter-domain cross-links (XL_{ISWI} 1–3), which exhibited excellent fragmentation data during MS/MS analysis, as distance restraints to guide the computational docking of the ATPase lobes. The maximum distance thresholds were set to 20, 25, and 29 Å for the UV-, BS^2G-, and BS^3-derived cross-links, respectively. The ATTRACT software then provided a score-based ranking of the generated models of the ATPase module. The top-ranked 200 models were further subjected to flexible refinement. Importantly, all these 200 refined models of the ATPase module were fully consistent with the implemented distance restraints used for docking and furthermore displayed an overall highly similar topology as indicated by a model precision of 3.4 Å. Finally, the 200 different structures of the ATPase module were compared with the molecular shape information provided by the SAXS measurements of $ISWI_{\Delta HSS}$ in order to validate and select the most favorable structural model with respect to the experimental data. Consequently, the ATPase model with the lowest discrepancy between theoretical and experimental scattering curves, i.e. lowest χ-value, is generally shown as a representative structure in the following sections, unless stated otherwise, and will be termed "DmISWI ATPase model" hereafter.

Our DmISWI ATPase model is shown in Figure 14A. Interestingly, compared to the conformation of the initial ScChd1-based homology model, ATPase lobe 1 had to undergo a remarkable rotation of almost 180° relative to ATPase lobe 2 in order to fulfill the cross-linking distance restraints (Figure 14D). Such a striking, global rearrangement within the DmISWI ATPase module was unexpected considering that structures of related remodeling enzymes show a different relative orientation of both lobes (cf. section 2.2.1.2).

To further validate our structural model of the ATPase module with respect to the experimental data, I assessed the Cα-Cα distances between individual residue pairs for inter-domain cross-links not used during the docking procedure (i.e., XL_{ISWI} 4–12). Notably, the large majority of these additional inter-domain cross-links was in excellent agreement with the proposed DmISWI ATPase model with solely XL_{ISWI} 8 marginally violating the defined distance threshold by as much as 5 Å (cf. STable 1). The cross-linked residue K637 in XL_{ISWI} 8 is located in a potentially flexible loop region at the C-terminal region of the ATPase model, which in turn may provide a structure-based explanation for the minor inconsistency between experimental and computational data. Notably, also the SAXS scattering data for $ISWI_{\Delta HSS}$ showed consistency with the representative DmISWI ATPase model as reflected by a χ-value of 1.03 (Figure 14B). The proposed ATPase structure can be fitted well into the SAXS-derived shape envelope as illustrated in Figure 14C.

To evaluate the reliability and robustness of our DmISWI ATPase model, the docking procedure was repeated using all identified lobe-connecting cross-links (XL_{ISWI} 1–8). The obtained structural model resulted in an almost identical domain architecture with distinct DmISWI ATPase structures being well superimposable (Figure 14E) as indicated by an RMSD of 2.2 Å. Likewise, docking with all identified inter- and intra-domain cross-links for the ATPase module (XL_{ISWI} 1–12, 15–21) yielded superimposable structures (RMSD = 2.6 Å). These findings collectively demonstrate the robustness and reliability of our proposed DmISWI ATPase model.

Taken together, by combining several structural techniques, we successfully reconstructed the three-dimensional architecture of the catalytic core of the DmISWI enzyme under apo state conditions. Our experimental data provide evidence for an ATPase conformation, which was remarkably different from the one observed in the ScChd1 structure.

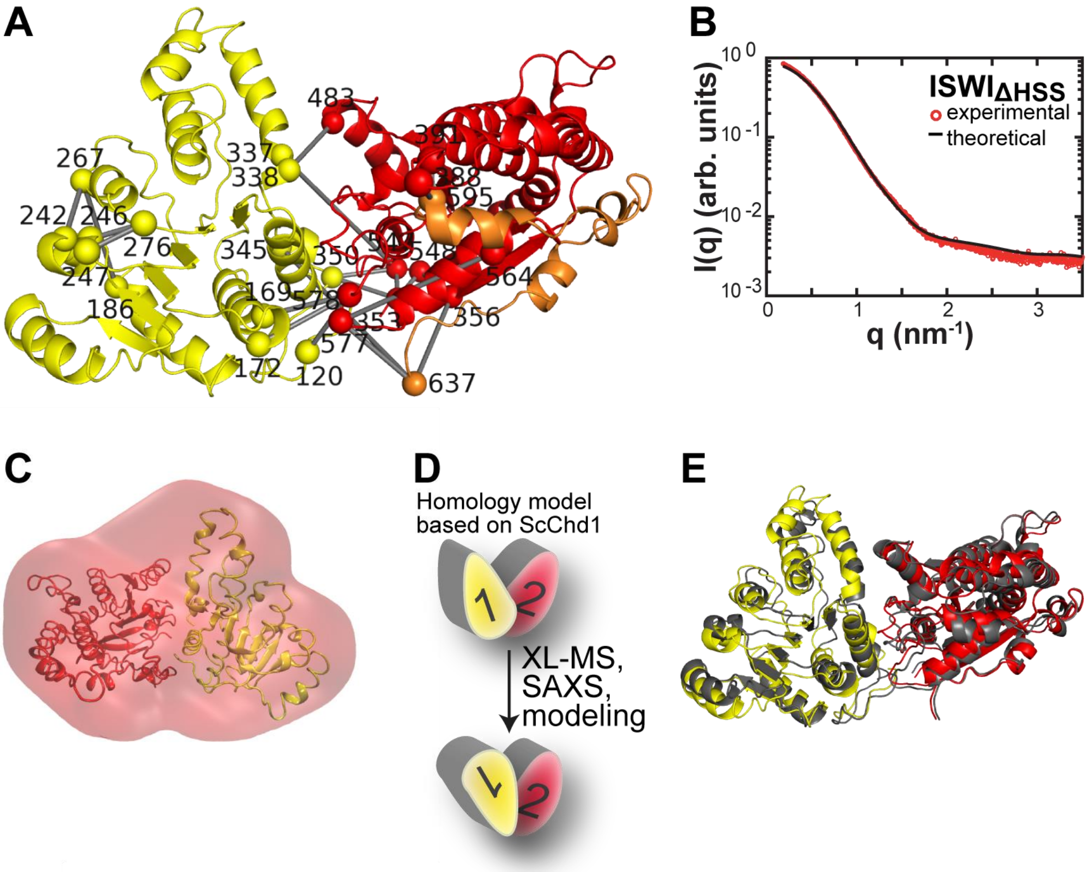

Figure 14: Architecture of the DmISWI ATPase domain determined by our integrative structural approach. (A) Structural model of the DmISWI ATPase module is shown with ATPase lobe 1, ATPase lobe 2, and the NegC domain being colored in yellow, red, and orange, respectively. Cross-linked amino acids are represented as spheres and are connected by grey rods. For individual distances spanned by the cross-linker see also STable 1. **(B)** The theoretical scattering curve obtained for the structural model depicted in (A) (black line) is in good agreement ($\chi = 1.03$) with the measured scattering data for the ISWI$_{\Delta HSS}$ variant (red circles). **(C)** The structural model of the DmISWI ATPase module shown in (A) can be fitted well into the SAXS-derived molecular shape envelope for the ISWI$_{\Delta HSS}$ construct. Note that 19% of residues are missing in the structural model, which explains the excess of electron density. **(D)** Schematic illustration of the domain orientation revealed by our structural approach. **(E)** Incorporation of all ATPase lobe 1-lobe 2 cross-links into the docking protocol led to a highly similar DmISWI ATPase model (grey; RMSD = 2.2 Å; cf. STable 1 for individual cross-linking distances). The structural model shown in (A) (yellow, red) is depicted for orientation. The panels (A), (B), and (E) were adapted from (1) in accordance with Elsevier's policies.

I expressed, purified, and cross-linked the DmISWI enzyme and analyzed the respective XL-MS data shown in panel (A). Dr. I. Forné (LMU, Munich) performed the MS analysis. Dr. L. Brützel (LMU, Munich) conducted and analyzed the SAXS-related data shown in panels (B) and (C). Dr. C. Schindler (TUM, Munich) generated the ATPase models depicted in panels (A), (C), and (E).

2.2.1.2. The DmISWI ATPase model shares a similar domain architecture with the MtISWI enzyme

To uncover common structural features between our proposed DmISWI ATPase model and structures of related Snf2 ATPases, I examined the compatibility of the identified inter-domain cross-links used for docking with the following enzymes: Sso1653 (154), DrRad54 (109), ScChd1 (141), MtSnf2 (153), MtISWI (146), and a former model of the DmISWI ATPase module (157). That is, I measured the Cα-Cα distances for the inter-domain cross-links used for docking (i.e., XL_{ISWI} 1–3) at homologous positions in the related remodeling enzymes. As detailed in Figure 15, all accessible Cα-Cα distances consistently exceeded the defined distance thresholds in the high-resolution structures of Sso1653 (pdb 1Z6A), DrRad54 (pdb 1Z3I), ScChd1 (pdb 3MWY), and MtSnf2 (pdb 5HZR) suggesting an overall deviating ATPase architecture for the DmISWI enzyme. The previous XL-MS-based DmISWI model by Forné *et al.* also displayed inconsistencies with our experimental data. For instance, the identified inter-lobe XL_{ISWI} 3 as well as XL_{ISWI} 5 (34.7 Å) do not lead through solvent-occupied space and furthermore exceed the defined distance requirements. Strikingly, superimposition of our ATPase model of the DmISWI enzyme and the crystal structure of the MtISWI protein (pdb 5JXR) revealed an almost identical configuration of both ATPase lobes with an RMSD of 4.5 Å (cf. Figure 15). Indeed, all identified intra- and inter-ATPase lobe-lobe cross-linking distances (XL_{ISWI} 1−7, 15−22) were in excellent agreement with the crystal structure for the catalytic core of the MtISWI protein (cf. STable 1). In addition, the conformation of MtISWI is consistent with our SAXS data for $ISWI_{\Delta HSS}$. The predicted scattering profile of a homology model of monomeric MtISWI provided an excellent fit to our experimental data ($\chi = 0.71$; Note that, only 5% of residues are missing in the homology model of MtISWI compared to 19% in DmISWI ATPase). With the exception of ScChd1, other ATPase conformations of Sso1653, DrRad54, and MtSnf2 fitted the SAXS data significantly worse (i.e., χ(ScChd1) = 0.61, χ(Sso1653) = 2.69, χ(DrRad54) = 2.22, χ(MtSnf2) = 3.02).

Consequently, our solution-phase XL-MS data for the DmISWI enzyme collectively provide evidence for a similar ATPase architecture as has been reported for the related MtISWI protein without prior knowledge of the crystal structure.

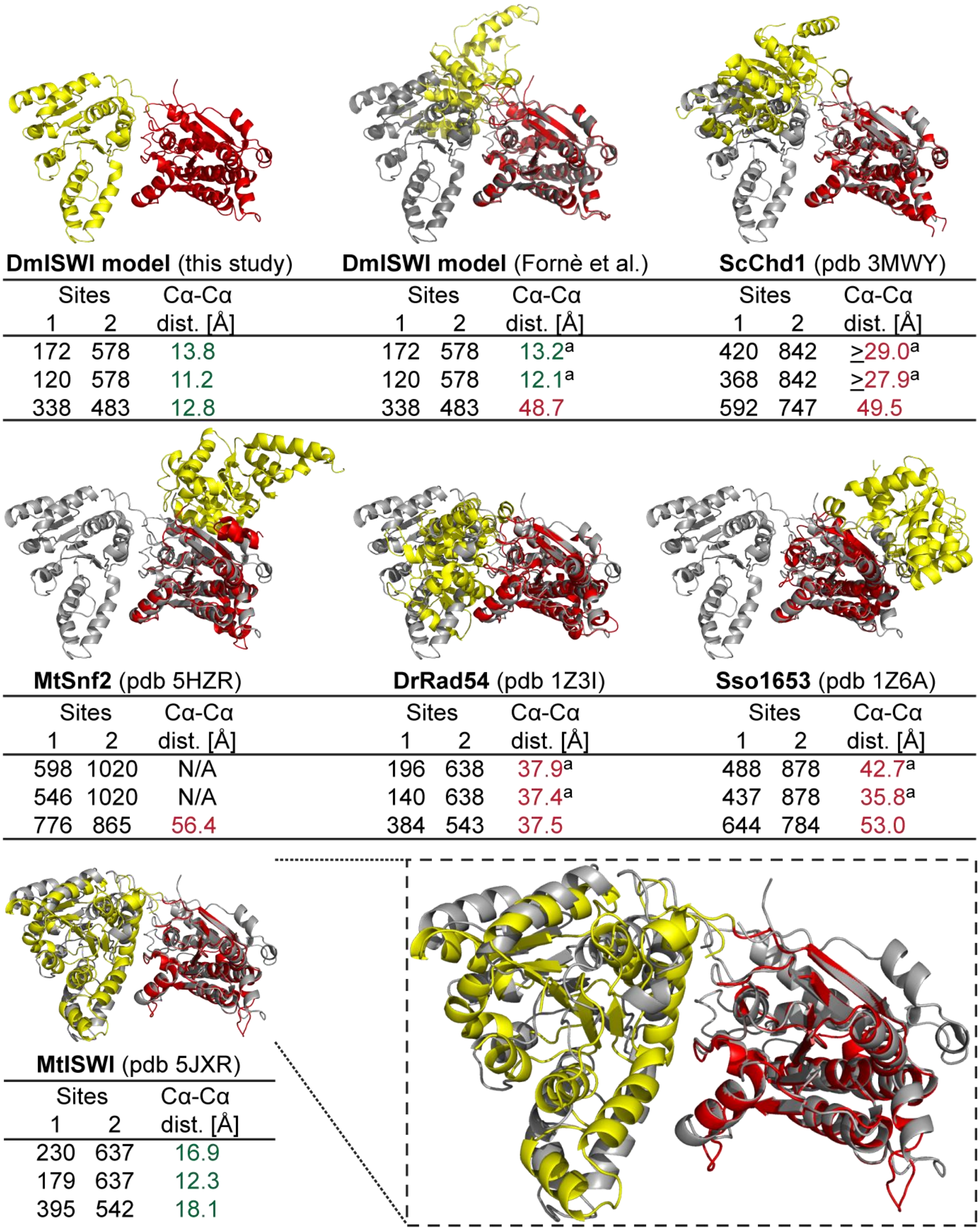

DmISWI model (this study)

Sites 1	Sites 2	Cα-Cα dist. [Å]
172	578	13.8
120	578	11.2
338	483	12.8

DmISWI model (Fornè et al.)

Sites 1	Sites 2	Cα-Cα dist. [Å]
172	578	13.2[a]
120	578	12.1[a]
338	483	48.7

ScChd1 (pdb 3MWY)

Sites 1	Sites 2	Cα-Cα dist. [Å]
420	842	≥29.0[a]
368	842	≥27.9[a]
592	747	49.5

MtSnf2 (pdb 5HZR)

Sites 1	Sites 2	Cα-Cα dist. [Å]
598	1020	N/A
546	1020	N/A
776	865	56.4

DrRad54 (pdb 1Z3I)

Sites 1	Sites 2	Cα-Cα dist. [Å]
196	638	37.9[a]
140	638	37.4[a]
384	543	37.5

Sso1653 (pdb 1Z6A)

Sites 1	Sites 2	Cα-Cα dist. [Å]
488	878	42.7[a]
437	878	35.8[a]
644	784	53.0

MtISWI (pdb 5JXR)

Sites 1	Sites 2	Cα-Cα dist. [Å]
230	637	16.9
179	637	12.3
395	542	18.1

Figure 15: Comparison of our DmISWI ATPase model with available apo structures of related ATPases. The orientation of both ATPase lobes (yellow: ATPase lobe 1, red: ATPase lobe 2) in our model of the DmISWI ATPase module (upper left corner, cf. Figure 14A) deviates from the one observed for Sso1653, DrRad54, ScChd1, MtSnf2, and a former model of the DmISWI ATPase module (157). Notably, the large majority of Cα-Cα distances between cross-linked residue pairs substantially violated the defined distance threshold in the investigated structures (red values). Strikingly, our DmISWI ATPase model exhibits a similar domain architecture as observed for the MtISWI enzyme with respective Cα-Cα distances being in the expected range (green values). Structures of related enzymes are aligned to ATPase lobe 2 of our DmISWI ATPase model, which is shown in grey color for orientation. [a]: Calculated distances were taken from (157). N/A: Not available, K1020 and neighboring residues are missing in the structure, precluding a measurement. Dm: *Drosophila melanogaster*; Sc: *Saccharomyces cerevisiae*; Dr: *Danio rerio*; Sso: *Sulfolobus solfataricus*; Mt: *Myceliophthora thermophila*.

2.2.1.3. The catalytic domain of ISWI adopts a resting conformation under apo state conditions

The ATPase domain from the Snf2 family of ATPases generally comprise several conserved structural helicase-like motifs, which play a key role in ATP hydrolysis (232). Motifs I and II on ATPase lobe 1 assist in binding of ATP and Mg^{2+}. These motifs work cooperatively with motif VI on ATPase lobe 2, which acts as an “arginine finger” to assist catalysis. The spatial arrangement of these individual motifs is assumed to determine the catalytic activity of the enzyme and consequently, both ATPase lobes must align to become competent to hydrolyze ATP. Interestingly, individual motifs were not oriented towards each other in our DmISWI ATPase model (cf. Figure 17A). Instead, the motifs were twisted towards opposite sides implying that the catalytic core of DmISWI rests in an inactive conformation under apo state conditions in solution. Thus, the proposed DmISWI ATPase model may provide a structural basis for the well documented repressed basal ATPase activity (140).

To rule out that the employed docking protocol inherently favored the presumably inactive conformation of the ATPase domain, we repeated the docking procedure for the catalytic core in the absence of any XL-MS-derived distance restraints (*ab-initio* docking; only the obvious distance between amino acids 351 and 352 was restraint). As depicted in Figure 16, the top-ranked *ab-initio* model exhibits a completely different orientation of both ATPase lobes and is, to a large extent, inconsistent with the experimental XL-MS data (cf. STable 1). In particular, cross-links that bridged distant residue pairs with regard to the primary protein sequence (i.e., $\geq$ 400 residues) were prone to be inconsistent with the generated *ab-initio* ATPase model. Considering that the *ab-initio* docking resulted in a substantially different domain architecture as observed for the XL-MS-based DmISWI ATPase model, an inherent bias towards the inactive conformation can most likely be ruled out. Intriguingly, the catalytically important motifs were found in close spatial proximity to each other in the *ab-*

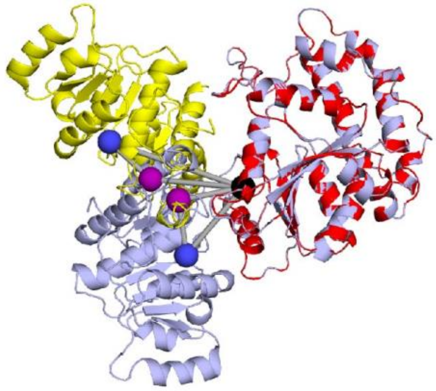

Figure 1: *Ab-initio* docking model of DmISWI ATPase module. The orientation of both ATPase lobes in the *ab-initio* structure (light blue) was modeled in the absence of distance restraints. The *ab-initio* model was then aligned to lobe 2 of the XL-MS-derived DmISWI ATPase model (yellow, red; cf. Figure 14A). Motifs I (purple), II (blue) and VI (black), are highlighted as spheres for both models. See also STable 1 for measured Cα-Cα distances. The figure was adapted from (1) in accordance with Elsevier’s policies.

Dr. C. Schindler (TUM, Munich) generated the ab-initio model of the ATPase module.

initio model, which perhaps reflects structural properties of an active configuration of the ATPase module. Consequently, activation of the DmISWI enzyme potentially relies on large-scale conformational rearrangements to align the conserved, catalytically important ATPase motifs.

To further characterize and validate the presumably inactive ATPase conformation, I perturbed a proposed interaction site between both DmISWI ATPase lobes by introducing point mutations and monitored the ATPase activity. We hypothesized that the disruption of a potential salt bridge in the lobe-lobe interface (i.e., K337-D485, cf. Figure 17B) by charge-reversal mutations (K337D or D485K; Figure 17C) could lead to a destabilization of the inactive conformation and thus to an increased ATPase activity of the DmISWI enzyme. Notably, the MtISWI protein comprises corresponding charged residues in the ATPase lobe-lobe interface (R394 and D544, pdb 5JXR) that point towards each other (Figure 17B). Consistent with our hypothesis, weakening of the lobe-lobe interface by mutation of D485K resulted in a nearly two-fold increase in ATPase activity, whereas double mutation of both residues completely restored wild-type ATPase levels (Figure 17E). Surprisingly, $\text{ISWI}_{\text{K337D}}$ exhibited a decreased ATPase activity. I therefore inspected our DmISWI ATPase model in order to pinpoint surrounding residues, which potentially interact with the negatively charged aspartic acid through a hydrogen bond or salt bridge. Two basic residues, H483 and R486, exist within a 12 Å radius (i.e., four times the median distance of a salt bridge (233) to account for protein flexibility), which may form compensatory interactions upon mutation (Figure 17B). Finally, one has to keep in mind that residue K337 in the DmISWI protein may serve other important functions in addition to stabilizing the lobe-lobe interface and that charge-reversal at this position could cause unexpected side effects.

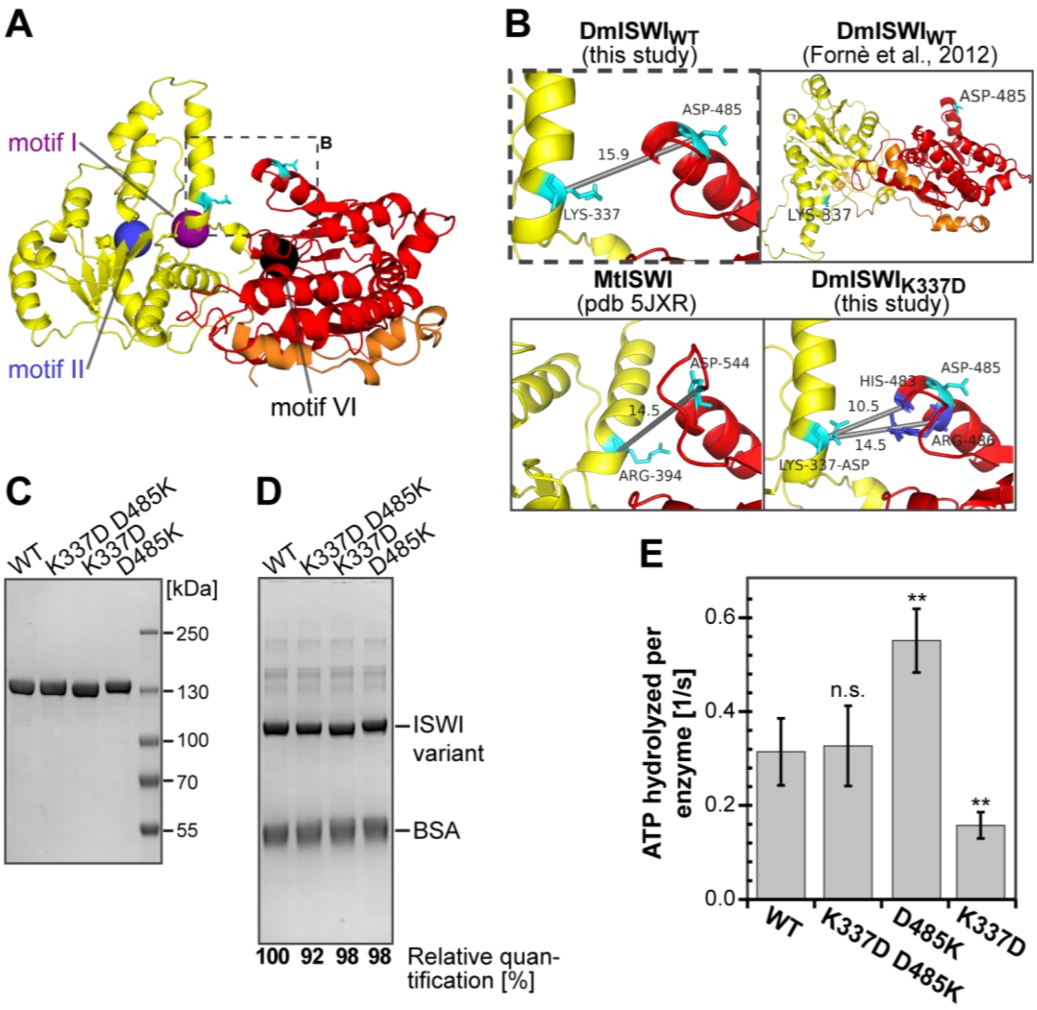

Figure 17: The DmISWI ATPase module most likely assumes an inactive conformation under apo state conditions. (A) Structural motifs involved in ATP hydrolysis are represented as spheres in our ATPase model of the DmISWI enzyme (cf. Figure 14A). **(B)** Illustration of a potential inhibitory interaction between two residues of ATPase lobe 1 and lobe 2 in the apo state. The residues K337 and D485 (cyan) are located at the lobe interface in the ATPase model of DmISWI and might be sufficiently close to interact with each other (top left; section corresponds to dotted rectangle in (A)). The corresponding residues in the structure of MtISWI (pdb 5JXR) show a remarkably similar orientation (bottom left). On the contrary, in the ISWI model of Forné and co-workers (157), in which both lobes adopt a different orientation to each other, both residues are located in a way that an interaction is unfavorable (top right). I introduced charge-reversal mutations to perturb the proposed interaction between K337 and D485 in the DmISWI enzyme. However, a possible compensatory interaction might be formed between K337D and H483 or R486 (blue), respectively, in the ISWI$_{K337D}$ variant (bottom right). **(C)** Sample purity of DmISWI constructs evaluated by SDS-PAGE analysis and Coomassie staining. **(D)** Comparability of enzyme amounts used in ATPase assay. A fraction of each assay reaction mixture used in (E) was separated by SDS-PAGE, stained with Coomassie, and bands corresponding to ISWI quantified by densitometry relative to ISWI$_{WT}$ (n = 1). **(E)** Comparison of the ATPase activity for ISWI$_{WT}$ and lobe interface mutants. The reactions were performed in the presence of saturating concentrations of ATP and DNA. Errors bars represent standard deviations of ≥ 3 independent measurements. The unstimulated basal activity was ≤ 0.005 s^{-1} for all enzyme variants. A two-tailed t test was performed to determine statistical significance. **, $p \leq 0.01$; n.s., not significant, $p \geq 0.05$. The panels (B)–(E) were adapted from (1) in accordance with Elsevier's policies.

2.2.2. The HSS domain contacts the ATPase domain in solution

With the structural model of the ATPase module in our hand, we subsequently set out to elucidate the relative orientation of the HSS domain in the full-length DmISWI remodeling enzyme.

The XL-MS analysis of the DmISWI protein yielded a total of 31 cross-linked residue pairs (XL_{ISWI} 31–61; STable 2) that mapped to the HSS domain. A subset of these cross-links (XL_{ISWI} 31–48) connected the HSS domain and the ATPase module (Figure 18). The cross-linker sometimes bridged distant residue pairs (XL_{ISWI} 34, 35, and 37) with regard to the primary protein sequence (≥ 700 residues), suggesting a compact protein structure formed by the ATPase and HSS modules. Spatial proximity between the HSS domain and the ATPase module was evident from both chemical and UV-induced cross-linking. Numerous cross-links between the ATPase module and the HSS domain mapped to the SLIDE region (XL_{ISWI} 31, 34, 35, 37–39, 41). The well-distributed lysine residues of the HAND region, however, reacted with the cross-linking agent to form mono-links (data not shown). The enrichment of mono-links implies that the HAND region most likely remains solvent-accessible and is not part of the ATPase-HSS interface under apo state conditions.

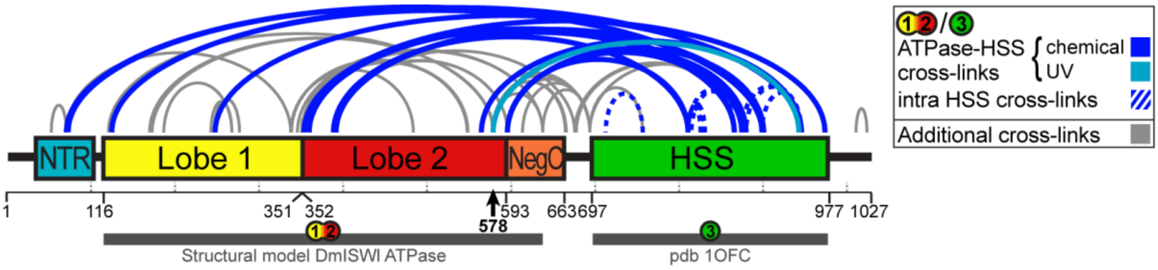

Figure 18: Identified cross-links for the full-length DmISWI protein under apo state conditions in solution. Identified cross-links for the DmISWI enzyme are schematically illustrated in an arc plot. The UV and chemical cross-links that bridge the ATPase module ("①②": residues 116–637) and the HSS domain ("③": residues 697–977) are further highlighted in blue and cyan color, respectively. Residue numbering is denoted below each DmISWI domain. The arrow indicates the position of the Bpa-substituted amino acid. STable 2 provides details for each colored cross-link. NTR, N-terminal region; HSS, HAND-SANT-SLIDE. The figure was adapted from (1) in accordance with Elsevier's policies.

Dr. I. Forné (LMU, Munich) performed the MS analysis.

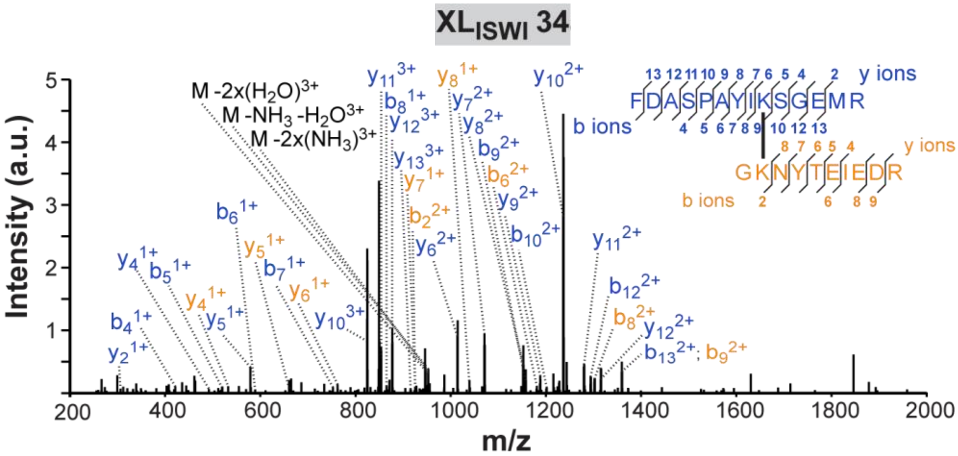

Figure 19: Representative MS/MS spectrum for a single cross-link used for docking of full-length DmISWI. The cross-linked peptides were assigned based on the observed fragment ions. The monoisotopic peaks of y- and b-fragment ions from both peptides (blue and orange) are denoted in the MS/MS spectrum and are furthermore indicated in the sequence of the cross-linked peptides. Notably, the quality of the MS/MS spectrum as well as the number of fragment ions (e.g., consecutive y_{13}-y_4-ion series for the blue peptide) allows unambiguous sequence assignments and the identification of the cross-linking site. We also detected the triply charged precursor ion (M, black) with modifications, i.e. neutral losses of NH_3 and/or H_2O. SFigure 5 shows additional fragmentation spectra of cross-links, which were used to guide the computational docking. The figure was reprinted from (1) in accordance with Elsevier's policies.

Dr. I. Forné (LMU, Munich) performed the MS analysis.

In addition to XL-MS analysis, we collected information about the molecular shape of both the full-length DmISWI enzyme and the HSS domain (i.e., $ISWI_{691\text{-}1027}$) under apo state conditions in solution by SAXS measurements. The SAXS data for both DmISWI constructs collected at different protein concentrations resulted in largely superimposable scattering curves after rescaling by intensity (Figure 20A and C). However, slight concentration effects in the low q-region were observed for both DmISWI constructs at the highest sample concentrations indicating attractive interactions between individual particles, which could result in unspecific protein aggregation (234). To obtain optimum data quality, our collaboration partner Dr. L. Brützel (LMU, Munich) scaled and merged the low angle data from the lowest protein concentration with the high angle data from the highest concentration. The comparison between experimental and theoretical (pdb 1OFC) scattering profiles for the HSS domain (Figure 20B) yielded a χ-value of 1.84. This discrepancy could originate from the missing atomic coordinates for 16% of the residues in the high-resolution structure of the HSS module compared to our measured construct or could point towards slight differences in protein conformation.

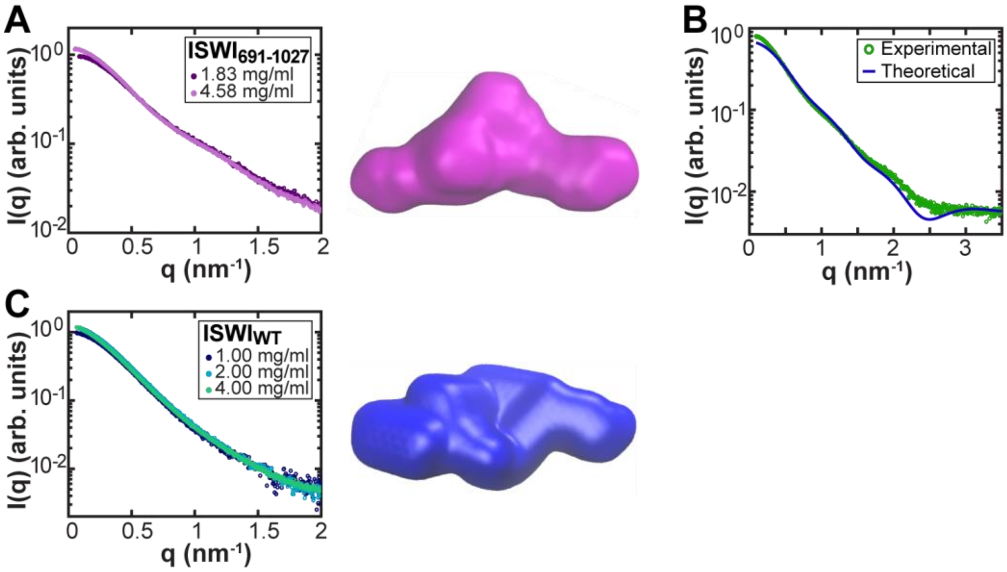

Figure 20: SAXS data for the full-length DmISWI enzyme and its HSS domain. (A) The extrapolated scattering curves for the HSS domain of the DmISWI enzyme are shown for different protein concentrations (left). Notably, these curves are largely superimposable. The *ab-initio* determined shape envelope for the HSS domain is depicted on the right side. **(B)** Superimposition of the experimental (green circles) and theoretical (blue line, pdb 1OFC) scattering profiles of the HSS domain of the DmISWI enzyme yielding a χ-value of 1.84. **(C)** Same representation as shown in (A) for the full-length DmISWI enzyme. The molecular envelope depicted on the right side implies that the full-length protein adopted a compact conformation under apo state conditions. The panel (C), left was adapted from (1) in accordance with Elsevier's policies.

I purified both DmISWI protein constructs and prepared the samples for SAXS measurements, which were conducted and analyzed by Dr. L. Brützel (LMU, Munich).

To visualize the relative orientation of the ATPase and HSS modules to each other in the full-length DmISWI enzyme, our collaboration partner Dr. C. Schindler (TUM, Munich) docked an ensemble of ten DmISWI ATPase models, which were most consistent with the collected SAXS data for ISWI$_{\Delta HSS}$ (cf. section 2.2.1.1), against the available HSS crystal structure (pdb 1OFC). The two-body docking was performed in an identical manner as described for the ATPase module in section 2.2.1.1. The docking was guided by five distance restraints, which were derived from identified inter-domain cross-links (XL$_{ISWI}$ 31–35; cf. STable 2) that yielded excellent fragmentation data during MS/MS analysis (Figure 19 and SFigure 5). The top-ranked 200 models showed convergence with regard to the spatial arrangement of the ATPase module and the HSS domain as indicated by an overall model precision of 3.3 Å. The model with the lowest χ-fit to the SAXS data of ISWI$_{WT}$ was selected as the representative model of the full-length DmISWI enzyme (Figure 21).

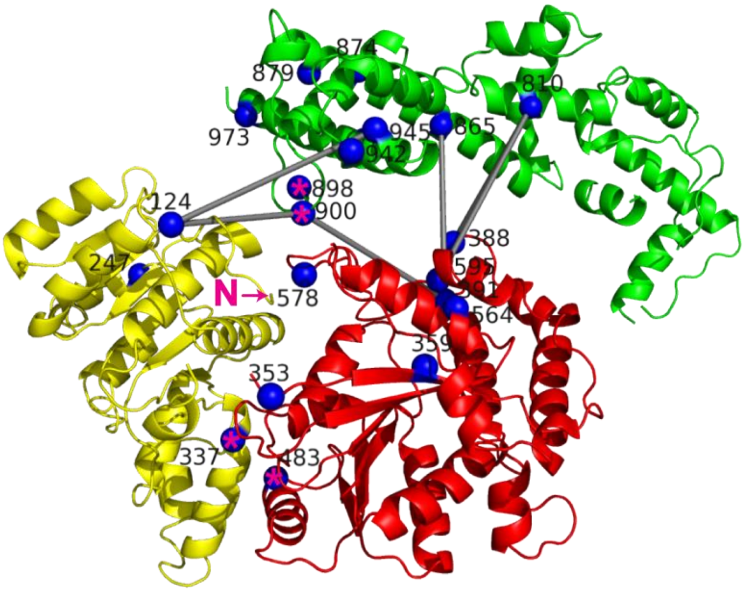

Figure 21: Structural model of the full-length DmISWI enzyme under apo state conditions in solution. Our structural model of the full-length DmISWI enzyme is shown with ATPase lobe 1, ATPase lobe 2, and the HSS domain being colored in yellow, red, and green, respectively. Cross-linked amino acids are represented as spheres. Pink asterisks indicate residues that cross-linked to the NTR, for which atomic coordinates are lacking in the structural model. Grey rods connect individual residues of identified inter-domain cross-links, for which the distance was restrained during the two-body docking procedure. STable 2 provides further details for individual cross-links. The arrow denotes the N-terminus of the model (N; residue 116). The Figure was adapted from (1) in accordance with Elsevier's policies.

I expressed, purified, and cross-linked the DmISWI enzyme and analyzed the respective XL-MS data. Dr. I. Forné (LMU, Munich) performed the MS analysis. Dr. C. Schindler (TUM, Munich) generated the full-length DmISWI model.

To evaluate our full-length DmISWI model, Dr. C. Schindler (TUM, Munich) first compared the proposed model to the scattering data for $ISWI_{WT}$. Notably, experimental and theoretical scattering data were found to be in overall good agreement as indicated by a χ-value of 1.04 (Figure 22A). The SAXS-derived shape envelope allows for accommodation of the computed full-length DmISWI structure (Figure 22B). In a second step, I measured the Cα-Cα distances between cross-linked residue pairs in the full-length DmISWI model. The majority of cross-links was largely consistent with the proposed DmISWI model (cf. STable 2). However, three cross-links (XL_{ISWI} 37, 38, and 40) exceeded the defined distance threshold by more than 20 Å. The cross-linked lysine residues in XL_{ISWI} 37 and 38 (i.e., K247, K945, and K353) are located in or are very close to flexible regions of the DmISWI enzyme, such that local protein dynamics at least partially account for the observed discrepancy between the computational and experimental data. The incompatibility of individual cross-linking distances with the proposed structural model (in particular XL_{ISWI} 40) could also arise from false sequence assignments or conformational heterogeneity of the protein sample.

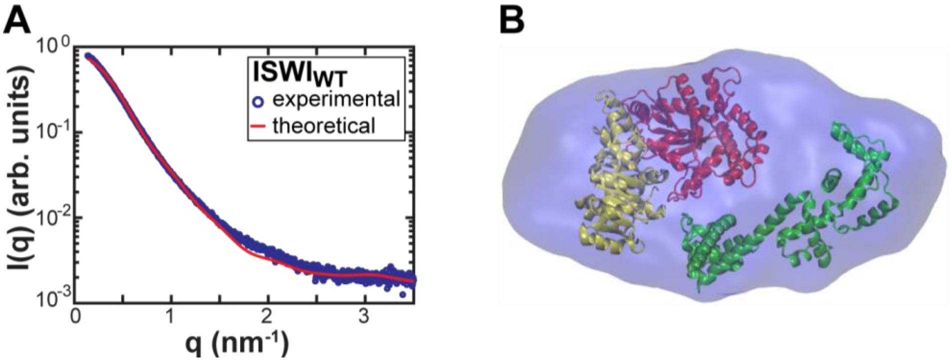

Figure 22: SAXS analysis of the full-length DmISWI enzyme. (A) The theoretical scattering profile obtained for the structural model depicted in Figure 21 (red line) is in good agreement (χ = 1.04) with the measured scattering data for the full-length DmISWI protein (blue circles). **(B)** SAXS envelope reconstruction of collected SAXS data of ISWI$_{WT}$ (residues 1-1027). The model shown in Figure 21 fits well into the reconstructed envelope. Note that, 22% of residues are missing in the full-length model, explaining the excess of electron density. L. Brützel (LMU, Munich) initially prepared the figures. Panel (A) and (B) were adapted and reprinted from (1), respectively, in accordance with Elsevier's policies.

Dr. L. Brützel (LMU, Munich) obtained and analyzed the SAXS data for ISWI$_{WT}$. Dr. C. Schindler (TUM, Munich) generated the full-length DmISWI model.

Our collaboration partner Dr. C. Schindler (TUM, Munich) assessed whether the implementation of additional, XL-MS-derived distance restraints between the ATPase module and the HSS domain would result in an improved full-length DmISWI model with respect to the experimental data. Repetition of the two-body docking procedure using all available inter-domain distance restraints (XL$_{ISWI}$ 31–40 and 42–45, cf. STable 2) resulted in a similar structural architecture for the DmISWI enzyme (Figure 23A). However, we could again not obtain a single model that satisfied all cross-linking distances at once (cf. STable 2).

We then considered that our models of the ATPase module might not be optimal. Dr. C. Schindler (TUM, Munich) thus separated the ATPase lobes at the hinge region of the ATPase module and docked them against the HSS domain in a three-body docking approach. The two separated ATPase lobes docked in a similar fashion against the HSS domain with an overall structural architecture of the full-length DmISWI enzyme resembling the one observed for the two-body docking approach (Figure 23B). Several distance restraints (cf. Table S1 and Table S2) as well as the fit to the SAXS data (χ = 0.85) were in better agreement with the generated model of the three-body docking approach. Nevertheless, XL$_{ISWI}$ 37, 38, and 40 still severely violated the distance thresholds by as much as > 20 Å. Consequently, it appears plausible that the well-documented flexibility of DmISWI domains (114, 129, 140) does not allow us to compute a single structural model of the enzyme that fits all cross-linking data at once.

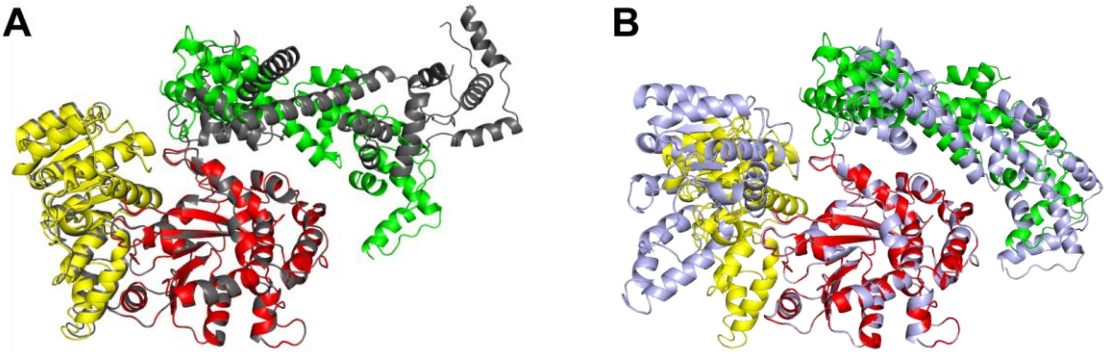

Figure 23: Evaluation of the structural model of the full-length DmISWI enzyme. (A) Incorporation of all identified ATPase-HSS cross-links into the two-body docking algorithm resulted in a similar domain arrangement (grey) as observed for the representative DmISWI model (colored) depicted in Figure 21. Structural models are aligned to ATPase lobe 2 for comparison. **(B)** Results of the three-body docking approach (light blue) are compared to our representative DmISWI model shown in Figure 21. The structural architecture in both full-length DmISWI models is similar. STable 1 and STable 2 provides cross-linking distances for both models. The Figure was adapted from (1) in accordance with Elsevier's policies.

Dr. C. Schindler (TUM, Munich) performed the computational modeling of the depicted structures.

I subsequently evaluated whether the proposed domain architecture for the full-length DmISWI protein allows for DNA binding by the HSS domain as has been demonstrated in previous studies (23, 116, 127, 151). I thus superimposed the crystal structure of the Isw1a HSS domain in complex with DNA (pdb 2Y9Z, (151)) onto our structural model of the full-length DmISWI enzyme (cf. Figure 21). Superimposition resulted in a direct steric clash between the ATPase module and the DNA strand (Figure 24) implying that the HSS domain in our DmISWI model is incapable of binding DNA without prior conformational changes. Notably, such a binding-incompetent orientation of the HSS domain supports the notion that the DmISWI enzyme assumes a resting conformation under apo state conditions in solution.

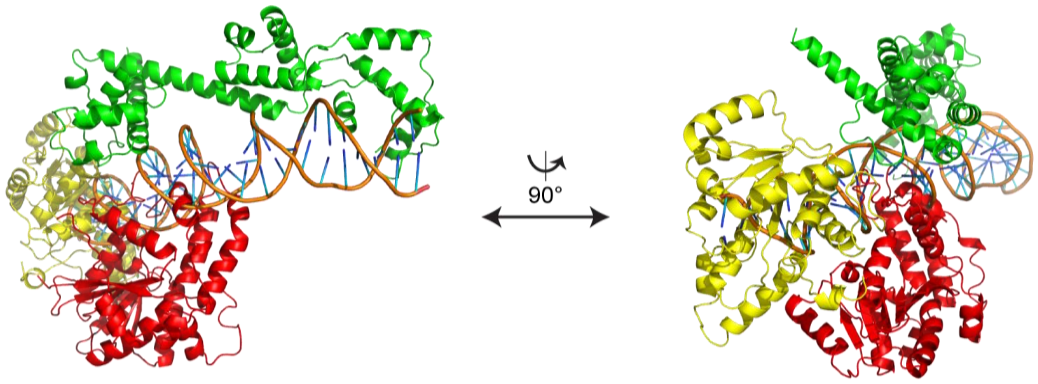

Figure 24: The full-length DmISWI model is not compatible with DNA binding via the HSS domain. The crystal structure of the HSS domain of ScISW1a (pdb 2Y9Z, (151); only the DNA is shown for clarity) was superimposed onto our structural model of the full-length DmISWI enzyme (ATPase lobe 1, yellow; ATPase lobe2, red; HSS domain, green; cf. Figure 21). Steric clashes between the ATPase module and the DNA strand can be observed. Consequently, our obtained model of DmISWI appears to be incompetent to bind DNA via the HSS domain. The Figure was adapted from (1) in accordance with Elsevier's policies.

Dr. C. Schindler (TUM, Munich) performed the modeling of the full-length DmISWI enzyme.

In summary, we propose a potential structure for the full-length DmISWI enzyme under apo state conditions in solution by using an integrative approach. The results from XL-MS analysis and computational docking collectively suggest that the C-terminus of the HSS domain packs against the ATPase module. The proposed arrangement of the HSS domain appears to be incapable of binding to DNA without prior conformational changes. The minor inconsistencies observed between experimental and computational data may arise from inherent protein flexibility in one or more parts of the DmISWI enzyme.

2.2.3. The NTR bridges both ATPase lobes and contacts the HSS

In a recent study by Ludwigsen and co-workers (115), several NTR residues of the DmISWI enzyme formed cross-links with Bpa substituted at position H483 of ATPase lobe 2. However, the relative orientation of the NTR region in the full-length DmISWI protein has remained unclear. Here, I identified an additional, chemical cross-link candidate (XL_{ISWI} 13; cf. STable 1), which connects the autoregulatory NTR region and ATPase lobe 1. Although high-resolution structures for the NTR are lacking for the DmISWI protein, the partner cross-linking sites were found in close spatial proximity to the ATPase lobe-lobe interface in our structural model of the full-length enzyme (cf. pink asterisks in Figure 21). Consequently, the results by Ludwigsen *et al.* and my findings collectively suggest that the NTR domain is neighboring the ATPase lobe-lobe interface under apo state conditions in solution.

The MtISWI protein has recently been crystalized with large parts of the NTR domain (pdb 5JXR) (146), which in turn allowed Dr. C. Schindler (TUM, Munich) to generate an MtISWI-based homology model of the ATPase module. Using this homology model, I measured the Cα-Cα distances between cross-linked residue pairs of the NTR domain and the ATPase module. The here identified XL_{ISWI} 13 as well as the published cross-links by Ludwigsen *et al.* did not violate the distance threshold for the UV- and chemical cross-linkers (range 7.9–25.3 Å) and thus were consistent with the MtISWI-based homology model (Figure 25). This finding is consistent with the notion that the NTR region of the DmISWI protein contacts the ATPase domain in a similar fashion as observed in the MtISWI structure and that the interaction site on the ATPase domain may be conserved between these two remodeling enzymes.

Unexpectedly, I also identified inter-domain cross-links that connect the NTR domain and the HSS domain. The cross-linker bridged distant residue pairs (XL_{ISWI} 46–48, cf. STable 2) with respect to the primary protein sequence (i.e., > 800 amino acids), which indicates spatial proximity between the SLIDE region and the NTR domain. Mapping these cross-linking sites onto the HSS domain in our full-length DmISWI model (cf. pink asterisks in Figure 21) revealed that the cross-linked residues are also located in close spatial proximity to the lobe-lobe interface of the ATPase module.

Our collaboration partner Dr. C. Schindler (TUM, Munich) subsequently generated an MtISWI-based structural model of the full-length DmISWI enzyme that includes large parts of the NTR region. We applied the same docking protocol, including identical Cα-Cα distance restraints, to generate the MtISWI-based model as described for our representative full-length structure shown in Figure 21. The only difference was that an MtISWI-based homology model of the ATPase module (i.e., encompassing residues 38–592), instead of the ScChd1-based ATPase model, served as input structure. I subsequently assessed the compatibility of identified NTR-HSS cross-links (XL_{ISWI} 46–48) with the MtISWI-based structural model. Notably, the Cα-Cα distances between these cross-linked residue pairs consistently exceeded the distance threshold by almost 20 Å on average in the MtISWI-based model (cf. STable 2). However, the MtISWI-based model showed remarkable consistency with the experimental SAXS data for the full-length DmISWI enzyme as indicated by a χ-value of 0.88.

We reasoned that the implementation of distance restraints that map to the NTR region (XL_{ISWI} 46–48) would result in an MtISWI-based structural model that is more consistent with the experimental XL-MS data. Implementation of these additional distance restraints during docking indeed substantially improved the observed Cα-Cα distances between cross-linked residues of the NTR region and the HSS domain for XL_{ISWI} 46–48 by approximately 10 Å on average (Figure 25 and STable 2). However, this alternative MtISWI-based model resulted in a significantly poorer fit to the experimental SAXS data for the $DmISWI_{WT}$ enzyme as indicated by a χ-value of 2.92. Possible explanations for the increased discrepancy between experimental and theoretical SAXS data upon implementation of NTR-HSS distance restraints is discussed in section 3.2.

Taken together, our XL-MS data collectively suggest that the NTR domain is located near the interface of both ATPase lobes and potentially assumes a similar conformation as observed in the recent crystal structure of the MtISWI enzyme. In addition, the SLIDE region of the HSS module packs against the ATPase domain in spatial proximity to the NTR region. Consequently, the catalytic core of the DmISWI protein appears to be caged by the NTR domain and the C-terminal region of the HSS module, which may lock the remodeling enzyme in a resting conformation under apo state conditions in solution.

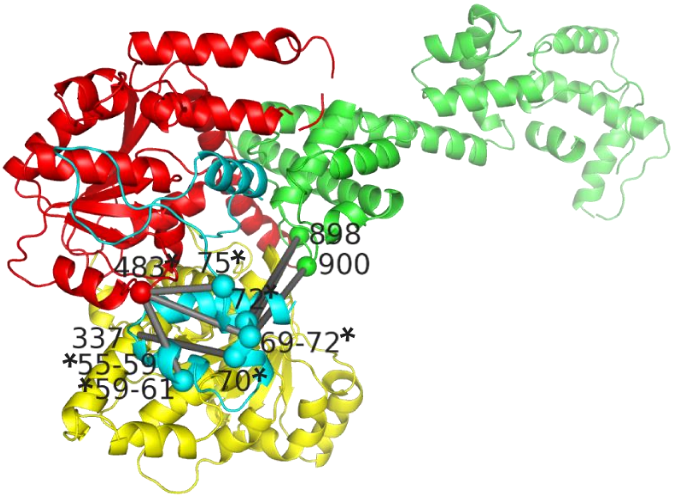

Figure 25: The NTR is neighboring both ATPase lobes and the HSS domain in the full-length DmISWI enzyme. Identified cross-links originating from the NTR are shown in a structural model of full-length DmISWI including the NTR domain. Protein domains are colored according Figure 12. An MtISWI-based homology model of the ATPase module (NegC was omitted, discussed in section 2.2.4) was docked onto the HSS domain using cross-linking distance restraints as guides. Cross-links originating from the NTR (XL_{ISWI} 13, 46–48 and published cross-links from (115)) are shown as rods. Cross-linked residue pairs published in (115) are furthermore marked by an asterisk. The measured Cα-Cα distances between individual residue pairs were below the distance threshold of the cross-linkers (see also STable 1 and STable 2 for individual values) suggesting a comparable orientation of the NTR in the full-length DmISWI and MtISWI enzymes under apo state conditions.

Dr. C. Schindler (TUM, Munich) performed the computational modeling of the depicted structure.

2.2.4. The NegC adopts a Chd1-like conformation

As of today, two significantly distinct conformations of the NegC domain have been reported. In the crystal structure of the ScChd1 protein (pdb 3MWY), the NegC domain bridges both ATPase lobes thereby locking the enzyme in an inactive state (114, 141) (Figure 26A). In contrast, the NegC domain protrudes from the catalytic core and interacts with a neighboring protomer in the crystal structure of the MtISWI protein (pdb 5JXR) (146). Consequently, XL-MS analysis provided an excellent opportunity to probe the orientation of the NegC domain in the full-length DmISWI enzyme under apo state conditions in solution.

We identified a total of 16 cross-linked peptides, which revealed five cross-linked residue pairs between the NegC domain and the ATPase module (XL_{ISWI} 8–12, cf. STable 1). Notably, the Cα-Cα distances between cross-linked lysine residues of XL_{ISWI} 9–12 complied with the defined distance threshold not only in our ScChd1-based model of the DmISWI ATPase module but also with the crystal structure of the ScChd1 protein (pdb 3MWY). Solely XL_{ISWI} 8 modestly violated the maximal distance in our structural model of the ATPase module, as already discussed above, as well as in the ScChd1 crystal structure by less than 5 Å.

In order to evaluate whether our XL-MS results are compatible with a protruding NegC conformation as observed recently for the MtISWI enzyme, I measured the Cα-Cα distances between cross-linked residue pairs, which map to the NegC region in the respective crystal structure. I thereby measured the distances between residues of a single protomer as well as between two neighboring protomers (see STable 1 for individual values). The XL-MS-derived distance restraints of XL_{ISWI} 9–12 were satisfied in the MtISWI dimer, in which the NegC domain serves as a dimerization interface. Thus, our XL-MS data could indicate a similar protruding conformation of the NegC region for the DmISWI enzyme presupposed that the protein is present as a dimer under the tested conditions. However, although the MtISWI enzyme has been crystalized as a homodimer, Yan and co-workers emphasized in the same study that the protein is predominantly (> 90%) present as a monomer in solution (146). We also hold experimental evidence that the DmISWI enzyme is present as a monomer under apo state conditions in solution. In particular, the SEC analyses of native and cross-linked DmISWI protein (Figure 26B) as well as the SAXS-derived molecular envelope (cf. section 2.2.2.) showed consistency with a monomeric solution state of the remodeling enzyme.

The large majority of XL-MS-derived distance restraints, however, were severely violated in the monomeric MtISWI structure (Figure 26C and STable 1). That is, XL_{ISWI} 8 and XL_{ISWI} 10–12 exceeded the defined Cα-Cα distance threshold by almost a factor two with cross-linked residue pairs frequently being 50 Å apart from each other. Consequently, given that the DmISWI protein appears to be present as a monomer under apo state conditions in solution, the XL-MS data for our remodeling enzyme are inconsistent with a protruding NegC conformation.

To further rule out that the NegC domain is protruding from the catalytic core in the DmISWI enzyme, Dr. C. Schindler (TUM, Munich) computationally docked the HSS domain (pdb 1OFC) against an MtISWI-based homology model of the ATPase module comprising the NegC region (i.e., encompassing residues 38–651). The resulting structural model of the DmISWI protein displayed a deviating domain architecture with the HSS domain packing differently against the ATPase module (Figure 26D) when compared to our proposed, ScChd1-based structure of the full-length enzyme depicted in Figure 21. Importantly, the large majority of distance restraints (> 88%) between the ATPase and HSS module (XL_{ISWI} 31–48; cf. STable 2) suddenly exceeded the distance threshold of the cross-linking agent in the MtISWI-based structural model. Notably, this model furthermore exhibited a poorer fit to the SAXS-derived scattering data for $DmISWI_{WT}$ as indicated by a χ-value of 2.53. To test whether the protruding NegC conformation biased the docking towards a deviating domain architecture, Dr. C. Schindler (TUM, Munich) repeated the docking protocol in the absence of the NegC domain (i.e., residues 593−651 were removed from the ATPase module). The MtISWI-based structural model, in which the NegC region was removed, was well superimposable with our proposed, ScChd1-based model of the full-length DmISWI enzyme. The large majority of inter-domain cross-links between the ATPase and HSS module complied with the distance requirements of the cross-linking agent and we obtained a good fit to the SAXS data for $DmISWI_{WT}$ as indicated by a χ-value of approximately 1. Consequently, the computational simulations on the MtISWI-based homology model of the ATPase module further underscored that our experimental data for DmISWI are incompatible with a protruding NegC conformation.

In summary, our experimental SAXS and XL-MS data as well as computational simulations collectively imply that the NegC domain of the DmISWI enzyme adopts a similar conformation under apo state conditions as has been observed for the related ScChd1 protein.

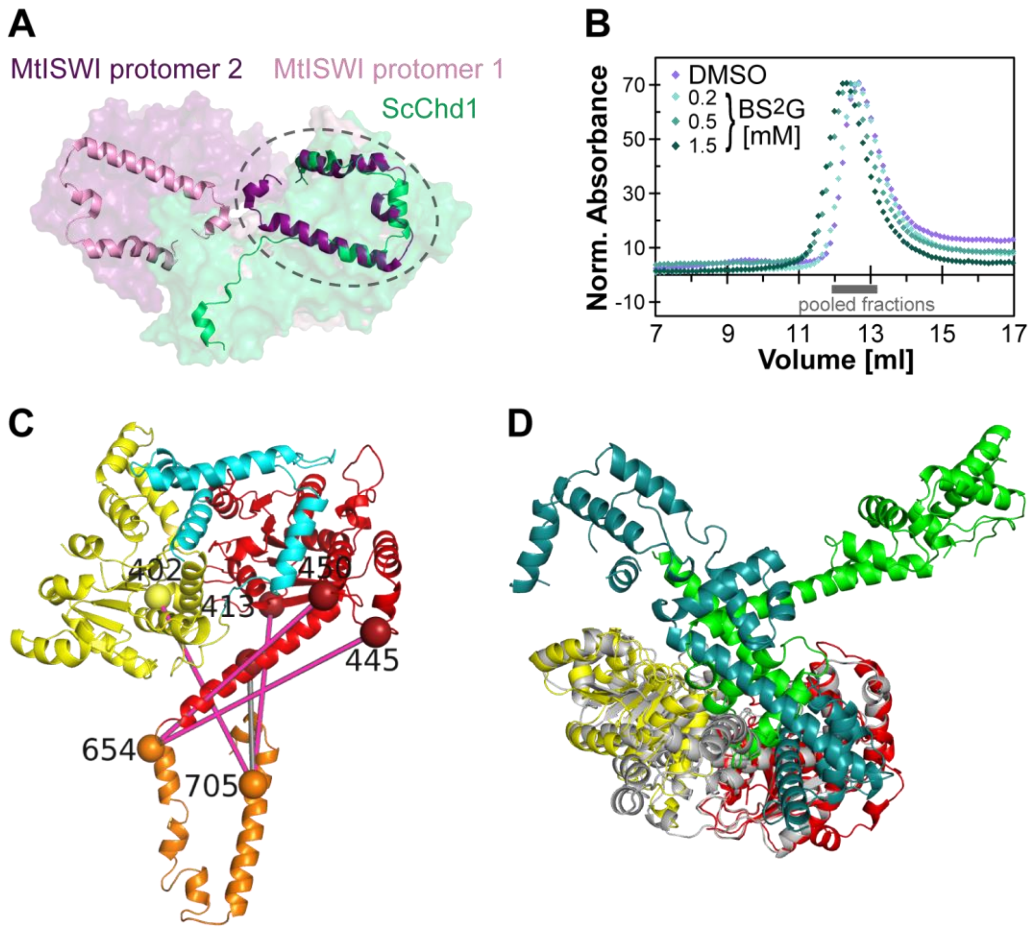

Figure 26: XL-MS data for DmISWI are inconsistent with a protruding NegC conformation. (A) The NegC conformations in the structures of MtISWI and ScChd1. Protomer 1 of dimeric MtISWI (light pink; pdb 5JXR) was aligned with monomeric ScChd1 (green; pdb 3MWY) on ATPase lobe 2. The NegC of MtISWI protomer 1 (light pink) protrudes from the surface to interact with protomer 2 (dark pink). Likewise, the NegC region of MtISWI protomer 2 bridges across the ATPase module of protomer 1. Remarkably, the NegC of ScChd1 (green) and of MtISWI protomer 2 pack against the ATPase domain in a similar manner (dashed ellipse). **(B)** Size-exclusion chromatography of cross-linked and DMSO-treated DmISWI$_{WT}$. Superdex 200 10/300 GL elution profiles of DMSO-treated and cross-linked full-length DmISWI protein did not provide evidence for dimerization. **(C)** NegC cross-links mapped onto the structure of a single MtISWI protomer (pdb 5JXR). The majority of Cα-Cα distances between NegC and the ATPase lobes are violated (pink rods) in the MtISWI protomer. See also STable 1 for individual spanned distances of the cross-linker. Cyan, NTR; yellow, ATPase lobe 1; red, ATPase lobe 2; orange, NegC. **(D)** An MtISWI-based homology model including the NegC region (grey) was docked against the HSS domain (teal, pdb 1OFC). We observe a substantially different orientation of the HSS domain in the MtISWI- and ScChd1-based (yellow, red, green; cf. Figure 21) models of the DmISWI enzyme. See also STable 2 for individual distances spanned by the cross-linker. The panels (A)–(C) were adapted from (1) according in accordance with Elsevier's policies.

Dr. C. Schindler (TUM, Munich) performed the computational modeling of the structures in panel (D).

2.3. Solution structure of the Snf2H enzyme under apo state conditions

To corroborate our findings for DmISWI (e.g., domain orientation, see section 2.2), we probed the in-solution structural architecture of the orthologous, human remodeling enzyme Snf2H using a similar integrative approach (i.e., XL-MS, SAXS, and computational modeling). We were in particular interested in elucidating whether Snf2H assumes an overall comparable conformation under apo state conditions as the DmISWI protein.

Despite the availability of a low-resolution Snf2H structure (150), molecular details of the full-length Snf2H enzyme as well as the mechanism of action have remained elusive. The human Snf2H remodeling enzyme shares 79% overall sequence identity with its *Drosophila* counterpart (Clustal Omega web service, EMBL-EBI). While residues of the functionally important ATPase, NegC, and HSS domains appear to be largely conserved across these two species, sequence homology is somewhat lost in the autoregulatory NTR region (< 32% sequence identity) (140). Considering the remarkable sequence homology, we envisaged that studying the structural architecture of human Snf2H in solution would not only allow us to indirectly validate the findings for DmISWI but also to draw mechanistic inferences on this important class of proteins.

2.3.1. The Snf2H domain architecture viewed by chemical cross-linking

To obtain structural information about the full-length Snf2H enzyme under apo state conditions, I chemically cross-linked the protein using the BS^3 cross-linking agent and analyzed the XL-MS data (cf. sections 4.2.4.1.2 and 4.2.4.5), while our collaboration partner Dr. I. Forné (LMU, Munich) was responsible for high-resolution MS analysis (cf. section 4.2.4.4).

MS analysis resulted in the identification of 115 cross-linked peptides yielding a total of 84 unique residue pairs for the Snf2H enzyme (Figure 27, STable 3). The large majority (81%) of these cross-linked residue pairs were reproduced in at least a technical replicate as further specified in column “Reproducibility group” in STable 3.

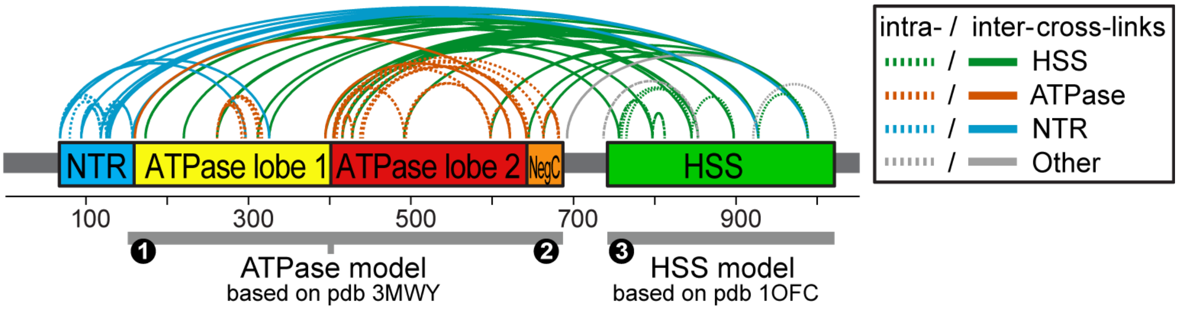

Figure 27: Identified BS^3 cross-links for the full-length Snf2H enzyme under apo state conditions in solution. Schematic representation of Snf2H domains with identified inter- and intra-domain cross-links being indicated as solid and dotted arcs (cf. color scheme), respectively. Numbers refer to the residue numbering of the Snf2H enzyme. The grey bars below the arc plot specify the range of the generated homology models. STable 3 provides further details for each cross-link. NTR: N-terminal region; HSS: HAND-SANT-SLIDE.

Dr. I. Forné (LMU, Munich) performed the MS analysis.

Due to the lack of high-resolution structures for the Snf2H enzyme, our collaboration partner Dr. C. Schindler (TUM, Munich) homology modeled the ATPase module (residues 120–689) and HSS domain (residues 743–1012) according to the structures of ScChd1 (pdb 3MWY, 41% sequence identity,) and DmISWI (pdb 1OFC, 81% sequence identity), respectively. The ATPase module was cleaved at a predicted hinge region into two structural bodies (i.e., residues 120−403 and 404−689).

I validated these homology models based on identified intra-domain cross-links (cf. STable 3) for the HSS domain (XL_{Snf2H} 70–75), ATPase lobe 1 (XL_{Snf2H} 64–69), and ATPase lobe 2 (XL_{Snf2H} 53–63) (Figure 28). Importantly, all HSS cross-linking distance restraints were consistent with the homology model of the Snf2H domain. Likewise, the large majority of intra-domain linkages for individual structural bodies of the ATPase module were in excellent agreement with only two cross-links (XL_{Snf2H} 63 and 67) negligibly violating the defined Cα-Cα distance threshold by $\leq$ 0.4 Å. Taken together, the generated homology models for the HSS domain and ATPase lobes were consistent with the XL-MS data and thus could be used to elucidate the overall structural architecture of the Snf2H enzyme.

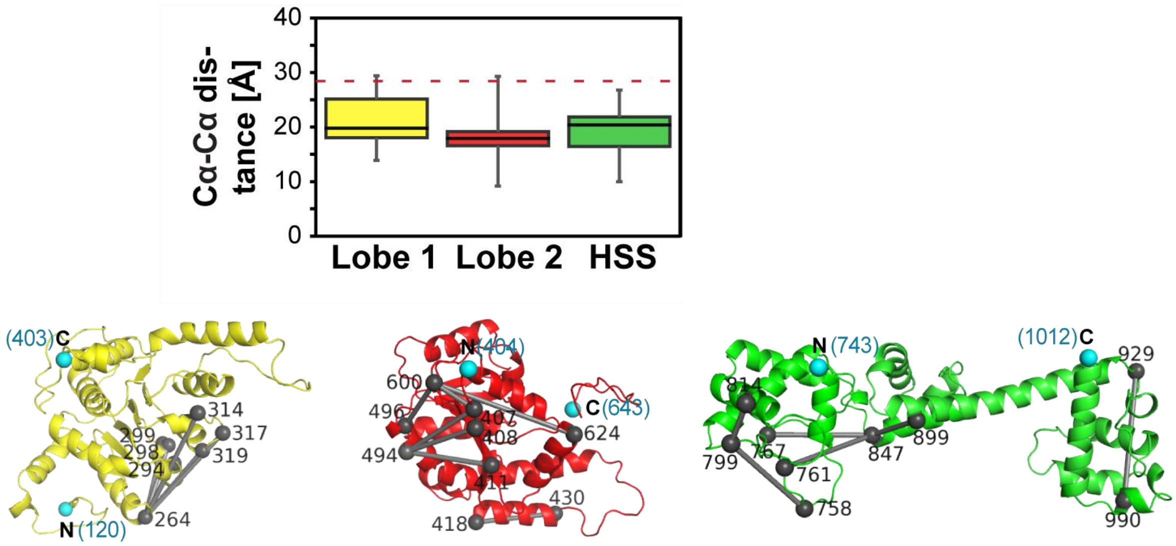

Figure 28: XL-MS-based evaluation of homology models for distinct Snf2H domains. I measured the Cα-Cα distances between residues of identified intra-domain cross-links in the respective homology models of ATPase lobe 1 (yellow; i.e., XL$_{\mathrm{Snf2H}}$ 64–69; STable 3), ATPase lobe 2 (red; i.e., XL$_{\mathrm{Snf2H}}$ 53–63) and the HSS domain (green; i.e., XL$_{\mathrm{Snf2H}}$ 70–75) of the Snf2H enzyme. Cross-links are indicated as grey lines and spheres in the homology models, in which the N- and C-termini are furthermore highlighted in cyan for orientation. The presented box plots signify the median (solid line) and the third and first quartile range (box) of the measured Cα-Cα distances in the respective Snf2H domain. The whiskers indicate the minimum and maximum measured Cα-Cα distances. The distance threshold given by the cross-linking agent is shown as a red dotted line in the box plot diagram.

Dr. C. Schindler (TUM, Munich) performed the homology modeling of individual Snf2H domains.

I identified a total 50 inter-domain cross-links that restricted the relative orientation of Snf2H domains to each other. A subset of these linkages connected the two ATPase lobes with the HSS domain (XL$_{\mathrm{Snf2H}}$ 1–29, STable 3) with cross-linked peptides (i.e., XL XL$_{\mathrm{Snf2H}}$ 7–12, 14, 26, 28, 29) frequently providing excellent fragmentation data during MS analysis (SFigure 6).

Intriguingly, we noticed that the majority of contacts from the ATPase module to the HSS domain were formed to the C-terminal SLIDE domain (cf. STable 3). In particular, lysine residues K929 and K990 of the SLIDE region appeared to represent cross-linking hotspots (Figure 29A). Cross-links originating from either K929 or K990 mapped to broadly distributed lysine residues of ATPase lobe 1 and ATPase lobe 2 (Figure 29B, C). Such a wide-ranging distribution of partner cross-linking sites was not observed for any other lysine residue and may indicate inherent protein flexibility in one or more regions of the Snf2H enzyme as further discussed in section 3.2. Consequently, a considerable number of cross-links substantiated the notion of spatial proximity between the SLIDE domain and the ATPase module in the Snf2H enzyme under apo state conditions.

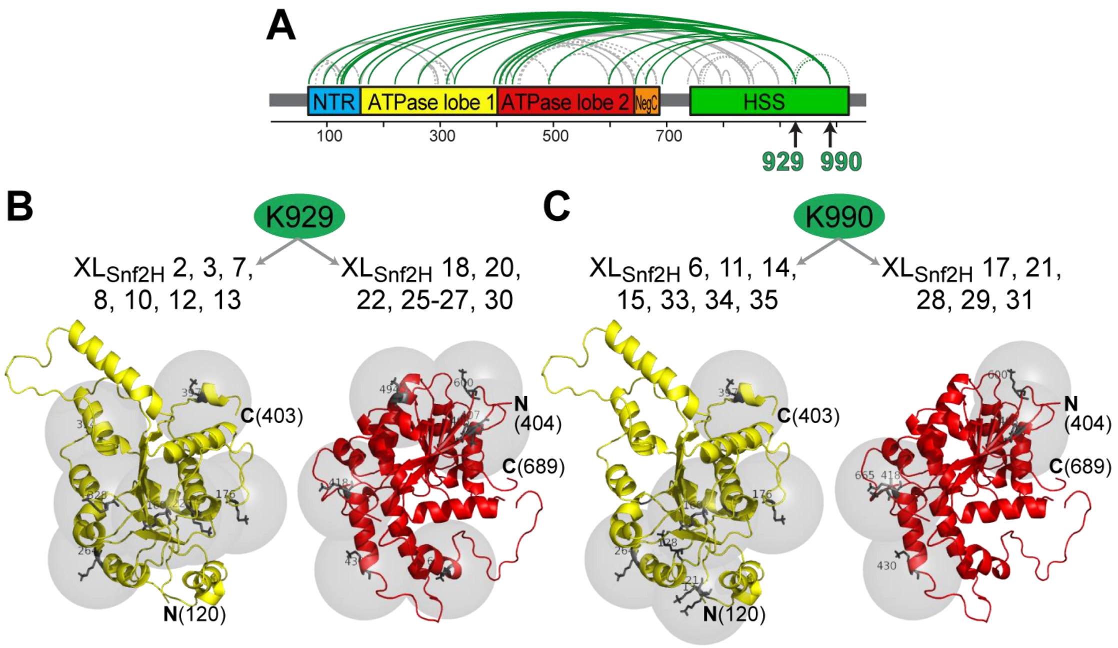

Figure 29: Cross-linking hotspots of the SLIDE region. (A) Arc plot of identified cross-links for the Snf2H enzyme shown in Figure 27 with cross-links originating from lysine residues 929 and 990 of the SLIDE domain being colored in green. Remaining cross-links are depicted as grey arcs. **(B)** Mapping of partner cross-linking sites for residue K929 onto Snf2H homology models of ATPase lobe 1 (yellow) and ATPase lobe 2 (red). The partner cross-linking sites on the ATPase lobes are indicated as grey spheres with the radius of the spheres corresponding to the length of the BS^3 spacer arm (i.e., 11.4 Å). The N- and C-termini of the Snf2H homology models are denoted for orientation. **(C)** Mapping of partner cross-linking sites for residue K990 as shown in (B).

Dr. C. Schindler (TUM, Munich) performed the homology modeling of individual Snf2H domains.

MS analysis of cross-linked Snf2H samples only resulted in the identification of a single cross-linked residues pair (i.e., XL_{Snf2H} 43, STable 3) that restricted the relative orientation of both ATPase lobes to each other. That is, I found that K397 of ATPase lobe 1 cross-linked to K624 of lobe 2 suggesting spatial proximity between the C-termini of both ATPase lobes. I subsequently checked the compatibility of the identified ATPase lobe-lobe cross-link XL_{Snf2H} 43 with our structural model of DmISWI (cf. Figure 21) as well as published structures of ScChd1 (pdb 3MWY) and MtISWI (pdb 5JXR). The Cα-Cα distance slightly exceeded the distance threshold by < 6.5 Å in the structures of DmISWI and MtISWI but showed consistency with the domain orientation of the ScChd1 protein. The increased Cα-Cα distance in the DmISWI and MtISWI structures may arise from local protein dynamics considering that the cross-linked lysine residue K397 resides in an unstructured and thus probably flexible Snf2H region. In conclusion, the limited number of identified lobe-lobe cross-links only provides a rough approximation of the relative orientation of both ATPase lobes to each other and does not allow for a conclusive statement.

The relative position of the autoregulatory NegC domain in the full-length Snf2H enzyme was restricted by a total of ten inter-domain cross-links (XL_{Snf2H} 30–32 and 44–50, STable 3). These cross-links mapped to either the above-mentioned hotspot residues K929 and K990 of the SLIDE domain (i.e., XL_{Snf2H} 30–32) or both ATPase lobes (XL_{Snf2H} 44–50). A single cross-link (XL_{Snf2H} 44) connected the very N-terminus of ATPase lobe 1 with the NegC domain raising the possibility that NegC bridges the ATPase lobe-lobe interface under apo state conditions. The Cα-Cα distance restraints between cross-linked residue pairs of ATPase lobe 2 and NegC (XL_{Snf2H} 45–50) were consistent with our ScChd1-based homology model of the respective domains (Figure 30A). Assuming that the Snf2H is present as a monomer in solution (cf. SAXS data for Snf2H in section 2.3.2), the identified NegC-ATPase lobe 2 cross-links argue against a protruding NegC conformation as depicted in the MtISWI crystal structure (pdb 5JXR). That is, mapping XL_{Snf2H} 45–50 onto a single MtISWI protomer consistently violated the defined BS^3 distance threshold by a factor of 1.7 to 3.1 (Figure 30B).

In conclusion, I find that the NegC regions potentially assumes a ScChd1-like conformation in the full-length Snf2H enzyme with the autoregulatory domain packing against both ATPase lobe and the SLIDE region of the HSS domain. As such, XL-MS data for the NegC region appear to be similar for the full-length Snf2H and DmISWI enzymes under apo state conditions in solution (Figure 30C).

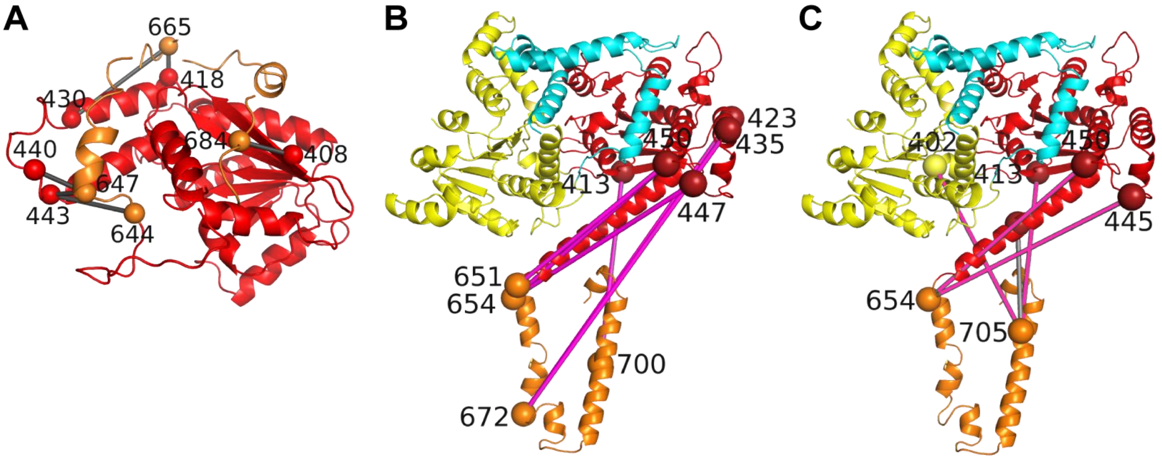

Figure 30: XL-MS data for the Snf2H enzyme are consistent with a ScChd1-like orientation of the NegC domain. (A) NegC cross-links mapped onto our ScChd1-based homology model of ATPase lobe 2 (red) and the NegC domain (orange). Identified inter-domain cross-links that connect these two regions (XL_{Snf2H} 45–50) are indicated as grey rods. The Cα-Cα distance restraints between individual NegC-ATPase lobe 2 residue pairs were all satisfied in our homology model. **(B)** NegC cross-links mapped onto the structure of a single MtISWI protomer (pdb 5JXR). All Cα-Cα distances between NegC (orange) and ATPase lobe 2 (red) are violated (pink rods; XL_{Snf2H} 45–50) and exceed the distance threshold by 19–60 Å in the MtISWI protomer. Cyan, NTR; yellow, ATPase lobe 1. **(C)** Identified NegC cross-links for the DmISWI enzyme are mapped onto the MtISWI crystal structure for comparison (Figure identical to Figure 26C). The comparison between (B) and (C) reveals similar cross-linked residue pairs suggesting a similar, ScChd1-like conformation of the NegC region in both Snf2H and DmISWI enzymes.

Dr. C. Schindler (TUM, Munich) performed the homology modeling shown in panel (A).

In the case of the NTR region, various lysine residues of ATPase lobe 1 and the SLIDE domain formed cross-links with reactive residues of the NTR ($\mathrm{XL}_{\mathrm{Snf2H}}$ 33–42, STable 3). In particular lysine residues K121, K128, and K129 of the NTR, which are in close spatial proximity to the N-terminus of ATPase lobe 1, formed intra- and inter-domain linkages with surrounding residues ($\mathrm{XL}_{\mathrm{Snf2H}}$ 76–82 and 33, 34, 40–42, respectively). The structural interpretation of these XL-MS results in light of the limited number of available high-resolution structures is difficult due to the inherently low sequence homology in the NTR region among related remodeling enzymes. I evaluated the Cα-Cα distances for NTR-ATPase cross-links between corresponding sites in the recently published MtISWI structure (pdb 5JXR) that comprises large parts of the NTR (Table 1). Notably, the identified inter-domain cross-links $\mathrm{XL}_{\mathrm{Snf2H}}$ 40–42 were in excellent agreement with the MtISWI structure with Cα-Cα distances ranging from 24.8–29.1 Å. The validity of $\mathrm{XL}_{\mathrm{Snf2H}}$ 38 and 39 could, however, not be assessed due to the lack of atomic coordinates in the NTR region that harbors the respective cross-linked residue.

Table 1: The Cα-Cα distances of NTR cross-links in the structure of MtISWI.

	Snf2H (this study)			**MtISWI** (pdb 5JXR)		
$\mathrm{XL}_{\mathrm{Snf2H}}$	Site 1	Site 2	Dist. thres-hold [Å]	Site 1	Site 2	Dist. [Å]
40	K160	K121	≤ 29	K166	K123	29.1
41	K160	K128	≤ 29	K166	R136	24.8
42	K160	K129	≤ 29	K166	K137	27.4

In summary, our XL-MS findings are consistent with an MtISWI-like conformation of the NTR region with the SLIDE domain being in close spatial proximity to the NTR region in the full-length Snf2H enzyme.

In overall conclusion, our XL-MS data for the full-length Snf2H protein collectively point towards a rather compact enzyme conformation under apo state conditions. That is, the identified cross-links are consistent with the notion that the autoregulatory NTR and NegC regions pack against the ATPase lobes. In addition, I identified the SLIDE region of the HSS domain to form various contacts to the ATPase module including the NTR, NegC, and both ATPase lobes. From a XL-MS perspective, it thus appears possible that the Snf2H and DmISWI remodeling enzymes assume a similar conformation under the investigated solution conditions.

2.3.2. The Snf2H domain architecture viewed by computational modeling and SAXS

To computationally resolve the structural architecture of the Snf2H enzyme under apo state conditions, we decided to perform a three-body docking using the ScChd1- and DmISWI-based homology models for both ATPase lobes and the HSS domain (cf. section 2.3.1), respectively. Our collaboration partner Dr. C. Schindler (TUM, Munich) performed the computational docking of individual Snf2H domains by employing a total of eleven XL-MS-derived distance restraints (i.e., XL_{Snf2H} XL 7–12, 14, 26, 28, 29, 44; STable 3). These distance restraints were selected because the respective cross-linked peptides showed excellent fragmentation data during MS/MS analysis (SFigure 6). Notably, the modeling procedure for the Snf2H protein differed to the one described for DmISWI (i.e., two two-body docking procedure, cf. section 2.2.2) in order to overcome the limited number of identified cross-links between the two ATPase lobes. Using a three-body docking protocol, the arrangement of both ATPase lobes in the modeled Snf2H structure would primarily depend on their relative orientation towards the HSS domain. Briefly, the orientation of initially randomly orientated Snf2H domains ($1x10^5$ starting configurations) was guided by XL-MS derived upper harmonic distance restraints using the ATTRACT modeling software. The computed models were ranked by their ATTRACT energy score and the top-ranked 200 models were selected for atomistic refinement with iATTRACT.

We observed a considerable heterogeneity among the generated structural models of the full-length Snf2H enzyme under apo state conditions. For instance, structural alignment of the two top-ranked Snf2H models resulted in an RMSD of approximately 9.5 Å underscoring their divergent domain architecture. In particular the docking geometry of the HSS domain relative to the ATPase module remained ambiguous as shown in Figure 31A for 18 out of the total 200 generated full-length Snf2H models (i.e., the top five and every fifteenth model).

To validate individual Snf2H models with respect to the XL-MS data, I subsequently measured the Cα-Cα distances between cross-linked residue pairs of all accessible inter-domain cross-links, including cross-links used for docking, in the representative structures depicted in Figure 31A. The observed distribution of measured Cα-Cα distances for each inter-domain cross-link is summarized in Figure 31B. Importantly, none of the selected structural models of the full-length Snf2H enzyme was entirely consistent with the implemented distance restraints used for docking and the majority of additional identified inter-domain cross-links exceeded the BS^3 distance threshold. Possible reasons for the discrepancy between the XL-MS and computational data may have diverse origins, which are further discussed in section 3.1.

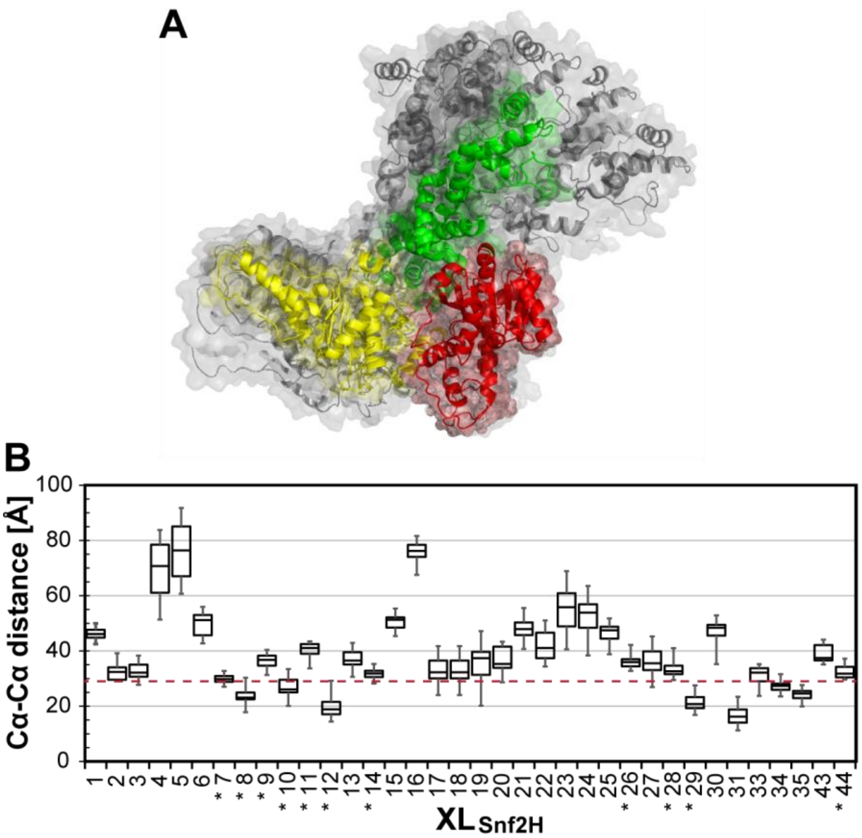

Figure 31: Structural models of the Snf2H enzyme under apo state conditions in solution. (A) The top-ranked Snf2H models (i.e., models #1-5 and every other fifteenth model) are shown and aligned to ATPase lobe 2 of model #1. ATPase lobe 1, ATPase lobe 2, and the HSS domain of model #1 are colored in yellow, red, and green, respectively. The remaining structures are depicted in grey color. **(B)** The Cα-Cα distances between reactive residues of identified inter-domain cross-links were measured in each Snf2H model shown in (A). Individual box plots summarize the observed distribution of measured Cα-Cα distances for each inter-domain cross-link. That is, each box plot shows the median (solid line), the Q3-Q1 range (box), and the minimum and maximum measured Cα-Cα distance (whiskers). Cross-links are numbered according to STable 3. Cross-links with an asterisk were used as distance restraints during computational docking. The Cα-Cα distance threshold given by the cross-linking agent is shown as a red dotted line in the box plot diagram.

Dr. C. Schindler (TUM, Munich) performed the computational docking of the full-length Snf2H enzyme shown in panel (A).

As an additional complementary approach to XL-MS analysis, Dr. L. Brützel (LMU Munich) performed SAXS measurements on the full-length Snf2H protein in order to deduce the molecular shape of the remodeling enzyme under apo state conditions in solution. A series of SAXS measurements at different Snf2H concentrations resulted in well superimposable scattering profiles (Figure 32A). Reconstruction of the molecular envelope showed that the Snf2H protein predominantly assumes an overall globular, yet slightly elongated conformation (Figure 32B). The SAXS data thus show consistency with the computationally generated Snf2H models considering that representative structures can be fitted well into the molecular envelope (e.g., model #1; Figure 32B). Comparison between the experimental and the theoretical scattering curves for the investigated Snf2H models depicted in Figure 31A resulted in an average χ-value of 4.2 ± 0.3, which is close to the upper limit of the acceptance criterion range of < 2 (172) to 5 (173).

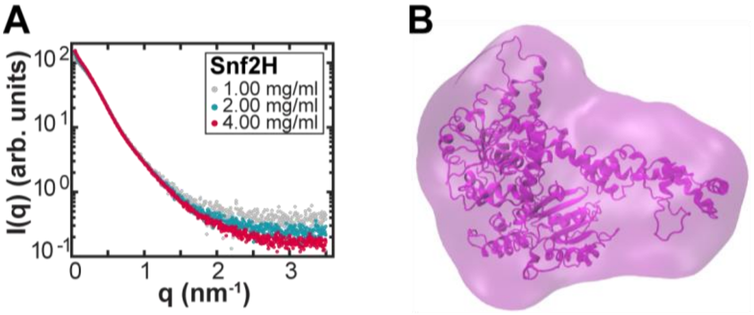

Figure 32: SAXS analysis of the Snf2H enzyme. (A) The extrapolated scattering curves for the Snf2H enzyme are shown for three different protein concentrations. The curves are well superimposable and indicate good data quality. **(B)** The top-ranked structural model #1 (cf. Figure 31A) can be fitted well into the SAXS-derived molecular envelope of the full-length Snf2H enzyme. Notably, 20% of residues are missing in the Snf2H model, which explains the excess of electron density.

I purified the full-length Snf2H enzyme and prepared the samples for SAXS measurements, which were conducted and analyzed by Dr. L. Brützel (LMU, Munich) shown in panels (A) and (B). Dr. C. Schindler (TUM, Munich) generated the full-length model in panel (B).

In conclusion, the ambiguous nature of the modeling results and the limitations in narrowing down the pool of candidate conformations by experimental data do not allow us to propose a single Snf2H structure for the remodeling enzyme under apo state conditions with the desired confidence.

2.4. Probing the conformation of remodeling enzymes upon changing the ATP state

Our proposed structural model of the DmISWI ATPase module implies that both ATPase lobes are twisted against each other under apo state conditions such that motifs important for catalysis are not oriented towards each other (cf. section 2.2.1.3). It appears plausible that the catalytic core of the Snf2H enzyme favors a similar resting state under comparable solution conditions. The ATPase modules of both remodeling enzymes may have to undergo substantial conformational rearrangements in order to assume a catalytically competent configuration. The nucleotide analog adenosine-5′-diphosphate beryllium-fluoride (ADP-BeF$_x$) has been shown to induce various nucleotide-dependent states of the Snf2H enzyme including the transition state during ATP hydrolysis (159). We thus envisaged that binding of ADP-BeF$_x$ to the Snf2H protein would shift the conformational ensemble towards an active enzyme conformation, which we could probe by XL-MS analysis, SAXS measurements, and computational modeling. To assess saturating ADP-BeF$_x$ concentrations, a competitive, thin-layer chromatography (TLC)-based ATPase assay was used to follow hydrolysis of [γ-^{32}P]ATP in the presence of increasing concentrations of the nucleotide analog (cf. Materials and Methods section 4.2.7.2.1). The ATP hydrolysis activities of DmISWI, DmISWI$_{\Delta HSS}$, and Snf2H decreased with increasing ADP-BeF$_x$ concentrations with [γ-^{32}P]ATP turnover being negligible at a nucleotide analog concentration of > 0.5 mM (SFigure 2). Consequently, these preliminary findings suggested that 3 mM ADP-BeF$_x$ are sufficient to shift the conformational ensemble of the studied remodeling enzymes towards the transition state during ATP hydrolysis.

The following subsections provide a detailed summary of the results obtained for the Snf2H enzyme in the presence of the nucleotide analogue ADP-BeF$_x$. Furthermore, a side-by-side comparison of the XL-MS data for the Snf2H protein in the presence and absence of ADP-BeF$_x$ allows for the identification of nucleotide-dependent changes in the higher-order structure of the remodeling enzyme.

2.4.1. Elucidating the conformational impact of nucleotide analog binding on the Snf2H enzyme using XL-MS analysis and computational modeling

To investigate the conformational impact of nucleotide analog binding on the Snf2H protein, we collected XL-MS data of the remodeling enzyme in the presence of ADP-BeF$_x$ in an identical manner as described for the Snf2H enzyme under apo state conditions (cf. section 2.3.1). I identified a total 154 unique, cross-linked residue pairs for the Snf2H enzyme in the presence of ADP-BeF$_x$ (Figure 33 and STable 4) with the majority (76%) of cross-linking sites being reproduced in technical replicates (cf. STable 4, column “Reproducibility group”).

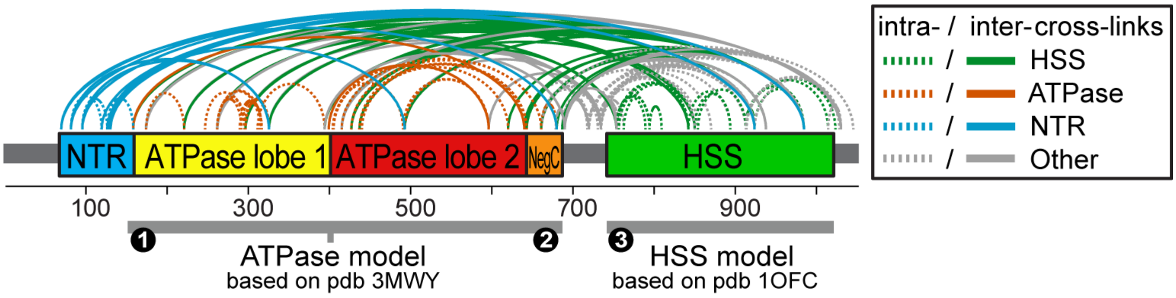

Figure 33: Identified cross-links for the full-length Snf2H enzyme in the presence of ADP-BeF$_x$. Schematic representation of Snf2H domains with identified inter- and intra-domain cross-links (cf. STable 4) being indicated as solid and dotted arcs (cf. color scheme), respectively. The residue numbering is denoted below. The grey bars below the arc plot define the generated homology models of the distinct Snf2H domains (cf. section 2.3.1). NTR, N-terminal region; HSS, HAND-SANT-SLIDE.

Dr. I. Forné (LMU, Munich) performed the MS analysis.

The number of identified cross-links for Snf2H was thus considerably higher in the ADP-BeF$_x$ state than under apo state conditions. The increased number of identifications was primarily due to novel cross-links that map to either the NegC-HSS interconnecting region (i.e., residues 690–742) or the very C-terminal segment (i.e., residues 1023–1052) of the Snf2H enzyme (Figure 34), for which we lack atomic coordinates in our structural models.

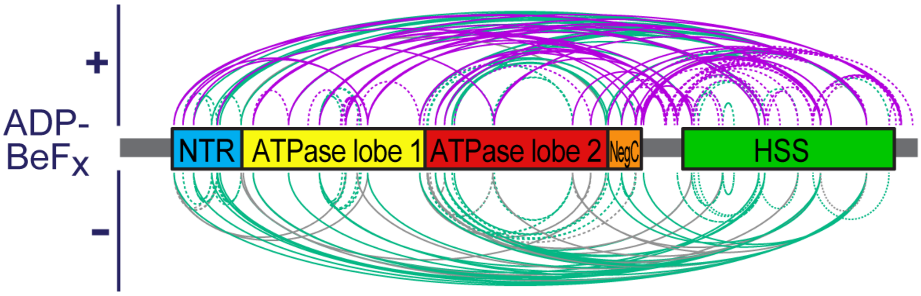

Figure 34: Comparison of identified cross-links for the Snf2H enzyme in the presence and absence of ADP-BeF$_x$. Schematic representation of Snf2H domains with identified inter- and intra-domain cross-links being indicated as solid and dotted arcs, respectively. Arcs on the top and bottom side refer to identified cross-links for the Snf2H enzyme in the presence and absence of ADP-BeF$_x$, respectively. Individual cross-links, which were identified under both conditions, are highlighted in cyan. Cross-links that were exclusively observed upon binding of ADP-BeF$_x$ or under apo state conditions are colored in purple and grey, respectively. NTR, N-terminal region; HSS, HAND-SANT-SLIDE.

I also observed novel intra-domain cross-links for the ATPase module and the HSS domain in the ADP-BeF$_x$ state. In a first step, I thus evaluated the compatibility of all identified intra-domain cross-links for ATPase lobe 1 ($XL_{Snf2H,nt}$ 67–78), ATPase lobe 2-NegC ($XL_{Snf2H,nt}$ 85–90 and $XL_{Snf2H,nt}$ 59), and the HSS domain ($XL_{Snf2H,nt}$ 94–107) with the previously generated homology models of the respective Snf2H domains. As illustrated in Figure 35, the experimental distance restraints for these functional domains still showed excellent consistency with the computed structures.

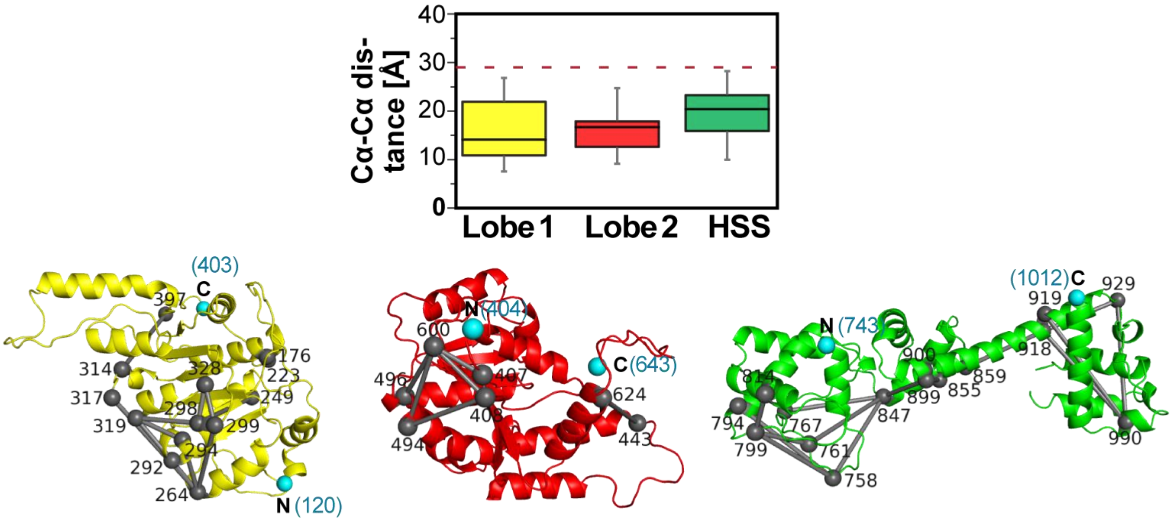

Figure 35. Intra-domain cross-links for the Snf2H enzyme in the presence of ADP-BeF$_x$. I measured the Cα-Cα distances between residues of identified intra-domain cross-links in the respective homology models of ATPase lobe 1 (yellow; i.e., XL$_{\mathrm{Snf2H,nt}}$ 67–78), ATPase lobe 2 (red; i.e., XL$_{\mathrm{Snf2H,nt}}$ 85–90), and the HSS domain (green, i.e., XL$_{\mathrm{Snf2H,nt}}$ 94–107) of the Snf2H enzyme. Cross-links are depicted as grey rods in the homology models, in which the N- and C-termini are furthermore highlighted as cyan spheres for orientation. Notably, XL$_{\mathrm{Snf2H,nt}}$ 68, which connects residues 249 and 298 in ATPase lobe 1, fulfilled the BS^3 distance threshold but resulted in a direct steric clash by extending through the bulk of the domain. Thus, XL$_{\mathrm{Snf2H,nt}}$ 68 may represent a false positive identification. The presented box plots signify the median (solid line), the Q3-Q1 range (box), and the minimum and maximum measured Cα-Cα distance (whiskers) for all intra-domain cross-links of a given domain. The Cα-Cα distance threshold given by the cross-linking agent is shown as a red dotted line in the box plot diagram. STable 4 provides further details for each cross-link.

Dr. C. Schindler (TUM, Munich) performed the homology modeling of individual Snf2H domains.

In a next step, I focused on inter-domain cross-links for the HSS domain and the ATPase module in order to elucidate similarities and differences in the cross-linking pattern for the Snf2H enzyme in the absence and presence of ADP-BeF$_x$. Interestingly, approximately 70% of inter-domain cross-links that were identified under apo state conditions were also detected in the ADP-BeF$_x$ state pointing towards an overall similar structural architecture of the remodeling enzyme (Table 2). In line with this qualitative comparison, I found that the identified inter-domain cross-links for the ADP-BeF$_x$ state were consistent with a ScChd1-like conformation of the NegC region (XL$_{\mathrm{Snf2H,nt}}$ 50–53, STable 4; Figure 36A) and with the HSS domain being in spatial proximity to the ATPase lobes (XL$_{\mathrm{Snf2H,nt}}$ 1–18, 23–29) as well as the autoregulatory NTR and NegC domains (XL$_{\mathrm{Snf2H,nt}}$ 37–46 and XL$_{\mathrm{Snf2H,nt}}$ 54–58).

Cross-links that connected the NTR with the ATPase lobes did not map to identical sites in the Snf2H enzyme in the apo (XL_{Snf2H} 38, 39; Table 3) and ADP-BeF$_x$ state ($XL_{Snf2H,nt}$ 34–36; STable 4). The novel NTR-ATPase lobe cross-links $XL_{Snf2H,nt}$ 34–36, however, remained consistent with the MtISWI crystal structure (pdb 5JXR) suggesting a similar positioning of the NTR in the ADP-BeF$_x$-bound Snf2H enzyme (Figure 36B).

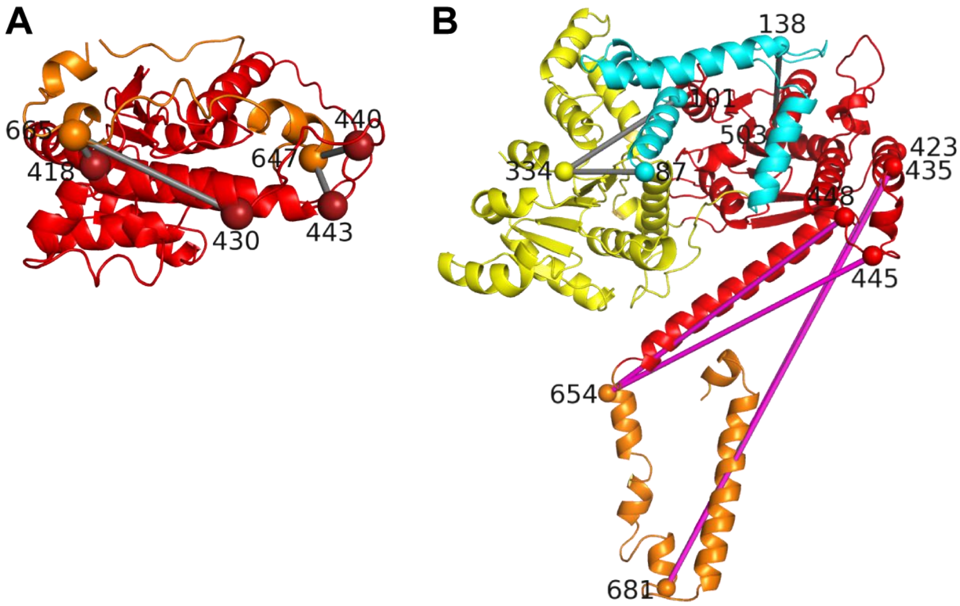

Figure 36: Evaluation of NTR and NegC cross-links for the ADP-BeF$_x$-bound Snf2H enzyme. (A) NegC cross-links mapped onto our ScChd1-based homology model of ATPase lobe 2 (red) and the NegC domain (orange). Identified inter-domain cross-links that connect these two regions ($XL_{Snf2H,nt}$ 50–53, STable 4) are indicated as grey rods with respective Cα-Cα distances being all satisfied. **(B)** NegC cross-links mapped onto the structure of a single MtISWI protomer (pdb 5JXR). All Cα-Cα distances between the NTR (cyan) and the ATPase lobes (ATPase lobe1, yellow and ATPase lobe 2, red) were satisfied. In contrast, all Cα-Cα distances between NegC (orange) and ATPase lobe 2 are violated (pink rods; $XL_{Snf2H,nt}$ 50–53) and exceed the distance threshold by 26–60 Å in the MtISWI protomer.

Dr. C. Schindler (TUM, Munich) performed the homology modeling of the depicted structure in panel (A).

Similar to the XL-MS results for the Snf2H protein under apo state conditions, I only obtained a single ATPase lobe-lobe cross-link that restricted the relative orientation of both ATPase lobes to each other in the ADP-BeF$_x$ state. The respective candidate ($XL_{Snf2H,nt}$ 84, STable 4) was identified on the basis of two distinct cross-linked peptides of various charge states and bridged the sequence-wise distant C-termini of both ATPase lobes in a similar manner as described for Snf2H under apo state conditions. This ATPase lobe-lobe cross-link for the ADP-BeF$_x$-bound Snf2H enzyme, however, could not be used to distinguish between the markedly distinct orientations of both ATPase lobes depicted in available apo (cf. Figure 4) and nucleosome-bound structures of related remodeling enzymes. That is, the Cα-Cα distance between corresponding sites was consistently $\leq$ 15.6 Å in the structures of ScChd1 (pdb

3MWY and 5O9G), Sso1653 (pdb 1Z6A), DrRad54 (pdb 1Z3I), MtSnf2 (pdb 5JXR), and ScSnf2 (pdb 5X0Y and 5X0X).

In conclusion, the XL-MS data delineate a rather compact conformation of the ADP-BeF$_x$-bound Snf2H protein considering that the cross-linking agent bridged numerous domain interfaces. Alternatively, the increased number of identified cross-links in the ADP-BeF$_x$ state relative to apo state conditions could derive from enhanced flexibility of the Snf2H enzyme upon binding of the nucleotide analog. The high number of identical/similar cross-linked residue pairs for Snf2H in the presence and absence of ADP-BeF$_x$ may point towards an overall similar structural architecture of the remodeling enzyme under these solution conditions. However, I cannot rule out that potential ADP-BeF$_x$-induced conformational changes in these Snf2H regions may remained undetected due to the resolution limit of the XL-MS approach using the chemical BS^3 cross-linking agent.

Table 2: Identical and similar inter-domain cross-links for the Snf2H enzyme in the apo and ADP-BeF$_x$ state. Site 1 and site 2 of the cross-linked peptides, the respective protein domains, and the corresponding cross-link identification numbers are specified for each identical and similar inter-domain cross-link that was identified in both apo and ADP-BeF$_x$ states (cf. STable 3 and STable 4). Cross-linked peptides were considered similar if the cross-linking sites were within ± 10 amino acids with respect to the primary protein sequence. Similar cross-links are denoted in grey. Inter-domain cross-links that mapped to either the NegC-HSS interconnecting region (i.e., residues 690–742) or the very C-terminal segment (i.e., residues 1023–1052) are not included in the table.

Site 1	Domain site 1	Site 2	Domain site 2	Apo state XL$_{Snf2H}$	ADP-BeF$_x$ state XL$_{Snf2H,nt}$
71	NTR	990	HSS	37	38
97	NTR	990	HSS	36	40
121	NTR	990	HSS	34	46
128	NTR	990	HSS	33	45
129	NTR	990	HSS	app. 33	44
132	NTR	990	HSS	35	41
160	NTR	644	NegC	44*	33
160	NTR	929	HSS	13	42
176	ATPase lobe 1	847	HSS	app. 9*	1
176	ATPase lobe 1	855	HSS	9*	2*
176	ATPase lobe 1	929	HSS	12*	3*
176	ATPase lobe 1	990	HSS	14*	4*
223	ATPase lobe 1	929	HSS	10*	6*
264	ATPase lobe 1	847	HSS	16	11*
264	ATPase lobe 1	929	HSS	8*	8*
264	ATPase lobe 1	990	HSS	11*	9*
328	ATPase lobe 1	929	HSS	3	14
397	ATPase lobe 1	758	HSS	4	10
397	ATPase lobe 1	929	HSS	7*	15*
397	ATPase lobe 1	990	HSS	6	18*
407	ATPase lobe 2	929	HSS	27	app. 15*
408	ATPase lobe 2	929	HSS	18	app. 23
408	ATPase lobe 2	990	HSS	17	app. 24*
418	ATPase lobe 2	665	NegC	48	53
418	ATPase lobe 2	929	HSS	26*	23
418	ATPase lobe 2	990	HSS	29*	24*
430	ATPase lobe 2	665	NegC	49	52

** continues next page **

430	ATPase lobe 2	855	HSS	24	25
430	ATPase lobe 2	990	HSS	28*	26*
440	ATPase lobe 2	647	NegC	45	51
443	ATPase lobe 2	644	NegC	46	app. 50
443	ATPase lobe 2	647	NegC	47	50
647	NegC	929	HSS	30	54
665	NegC	990	HSS	31	57

*: Cross-links with an asterisk were used for computational docking of the full-length Snf2H enzyme in the apo or ADP-BeF$_x$ state.
app.: Approximately

Table 3: ADP-BeF$_x$-dependent inter-domain cross-links for the Snf2H enzyme. Site 1 and site 2 of the cross-linked peptides, the respective protein domains, and the corresponding cross-link identification number (cf. STable 4) are specified for each ADP-BeF$_x$-dependent inter-domain cross-link. Inter-domain cross-links that mapped to either the NegC-HSS interconnecting region (i.e., residues 690–742) or the very C-terminal segment (i.e., residues 1023–1052) are not included in the table.

Site 1	Domain site 1	Site 2	Domain site 2	ADP-BeF$_x$ state XL$_{Snf2H,nt}$
71	NTR	684	NegC	32
71	NTR	929	HSS	37
83	NTR	328	ATPase lobe 1	35
83	NTR	929	HSS	39
97	NTR	328	ATPase lobe 1	36
128	NTR	929	HSS	43
129	NTR	496	ATPase lobe 2	34
223	ATPase lobe 1	855	HSS	5
264	ATPase lobe 1	758	HSS	7
299	ATPase lobe 1	855	HSS	12*
299	ATPase lobe 1	929	HSS	13*
299	ATPase lobe 1	990	HSS	16*
328	ATPase lobe 1	990	HSS	17*
402	ATPase lobe 1	600	ATPase lobe 2	84
440	ATPase lobe 2	990	HSS	27
496	ATPase lobe 2	990	HSS	29
624	ATPase lobe 2	990	HSS	28
647	NegC	990	HSS	55
665	NegC	929	HSS	56*
684	NegC	990	HSS	58

*: Cross-links with an asterisk were used for computational docking of the full-length Snf2H enzyme in the ADP-BeF$_x$ state.

Despite the similarities between cross-linking results for the Snf2H enzyme in the presence and absence of the nucleotide analog, I detected several inter-domain cross-links between the ATPase module and the HSS domain that were exclusively found in the ADP-BeF$_x$ state (Table 3) using comparable filtering criteria during MS data analysis (cf. Table 15 in Materials and Methods section). It thereby appeared that especially residues of the autoregulatory NTR region and ATPase lobe 1 formed cross-links with the HSS domain in an ADP-BeF$_x$-dependent manner. Notably, many of these ADP-BeF$_x$-dependent linkages for Snf2H were repeatedly observed across distinct XL-MS analyses as further specified in column ‘Reproducibility group’ in STable 4.

To resolve and visualize these potential ADP-BeF$_x$-induced structural changes in the full-length Snf2H enzyme, our collaboration partner Dr. C. Schindler (TUM, Munich) performed a three-body docking with homology models of both ATPase lobes and the HSS domain in a similar manner as described in section 2.3.2. The docking procedure was guided by a total of 16 inter-domain distance restraints (i.e., XL$_{\text{Snf2H,nt}}$ 2–4, 6, 8, 9, 11–13, 15–18, 24, 26, 56; cf. STable 4), for which we obtained excellent fragmentation data during MS/MS analysis (cf. SFigure 7). As such, the docking procedure relied on previously implemented distance restraints as well as ADP-BeF$_x$-dependent linkages between ATPase lobe 1, NegC, and the HSS domain (cf. asterisks in Table 3). Figure 37A shows our representative structural models of the ADP-BeF$_x$-bound Snf2H enzyme (i.e., the top-ranked models #1−5 and every other fifteenth model). These structural models of the Snf2H enzyme in the presence of ADP-BeF$_x$ were rather heterogeneous. In particular, the orientation of the HSS domain relative to both ATPase lobes remained ambiguous, while the ATPase module itself displayed recurrent structural characteristics.

I subsequently evaluated the quality of the structural models depicted in Figure 37A with respect to the experimental XL-MS and SAXS data. Measuring the Cα-Cα distances between cross-linked residue pairs revealed that none of the investigated Snf2H models satisfied all implemented distance restraints used for docking at once (Figure 37B, marked with an asterisk). Furthermore, the majority of additional identified inter-domain cross-links listed in Table 2 and Table 3 exceeded the BS^3 distance threshold (Figure 37B). It thus appears plausible that the well-documented flexibility in one or more parts of the full-length Snf2H enzyme (89, 129) may hinder us from modeling a single ADP-BeF$_x$-bound conformation of the remodeling enzyme. Nevertheless, the SAXS-derived scattering profile of the ADP-BeF$_x$-bound Snf2H protein (see section 2.4.2) showed partial consistency with the theoretical scattering curves of the investigated structural models as reflected by an average χ-value of 3.0 ± 0.23.

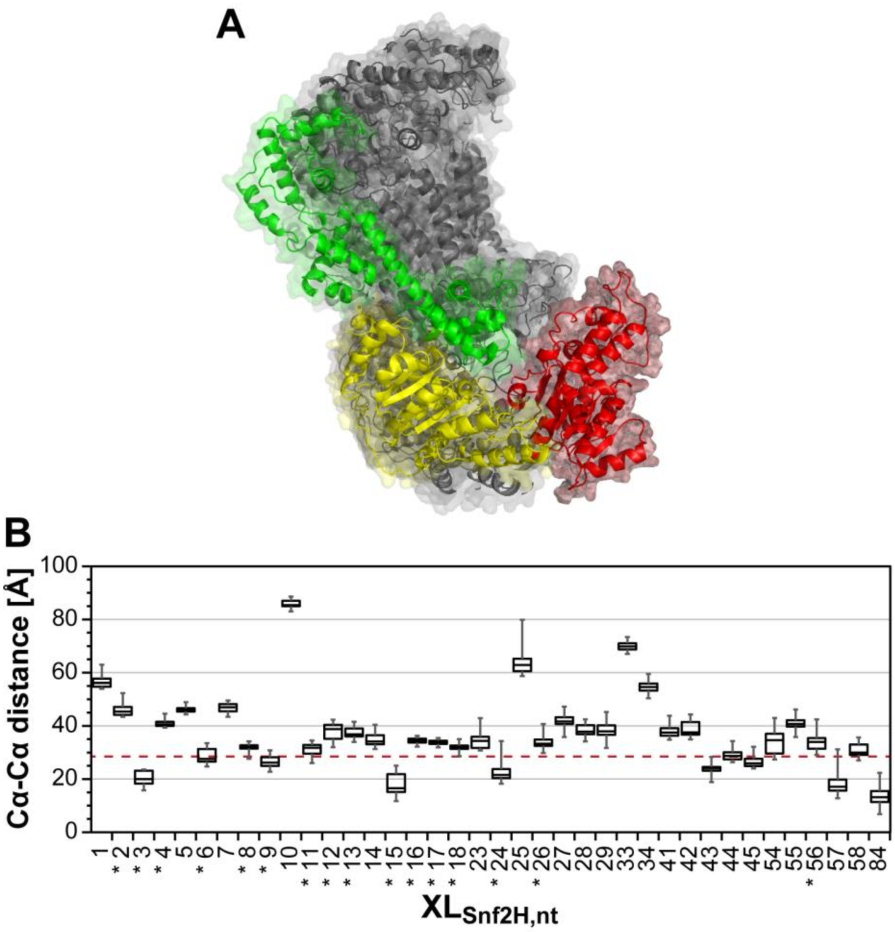

Figure 37: Structural models of the full-length Snf2H enzyme in the presence of ADP-BeF$_x$. (A) The top-ranked structural models for the ADP-BeF$_x$-bound Snf2H enzyme (i.e., models #1−5 and every other fifteenth model) are shown and aligned to ATPase lobe 2 of model #1. ATPase lobe 1, ATPase lobe 2, and the HSS domain are colored in yellow, red, and green for model #1, respectively. The remaining structures are depicted in grey color. **(B)** I measured the Cα-Cα distances between reactive sites of identified inter-domain cross-links in each Snf2H model shown in (A). Individual box plots summarize the observed distribution of measured Cα-Cα distances for each inter-domain cross-link. That is, each box plot shows the median (solid line), the Q3-Q1 range (box), and the minimum and maximum measured Cα-Cα distance (whiskers). Cross-links are numbered according to STable 4. Cross-links with an asterisk were used as distance restraints during computational docking. The Cα-Cα distance threshold given by the BS^3 cross-linking agent is shown as a red dotted line in the box plot diagram.

Dr. C. Schindler (TUM, Munich) performed the computational docking of the full-length Snf2H enzyme shown in panel (A).

Despite the above outlined, partial inconsistencies between XL-MS and computational data, it is interesting to compare our representative models of the full-length Snf2H enzyme in the apo (cf. section 2.3.2) and ADP-BeF$_x$ state with each other. For a more structural perspective, I superimposed and aligned the top five structural models of each state with regard to the ATTRACT score (Figure 38). The superimposition of individual structural models suggests that ATPase lobe 1 rotates approximately 180° relative to ATPase lobe 2 upon changing the nucleotide state. Furthermore, I observed that the orientation of the HSS domain relative to

ATPase lobe 2 is substantially different between Snf2H models for the apo and ADP-BeF$_x$ states. The drastically different modeling outcomes for the Snf2H enzyme in the apo and ADP-BeF$_x$ state are surprising considering that the large majority of distance restraints used to guide the computational docking was identical. The direct comparison of these structural models points towards the possibility that the Snf2H protein may undergo major conformational changes upon nucleotide analogue binding with identical/similar cross-linked residue pairs being formed in both states. However, the comparison between XL-based modeling results for the apo and ADP-BeF$_x$ states should be done with caution. That is, our structural models are too ambiguous to draw conclusive mechanistic inferences with the desired confidence.

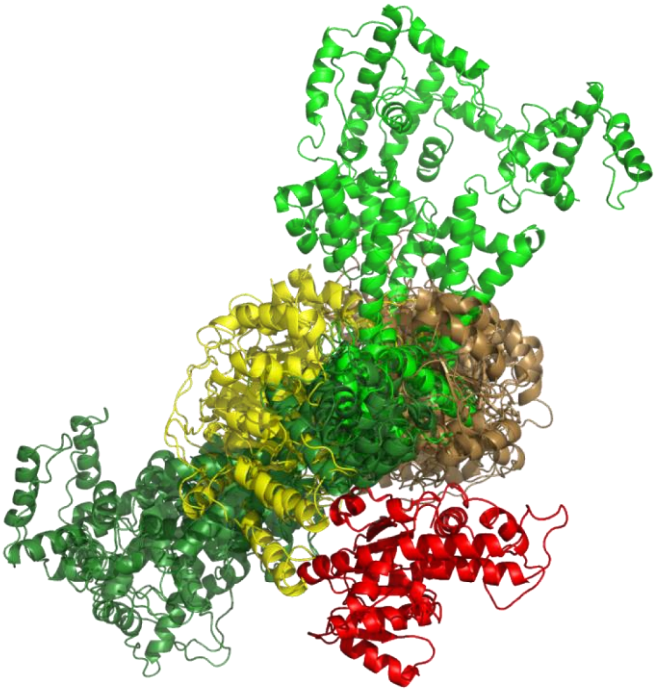

Figure 38: Superimposition of structural models of the full-length Snf2H enzyme in the presence and absence of ADP-BeF$_x$. The top five ATTRACT-scored docking models of the full-length Snf2H enzyme in the apo (cf. Figure 31A) and ADP-BeF$_x$-bound state (cf. Figure 37A) are aligned on ATPase lobe 2 (red). The superimposition of structures suggests that ATPase lobe 1 (colored in sand and yellow for the apo and ADP-BeF$_x$ state, respectively) undergoes a rotation of approximately 180° upon binding of the nucleotide analog. Likewise, the orientation of the HSS domain is markedly different in the apo (dark green) relative to the ADP-BeF$_x$ state (light green).

Dr. C. Schindler (TUM, Munich) performed the computational docking of the full-length Snf2H enzyme in the apo and ADP-BeF$_x$-bound state.

2.4.2. Nucleotide-induced conformational changes in ISWI-type remodeling enzymes viewed by SAXS analysis

To further investigate nucleotide-dependent conformational changes in the Snf2H protein, our collaboration partner Dr. L. Brützel (LMU, Munich) performed SAXS measurements on the remodeling enzyme in the presence and absence of ADP-BeF$_x$ and compared the respective structural parameters with each other (Figure 39A). In addition, we examined whether the full-length DmISWI enzyme would exhibit a similar conformational response to the binding of the nucleotide analog (Figure 39B).

Binding of ADP-BeF$_x$ resulted in a 6.7% and 10.4% decreased radius of gyration for the full-length DmISWI$_{WT}$ and Snf2H remodeling enzymes (Figure 39D), respectively. These findings suggest that the tested nucleotide analog induces an overall more compact solution-phase structure of both full-length proteins.

In a subsequent step, we examined the impact of ADP-BeF$_x$ binding on the catalytic core of the DmISWI enzyme. Dr. L. Brützel (LMU, Munich) therefore conducted additional SAXS measurements on DmISWI$_{\Delta HSS}$ in the presence of the nucleotide analog and compared these results to corresponding data obtained under apo state conditions (Figure 39C, cf. section 2.2.1.1). Interestingly, a similar compaction in the ISWI$_{\Delta HSS}$ variant was observed upon ADP-BeF$_x$ ligation considering that the R$_g$ value decreased by 5.3% relative to apo state conditions (Figure 39D). This finding implies that the ATPase module undergoes a global conformational change in response to ADP-BeF$_x$ binding.

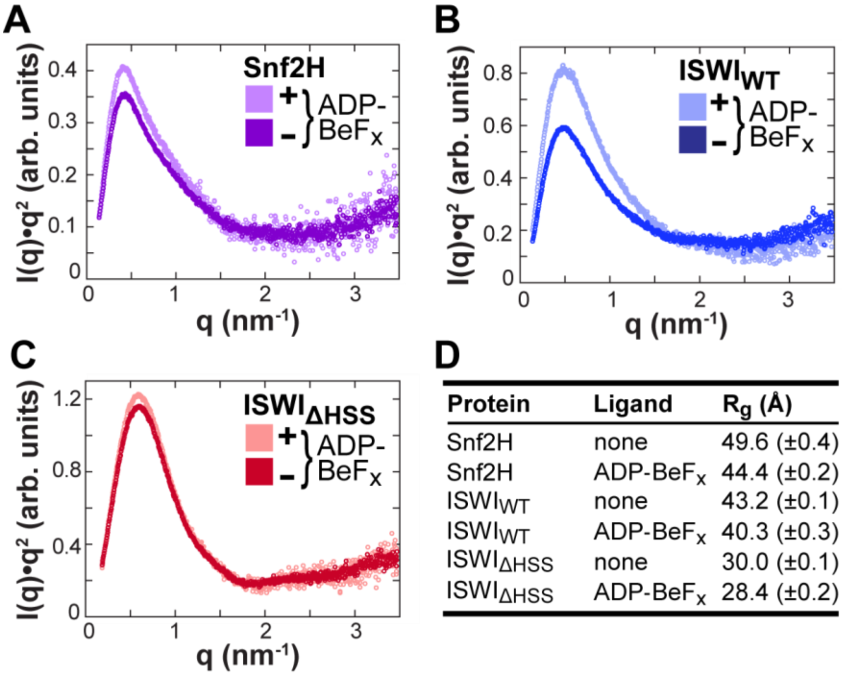

Protein	Ligand	R_g (Å)
Snf2H	none	49.6 (±0.4)
Snf2H	ADP-BeF$_x$	44.4 (±0.2)
ISWI$_{WT}$	none	43.2 (±0.1)
ISWI$_{WT}$	ADP-BeF$_x$	40.3 (±0.3)
ISWI$_{\Delta HSS}$	none	30.0 (±0.1)
ISWI$_{\Delta HSS}$	ADP-BeF$_x$	28.4 (±0.2)

Figure 39: ADP-BeF$_x$-induced compaction of remodeling enzymes. Kratky representations for **(A)** full-length Snf2H, **(B)** full-length ISWI$_{WT}$, and **(C)** ISWI$_{\Delta HSS}$ are shown. **(D)** Tabular overview of the radii of gyration for the investigated remodeling enzymes in the presence and absence of the nucleotide analog. Data represent means ± standard deviation (n = 2−3). The presented data (A−D) collectively suggest an ADP-BeF$_x$-dependent compaction of the remodeling enzymes in solution. The panels (B) and (C) as well as values of (D) were adapted from (1) in accordance with Elsevier's policies.

I purified all protein constructs and prepared the samples for SAXS measurements, which were conducted and analyzed by Dr. L. Brützel (LMU, Munich).

2.5. Probing the interaction between remodeling enzyme(s) and nucleosomes

Remodeling complexes have to recognize and bind to their substrate in order to fulfill their essential functions such as the reposition of nucleosomes along DNA. Detailed structure-function relationships will pave the way towards a better mechanistic understanding of remodeling enzymes and how they interact with nucleosomes on a molecular level. However, the majority of structural information for individual enzyme-nucleosome complexes is either of low resolution (150), which does not allow for detailed mechanistic inferences or derive from truncated enzyme variants (21). The recently determined high-resolution, cryo-EM structure of the ScChd1 enzyme in complex with a nucleosome (pdb 5O9G) (24) shows how the monomeric ATPase module interacts with nucleosomal DNA at SHL +2 and how it is anchored to the N-terminal tail histone H4. The DNA-binding SANT and SLIDE domains furthermore contact the extranucleosomal DNA around SHL –7. The binding of remodeling enzymes to flanking DNA stretches, as observed in the ScChd1 structure, has been well documented (23, 116, 127). However, recent studies suggest an alternative binding mode for the HSS domain of the Snf2H enzyme (28, 129). That is, the HSS domain has been suggested to bind to the nucleosome core during the DNA translocation step.

To better understand how the Snf2H protein engages its nucleosomal substrate, we performed XL-MS analyses of the ADP-BeF_x-bound remodeling enzyme in the presence and absence of nucleosomes. The following subsections provide a step-by-step summary of obtained experimental results from XL-MS analysis and computational modeling. By comparing cross-linking data in the presence and absence of nucleosomes in a quantitative manner, I was able to gain information about possible substrate-induced conformational changes in the Snf2H enzyme.

2.5.1. In-vitro reconstitution of remodeling enzyme-nucleosome complexes

The four *Drosophila* core histones were either purified from inclusion bodies or using the RHP method (cf. Materials and Methods section 4.2.2.4). Lyophilized histone proteins were mixed under denaturing solution conditions and were assembled into histone octamers by dialyzing the samples against a high salt refolding buffer. Histone octamers were subsequently purified by size-exclusion chromatography as specified in Materials and Methods section 4.2.3.2. The DNA for mononucleosomes derived from cut plasmids and was isolated by a native PAGE approach (cf. Materials and Methods section 4.2.3.1). Purified DNA fragments of 187 bp length comprised the 601 positioning sequence (235) and a flanking DNA stretch. Reconstitution of histone octamers with DNA was accomplished by using a salt gradient dialysis approach (cf. Materials and Methods section 4.2.3.3). For samples subjected to XL-

MS analysis, excess of unbound DNA was subsequently removed by glycerol gradient centrifugation. As mentioned above, mononucleosomes comprised a one-sided linker DNA of 40 bp length, which will be referred to as “0N40 mononucleosomes” hereafter. This extranucleosomal DNA stretch may serve as an interaction site for the HSS domain in the Snf2H-nucleosome complex (23, 151).

In a next step, I screened for suitable conditions that allow for the formation of DmISWI- or Snf2H-nucleosome complexes in solution. I therefore incubated increasing concentrations of either the DmISWI or Snf2H remodeling enzyme with a constant amount of 0N40 mononucleosomes as well as 3 mM ADP-BeF$_x$ and evaluated complex formation by an electrophoretic mobility shift assay (EMSA, cf. Materials and Method section 4.2.7.1). I decided to use ADP-BeF$_x$ for the reconstitution due to the reported potential of this particular nucleotide analog to increase the binding affinity of the Snf2H enzyme towards 0N40 mononucleosomes (150).

DmISWI as well as Snf2H appeared to form complexes with 0N40 mononucleosomes (Figure 40). However, I observed a certain tendency of both remodeling enzymes to form aggregates in the presence of substrate (Figure 40A, B). Under comparable solution conditions at elevated protein concentrations, I often observed more visible aggregates during EMSA analysis for DmISWI than for Snf2H samples. The tendency of the DmISWI enzyme to form protein aggregates in the presence of nucleosomes has also been reported recently in the context of structural studies of the remodeler (236). I consequently endeavored to prevent aggregation of the DmISWI-nucleosome complex by changing potentially critical experimental parameters. My efforts encompassed the testing of alternative nucleotides (e.g., ADP and the non-hydrolyzable AMP-PNP analog), substitution of 0N40 with 0N0 nucleosomes, and the use of distinct buffer solutions (cf. section 6.3 in Appendix) commonly employed in nucleosome-based experiments (116, 150). Despite the sometimes promising EMSA results for the DmISWI enzyme for individual conditions (SFigure 3), the handling of these samples remained challenging. I therefore decided to focus on the Snf2H enzyme to study structural characteristics of an ISWI-type remodeling enzyme in complex with its nucleosomal substrate by means of XL-MS analysis.

The EMSA results suggested that up to three Snf2H molecules might be bound to a single nucleosome in solution (Figure 40B) and that Snf2H-nucleosome complexes are compatible with the use of chemical cross-linking agents (Figure 40C). The single particle EM study by Racki et al. (150) already suggested that two Snf2H molecules bind to a single nucleosome in the presence of ADP-BeF$_x$ in order to facilitate the bidirectional movement of the substrate along DNA in a cooperative manner. The observation that up to three Snf2H engage the nucleosome in the present study may be explained by assuming an additional binding site on the flanking DNA stretch (237). Attempts to separate these different Snf2H-nucleosome complexes and to remove unbound protein species by size-exclusion chromatography have remained ineffective because Snf2H-nucleosome complexes could not be eluted from the size-exclusion column (data not shown). Notably, other laboratories also experienced challenges in separating different protein species in ISWI-nucleosome samples (i.e., free nucleosomes, several remodeler-nucleosome complexes as well as free remodeler, and aggregates) by size-exclusion chromatography (236).

In conclusion, I decided not to pursue XL-MS analysis of the substrate-bound DmISWI protein due to the experienced challenges associated with the handling of these samples. Instead, I focused on Snf2H-nucleosome complexes and found the following conditions to be most promising for XL-MS analysis: 1.5 µM Snf2H enzyme in the presence of either 1.5 or 0.8 µM 0N40 mononucleosomes, 3 mM ADP-BeF$_x$, and 1 mM BS^3 cross-linker in buffer solution [15 mM Hepes-KOH (pH 7.6), 4% glycerol, 70 mM KCl, 1 mM DDT, and 1 mM MgCl$_2$]. Although the sample heterogeneity under these conditions could complicate the interpretation of experimental results (Figure 40C), I envisaged having enough Snf2H-nucleosome complexes in solution that allow the unambiguous identification of intermolecular cross-links during MS/MS analysis.

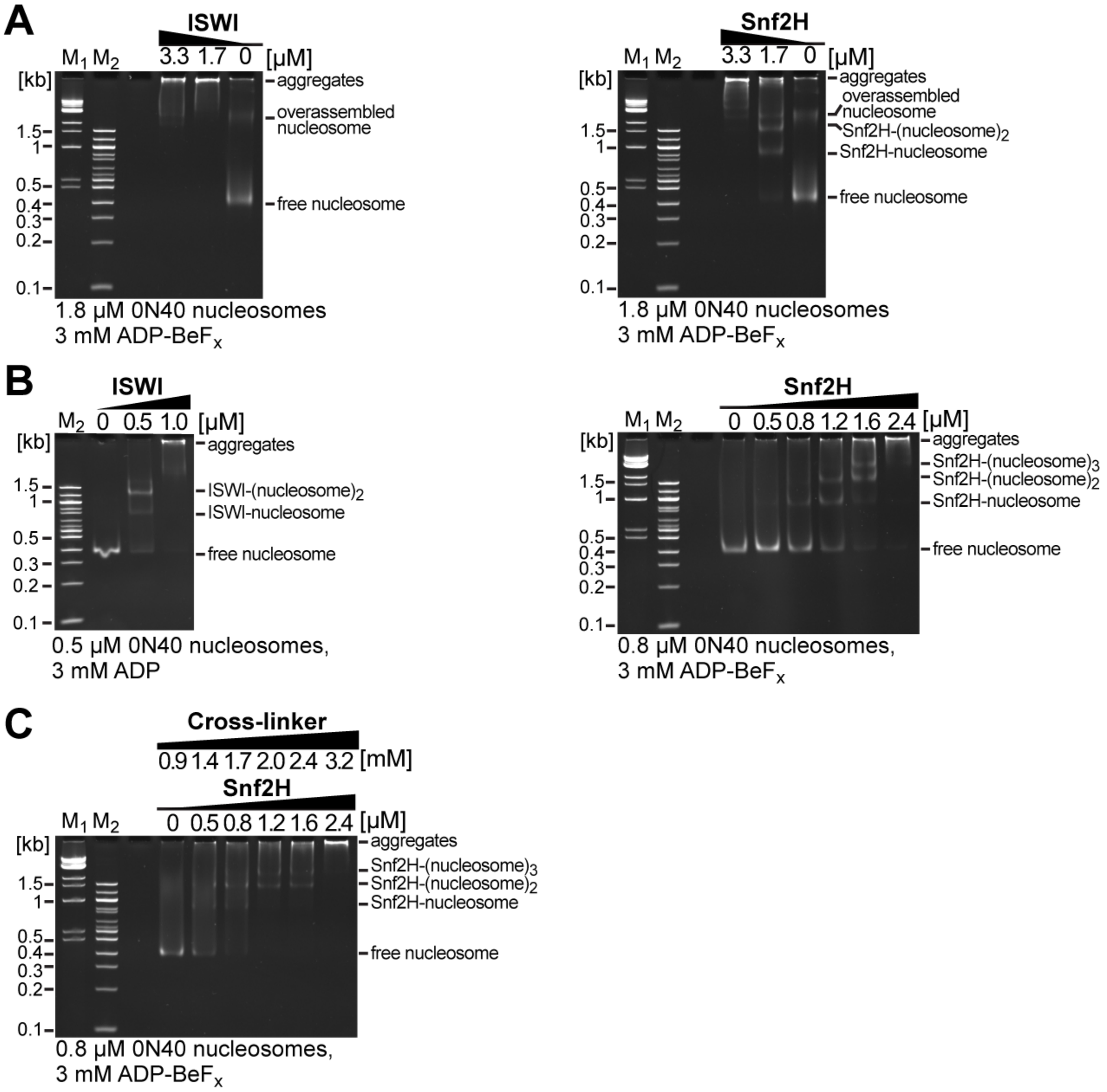

Figure 40: Monitoring the interaction of DmISWI and Snf2H with mononucleosomes. I monitored complex formation between 0N40 mononucleosomes and either Snf2H or DmISWI by a 4.5% native PAGE/0.2x TBE approach and ethidium bromide staining. **(A** and **B)** I incubated increasing concentrations of DmISWI (left) and Snf2H (right) with 0N40 mononucleosomes and the indicated nucleotide (ADP or ADP-BeF_x) in EMSA buffer #4 (cf. Table 12). I predominantly observed protein aggregates at DmISWI concentrations ≥ 1 µM. In contrast, protein aggregation was less pronounced for the Snf2H enzyme under comparable solution conditions. Titration furthermore revealed that more than one Snf2H molecules may bind to a single nucleosome. Notably, the nucleosomes used in (A) were not purified over a glycerol gradient, which explains the band corresponding to ‘overassembled nucleosomes’. **(C)** The formation of Snf2H-nucleosome complexes appeared to be compatible with the use of chemical cross-linkers. M: Marker. See also SFigure 3 for additional EMSA results.

2.5.2. Cross-linking of the Snf2H-nucleosome complex

I cross-linked the Snf2H enzyme in the presence of its nucleosomal substrate (i.e., 0N40 mononucleosomes) using the BS^3 cross-linker to gain a better structural understanding of this interaction and to uncover potential conformational changes in the target proteins upon complex formation. The XL-MS workflow was essentially the same as described above for the Snf2H enzyme with MS analysis being conducted by our collaboration partner Dr. I. Forné (LMU, Munich).

A total of 253 peptides passed the filtering criteria during peptide identification (cf. Table 15 in Materials and Methods) yielding 181 unique cross-linked residue pairs for the Snf2H-nucleosome state (Figure 41, STable 5). Notably, the large majority of these cross-linking sites (74%) were reproducible in at least technical replicates as further specified in STable 5. Cross-linking candidates, for which the spacing between reactive sites was below ten amino acids, were not considered for further analysis. These candidates were often found in individual histone tails, which are very rich in surface-exposed lysine residues.

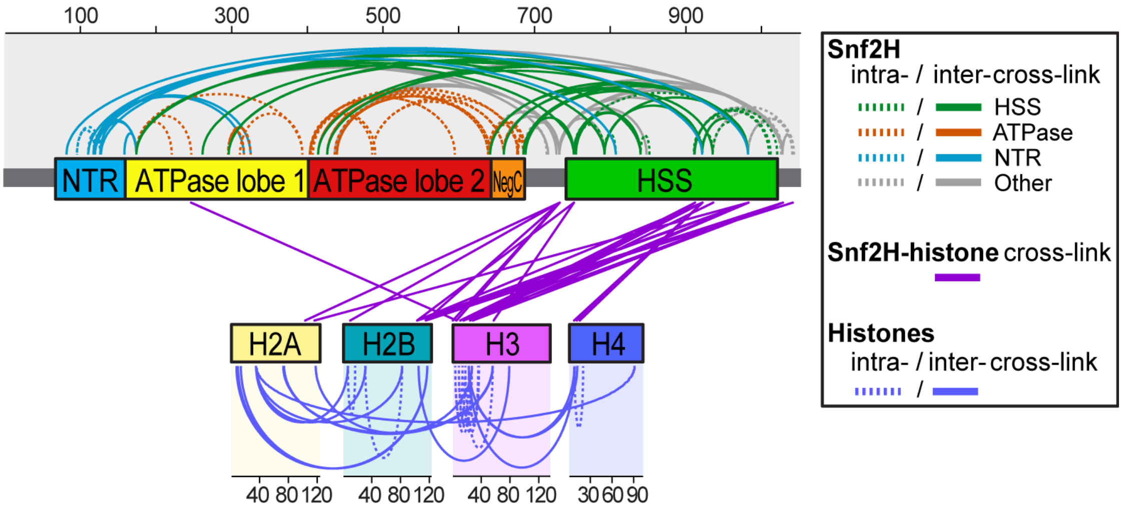

Figure 41: Identified cross-links for the full-length Snf2H enzyme in complex with nucleosomes and ADP-BeF$_x$. Schematic representation of the Snf2H enzyme and individual histone proteins with identified inter- and intra-domain cross-links being indicated as solid and dotted arcs (cf. color scheme), respectively. STable 5 provides further details for each presented cross-link. Identified inter-molecular cross-links (cf. SFigure 11 for MS/MS spectra) are shown as purple lines. Numbers refer to the amino acid numbering of the individual proteins. NTR, N-terminal region; HSS, HAND-SANT-SLIDE.

Dr. I. Forné (LMU, Munich) performed the MS analysis.

In a first step, I focused on the identified intra-molecular cross-links for both the full-length Snf2H enzyme and the histone octamer. In the case of the octamer, the identified linkages were sometimes confined to a single subunit ($XL_{Snf2H,c}$ 1–17; STable 5) but frequently also provided information about the distance between two histone proteins ($XL_{Snf2H,c}$ 18–31). To examine potential conformational changes in the octamer upon Snf2H binding as suggested recently (238), I mapped the identified intra-molecular cross-links onto an available crystal structure of the nucleosome (pdb 2PYO). The majority of these linkages ($XL_{Snf2H,c}$ 1, 3–17, 19, 20, 23, 25, 28, 30, 31), however, mapped to nucleosomal regions (e.g., histone tails) for which atomic coordinates are lacking in the crystal structure. Accessible cross-links for the histone octamer ($XL_{Snf2H,c}$ 2, 18, 21, 22, 24, 26, 27, 29) are illustrated in Figure 42A and showed consistency with the nucleosome structure because Cα-Cα distances between cross-linked lysine residues did not violate the defined distance threshold of the BS^3 agent. Thus, our cross-linking data for the Snf2H-nucleosome state do not provide further experimental evidence for binding-induced conformational changes in the histone octamer within the resolution of the XL-MS approach.

In the case of the Snf2H enzyme, I identified several intra-domain cross-links ($XL_{Snf2H,c}$ 86–119), which I mapped onto the respective homology models (cf. section 2.3.1). I found that all distance restraints ($XL_{Snf2H,c}$ 90–103) were fulfilled in our structural models of both ATPase lobes (Figure 42B). Likewise, the large majority of intra-domain distance restraints for the HSS domain ($XL_{Snf2H,c}$ 104–119) were satisfied (Figure 42B). However, three cross-links that connect residues of the HAND and SLIDE regions ($XL_{Snf2H,c}$ 117–119) substantially exceeded the BS^3 distance threshold by a factor of 2−3 (Figure 42C). This apparent mismatch between experimental data and our homology model of the DNA-binding domain may point towards a nucleosome-dependent conformational change of the HSS domain. However, the possibility that these incompatible cross-links were formed between two Snf2H molecules cannot be ruled out. The probability of false sequence assignments for $XL_{Snf2H,c}$ 117 and 118 is low given the consecutive ion series and good signal intensities of the fragment ions detected during MS/MS analysis of these candidates (SFigure 8).

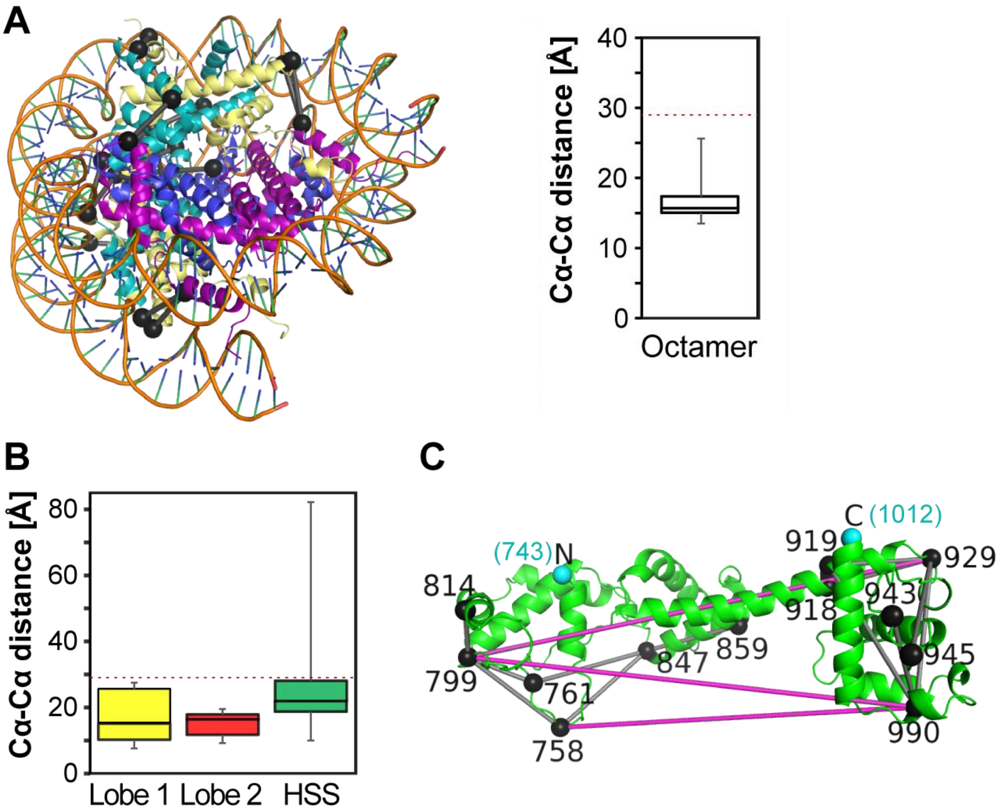

Figure 42: Mapping of identified intra-molecular and intra-domain cross-links for the Snf2H enzyme in the presence of nucleosomes. (A) The crystal structure of the nucleosome (pdb 2PYO) is shown with individual histone proteins being colored as specified in Figure 41. All accessible intra-molecular cross-links for the histone octamer are depicted as grey rods and spheres in the nucleosome structure. The box plot signifies the median (solid line), the Q3-Q1 range (box), and the minimum and maximum measured Cα-Cα distance (whiskers) for all intra-molecular cross-links of the nucleosome. The Cα-Cα distance threshold of the BS^3 cross-linker is indicated as a red dotted line in the box plot diagram. **(B)** The Cα-Cα distances between cross-linked residues of identified intra-domain linkages were measured in the respective homology models of ATPase lobe 1, ATPase lobe 2, and the HSS domain of the Snf2H enzyme. The presented box plots signify the median (solid line), the Q3-Q1 range (box), and the minimum and maximum measured Cα-Cα distance (whiskers) for all intra-domain cross-links of a given domain. The Cα-Cα distance threshold of the BS^3 cross-linker is shown as a red dotted line. **(C)** Identified cross-links for the HSS domain of the Snf2H enzyme in the presence of nucleosomes are mapped onto the respective homology model. Intra-domain cross-links ($XL_{Snf2H,c}$ 104–119) are indicated as rods and spheres in the homology model, in which the N- and C-termini are furthermore highlighted in cyan for orientation. Grey and pink rods connect cross-linked residue pairs for which the Cα-Cα distance threshold is satisfied and violated, respectively. STable 5 provides further details for individual cross-links. MS/MS spectra of cross-links $XL_{Snf2H,c}$ 117–119 are provided in SFigure 8.

Dr. C. Schindler (TUM, Munich) performed the homology modeling of individual Snf2H domains, which were used in panels (B) and (C) for the evaluation of XL-MS data.

In a next step, I examined the 86 inter-domain cross-links that were identified for the Snf2H enzyme in the presence of 0N40 mononucleosomes ($XL_{Snf2H,c}$ 32–85, 90, 91, and 120–149; STable 5). Approximately two-thirds of these linkages (i.e., $XL_{Snf2H,c}$ 38, 41, 42, 46–58, 75–85, 91 and 120–149) mapped to either the NTR, the NegC-HSS interconnecting region (i.e., residues 690–742) or the very C-terminal segment (i.e., residues 1023–1052) of the Snf2H protein, for which we lack atomic coordinates in our structural models. Furthermore, I noticed that numerous cross-linked residue pairs for the Snf2H-nucleosome state were identical or highly similar to the ones detected in the apo and ADP-BeF$_x$-bound states (Table 4). These cross-links listed in Table 4 predominantly mapped to the HSS domain implying that the SLIDE region is spatially neighboring both ATPase lobes ($\mathrm{XL}_{\mathrm{Snf2H,c}}$ 32–37, 39, 40, and 43–45) as well as the autoregulatory NTR and NegC domains ($\mathrm{XL}_{\mathrm{Snf2H,c}}$ 53–58 and 71–74). The structural interpretation of shared inter-domain cross-links is not straightforward because these cross-links could also originate from unbound Snf2H molecules and thus may not reflect structural properties of the nucleosome-bound remodeling enzyme. As outlined above, attempts to separate complexed and unbound Snf2H molecules after the cross-linking reaction by size-exclusion chromatography have remained unsuccessful.

Table 4: Identical and similar inter-domain cross-links for the Snf2H enzyme in the apo, ADP-BeF$_x$, and nucleosome state. Site 1 and site 2 of the cross-linked peptides, the respective protein domains, and the corresponding cross-link identification numbers are specified for each identical and similar inter-domain cross-link that was identified in the apo, ADP-BeF$_x$, and nucleosome state (cf. STable 3–STable 5 and SFigure 9 for MS/MS spectra). Cross-linked peptides were considered similar if the cross-linking sites were within ± 10 amino acids with respect to the primary protein sequence. Similar cross-links are denoted in grey. Inter-domain cross-links that mapped to either the NegC-HSS interconnecting region (i.e., residues 690–742) or the very C-terminal segment (i.e., residues 1023–1052) are not included in the table.

Site 1	Domain site 1	Site 2	Domain site 2	Apo state $\mathrm{XL}_{\mathrm{Snf2H}}$	ADP-BeF$_x$ state $\mathrm{XL}_{\mathrm{Snf2H,nt}}$	Nucleosome state $\mathrm{XL}_{\mathrm{Snf2H,c}}$
121	NTR	990	HSS	34	46	56
121	NTR	929	HSS	N/D	app. 43	57
128	NTR	929	HSS	N/D	43	app. 57
119	NTR	990	HSS	app. 34	app. 46	55
128	NTR	990	HSS	33	45	app. 58
129	NTR	990	HSS	app. 33	44	58
132	NTR	990	HSS	35	41	app. 58
176	ATPase lobe 1	847	HSS	N/D	1	32
176	ATPase lobe 1	929	HSS	12	3	33
176	ATPase lobe 1	990	HSS	14	4	34
264	ATPase lobe 1	929	HSS	8	8	35
299	ATPase lobe 1	929	HSS	N/D	13	36
299	ATPase lobe 1	990	HSS	N/D	16	37
418	ATPase lobe 2	665	NegC	48	53	67
418	ATPase lobe 2	990	HSS	29	24	43
430	ATPase lobe 2	665	NegC	49	52	66
430	ATPase lobe 2	990	HSS	28	26	45
440	ATPase lobe 2	647	NegC	45	51	64
443	ATPase lobe 2	644	NegC	46	app. 50	62
443	ATPase lobe 2	647	NegC	47	50	63
647	NegC	929	HSS	30	54	72
647	NegC	990	HSS	N/D	55	74
665	NegC	929	HSS	N/D	56	71
665	NegC	990	HSS	31	57	73

app.: Approximately
N/D: Not determined

However, I identified several inter-domain cross-links for the Snf2H enzyme that were solely detected in the presence of the nucleosomal substrate (Table 5). These nucleosome-dependent cross-links predominantly connected the autoregulatory NTR and NegC domains with ATPase lobe 1 and ATPase lobe 2, respectively. The qualitative comparison of XL-MS data for the Snf2H enzyme in the ADP-BeF$_x$ and nucleosome states may point towards conformational changes in the autoregulatory NTR and NegC regions upon substrate binding. Interestingly, both the NTR and the NegC region have previously been reported to undergo substrate-dependent conformational changes with molecular details, however, remaining elusive and being the subject of extensive debate (28, 115, 140, 146). The identified cross-links for the nucleosome state, listed in Table 4 and Table 5, are consistent with the notion that the NTR and NegC of the Snf2H enzyme are spatially neighboring ATPase lobe 1 and ATPase lobe 2, respectively. Furthermore, both autoregulatory regions may contact the DNA-binding domain in the presence of substrate.

Table 5: Nucleosome-dependent inter-domain cross-links for the Snf2H enzyme. Site 1 and site 2 of the cross-linked peptides, the respective protein domains, and the corresponding cross-link identification number (cf. STable 3, STable 5 and SFigure 10 for MS/MS spectra) are specified for each inter-domain cross-link. None of the listed cross-links was found in the ADP-BeF$_x$ state. However, some ATPase lobe 2-NegC and ATPase lobe 2-HSS cross-links that were identified in the presence of nucleosomes were also detected under apo state conditions. Similar cross-links are denoted in grey. Inter-domain cross-links that mapped to either the NegC-HSS interconnecting region (i.e., residues 690–742) or the very C-terminal segment (i.e., residues 1023–1052) are not included in the table.

Site 1	Domain site 1	Site 2	Domain site 2	Apo state XL_{Snf2H}	ADP-BeF$_x$ state $XL_{Snf2H,nt}$	Nucleosome state $XL_{Snf2H,c}$
83	NTR	990	HSS	N/D	N/D	53
112	NTR	814	HSS	N/D	N/D	54
119	NTR	328	ATPase lobe 1	N/D	N/D	50
121	NTR	176	ATPase lobe 1	N/D	N/D	52
121	NTR	319	ATPase lobe 1	N/D	N/D	51
128	NTR	176	ATPase lobe 1	N/D	N/D	91
160	NTR	176	ATPase lobe 1	N/D	N/D	90
176	ATPase lobe 1	758	HSS	N/D	N/D	39
176	ATPase lobe 1	799	HSS	N/D	N/D	40
407	ATPase lobe 2	684	NegC	app. 50	N/D	70
408	ATPase lobe 2	684	NegC	50	N/D	69
418	ATPase lobe 2	684	NegC	app. 50	N/D	68
430	ATPase lobe 2	647	NegC	app. 45	N/D	65
430	ATPase lobe 2	929	HSS	25	N/D	44
440	ATPase lobe 2	647	NegC	45	N/D	app. 65
490	ATPase lobe 2	647	NegC	N/D	N/D	59
490	ATPase lobe 2	665	NegC	N/D	N/D	60
490	ATPase lobe 2	684	NegC	N/D	N/D	61

app.: Approximately
N/D: Not determined

2.5.3. Quantitative cross-linking revealed conformational change of the HSS domain triggered by nucleosomes

To further explore the possibility of a nucleosome-dependent reorientation of the HSS domain relative to the ATPase module in the full-length Snf2H enzyme, I pursued a quantitative cross-linking strategy that relies on the use of a “light” cross-linker and its deuterated, “heavy” analog (239). Briefly, I used the light BS^3-H_4 and heavy BS^3-D_4 analogs for the relative quantification of shared inter-domain cross-links for the Snf2H enzyme in the ADP-BeF_x and nucleosome state (cf. Table 4). These analogs display a constant mass difference of nearly 4 Da and thus give rise to doublet signals during mass analysis. For my purpose, I cross-linked the ADP-BeF_x-bound Snf2H enzyme in the absence and presence of 0N40 nucleosomes with the BS^3-H_4 and BS^3-D_4 cross-linking agent, respectively. Subsequent to the quenching of the cross-linking reaction, both protein fractions were mixed in a 1:1 molar ratio and the combined sample was subjected to tryptic digestion. Cross-linked peptides were enriched by size-exclusion chromatography and the samples were measured in collaboration with Dr. I. Forné (LMU, Munich) by LC-MS/MS analysis. In a final step, I integrated the peak areas of the light- and heavy-labeled cross-linking candidates using the Skyline software and calculated the ratio between the two cross-linker analogs (cf. Materials and Methods section 4.2.4.6).

In a first step, I validated the quantification approach using a simplified experimental setup. That is, I cross-linked the Snf2H protein under apo state conditions with either BS^3-H_4 or BS^3-D_4 and mixed the two protein samples in a 1:1 molar ratio. Under these experimental conditions, I expected to find equal peak areas for the light- and heavy-labeled cross-links and thus a BS^3-H_4/BS^3-D_4 ratio of approximately 1. I focused on the relative quantification of five cross-links in this control experiment: XL_{Snf2H} 48 and XL_{Snf2H} 31 were consistently identified in all investigated Snf2H states (cf. Table 4) and the remaining cross-links XL_{Snf2H} 3, 19, and 29 were selected due to favorable signal intensities in combination with good fragmentation data during MS/MS analysis. I assigned these cross-linking candidates in the Skyline software based on extracted ion chromatograms and the following criteria: (i) correct retention time, (ii) correct assignment of the elution peak boundaries used for integration, (iii) precursor mass accuracy < 7.5 ppm, (iv) correct charge state, and (v) correct isotope distribution of the precursor ions. I then integrated the peak areas and calculated the BS^3-H_4/BS^3-D_4 ratio for each cross-linked peptide. The integration was performed for two technical replicates, different size-exclusion fractions, and different charge states of the precursor ions (see blue diamond symbols in Figure 43C). The BS^3-H_4/BS^3-D_4 ratio for each cross-link was calculated as the average of all supporting ratios for that linkage (see blue bars in Figure 43C). The analyzed cross-links in this control experiment displayed an average BS^3-H_4/-D_4 ratio of 0.8 ± 0.1 (see blue dotted line in Figure 43C), which is close to the expected value of 1. Consequently, the preliminary results overall indicated that the sample preparation procedure and the defined assignment criteria are adequate to relatively quantify individual inter-domain cross-links for the Snf2H enzyme.

I proceeded to study the conformational impact of nucleosome binding on the Snf2H enzyme as described in the above paragraphs. I therefore determined the BS^3-H_4/BS^3-D_4 ratio for shared inter-domain cross-links listed in Table 4 (Figure 43C). These cross-links predominantly connected the HSS domain with the ATPase module but sometimes also bridged the NegC region and ATPase lobe 2. In the case of individual NTR-HSS cross-links, I observed equal peak areas between the ADP-BeF_x and nucleosome state suggesting that binding of the nucleosome did not alter the likelihood of cross-linking reactions between the respective Snf2H regions. Likewise, the large majority of NegC-HSS cross-links exhibited a BS^3-H_4/BS^3-D_4 ratio of approximately 1. However, linkages between both ATPase lobes and the HSS domain appeared to be enriched in the ADP-BeF_x state relative to the nucleosome-bound state with average BS_3-H_4/BS_3-D_4 ratios ranging from 1.7 to 3.6. These results imply that binding of the nucleosome to the Snf2H enzyme hampered the formation of cross-links between the HSS domain and both ATPase lobes and potentially point towards a nucleosome-dependent reorientation of the DNA-binding domain relative to the catalytic core. In contrast, four out of five cross-linked residue pairs between ATPase lobe 2 and NegC exhibited a decreased BS^3-H_4/BS^3-D_4 ratio suggesting that the formation of ATPase lobe 2-NegC cross-links is favorable in the presence of nucleosomes.

In conclusion, the results for the relative quantification of inter-domain cross-links are consistent with the notion that binding of the nucleosome to the Snf2H enzyme resulted in a reorientation of the HSS domain relative to the catalytic core. These substrate-induced structural changes in the full-length Snf2H enzyme may encompass the partial disruption of the interface between the ATPase module and the HSS domain. Together with the observation that Snf2H-nucleosome cross-links almost exclusively mapped to the HSS domain (cf. STable 5), it is tempting to speculate that the position of the DNA-binding domain changes in a substrate-dependent manner such that it can contact the nucleosome core during the catalytic cycle.

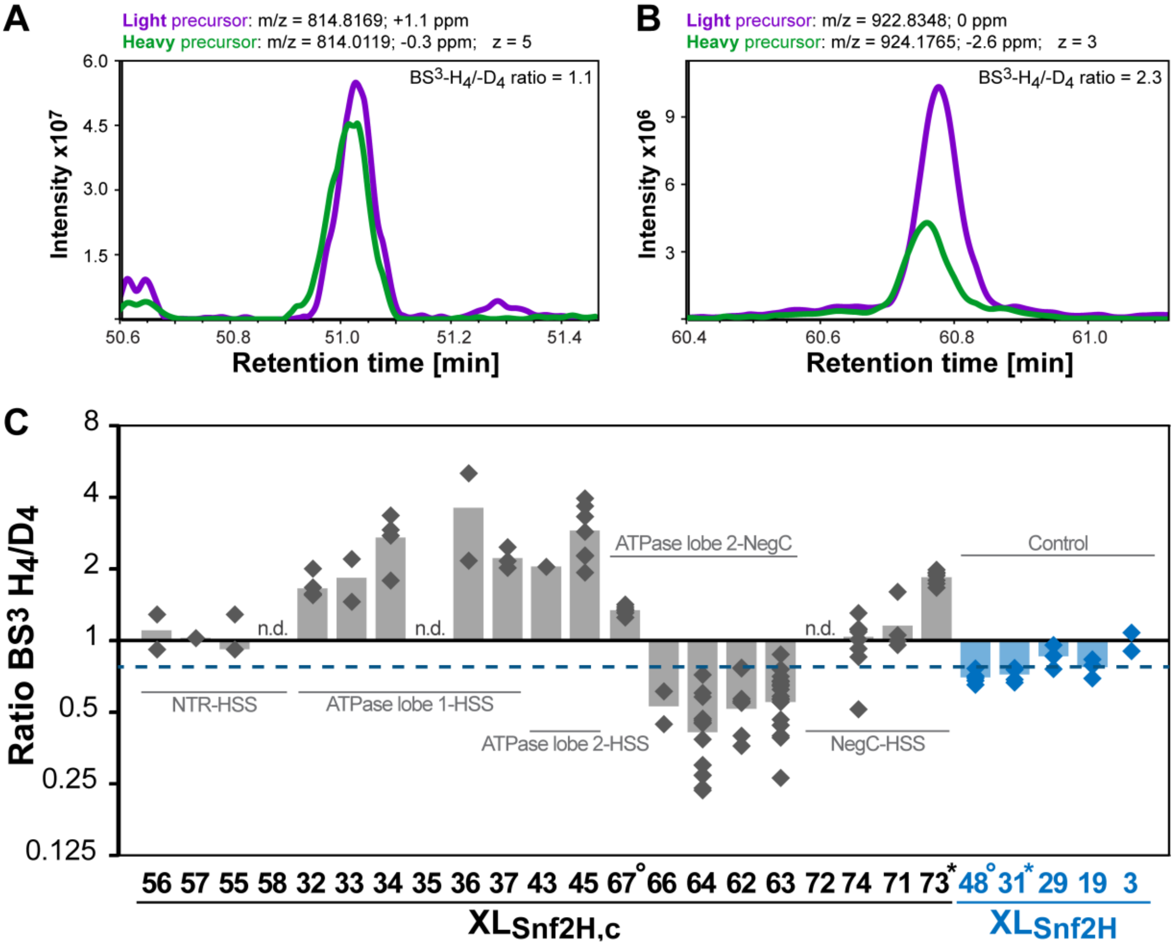

Figure 43: Quantitative cross-linking of the Snf2H enzyme. (A) Representative extracted ion chromatograms for $XL_{Snf2H,c}$ 71 that connected the NegC region and the HSS domain. The purple and green signal corresponds to the candidate cross-linked with the light and the heavy BS^3 analog, respectively. The peak areas for the light- and heavy-labeled peptides are similar as indicated by a BS^3-H_4/-D_4 ratio close to 1. **(B)** Representative extracted ion chromatograms for $XL_{Snf2H,c}$ 45 that connected ATPase lobe 2 and the HSS domain. This cross-linked residue pair exhibited a substantially increased BS^3-H_4/-D_4 ratio suggesting that binding of the nucleosome to the Snf2H enzyme hampered the formation of this particular cross-link. **(C)** Quantitative analysis of inter-domain cross-links for the Snf2H enzyme. The BS^3-H_4/-D_4 ratio for individual inter-domain cross-links listed in Table 4 (colored in grey) and the control experiment (colored in blue, see main text) are shown. Diamond symbols represent determined BS^3-H_4/-D_4 ratios for a particular cross-linked residue pair with average values being shown as bars. For the control experiment, the Snf2H enzyme was cross-linked with either BS^3-H_4 or BS^3-D_4 under apo state conditions and individual quantified cross-links are denoted according to their XL_{Snf2H} identification number provided in STable 3. The average BS^3-H_4/-D_4 ratio across all control peptides was 0.8 (blue dotted line), which is close to the expected value of 1. For inter-domain cross-links (‘$XL_{Snf2H,c}$’, cf. STable 5) listed in Table 4, values above and below 1 signify an enrichment of a particular cross-link in the ADP-BeF_x and nucleosome state, respectively. Cross-links, for which no quantification could be performed, are marked with ‘n.d.’ (n.d. = not determined). Superscript circles and asterisks indicate identical cross-links.

Dr. I. Forné (LMU, Munich) collected the LC-MS/MS data that were used to quantify individual cross-links.

2.5.4. Binding of the HSS domain to the nucleosome

ISWI-type remodeling enzymes have been demonstrated to interact with DNA that flanks the nucleosome via their characteristic HSS domain (23, 116, 127). Likewise, the SS domain of the ScChd1 enzyme has been observed to contact extranucleosomal DNA (24) thereby contributing to the affinity between the enzyme and the nucleosomal substrate (145). Recent experimental evidence point towards a conformational switch of the HSS domain during the transition from a DNA length sensing to a translocation-competent state. That is, the HSS domain is released from the flanking DNA stretch to interact with the core of the nucleosome (28, 129). XL-MS analysis provided an excellent opportunity to investigate how the HSS domain of the Snf2H enzyme interacts with the 0N40 mononucleosomes in the presence of ADP-BeF_x.

As indicated in Figure 41, I identified a total of 32 cross-links that connected the Snf2H enzyme and the histone octamer ($XL_{Snf2H,c}$ 150–181, STable 5; MS/MS spectra are provided in SFigure 11). Cross-links originating from individual histone proteins mapped to either ATPase lobe 1, the NegC-HSS interconnecting region (i.e., residues 690–742), the HSS domain or the very C-terminal segment (i.e., residues 1023–1052) of the full-length Snf2H enzyme. In particular, the SLIDE region of the HSS domain readily cross-linked to the histone octamer ($XL_{Snf2H,c}$ 150, 153–155, 164–167, 169, 170, 173–176, 179–181). The lack of adequate high-resolution structural data for the histone tails, the NegC-HSS interconnecting region, and the very C-terminal segment of the Snf2H enzyme, however, hampered an in-depth structural interpretation of most Snf2H-nucleosome interactions. Instead, I noticed that the distribution of cross-linked lysine residues significantly differed for individual histone proteins of the octamer assembly. That is, inter-molecular cross-links for the H3 and H4 proteins mapped to the histone tails, whereas cross-linking sites for the H2A and H2B subunits were preferentially found at the nucleosome core (cf. STable 5). Interestingly, the cross-linked residues in H2B (i.e., K105, K117, and K122) were located at the αC-helix and thus were in spatial proximity to the solvent-exposed acidic patch of the nucleosome, which has been proposed to serve as an important interaction surface for the autoregulatory NTR and NegC domains of the Snf2H enzyme (28). Of particular interest are $XL_{Snf2H,c}$ 153−155, in which the BS^3 cross-linker bridged individual residues close to the acidic patch and the SLIDE domain. We lack atomic coordinates in our Snf2H homology models for the remaining Snf2H-nucleosome cross-links that mapped to the acidic patch region ($XL_{Snf2H,c}$ 151, 152, 156−158, 160, and 161).

To visualize potential binding modes of the HSS domain to the nucleosome, our collaboration partner Dr. C. Schindler (TUM, Munich) modeled the DNA-binding domain of DmISWI (pdb 1OFC) onto the *Drosophila* nucleosome (pdb 2PYO) in a two-body docking procedure. The computational docking was performed in a similar manner as described in the above sections and was guided by a single distance restraint ($XL_{Snf2H,c}$ 154, Figure 44A). The remaining Snf2H-nucleosome cross-links $XL_{Snf2H,c}$ 150, 153, and 155 could not be considered as distance restraints during computational modeling because these linkages were not identified until the docking was completed. In addition, identified inter-molecular cross-links, which mapped to the histone tails, could not be considered during docking due to the lack of atomic coordinates for the respective residues in the nucleosome structure.

The final 200 models of the HSS-nucleosome complex were validated with respect to XL-MS data by assessing the Cα-Cα distances between cross-linked residue pairs of accessible, inter-molecular linkages ($XL_{Snf2H,c}$ 150 and 153–155). Model #22 was most consistent with the experimental data among the top-ranked docking structures and is depicted in Figure 44B. Notably, the measured Cα-Cα distances for individual SLIDE-H2B cross-links ($XL_{Snf2H,c}$ 153–155) were all compatible with model #22 of the HSS-nucleosome complex. The detected SLIDE-H2A cross-link ($XL_{Snf2H,c}$ 150), however, exceeded the BS^3 distance threshold by 13 Å. The cross-linked K118 residue of $XL_{Snf2H,c}$ 150 is located in an unstructured and potentially flexible H2A region at the C-terminal tail, which provides a structure-based explanation for the violated Cα-Cα distance.

In summary, our XL-MS data suggest that the SLIDE region of the Snf2H enzyme is in spatial proximity to the nucleosome core upon complex formation. The representative structural model of the HSS-nucleosome complex shown in Figure 44B illustrates a potential binding mode of DNA-binding domain to the histone octamer, which is largely consistent with the experimental XL-MS data. As such, these findings provide novel evidence for an alternative binding position of the HSS domain during the catalytic cycle of the Snf2H protein that are consistent with recent experimental results from the Narlikar laboratory (28, 129).

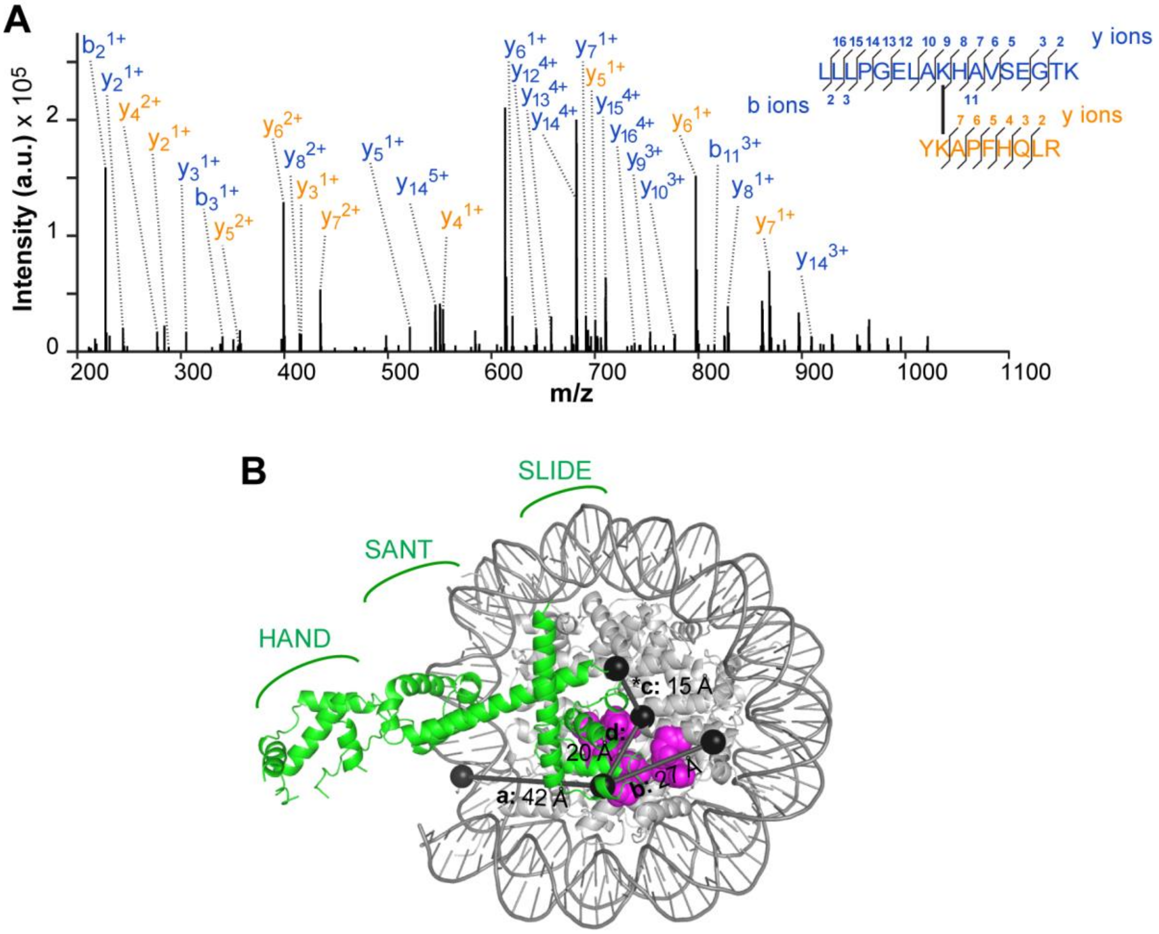

Figure 44: Proposed binding mode of the HSS domain. (A) MS/MS spectrum of XL$_{\mathrm{Snf2H,c}}$ 154, which was used to guide the docking of the HSS-nucleosome complex shown in (B). The monoisotopic peaks of y- and b-fragment ions from the cross-linked H2B (blue) and SLIDE (orange) peptides are denoted. SFigure 11 shows additional MS/MS spectra of cross-links depicted in (B). **(B)** Our XL-MS-based structural model of the HSS domain (green, pdb 1OFC) in complex with the nucleosome (grey, pdb 2PYO) is shown. Notably, the SLIDE domain is in close spatial proximity to residues of the acidic patch (magenta spheres) of the histone octamer. The black lines and spheres (labeled a–d) represent identified inter-molecular cross-links (i.e., XL$_{\mathrm{Snf2H,c}}$ 150, 153, 154, and 155; cf. STable 5). The cross-link with an asterisk was used as a distance restraint during computational docking.

Dr. I. Forné (LMU, Munich) performed the MS analysis shown in panel (A). Dr. C. Schindler (TUM, Munich) performed the computational docking of the HSS-nucleosome complex depicted in panel (B).

3. Discussion

Changes in chromatin structure rely on the action of specialized chromatin remodeling complexes, which operate in any eukaryotic cell in an ATP-dependent manner and thus play a pivotal role in a vast variety of important cellular processes (82, 240, 241). Not surprisingly, mutation and misregulation of these chromatin remodeling complexes are linked to cancer and a plethora of severe diseases (242-244). The ISWI-family of chromatin remodeling complexes has been demonstrated to catalyze nucleosome assembly and sliding *in vitro* (85, 138, 245, 246), and indeed most of the activity can be recapitulated by the ISWI remodeling enzyme itself. In the present thesis, I studied the structural architecture and function of two prototypical ISWI-type remodeling enzymes, DmISWI and Snf2H, using an integrative structural approach. The implications of the presented findings are discussed in the context of the existing structural and functional framework for ISWI-type and related enzymes in the following sections.

3.1. Structure determination by an integrative approach

X-ray crystallography and NMR spectroscopy have proven to be highly useful approaches for high-resolution structure elucidation of proteins and protein complexes and thus have been considered indispensable tools in modern structural biology. However, structure determination by these traditional methods often fails for larger, more heterogeneous, and/or more dynamic target proteins (247-249). ISWI-type chromatin remodeling enzymes have proven to be refractory to traditional X-ray crystallography and NMR spectroscopy, which is perhaps best reflected by the lack of comprehensive high-resolution structures for this class of proteins (cf. section 1.2.3).

In this PhD project, I studied the structural architecture of ISWI-type remodelers across different steady-state conditions using an integrative structural approach that combines two complementary experimental data sources with computational modeling. We integrated SAXS and XL-MS analysis into our structural approach because we envisaged that these low and intermediate resolution techniques provide excellent complementary data to narrow down possible solution conformations of the DmISWI and Snf2H remodeling enzymes. That is, the combination of XL-MS data and computational modeling has proven useful to restrict the conformational search space during the docking procedure by implementing identified inter-domain cross-links as distance restraints. Likewise, the global shape information provided by SAXS measurements was essential to select and validate individual DmISWI and Snf2H models from the ensemble of computed structures. The available high-resolution structures of related ATPases under apo state conditions differ drastically with respect to each other (Figure 4) and thus did not provide molecular clues for the validity of the modeling outcomes. Our proposed model of the DmISWI ATPase domain under apo state conditions (Figure 14A) exhibited a novel orientation of both ATPase lobes at the time the computational docking was completed. The XL-MS based model achieved an accuracy that was instrumental to driving further experimental investigations including for instance charge-reversal mutations in the putative lobe-lobe interface. Strikingly, the recently published crystal structure of the MtISWI protein (146) depicts an almost identical configuration of both ATPase lobes (Figure 15). Considering that X-ray crystal structures represent stable solid-state conformations, which is often a poor indicator for the most populated conformation in solution and solution-state dynamics (250), our structural data provide an independent validation of the MtISWI ATPase structure in solution. Consequently, our study is an excellent example of how docking driven by lower-resolution experimental data can offer an alternative to classical structure determination, especially when higher-resolution techniques such as X-ray crystallography prove difficult to be applied. Assuming that our model of the ATPase domain reflects the predominant conformation under apo state conditions, the implementation of XL-MS-derived distance restraints to guide computational docking was essential for the success of this study. That is, the *ab-initio* docking resulted in a substantially different and potentially irrelevant orientation of both ATPase lobes for DmISWI (Figure 16) underscoring the well-documented advantages of integrative modeling over *ab-initio* structure prediction (251).

Despite the promising results for the DmISWI ATPase domain, I encountered several experimental challenges using the integrative structural approach. While chemical cross-linking generally resulted in numerous cross-links between the HSS domain and the ATPase module for both remodeling enzymes, I identified only a limited set of linkages that connected both ATPase lobes. This discrepancy in terms of number of identified inter-domain cross-links for particular regions of the remodeling enzymes could have diverse origins. It appears most likely that the conformation of the ATPase domain was unfavorable for the formation of chemical ATPase lobe-lobe cross-links. Alternatively, these cross-linked products may exhibit less favorable ionization properties than other inter-domain cross-links or they were simply not detected/identified during MS/MS analysis due to interfering ion species and/or insufficient fragmentation data. The identification of cross-linked peptides based on LC-MS/MS data is tightly coupled to the criteria listed in Table 15. Lowering these identification criteria, however, increases the risk of false-positive identifications during data analysis.

To rationalize potential reasons for the low number of identified ATPase lobe-lobe cross-links, I listed all theoretically possible cross-links for the full-length DmISWI model under apo state conditions (Figure 21) using the Xwalk software (http://www.xwalk.org/) (252) with the following settings: first and second residue in cross-links: Lys, intra-protein cross-links, and maximum Euclidean distance: 29 Å. Notably, only 7% of the predicted 399 cross-links connected both ATPase lobes. Considering that solvent-accessibility of reactive sites, steric constraints in the DmISWI protein, and the ionization properties of the cross-linked products were neglected during the Xwalk approximation, I would expect to find a low number of ATPase lobe-lobe linkages. In line with this notion, XL-MS analysis of the Snf2H enzyme in the presence of substrate and ADP-BeF$_x$ by Gamarra et al. (28) resulted in a comparably low number of ATPase lobe-lobe connecting cross-links with less than 1% of all uniquely identified cross-links restricting the orientation of both ATPase lobes to each other.

In the case of the DmISWI enzyme, we could counteract the low number of chemical cross-links between both ATPase lobes by including previously published data from site-directed UV cross-linking experiments (115, 157). The broader specificity of genetically encoded Bpa appears to be beneficial to extract structural information at a desired position in the target protein, for which chemical cross-linking is less promising. In the case of the Snf2H enzyme, our collaboration partner Dr. C. Schindler (TUM, Munich) performed a three-body docking protocol in order to overcome the limited number of identified ATPase lobe-lobe cross-links. Thus, the conformation of the ATPase lobes in our full-length Snf2H model almost exclusively relied on distance restraints between the ATPase module and the HSS domain. Modeling of the full-length Snf2H enzyme based on identified HSS cross-links turned out to be challenging because the large majority of linkages used for docking involved either residues K929 or K990, which were also found to contact broadly distributed residues of the NTR, ATPase lobe 1, ATPase lobe 2, and NegC (Figure 29). As a consequence, we were not able to obtain a full-length Snf2H model under apo state conditions, in which all distance restraints used for docking were satisfied at the same time (Figure 31B). Most likely, I captured different conformational sub-states of the Snf2H enzyme that are present under the tested apo state conditions. However, assignment of individual cross-links to unknown states of a co-existing conformational ensemble was not feasible using our modeling protocol. Attempts of detailed modeling based on partially ambiguous and/or conflicting cross-linking data has recently been performed for the yeast RNA polymerase III complex using an alternative modeling software, termed XL-MOD (253). In contrast to our modeling protocol, the XL-MOD software allows for the identification of alternative conformations by automatically weighing individual cross-links and by allowing subunit structures to be flexible during conformational sampling. While one could argue that the implementation of protein dynamics during conformational sampling might result in an even more complex and heterogeneous ensemble of computed structures, the classification of individual cross-links into conformation-specific subgroups is potentially worthwhile to explore.

In the present study, the modeling of ISWI-type remodeling enzymes was driven by selected XL-MS-derived distance restraints. The selection of distance restraints used for docking relied on the quality of fragmentation data obtained for cross-linked products during MS/MS analysis. This objective selection criterion allowed us to categorize cross-linked products as “low-“ and “high-confidence” cross-links thereby minimizing the risk of considering false-positive identifications during computational modeling. Several studies have been published, in which a subset of “high-confidence” cross-links were used to elucidate the structural architecture of the target protein(s) by integrative modeling (223, 254, 255). In the case of the full-length DmISWI protein, the computational results were most consistent with the experimental XL-MS and SAXS data when we used a subset of identified distance restraints in a three-body docking procedure (Figure 23B). That is, the large majority of distance restraints were satisfied in the respective DmISWI model as further specified in STable 1 and STable 2. Applying the same modeling strategy to the Snf2H enzyme, however, was less successful due to the above-mentioned limitations in terms of number of identified ATPase lobe-lobe cross-links as well as the ambiguous/conflicting nature of ATPase-HSS linkages. Consequently, performing UV cross-linking on the Snf2H protein might represent a promising future strategy to obtain more ATPase lobe-lobe cross-links that can be used to model the ATPase domain of the remodeling enzyme. Furthermore, incorporation of Bpa along the putative ATPase-HSS interface could give rise to complementary inter-domain distance restraints that do not include hotspot residues K929 and K990 of the DNA-binding domain.

In conclusion, I find that our developed integrative structural approach was highly useful to elucidate the structural architecture of the ISWI-type DmISWI and Snf2H remodeling enzymes, for which only limited high-resolution structural data exist. The combination of XL-MS, SAXS, and computational modeling allowed us to gain a first molecular glimpse of the full-length DmISWI enzyme under apo state conditions with the predicted ATPase domain sharing striking similarities with the crystallized MtISWI structure. Recent efforts of the Worldwide Protein Data Bank (wwPDB) to create a public database furthermore underscore the value of such an integrative approach and the resulting structural models (256). The developed modeling protocol has the potential to be applied for structural characterization of a large variety of proteins and protein complexes that have proven refractory to traditional structure determination techniques.

3.2. Structural characterization of ISWI-type enzymes under apo state conditions – A common regulatory mechanism?

It is often assumed that proteins with similar sequences – the homologous DmISWI and Snf2H remodeling enzymes share approximately 75% sequence identity (94) – will also exhibit a similar structural fold. Kosloff and Kolodny investigated the validity of this concept and describe pairs of proteins, which share considerable sequence identity but display significant structure dissimilarity (257). Remodeling ATPases are all related to each other, yet the orientation of RecA-like ATPase lobes differ drastically in available apo crystal structures (109, 141, 146, 153, 154) (Figure 4). Does the sequence conservation between DmISWI and Snf2H also ensure structural (dis)similarity and are there common principles in the regulation of ATP-dependent chromatin remodeling activity by ISWI-type enzymes?

We collected experimental XL-MS and SAXS data to reconstruct the structural architecture of these homologous remodelers under apo state conditions. These local and global structural information can be compared considering that individual protein regions fulfilled the prerequisites for comparison. That is, homology models of functionally important DmISWI and Snf2H domains are structurally highly similar as indicated by small RMSD values (i.e., RMSD_{HSS} = 1.19 Å; $\text{RMSD}_{\text{ATPase lobe1}}$ = 0.24 Å; $\text{RMSD}_{\text{ATPase lobe2-NegC}}$ = 0.18 Å). Furthermore, the number and distribution of chemically cross-linkable lysine residues are comparable across both remodeling enzymes with numerous intra-domain cross-links connecting identical/similar sites in the DmISWI and Snf2H proteins (Figure 45).

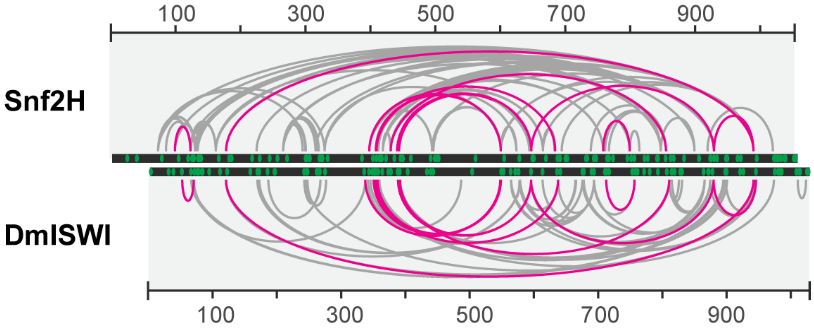

Figure 45: Comparison of identified cross-links for the DmISWI and Snf2H proteins under apo state conditions. Identified cross-links for the DmISWI and Snf2H enzymes under apo state conditions are schematically illustrated in arc plots. The arc plots were manually aligned with residue numbering being denoted for both proteins. Green dots indicate the position of individual lysine residues. Identical and similar DmISWI and Snf2H cross-links are highlighted as pink arcs. Cross-linked peptides were considered similar if the cross-linking sites were within ± 10 amino acids with respect to the corresponding primary protein sequence. The data presented in this Figure is identical to the data shown in Figure 12 and Figure 27.

Applying our integrative structural approach to the full-length DmISWI enzyme under apo state conditions revealed a novel orientation of both ATPase lobes, which shows remarkable consistency with the lobe orientation observed in the MtISWI crystal structure (146) (Figure 15). In our structural model of the DmISWI ATPase module, both ATPase lobes stack together with catalytically important motifs (i.e., motifs I, II, and VI) being twisted towards opposite directions (Figure 17A). The structural arrangement of both ATPase lobes is most consistent with the notion that the DmISWI protein assumes a resting conformation under apo state conditions in solution. Our findings thus provide a structure-based explanation for the low basal ATPase activity of DmISWI in the absence of substrate (140). In line with our interpretation of a resting DmISWI conformation, the related MtISWI protein (146) but also the MtSnf2 protein (153) have been proposed to adopt a catalytically incompetent state under apo state conditions. In order to become catalytically competent, these remodeling enzymes are thought to undergo activating conformational changes in their ATPase domain such that motifs involved in ATP binding and ATP hydrolysis are optimally positioned to cooperatively facilitate the enzymatic reaction. Likewise, the DmISWI protein is expected to undergo substantial structural rearrangements to become active (140). The active conformation of the DmISWI protein may be approximated by available structures of related enzymes including ScSnf2 (21), ScChd1 (24), and DmVasa (258), which were captured in complex with either RNA or the nucleosomal substrate. Superimposition of these catalytically competent structures shows a strikingly similar orientation of both ATPase lobes with motifs involved in catalysis occupying nearly identical positions in the three-dimensional space (Figure 46A). The convergence of these structures may point towards a common configuration of the active site that allows for efficient ATP hydrolysis. In order for the DmISWI enzyme to assume a comparable active conformation and thus to leave the resting state, we find that the ATPase domain has to undergo a considerable conformational change such that ATPase lobe 1 rotates by approximately 110−140° relative to ATPase lobe 2 around a predicted hinge region (Figure 46B). Comparable nucleosome-dependent changes in the relative orientation of both ATPase lobes have been described in the context of the substrate-bound structures of ScSnf2 (21) (Figure 46C) and ScChd1 (24) (Figure 46D).

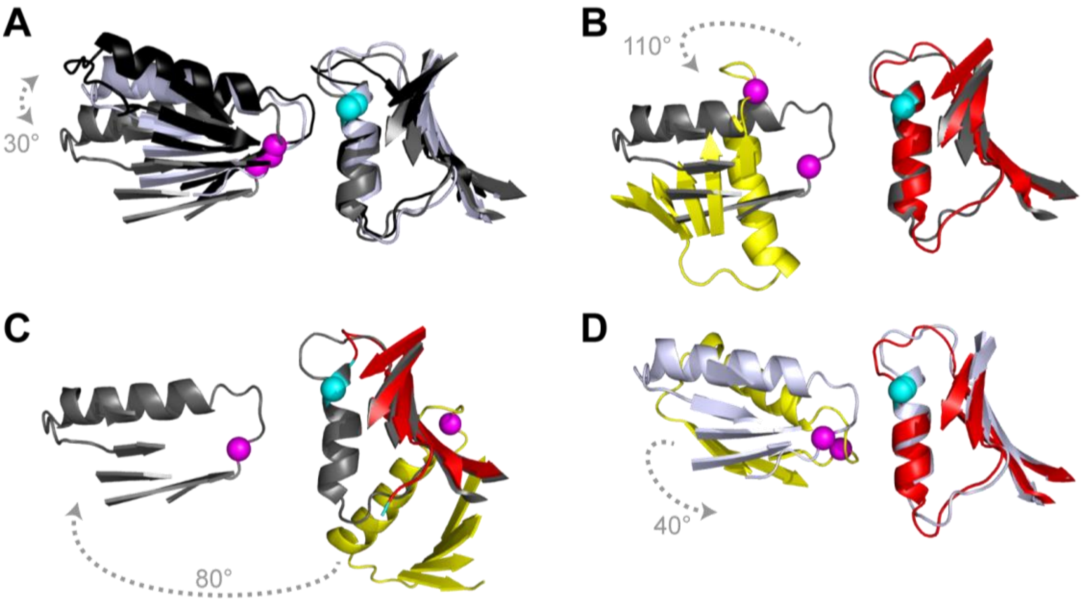

Figure 46: Conformational changes related to ATPase activation. Only the structures around central ß-sheets of ATPase domains of distinct enzymes are shown for clarity. All structures were aligned to ATPase lobe 2 of our DmISWI model. Spheres indicate catalytically important motifs on both lobes with motif I and motif VI being colored in magenta and cyan, respectively. **(A)** Superimposition of the active, nucleosome-bound ScSnf2 (grey, pdb 5X0Y) and ScChd1 (light grey, pdb 5O9G) structures as well as the active, RNA-bound DmVasa complex (black, pdb 2DB3). Both ATPase lobes as well as the structural motifs are similarly arranged to each other in the depicted structures. **(B)** To assume a comparable active conformation as seen for ScSnf2 (grey) in (A), ATPase lobe 1 (yellow) of the DmISWI enzyme (cf. Figure 14A) has to rotate relative ATPase lobe 2 (red). **(C)** Liu and co-workers compared the structures of the nucleosome-ScSnf2 complex (grey, pdb 5X0Y) and MtSnf2 in the resting state (yellow, red; pdb 5HZR) and proposed a comparable conformational change (21). **(D)** Structures of the inactive (yellow, red; pdb 3MWY) and active, nucleosome-bound ScChd1 enzyme (light grey, pdb 5O9G) are superimposed. Upon nucleosome binding, Farnung et al. suggest that ATPase lobe 1 moves relative to ATPase lobe 2 (24).

To investigate whether the homologous DmISWI and Snf2H enzymes share a comparable ATPase conformation under apo state conditions, I superimposed our respective models of the ATPase domain for these two remodeling enzymes (Figure 47). Alignment of our structural models for the DmISWI and Snf2H enzymes reveals a markedly different orientation of both ATPase lobes in the absence of nucleotide and substrate. How can such a deviating ATPase conformation for closely related remodeling enzymes under comparable solution conditions be explained? While we had several UV and chemical lobe-lobe cross-links available to model the ATPase domain of the DmISWI enzyme, the predicted lobe-lobe interface in the Snf2H protein is insufficiently covered by experimental data. Although our collaboration partner Dr. C. Schindler (TUM, Munich) restrained the distance between the two structural bodies of the ATPase module, the identified cross-links that restrict their orientation (i.e., XL_{Snf2H} 43, 44; STable 3) consistently exceeded the BS^3 distance threshold in the final models of the full-length Snf2H enzyme (Figure 31B). Consequently, the possibility of a similar ATPase conformation between the DmISWI and Snf2H enzyme should not be refused per se considering the challenges in modeling the orientation of both ATPase lobes based on ATPase-HSS cross-links and the overall ambiguity of the obtained full-length Snf2H models. In contrast, the DmISWI ATPase model displayed a remarkable model precision with the proposed structural architecture being largely consistent with experimental data and being robust across different modeling strategies.

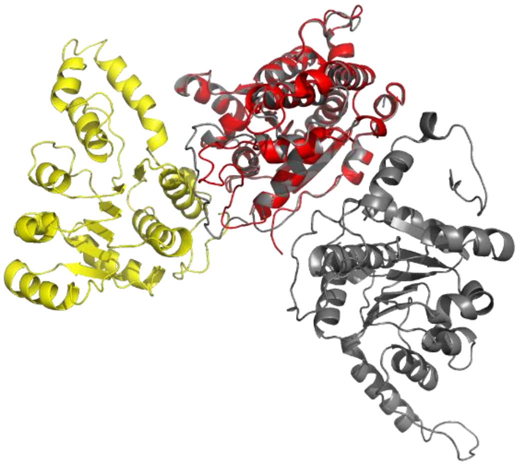

Figure 47: Superimposition of structural models of the DmISWI and Snf2H ATPase domain under apo state conditions. Our representative model of the DmISWI ATPase domain (yellow, red; cf. Figure 14A) is aligned on ATPase lobe 2 onto the catalytic core of Snf2H (grey; cf. model #1 in Figure 31A). Notably, these two structures display a markedly different orientation of both ATPase lobes.

Remodeling enzymes have evolved intricate strategies to regulate their catalytic activity to ensure that ATP hydrolysis only takes place in the presence of substrate. ISWI-type remodeling enzymes comprise the NTR and NegC regions, which flank the ATPase domain and that are critically involved in the autoregulation of the catalytic activity (28, 114, 115, 129, 146). How these auto-inhibitory modules are structurally organized in the full-length DmISWI and Snf2H enzymes, however, has remained elusive.

In the course of this PhD project, I identified several NTR cross-links for the DmISWI and Snf2H remodeling enzymes. In the case of the DmISWI protein, the partner cross-linking sites of these NTR linkages were invariably located near the interface of both ATPase lobes (Figure 21). Our XL-MS data for DmISWI (this study and (115)) may reflect an MtISWI-like conformation of the NTR, in which the autoregulatory domain bridges both ATPase lobes under apo state conditions. That is, in the MtISWI crystal structure (pdb 5JXR), the α3 helix of the NTR was found to span across the ATPase lobe-lobe interface such that the highly conserved AutoN motif can interact through H-bond/salt-bridge interactions with ATPase lobe 2 (146). Binding of the NTR to ATPase lobe 2 is thought to represent an important autoregulatory mechanism to keep the ATPase motor domain in a catalytically incompetent resting state in the absence of substrate. In line with this mode of inhibition, disruption of critical AutoN-ATPase lobe 2 interactions by site-directed mutagenesis or deletions of functionally important NTR regions has been shown to severely deregulate the activity of ISWI-type remodeling enzymes (114, 115, 146). Notably, the unrelated N-terminal chromodomains of ScChd1 also pack against a basic surface patch on ATPase lobe 2 potentially repressing activation of the enzyme under apo state conditions (141). In the case of the Snf2H protein, the identified NTR-ATPase lobe 1 cross-links show consistency with both our results for the DmISWI enzyme as well as the MtISWI structure. The apparent lack of chemical NTR-ATPase lobe 2 cross-links for Snf2H should not be over-interpreted considering that respective distance restraints in the DmISWI enzyme were exclusively found upon UV irradiation of the $ISWI_{H483B}$ variant (115).

Additional evidence that the NTR of the DmISWI and Snf2H assume a similar conformation in the absence of substrate is provided by the observation that the autoregulatory domain of both enzymes formed cross-linked products with the distant SLIDE region of the HSS domain. The notion of spatial proximity between the very N- and C-terminal domains in DmISWI and Snf2H are supported by chemical cross-linking results for the ScChd1 protein, for which the poorly conserved chromodomains were also found to form linkages to the DNA-binding domain in the absence of substrate (155). Overall, the detected NTR-HSS cross-links in DmISWI and Snf2H signify that the studied remodeling enzymes assume a compact solution structure with the catalytic domain being potentially caged by these domains. Implementation of NTR-HSS distance restraints in the modeling protocol, however, resulted in a significantly poorer fit of the DmISWI model to the experimental SAXS data for the full-length enzyme (Figure 25). Most likely, local conformational fluctuations in one or several functional domains of the DmISWI may not allow us to simultaneously satisfy all cross-linking information during rigid body docking. The possibility of false sequence assignments for the NTR-HSS cross-links is minimal considering the number of identified linkages and the concordance of experimental XL-MS data for the DmISWI, Snf2H, and ScChd1 remodeling enzymes (155).

The structural information gained from XL-MS analysis provided a further rationale to the regulation and autoinhibition mechanism of the full-length DmISWI and Snf2H enzymes by the NegC domain. The NegC domain has been suggested to play an important role in inhibiting the coupling of ATP hydrolysis to nucleosome sliding (114), DNA linker length sensing and nucleosome centering (129), as well as regulating the transition from a DNA length sensing to a translocation competent state (28, 129). Two different conformations of the NegC domain have been described for related chromatin remodeling enzymes. While the NegC domain protrudes from the globular ATPase domain to interact with a neighboring protomer in the MtISWI structure (pdb 5JXR) (146), the autoregulatory region bridges both ATPase lobes in the monomeric structure of ScChd1 (pdb 3MWY) (141) (Figure 26A). The identified NegC-ATPase cross-links for the Snf2H and DmISWI proteins were strikingly similar (compare Figure 30B with Figure 30C), which argues for a comparable arrangement of NegC in these homologous remodeling enzymes under apo state conditions. The observed cross-linking pattern for the NegC region are consistent with the ScChd1 structure with the large majority of NegC-ATPase distance restraints being furthermore satisfied in the proposed ScChd1-based structural models of the full-length DmISWI (Figure 21) and Snf2H proteins (Figure 30A). In stark contrast, I find that most distance restraints are markedly violated in the structure of a single MtISWI protomer (Figure 30B, C). I considered the possibility that the detected NegC-ATPase linkages may derive from intermolecular cross-linking of DmISWI and Snf2H homodimers. However, the results from size-exclusion chromatography of native and cross-linked protein (Figure 26B and SFigure 1B) as well as SAXS data for DmISWI (Figure 22) and Snf2H (Figure 32) argue against dimer formation under apo state conditions, in overall accordance with previous experimental data (140, 150, 157). Thus, the protruding NegC conformation observed in the MtISWI structure probably represents a physiologically irrelevant crystallization artifact. This notion is supported by the observation that NegC of protomer 1 contacts the ATPase domain of protomer 2 in a ScChd1-like manner in the MtISWI structure (Figure 26A). A ScChd1-like NegC conformation, in which both ATPase lobes are contacted, potentially enables the regulatory domain to sense and influence catalytic core actions (141).

Although the fundamental nucleosome sliding reaction does not rely on the HSS domain in DmISWI (140) and Snf2H (129), the DNA-binding domain has been suggested to facilitate chromatin remodeling by increasing the affinity and specificity of the enzyme for the nucleosomal substrate. In addition, the HSS domain may form interactions with accessory proteins in the multi-protein remodeling factors (105) and contributes to nucleosome positioning and spacing (23, 151, 259). Applying our integrative structural approach to DmISWI and Snf2H allowed us to resolve the relative orientation of the HSS domain in the full-length remodeling enzymes under apo state conditions.

In the case of DmISWI, implementing as set of reliable ATPase-HSS distance restraints during computational modeling resulted in a compact structural model, in which the HSS domain packs against the catalytic core (Figure 21). In a study by Hota and co-workers (127), residues in the presumable ATPase-HSS interface of ScIsw2 were mutated and resulted in almost an order of magnitude reduced nucleosome remodeling and ATP hydrolysis activity of the enzyme. The respective mutated residues are very close or being part of the predicted interface between the ATPase module and HSS domain in our structural model of the full-length DmISWI protein (Figure 48). Notably, the predicted ATPase-HSS interface was well restrained by experimental data with individual cross-links originating from complementary UV- and chemical cross-linking approaches connecting residues of both domains. Consequently, our structural DmISWI model reveals the previously predicted ATPase-HSS interface for ScIsw2, which might be of functional importance for catalysis and could be investigated in future studies.

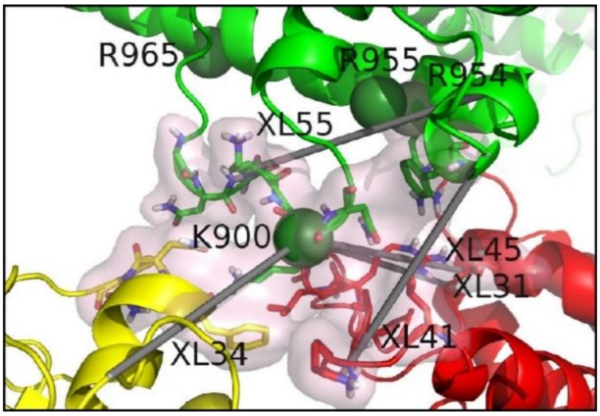

Figure 48: The proposed ATPase-HSS interface in DmISWI. The ATPase-HSS interface of our structural model of the full-length DmISWI enzyme (yellow, red, green; cf. Figure 21) is displayed. Residues of the ATPase-HSS interface in the DmISWI model were identified using an adapted version of the 'InterfaceResidue' script (Vertrees, 2009; https://pymolwiki.org/) and are shown in stick and surface representation. A previous study mutated residues in ScIsw2 (127). The corresponding four residues (i.e., K900, R954, R955, and R965) are shown as spheres and are very close or being part of the ATPase-HSS interface in the structural model of DmISWI. Cross-links originating from the interface are shown as grey lines and are numbered according to STable 2. The Figure was adapted from (1) in accordance with Elsevier's policies.

As a consequence of the tight packing of the HSS domain against the ATPase module, it appears unlikely that such a compact conformation is compatible with DNA binding to the HSS domain. That is, superimposition of the DNA-bound HSS domain of ScISW1a (pdb 2Y9Z, (151)) onto our structural model of the full-length DmISWI resulted in a direct steric clash between the DNA strand and the ATPase domain (Figure 24). This finding is consistent with the notion that the DmISWI protein is trapped in a resting state under apo state conditions with the HSS domain being unable to bind DNA. An occluded DNA-binding site on the HSS domain in the resting state may represent a regulatory strategy to prevent binding to unrelated DNA. In line with this argumentation, the ATPase-HSS interface is expected to break up upon activation of the DmISWI enzyme such that the HSS domain can reach its binding sites on flanking DNA (23, 116, 151) and the nucleosome core (28, 129) during the catalytic cycle.

In the case of the Snf2H enzyme, I also identified numerous cross-links that connected individual residues of the ATPase module and the HSS domain. As for DmISWI, the majority of these linkages mapped to the SLIDE region of the HSS domain. However, the key difference between the XL-MS data sets for the DmISWI and Snf2H remodeling enzymes under apo state conditions relies on the distribution of cross-linked residues in the HSS domain. That is, residues K929 and K990 in Snf2H represented cross-linking hotspots within the HSS domain, which accounted for 70% of all identified intra- and inter-domain cross-links that mapped to the DNA-binding domain (Figure 29A and STable 3). Comparable hotspot residues were absent for the DmISWI enzyme although the number and localization of lysine residues in the HSS domain appears to be highly similar for the homologous remodeling enzymes (data not shown). How can such cross-linking hotspots be explained? The tendency of individual residues to excessively form linkages to diverse target sites has been observed in cross-linking studies of human serum albumin (260) and the photosystem II protein complex (261). The diversity of Snf2H cross-links involving K929 and K990 might be best explained by assuming that these hotspot residues are easy accessible for the BS^3 cross-linker and that the C-terminal region of the HSS domain exhibits a pronounced dynamic behavior under apo state conditions. This notion is supported by the observation that the BS^3 cross-linking agent preferentially reacts with flexible regions of proteins (261, 262). An enhanced flexibility of the SLIDE region may increase the likelihood of the chemical cross-linker to first react with either K929 or K990, which is followed by scanning for a reachable target residue located in a less flexible part of the protein. Thus, the unequal distribution of cross-linked HSS residues between the DmISWI and Snf2H proteins could point towards different local dynamics in the DNA-binding domains. The conflicting nature of identified HSS-ATPase cross-links for the Snf2H enzyme may furthermore reflect the dynamic equilibrium of co-existing structures under apo state conditions with individual conformations of the Snf2H enzyme being present at a different ratio than for the DmISWI protein. This could explain the fact that our collaboration partner Dr. C. Schindler (TUM, Munich) was unable to obtain a single Snf2H model that satisfied all identified distance restraints at once. Notably, several other chromatin remodeling enzymes such as ALC1 (263) and SsoRad54 (158) have been suggest to exhibit a high degree of conformational heterogeneity under a given steady-state condition revealing potentially interesting parallels to our findings.

In overall conclusion, our integrative approach allowed us to delineate and compare the structural architecture of the full-length DmISWI and Snf2H remodeling enzymes under apo state conditions. Although we cannot claim for an identical domain arrangement between these homologous enzymes in the absence of substrate, our results point towards a shared molecular mechanism to regulate the ATPase activity of ISWI-types remodelers. That is, the XL-MS data for both DmISWI and Snf2H are consistent with an MtISWI-like conformation of the NTR domain (pdb 5JXR) as well as a ScChd1-like orientation of NegC (pdb 3MWY). These autoregulatory domains have been suggested to bridge the ATPase lobe-lobe interface thereby trapping the enzymes in a resting conformation under apo state conditions. In the case of the DmISWI enzyme, our structural model reveals that catalytically important motifs of the ATPase lobes are twisted towards opposite directions with productive ATP hydrolysis being unlikely to happen. The number of identified ATPase-HSS cross-links for both studied remodeling enzymes furthermore imply that the HSS domain is packing against the catalytic core with the very N- and C-terminal regions being in close spatial proximity to each other. As such, DmISWI and Snf2H appear to assume an overall compact conformation under apo state conditions. Given our more reliable model of the DmISWI protein, activation of ISWI-type remodelers would require a series of conformational changes including a reorientation of both ATPase lobe, release of the autoinhibition by NegC and NTR, and the HSS domain in order to become catalytically competent.

3.3. Impact of ADP-BeF$_x$-binding on ISWI-type remodeling enzymes

To uncover and visualize potential activating conformational changes in the catalytic core of ISWI-type remodeling enzymes, we applied our integrative structural approach to the prototypical Snf2H enzyme in the presence of a molar excess of the nucleotide analog ADP-BeF$_x$. That is, ADP-BeF$_x$ has been suggested to shift the conformational ensemble of ISWI-type remodelers from a presumably inactive conformation towards various nucleotide-dependent states including the functionally important transition state during the ATP hydrolysis reaction (159). This notion is supported by X-ray crystallography data for other SF2 ATPases such as the yeast DEAD box protein Mss116p (264). Notably, using 3 mM ADP-BeF$_x$ during chemical cross-linking and SAXS analysis, the large majority of Snf2H molecules should be bound to the nucleotide analog given the preliminary results from the competitive, TLC-based ATPase assay (SFigure 2).

Although I identified many identical/similar cross-linked residue pairs between the apo and ADP-BeF$_x$-bound Snf2H state (Table 2), I repeatedly detected several nucleotide analog-dependent inter-domain cross-links (Table 3). These ADP-BeF$_x$-dependent cross-links predominantly connected residues of either the NTR or ATPase lobe 1 with the HSS domain. Including a subset of these ATPase lobe 1-HSS cross-links as distance restraints during computational docking of individual Snf2H domains resulted in markedly different conformation of the ATPase domain. That is, comparison of structural models of the full-length Snf2H enzyme in the apo and ADP-BeF$_x$-bound states (Figure 38) suggested that binding of the nucleotide analog caused an approximately 180° rotation of ATPase lobe 1 relative to ATPase lobe 2. Interestingly, the ATPase lobes of several chromatin remodeling enzymes have been suggested to undergo large-scale reorientations in a nucleotide- and substrate-dependent manner (21, 24, 141, 154, 158). For instance, the Snf2 family ATPase core of the Rad54 protein from *Sulfolobus solfataricus* (SsoRad54) has been crystallized with and without bound DNA revealing an unexpected, outward-oriented placement of motifs IV to VI of ATPase lobe 2 in both states (154). The authors hypothesized that it requires a 180° flip of ATPase lobe 2 relative to ATPase lobe 1 in order to align structural motifs for efficient catalysis. Results from FRET experiments on the same SsoRad54 construct in the presence and absence of DNA and different nucleotides showed consistency with a highly dynamic conformational ensemble of the remodeling enzyme, in which one ATPase lobe may undergoes a 180° flip during the catalytic cycle (158). Thus, a high degree of flexibility between the two ATPase lobes may be of functional importance for chromatin remodeling and activity regulation furthermore explaining the substantially different conformations of the ATPase domain observed for distinct remodeling enzymes (Figure 4).

The notion of nucleotide-dependent conformational rearrangements in the ATPase domain was also substantiated by our SAXS measurements on the full-length DmISWI enzyme and the DmISWI$_{\Delta HSS}$ construct (Figure 39). Binding of ADP-BeF$_x$ to DmISWI and DmISWI$_{\Delta HSS}$ decreased the R$_g$ value by 7% and 5%, respectively. These findings collectively imply that the DmISWI enzyme assumes a more compact conformation upon nucleotide analog binding than under apo state conditions with structural rearrangements primarily taking place within the ATPase module. Notably, the full-length Snf2H enzyme exhibited a highly similar conformational response upon ADP-BeF$_x$ binding when compared to the SAXS results of the DmISWI protein (Figure 39). Interestingly, a nucleotide-dependent compaction has also been described in the context of the ScIsw2 remodeling enzyme (265). Furthermore, individual remodeling enzymes such as SsoRad54 (158) and ScChd1 (24, 141) have been proposed to sample distinct “open” and “closed” ATPase conformations during the catalytic cycle. It is tempting to speculate that the observed nucleotide-dependent compaction of DmISWI and Snf2H in the present study derives from the reorientation of both ATPase lobes. Thus, ADP-BeF$_x$ may shift the conformational ensemble of the studied ISWI-type remodeling enzymes towards a closed ATPase conformation, in which both ATPase lobes are not splayed apart anymore.

Our developed XL-MS protocol could also be applied to probe the conformational impact of ADP-BeF$_x$ binding on the DmISWI enzyme. However, due to time constraints, XL-MS analyses were not performed for the DmISWI protein in the presence of ADP-BeF$_x$. Taking into consideration that our structural model of the ATPase module of the DmISWI enzyme showed a remarkable model precision under apo state conditions, a comparison of XL-MS data for the DmISWI enzyme in the absence and presence of ADP-BeF$_x$ would be a promising approach to further pinpoint ADP-BeF$_x$-dependent conformational changes in ISWI-type remodeling enzymes.

In overall conclusion, our XL-MS and SAXS data are consistent with ADP-BeF$_x$-dependent conformational changes in the DmISWI and Snf2H proteins. These remodeling enzymes assume a more compact conformation in the presence of the nucleotide analog, which may reflect structural properties of a closed ATPase conformation and potentially involves a substantial reorientation of the ATPase lobes. The homologous DmISWI and Snf2H enzymes appear to respond in a similar manner to ADP-BeF$_x$ and thus may share a common molecular mechanism to reach a state primed for catalysis.

3.4. Structural characteristics of the Snf2H-nucleosome complex

The molecular interactions between chromatin remodeling enzymes and their nucleosomal substrates are of key importance for a large variety of essential cellular processes (82, 240, 241). Shedding light on structural characteristics of enzyme-nucleosome complexes is thought to increase our mechanistic understanding of how the chromatin landscape is remodeled in an ATP-dependent manner. In the present study, we probed the interaction between the ADP-BeF$_x$-bound Snf2H enzyme and 0N40 mononucleosomes using XL-MS analysis in combination with computational modeling. We envisaged that we could delineate the impact of nucleosome binding on the higher-order structure of the Snf2H enzyme by comparing the XL-MS data for the Snf2H-nucleosome complex and ADP-BeF$_x$-bound state from a qualitative and quantitative perspective. Furthermore, we reasoned that this comparison of XL-MS data might provide information about the molecular mechanism related to substrate recognition by ISWI-type remodeling enzymes.

According to EMSA analysis, the chosen conditions to study the structural characteristics of Snf2H-nucleosome complexes by XL-MS analysis resulted in considerable sample heterogeneity. That is, staining of the native PAGE gels by ethidium bromide revealed multiple Snf2H-nucleosome complexes, which differed in the Snf2H to nucleosome stoichiometry (Figure 40 and SFigure 3). I observed that up to three Snf2H molecules may bind to a single nucleosome with higher molecular weight complexes being preferentially formed at a molar excess of the Snf2H enzyme. Our findings from EMSA analysis thus show consistency with previous studies for ISWI-type remodeling enzymes, in which similar sample heterogeneity was detected in the presence of substrate (150, 236, 237). Fluorescence microscopy and spectroscopy experiments on living human cells indicated that the total concentration of all chromatin remodelers in the cell nucleus might be in the 10 µM range (266). Given an average nucleosome concentration of 140 µM in human cells (267), it has been inferred that the predominant bound Snf2H species *in vivo* is monomeric (237). In stark contrast, biophysical measurements on Snf2H (129, 150) and the human ACF complex (136) suggested that these remodelers modulate the chromatin landscape by acting as a dimeric ATPase motor on the nucleosomal substrate. Consequently, it may be important to understand how two Snf2H molecules can bind to a single nucleosome in order to cooperatively slide the substrate along DNA. The observation of $(Snf2H)_3$-nucleosome complexes in the present study could be a structural consequence of an additional Snf2H binding site on the 40 bp flanking DNA as suggested recently (237). Given a dissociation constant of approximately 260 nM for the Snf2H-0N40 complex in the presence of ADP-BeF_x (150), there was likely also a fraction of unbound Snf2H molecules under the employed solution conditions. The possibility of having unbound and complexed Snf2H molecules during chemical cross-linking complicated the structural interpretation of identified inter-domain cross-links for the remodeling enzyme. In particular, the origin of inter-domain cross-links that were identified in the ADP-BeF_x as well as nucleosome-bound state (cf. Table 4) remained ambiguous. I therefore pursued a quantitative cross-linking strategy for these shared inter-domain cross-links to uncover potential nucleosome-dependent conformational changes in the Snf2H enzyme. Interestingly, I found that the formation of cross-links between both ATPase lobes and the HSS domain was consistently less favorable in the nucleosome-bound state than for the ADP-BeF_x-bound state (Figure 43C). This finding may be interpreted as a reorientation of the DNA-binding domain relative to both ATPase lobes upon nucleosome binding, which could be accompanied by partial disruption of the predicted ATPase-HSS interface. Alternatively, the HSS domain may simply be less flexible in the presence of substrate such that the formation of ATPase-HSS cross-links is hampered in the nucleosome-bound state without disruption of the ATPase-HSS interface. The detected inter-molecular cross-links between the Snf2H enzyme and the histone octamer, however, collectively argue against the latter binding scenario. These inter-molecular cross-links exclusively derive from Snf2H-nucleosome complexes and they may only be explained by assuming that the SLIDE region of the HSS domain contacts the core of the nucleosomal substrate in the presence of ADP-BeF_x. Thus, it appears most likely that the ATPase-HSS interface is disrupted in the presence of substrate with Snf2H assuming an overall less compact conformation than in the apo and ADP-BeF_x-bound states.

Importantly, our findings show consistency with recent experimental results by the Narlikar laboratory for the Snf2H remodeling enzyme (28, 129). That is, results from a FRET-based assay, in which the dyes were attached to the end of a single 20 bp flanking DNA and the SLIDE region of the HSS domain, implied that the HSS domain moves away from the well-documented binding site on flanking DNA in a nucleotide-dependent manner (129). Using this approach, Leonard and Narlikar observed that the degree of energy transfer between the donor and acceptor dye was significantly higher in the presence of ADP than ADP-BeF$_x$. Together with thermodynamic data on the Snf2H-nucleosome complex, the authors speculated that the HSS domain is stabilizing the binding of the remodeling enzyme to the nucleosome core prior to the DNA translocation step. The notion of a nucleotide-dependent conformational switch of the HSS domain during the catalytic cycle of the Snf2H enzyme has subsequently been substantiated by XL-MS analysis using the zero-length, carbodiimide-based reagent EDC (28). Cross-links between the HSS domain and the H2A/H2B subunits thereby suggested that the DNA-binding domain binds to the acid patch region of the nucleosome in the presence of ADP-BeF$_x$. In the same study, Gamarra et al. provided experimental evidence for the acidic patch to be involved in the relief of autoinhibition by the NegC and NTR region and that these autoregulatory domains of the Snf2H enzyme also bind to the nucleosome core during the catalytic cycle. Interestingly, the acid patch may also play an important role in the catalysis of other ISWI-type remodeling enzymes (27) as well as the INO80 complex (28). Furthermore, a large variety of unrelated proteins and peptides including Bre1 (268), RCC1 (pdb 3MVD) (269), Sir3 (pdb 3TU4) (270), PRC1 (pdb 4R8P) (271), LANA peptide (pdb 1ZLA) (272), and CENP-C peptide (pdb 4INM) (273) were found to use the acidic patch as a nucleosome anchor.

Notably, our identified inter-molecular cross-links shown in Figure 44B also provide direct evidence for a HSS binding site in close proximity to the acidic patch. As such, our XL-MS data are most consistent with the notion of a translocation-competent Snf2H-nucleosome complex in the presence of ADP-BeF$_x$ as opposed to a DNA length sensing enzyme conformation. Interestingly, binding of the HSS domain to the acid patch may be accompanied by conformational changes within the DNA-binding domain itself. That is, I identified several nucleosome-dependent, intra-domain cross-links that connected distant residues of the SLIDE and HAND regions (Figure 42C). These long-range intra-domain linkages consistently violated the Cα-Cα distance threshold of the BS^3 cross-linker pointing towards the possibility of a bended HSS conformation in the presence of the nucleosomal substrate. Alternatively, these incompatible HSS cross-links may be formed between two nucleosome-bound Snf2H protomers and thus do not reflect binding-induced structural transitions in the HSS domain.

Considering the recent findings by Gamarra *et al.* (28), adjacent interaction sites of the HSS domain and both autoregulatory domains in the nucleosome-bound state may provide an explanation for the unchanged BS^3-H$_4$/-D$_4$ ratio for the studied NTR-HSS and NegC-HSS linkages during quantitative cross-linking (Figure 43C). The enrichment of ATPase lobe 2-NegC cross-links in the presence of substrate points towards a nucleosome-dependent reorientation of the NegC region within the full-length Snf2H enzyme (Figure 43C). The enrichment of these inter-domain cross-links in the nucleosome-bound state could be a consequence of changed steric constraints that favor the formation of covalent linkages between individual residues of ATPase lobe 2 and NegC using the BS^3 cross-linking agent.

Taken together, our XL-MS data are consistent with a translocation-competent Snf2H-nucleosome complex, in which the HSS domain bridges the nucleosome core to contact individual residues of the acidic patch region. The XL-MS-based structural model of the HSS-nucleosome complex (Figure 44B) visualizes a potential binding mode of the DNA-binding domain to the nucleosomal substrate that is largely consistent with the experimental XL-MS data.

3.5. Nucleosome sliding by ISWI-type remodeling enzymes

In the present study, we studied the mechanism of ISWI-type remodeling enzymes across different steady-state conditions using XL-MS and SAXS analyses in combination with computational modeling. Combining our results for the homologous DmISWI and Snf2H proteins with the structural and functional framework for ISWI-type enzymes as well as unrelated chromatin remodelers allows me to propose the following, speculative model of the nucleosome sliding mechanism (Figure 50).

Under apo state conditions (Figure 50A), DmISWI and Snf2H appear to assume a resting conformation in solution with catalytically important motifs of both ATPase lobes being twisted towards opposite directions. The proposed arrangement of ATPase lobes provides a structure-based explanation for the repressed basal ATPase activity of DmISWI (140). The autoregulatory NTR and NegC domains thereby keep the remodeling enzymes in a catalytically incompetent state by bridging the ATPase lobe-lobe interface. In addition, the HSS domain packs against the catalytic core to form an overall compact enzyme conformation with the very N- and C-termini of ISWI-type remodelers being in close spatial proximity to each other.

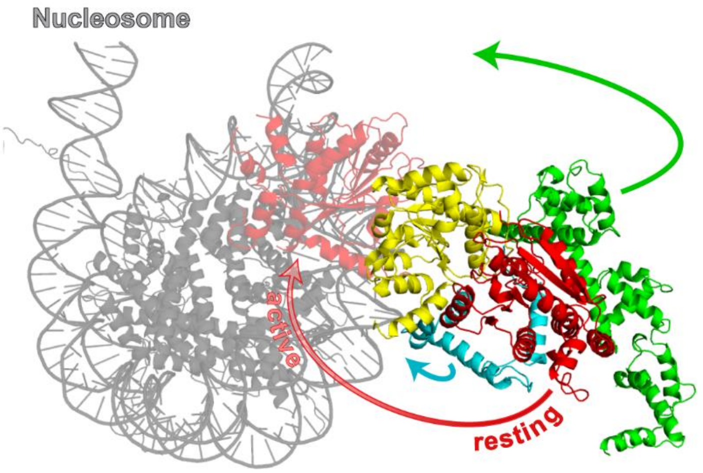

Figure 49: Proposed binding mode of ISWI-type remodeling enzymes to nucleosomes. The DmISWI enzyme assumes a compact resting conformation under apo state conditions. The NTR (cyan, pdb 5JXR) (146) and HSS domain (green) thereby pack against ATPase lobe 1 (yellow) and ATPase lobe 2 (dark red). This representative DmISWI model may bind to the nucleosome (grey, adapted from pdb 5O9G) *via* ATPase lobe 1. A series of conformational changes are expected to take place upon docking to the nucleosomal substrate (indicated by arrows) to reach a similar enzyme-nucleosome state as observed for the nucleosome-bound ScChd1 structure (pdb 5O9G) (24). The ATPase domain of the ScChd1 structure was aligned with our representative DmISWI model on ATPase lobe 1 with ATPase lobe 2 of the ScChd1 enzyme being colored in light red. The Figure was adapted and reprinted from (1) in accordance with Elsevier’s policies.

How does the remodeling enzyme become catalytically active? Our representative model of the resting DmISWI enzyme could theoretically bind the nucleosome at SHL +2 via ATPase lobe 1 without causing a direct steric clash with the substrate or relying on a prior conformational change (Figure 49). ATPase lobe 2 is expected to rotate relative to lobe 1 in order to reach its binding site on the nucleosomal substrate (Figure 49, red arrow) and to align the conserved structural motifs for efficient ATP binding and hydrolysis. The active site of the ATPase in DmISWI and Snf2H may share many structural features with the nucleosome-bound ScSnf2 (pdb 5X0Y) (21) and ScChd1 (pdb 5O9G) (24) structures, which are partially shown and aligned in Figure 46A. Our quantitative XL-MS data suggest that the interface between the ATPase and HSS domains disrupts in the presence of the nucleosomal substrate. As a consequence, the DNA binding site on the HSS domain may no longer be occupied such that it can bind to flanking DNA (Figure 49, green arrow) (23, 129, 151) giving rise to a DNA length sensing state (Figure 50B). Recognition of flanking DNA by the HSS domain likely represents the molecular basis to form evenly spaced nucleosomal arrays (22, 84, 259), which is followed by several conformational changes that facilitate the formation of a DNA translocation-competent enzyme-nucleosome complex (Figure 50C). That is, our identified inter-molecular cross-links between the Snf2H enzyme and the histone octamer (Figure 44B) as well as recent experimental findings by the Narlikar laboratory (28, 129) are consistent with the notion that the HSS domain is released from flanking DNA and that it binds to the nucleosome core in a nucleotide-dependent manner. While it is possible that binding of the HSS domain to the nucleosome core assists in stabilizing the translocation-competent enzyme-nucleosome complex (129), the mechanistic significance of this interaction with regard to DNA translocation remains to be further elucidated. Relief of autoinhibition by the NTR and NegC in the translocation-competent complex is presumably achieved by direct interactions of these regulatory domains with the acidic patch of the nucleosome core (28). Notably, the herein identified nucleosome-dependent, inter-domain cross-links for the NTR and NegC region (Table 5) are supportive of substrate-induced conformational changes in these domains for the Snf2H remodeling enzyme. Furthermore, it has been demonstrated that the basic patch of the H4 tail (not indicated in Figure 50) represents an important nucleosomal epitope for ISWI-type remodelers during the catalytic cycle (71, 114, 159). The underlying molecular mechanisms that confer maximal remodeling activity upon engagement of the H4 tail (124, 125), however, remain largely elusive taking into account recent experimental findings that argue against overlapping AutoN and H4 tail binding sites on ATPase lobe 2 (115, 146). Alternating switching between the DNA length sensing and the translocation-competent states allows ISWI-type remodeling enzymes to move nucleosomes relative to DNA by one (138) or more (28, 136) base pairs per catalytic cycle in an ATP-dependent manner (28, 129). The coupling of ATP hydrolysis to DNA translocation as well as the fundamental principles of the actual sliding reaction, however, are poorly understood.

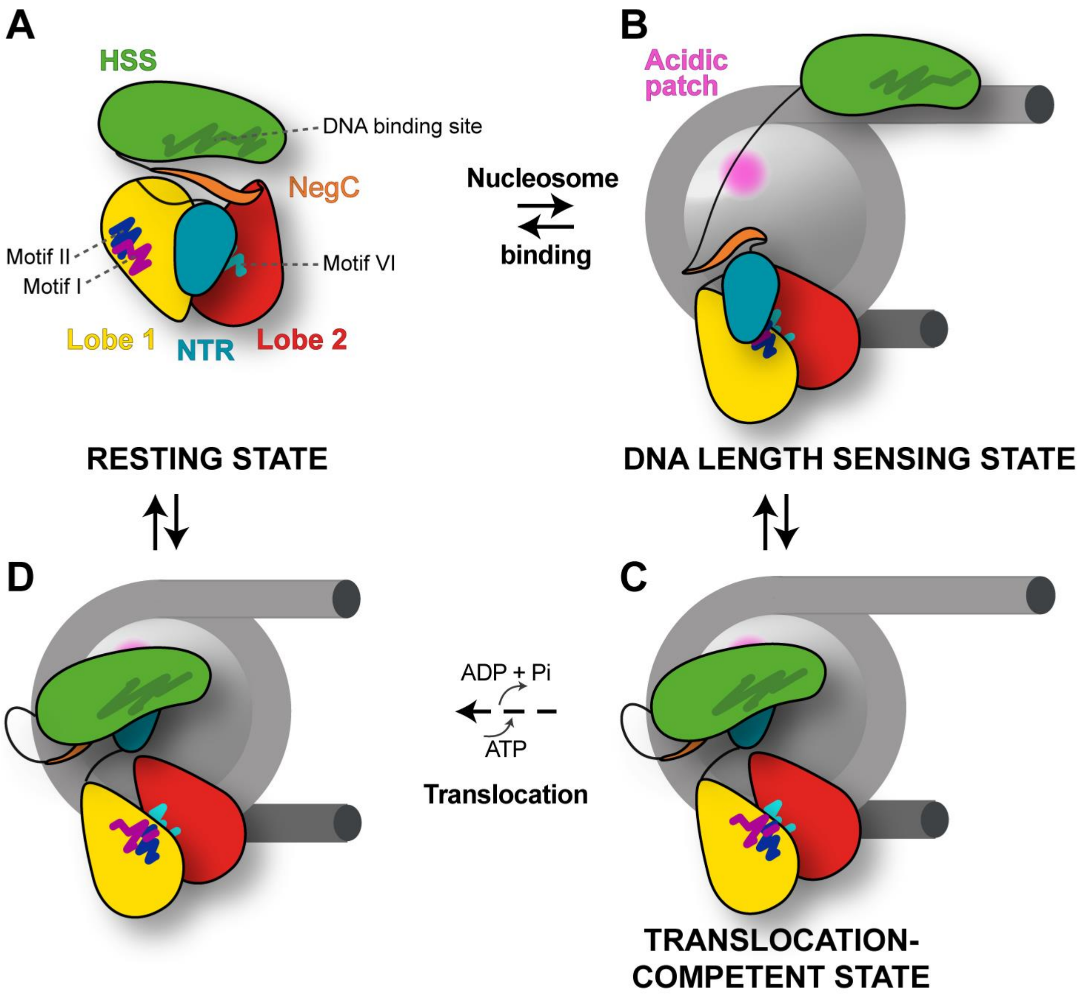

Figure 50: Model of nucleosome sliding by ISWI-type enzymes. **(A)** ISWI-type enzymes assume a compact resting conformation under apo state conditions with accessory domains packing against the ATPase domain. Motifs involved in ATP binding and hydrolysis are twisted towards opposite directions. **(B)** Several conformational changes are predicted upon nucleosome binding to reach a DNA length sensing state of the enzyme-nucleosome complex. These structural rearrangements include the reorientation of the ATPase domain as well as disruption of the HSS-ATPase domain such that the HSS domain can bind to flanking DNA (23, 129, 151). The NTR and NegC domains inhibit DNA translocation by the ATPase domain. **(C)** The DNA length sensing state is in equilibrium with the translocation-competent state (28). In this active enzyme-nucleosome configuration, the HSS domain binds to the nucleosome core and autoinhibition by NegC and NTR is relieved due to direct interaction of these autoregulatory domains with the acidic patch. Furthermore, the H4 tail (not indicated in the model) binds to ATPase lobe 2 (115, 146). **(D)** The nucleosome is moved relative to DNA in the translocation-competent state in an ATP-dependent manner.

3.6. Future perspectives

Despite groundbreaking achievements in establishing a structural and functional framework for chromatin remodeling enzymes, the underlying molecular mechanism by which the chromatin landscape is modulated by these proteins have remained elusive. The mechanism of action of ISWI-type remodelers appears to rely on a series of complex conformational changes that are difficult to capture by traditional structure determination techniques such as X-ray crystallography and NMR spectroscopy. In the present thesis, I probed the conformation of the prototypical DmISWI and Snf2H enzymes across different steady-state conditions using an integrative structural approach that combines XL-MS and SAXS analyses with computational modeling. Our findings for Snf2H and DmISWI provide valuable information about the structural architecture and conformational response of these remodeling enzymes to substrate and ADP-BeF$_x$ binding in a near-native environment. The obtained structural models for DmISWI and Snf2H resulted in several work hypotheses for the catalytic cycle of ISWI-type enzymes, which invite future investigations. In particular, it will be important to validate the herein proposed domain interfaces for the studied remodeling enzymes and to better understand the sequence of conformational rearrangements and the underlying allosteric couplings in the enzyme-nucleosome complex that facilitate chromatin remodeling.

To validate and/or refine our structural models for DmISWI and Snf2H, it might be beneficial to pursue an UV-based cross-linking strategy. The site-specific incorporation of Bpa at strategically favorable positions may not only result in additional, shorter distance restraints that can be used to guide computational modeling but also allows the interrogation of the current DmISWI and Snf2H models. Furthermore, it would be desirable to develop a modeling algorithm that can deal with distance restraints that derive from co-existing conformations in solution. Alternatively, one could consider finding solution conditions under which the sample heterogeneity is minimized.

Hydrogen/deuterium exchange mass spectrometry (HDX-MS) could represent a promising, complementary biophysical approach to probe the higher-order structure and dynamics of ISWI-type remodeling enzymes as well as their interactions with nucleosomes under near-native conditions in solution. The exchange of hydrogen to deuterium of backbone amides in a protein is critically dependent on the hydrogen bonding status with exchange rates being significantly slower when the amide hydrogens engage in a stable inter- or intra-molecular hydrogen bond (274-276). The target protein(s) are typically diluted into deuterated buffer and labeled for distinct time intervals. The exchange reaction is subsequently quenched, the sample subjected to proteolysis, and the deuterium uptake for individual protein regions determined by LC-MS analysis (277). As such, the HDX-MS technique has proven useful to map binding interfaces and to identify and characterize functionally important allosteric couplings within the target protein(s) (278-280). In particular, the potential of the HDX-MS approach to uncover allosteric couplings could be interesting in order to better understand how the chromatin landscape is remodeled in ATP-dependent manner by ISWI-type remodeling enzymes.

4. Materials and Methods

4.1. Materials

4.1.1. Technical devices

Table 6: Technical devices used in this study.

Description	Manufacturer
Centrifuge rotor, SW 41 Ti	Beckman Coulter
Centrifuge rotors, Sorvall SLA3000 and SS34	ThermoFisher Scientific
Centrifuge, Eppendorf 5417C	Eppendorf
Centrifuges, Sorvall RC 6 Plus, Heraeus Megafuge 2.0, Heraeus Multifuge X3R	ThermoFisher Scientific
Fluorescent Image Analyzer, FLA-3000	Fujifilm
FPLC systems ÄKTA FPLC, ÄKTApurifier, and ÄKTA Pure	GE Healthcare Life Sciences
French Pressure Cell Press, Model FA-078	Thermo Spectronic
Gel imaging system, ChemiDoc	Bio-Rad Laboratories
Gradient Master	BioComp
HPLC systems, UltiMate 3000 and RSLCnano	ThermoFisher Scientific
Incubator shaker, HT Multitron	Infors
Incubator shaker, New Brunswick Innova	Eppendorf
Lyophilizer Alpha 1–2 and connected pump RZ 2.5	Christ; Vacuubrand
Mass spectrometer, LTQ-Orbitrap XL and Q-Exactive HF	ThermoFisher Scientific
Microfluidizer, LM10	Microfluidics
Peristaltic pump, MINIPULS Evolution	Gilson
Sonicator, Sonifier S-250 D digital	Branson Ultrasonics
Spectralphotometer, PowerWave HT	BioTek
Thermocycler, Applied Biosystems 2720 Thermal Cycler	ThermoFisher Scientific
Thermomixer comfort	Eppendorf
Ultracentrifuge, Optima MAX-XP	Beckman Coulter
UV lamp	Ultra Violet Products
UV-Crosslinker, Bio-Link 365	Vilber
UV-Vis Spectrophotometer, NanoDrop ND1000	Peqlab Biotechnologie GmbH
UV-Vis Spectrophotometer, Ultrospec 2000	Pharmacia Biotech
Vacuum centrifuge, Concentrator Plus	Eppendorf
Whatman Elutrap electroelution system	GE Healthcare

4.1.2. Chemicals and Consumables

Table 7: Chemicals and consumables used in this study.

Description	Manufacturer
[γ-^{32}P]ATP	PerkinElmer
384 well plate	Greiner Bio One International GmbH
Acetic acid	Promega
Acetone	Merck
ACN	Carl Roth GmbH & Co
Acrylamide/bisacrylamide solution, Rotiphorese Gel 30 (37.5:1)	Carl Roth GmbH & Co
ADP	Merck
Agarose	Bio&SELL GmbH
Amicon Ultra-4 centrifugal filter units, 10 and 30 kDa MWCO	Merck Millipore
Ampicillin	Carl Roth GmbH & Co
AMP-PNP	Merck
Aprotinin	Genaxxon Bioscience
APS	Sigma
ATP	Merck
Benzonase	Merck Millipore
Bpa	Bachem
Bromophenol blue	Merck
BS^{2}G-H$_{4}$/D$_{4}$	ProteoChem
BS^{3}-H$_{4}$/D$_{4}$	ProteoChem
BSA	Merck
Chloramphenicol	Carl Roth GmbH & Co
Complete Protease Inhibitor Cocktail tablet	Roche Diagnostics GmbH
Coomassie Brilliant Blue R	Merck
DMSO	Merck
DTT	Carl Roth GmbH & Co
EDTA	Merck
Ethanol	Carl Roth GmbH & Co
Ethidium bromide	Merck
Formic acid	Merck
Glycerol	VWR
Guanidine hydrochloride	Merck
Hepes	Serva Electrophoresis GmbH
HisTrap HP column, 1 and 5 mL	GE Healthcare
HiTrap Q HP column, 5 mL	GE Healthcare
HiTrap SP column, 5 mL	GE Healthcare
HPF Millex syringe filter	Merck Millipore
IAA	Merck
Igepal CA-630	Merck
Imidazole	Carl Roth GmbH & Co
IPTG	Carl Roth GmbH & Co
KCl	Merck
KOAc	Merck

** continues next page **

LB agar	Serva Electrophoresis GmbH
Leupeptin	Genaxxon Bioscience
LiCl	Merck
L-lysine–HCl	Merck
$Mg(OAc)_2$	Merck
$MgCl_2$	VWR
Mono Q 5/50 GL column	GE Healthcare
Mono S 5/50 GL column	GE Healthcare
MultiScreen HTS plate, 96 well	Merck Millipore
NaCl	ThermoFisher Scientific
NADH	Merck
NaH_2PO_4	VWR
NaOAc	VWR
NH_4HCO_3	Merck
OMIX C18 pipette tip, 10–100 µL	Agilent Technologies
PEG 8000	Promega
Pepstatin	Genaxxon Bioscience
PMSF	Genaxxon Bioscience GmbH
Polypropylene tube, 14 x 89 mm	Beckman Coulter
SDS-PAGE gel, NuPAGE Bis-Tris Protein Gel, 10%, 12%, and 4-16%	Invitrogen
ReproSil-Pur C18-AQ 2.4 µm	Dr. Maisch GmbH
Rotilabo-syringe filter, 0.2 and 0.45 µm	Carl Roth GmbH & Co
Salmon sperm DNA	ThermoFisher Scientific
SDS	Serva Electrophoresis GmbH
Sep-Pak tC18 cartridge	Waters
Slide-A-Lyzer MINI dialysis device, 7000 Da MWCO	ThermoFisher Scientific
Spectra/Por dialysis tubing, 3500, 7000, and 6000–8000 Da MWCO	Spectrum
Superdex 200 10/300 GL column	GE Healthcare
Superdex 200 HiLoad 16/60 column	GE Healthcare
Superdex 200 Increase 10/300 GL column	GE Healthcare
Superdex Peptide PC 3.2/300 column	GE Healthcare
TCA	Merck
TEMED	Carl Roth GmbH & Co
TFA	Merck
Thiourea	Merck
TLC PEI cellulose F plate	Merck Millipore
Tris	Diagonal GmbH & Co. KG
Triton X-100	Merck
Trypton	BD Biosciences
Tween 20	Merck
Urea	Merck
Yeast extract	BD Biosciences

4.1.3. Enzymes, Kits and Markers

Table 8: Enzymes, kits and markers used in this study.

Description	Manufacturer
1 kb ladder	New England BioLabs
100 bp ladder	New England BioLabs
dNTP mix	New England BioLabs
DpnI	New England BioLabs
Lactate dehydrogenase	Merck
NucleoSpin Plasmid EasyPure	Macherey-Nagel GmbH & Co
peqGOLD protein marker IV	VWR
peqGOLD protein marker V	VWR
Phosphoenolpyruvate	Molekula
Phusion High-Fidelity DNA polymerase with 5x HF reaction buffer	New England BioLabs
Plasmid Mini, Midi, and Giga Kit	Qiagen
Pyruvate kinase	Merck
SmaI with 5x Buffer 4	New England BioLabs
T5 exonuclease	New England BioLabs
Taq ligase	New England BioLabs
Trypsin, Sequencing Grad Modified, with Trypsin Respuspension Buffer	Promega

4.1.4. Bacterial strains

Table 9: *E. coli* strains used in this study.

Strain	Manufacturer
BL21-Gold(DE3)	Agilent Technologies
Rosetta^{TM} 2(DE3)	Merck
DH5α	NEB 5-alpha, New England BioLabs

4.1.5. Plasmids

Table 10: Plasmids used in this study.

Name	Encoded sequence	Origin	Vector	Tag
pFMP210	ISWI 1−1027; full-length	Drosophila	pProExHT	His$_6$-TEV
pFMP383	ISWI; full-length K337D	Drosophila	pProExHT	His$_6$-TEV
pFMP384	ISWI; full-length D485K	Drosophila	pProExHT	His$_6$-TEV
pFMP386	ISWI; full-length K337D D485K	Drosophila	pProExHT	His$_6$-TEV
pFMP163	ISWI full-length with TAG amber codon at amino acid position 578	Drosophila	pProEX-Htb	His$_6$-TEV
pFMP302	Snf2H 1−1052; full-length	Human	pBH4	His$_6$-TEV
pFMP375	ISWI 691−1027	Drosophila	pProEX-Htb	His$_6$-TEV

** continues next page **

pFMP153	Suppressor tRNA and synthetic tRNA synthetase for genetically encoding Bpa			His$_6$-TEV
pFMP114	ISWI 26−648	Drosophila	pProEX-Htb	His$_6$-TEV
pFMP128	Histone H2A	Drosophila, codon optimized	pET15b	none
pFMP129	Histone H2B	Drosophila, codon optimized	pET15b	none
pFMP186	Histone H3	Drosophila	pET3c	none
pFMP187	Histone H4	Drosophila	pET3c	none
pFMP151	187 bp Widom 601 derivative		pUC18	none
pFMP109	147 bp Widom 601 derivative		pT7blue3	none

4.1.6. Oligonucleotides

Table 11: Oligonucleotides used in this study.

Name	5‘-3‘ Sequence	Usage
oFMP219	TGGATGATTTCGCTTTACGA	Forward primer, sequencing of pFMP210/383/384/386/114
oFMP220	GACGAATGGTTCAACACGAA	Forward primer, sequencing of pFMP210/383/384/386/114
oFMP221	GAATTTAACATGGACAACAGCG	Forward primer, sequencing of pFMP210/383/384/386
oFMP222	CAATTCGAGGGTGAGGATTG	Forward primer, sequencing of pFMP210/383/384/386
oFMP223	GATGCACTGAGTTGCAGGAT	Forward primer, sequencing of pFMP210/383/384/386/375
oFMP224	CAGAGATATGGTCTGCAGGG	Reverse primer, sequencing of pFMP210/383/384/386
oFMP709	GACCGCTAATCGTCTACTTATCAC	Forward primer, sequencing of pFMP386
oFMP742	GTGCTGGACCCTTTCCTGCTCCGTCGTC	Forward primer, point mutation in full-length DmISWI K337D: AAA to GAC
oFMP743	CAGGAAAGGGTCCAGCACGGCATGCAAAC	Reverse primer, point mutation in full-length DmISWI K337D: AAA to GAC
oFMP744	CACGAAAAGCGTAACAGGCAGATTCAGGAA	Forward primer, point mutation in full-length DmISWI D485K: GAT to AAG
oFMP745	CCTGTTACGCTTTTCGTGCGGCGTCTGA	Reverse primer, point mutation in full-length DmISWI D485K: GAT to AAG

4.1.7. Buffers and solutions

Table 12: Buffers and solutions. All buffers and solutions used for FPLC analysis were sterile filtered.

Buffer/solution name	Composition	Usage (section)
0.5x TBE	4.5 mM Tris-HCl (pH 8.3), 45 mM boric acid, 0.1 mM EDTA (pH 8.0)	Agarose gel electrophoresis (4.2.1.5)
1x TAE	40 mM Tris-HCl (pH 8.0), 20 mM acetic acid, 1 mM EDTA (pH 8.0)	Agarose gel electrophoresis (4.2.1.5)
5x Laemmli loading	250 mM Tris-HCl (pH 6.8), 10% (w/v) SDS, 0.1% (w/v) bromophenol blue, 50% (v/v) glycerol, 0.5 M DTT	SDS-PAGE analysis (4.2.1.7)
ATPase assay	25 mM Hepes-KOH (pH 7.6), 3 mM $MgCl_2$, 0.1 mM EDTA (pH 8.0), 10% (v/v) glycerol, 50 mM NaCl, 0.2 mg/mL BSA	NADH-coupled ATPase assay (4.2.7.2.2)
Coomassie Blue staining	0.1% (w/v) Coomassie Brilliant Blue R, 50% (v/v) ethanol, 10% (v/v) acetic acid	SDS-PAGE analysis (4.2.1.7)
c-XL #1	25 mM Hepes-KOH (pH 7.6), 0.1 mM EDTA (pH 8.0), 10% (v/v) glycerol, 100 mM KOAc, 1.5 mM $MgCl_2$, 2 mM DTT	Chemical cross-linking (4.2.4.1.2)
c-XL #2	25mM Hepes-KOH (pH 7.6), 210 mM KCl, 10% (v/v) glycerol, 1 mM $MgCl_2$, 1 mM DTT	Chemical cross-linking (4.2.4.1.2)
c-XL #3	20 mM Hepes-KOH (pH 8.3)	Chemical cross-linking (4.2.4.1.2)
c-XL #4	25 mM Hepes-KOH (pH 7.6), 1 mM $MgCl_2$, 0.1 mM EDTA (pH 8.0), 10% (v/v) glycerol, 50 mM NaCl, 1 mM DTT	Chemical cross-linking (4.2.4.1.2)
c-XL #5	15 mM Hepes-KOH (pH 7.6), 4% (v/v) glycerol, 70 mM KCl, 1.5 mM $MgCl_2$, 1 mM DTT	Chemical cross-linking (4.2.4.1.2)
EMSA #1	15 mM Hepes-KOH (pH 7.6), 0.1 mM EDTA (pH 8.0), 10% (v/v) glycerol, 70 mM KCl, 0.5 mM $MgCl_2$, 1 mM DTT	EMSA (4.2.7.1)
EMSA #2	15 mM Hepes-KOH (pH 7.6), 0.1 mM EDTA (pH 8.0), 10% (v/v) glycerol, 70 mM KCl, 0.5 mM $MgCl_2$, 0.1 mg/mL BSA, 1 mM DTT	EMSA (4.2.7.1)
EMSA #3	15 mM Hepes-KOH (pH 7.6), 0.1 mM EDTA (pH 8.0), 10% (v/v) glycerol, 70 mM KCl, 0.5 mM $MgCl_2$, 5% (w/v) sucrose, 1 mM DTT	EMSA (4.2.7.1)
EMSA #4	15 mM Hepes-KOH (pH 7.6), 4% (v/v) glycerol, 70 mM KCl, 1 mM $MgCl_2$, 1 mM DTT	EMSA (4.2.7.1)
EMSA #5	15 mM Hepes-KOH (pH 7.6), 4% (v/v) glycerol, 70 mM KCl, 1 mM $MgCl_2$, 0.02% (v/v) Igepal CA-630, 1 mM DTT	EMSA (4.2.7.1)

** continues next page **

Histone Q-A	15 mM Tris-KOH (pH 8.0)	Purification of histones, RHP protocol (4.2.2.4.2)
Histone Q-B	15 mM Tris-KOH (pH 8.0), 2 M NaCl	Purification of histones, RHP protocol (4.2.2.4.2)
Histone-unfolding	7 M guanidine-HCl, 20 mM Tris-HCl (pH 7.5), 10 mM DTT	Purification of histones, IBP protocol (4.2.2.4.1)
Histone-wash	50 mM Tris-HCl (pH 7.5), 100 mM NaCl, 1 mM EDTA (pH 8.0), 5 mM DTT, 0.2 mM PMSF	Purification of histones, IBP protocol (4.2.2.4.1)
HSS-Dialysis	20 mM Tris-HCl (pH 7.6), 500 mM NaCl, 20 mM imidazole (pH 7.4)	Purification of HSS$_{ISWI}$ (4.2.2.2.4)
HSS-NiA	20 mM Tris-HCl (pH 7.6), 500 mM NaCl	Purification of HSS$_{ISWI}$ (4.2.2.2.4)
HSS-NiB	20 mM Tris-HCl (pH 7.6), 500 mM NaCl, 500 mM imidazole (pH 7.4)	Purification of HSS$_{ISWI}$ (4.2.2.2.4)
HSS-SEC	20 mM Tris-HCl (pH 7.4), 500 mM NaCl	Purification of HSS$_{ISWI}$ (4.2.2.2.4)
ISWI dialysis	150 mM NaCl, 15 mM Tris-HCl (pH 7.4), 1 mM DTT	Purification of ISW$_{WT}$, ISWI$_{K337D}$, ISWI$_{D485K}$, ISWI$_{K337D\ D485K}$, (4.2.2.2.1); ISWI$_{M578B}$ (4.2.2.2.2)
ISWI His-A	50 mM Tris-HCl (pH 7.4), 300 mM NaCl	Purification of ISW$_{WT}$, ISWI$_{K337D}$, ISWI$_{D485K}$, ISWI$_{K337D\ D485K}$, (4.2.2.2.1); ISWI$_{M578B}$ (4.2.2.2.2)
ISWI His-B	50 mM Tris-HCl (pH 7.4), 300 mM NaCl, 400 mM imidazole (pH 7.4)	Purification of ISW$_{WT}$, ISWI$_{K337D}$, ISWI$_{D485K}$, ISWI$_{K337D\ D485K}$, (4.2.2.2.1); ISWI$_{M578B}$ (4.2.2.2.2)
ISWI MonoS-A	15 mM Tris-HCl (pH 7.4), 1 mM DTT	Purification of ISW$_{WT}$, ISWI$_{K337D}$, ISWI$_{D485K}$, ISWI$_{K337D\ D485K}$ (4.2.2.2.1)
ISWI MonoS-B	15 mM Tris-HCl (pH 7.4), 2 M NaCl, 1 mM DTT	Purification of ISW$_{WT}$, ISWI$_{K337D}$, ISWI$_{D485K}$, ISWI$_{K337D\ D485K}$ (4.2.2.2.1)
ISWI SEC	50 mM Hepes-KOH (pH 7.6), 0.2 mM EDTA (pH 8.0), 200 mM KOAc, 1 mM DTT	Purification of ISW$_{WT}$, ISWI$_{K337D}$, ISWI$_{D485K}$, ISWI$_{K337D\ D485K}$, (4.2.2.2.1); ISWI$_{M578B}$ (4.2.2.2.2)
ISWI ΔHSS Lysis	50 mM Tris-HCl (pH 7.4), 300 mM NaCl	Purification of ISWI$_{\Delta HSS}$ (4.2.2.2.3)
ISWI ΔHSS SEC	20 mM Hepes-KOH (pH 7.6), 200 mM KCl, 0.2 mM EDTA (pH 8.0), 1 mM DTT	Purification of ISWI$_{\Delta HSS}$ (4.2.2.2.3)
ISWI ΔHSS-A	25 mM Tris-HCl (pH 7.4), 130 mM KOAc, 0.06% (v/v) Tween 20, 10% (v/v) glycerol	Purification of ISWI$_{\Delta HSS}$ (4.2.2.2.3)
ISWI ΔHSS-B	25 mM Tris-HCl (pH 7.4), 130 mM KOAc, 0.06% (v/v)Tween 20, 10% (v/v) glycerol, 400 mM imidazole (pH 7.4)	Purification of ISWI$_{\Delta HSS}$ (4.2.2.2.3)
LB medium	10 g/L trypton, 5 g/L yeast extract, 10 g/L NaCl	Cultivation of *E. coli* cells (4.2.1.3)
LB medium, rich	20 g/L trypton, 10 g/L yeast extract, 10 g/L NaCl	Expression of Snf2H in *E. coli* cells (4.2.2.1)
Mononuc-0	20 mM Tris-HCl (pH 7.7), 0.1 mM, EDTA (pH 8.0), 1 mM DTT	Nucleosome reconstitution (4.2.3.3)

** continues next page **

Mononuc-2000	20 mM Tris-HCl (pH 7.7), 0.1 mM EDTA (pH 8.0), 2M KCl, 1 mM DTT	Nucleosome reconstitution (4.2.3.3)
Nucleosome binding	15 mM Hepes-KOH (pH 7.6), 70 mM KCl, 4% (v/v) glycerol, 1 mM $MgCl_2$, 1 mM DTT	Enzyme-nucleosome complex formation (4.2.3.3); EMSA (4.2.7.1)
Octamer refolding	2M NaCl, 10 mM Tris-HCl (pH 7.5), 1 mM EDTA (pH 8.0), 1 mM DTT	Octamer reconstitution (4.2.3.2)
Octamer unfolding	7 M guanidine-HCl, 20 mM Tris-HCl (pH 7.5), 10 mM DTT	Octamer reconstitution (4.2.3.2)
SAU	7.5 M Urea, 40 mM NaOAc (pH 5.2), 1 mM EDTA (pH 8.0), 10 mM L-lysine–HCl, 5 mM DTT	Purification of histones, IBP and RHP protocol (4.2.2.4)
SAXS	50 mM Hepes-KOH (pH 7.6), 1.5 mM $Mg(OAc)_2$, 0.2 mM KOAc, 10% (v/v) glycerol, 1 mM DTT	Preparation of proteins for SAXS measurements (4.2.5.1)
SDS-PAGE fixing	10% (v/v) acetic acid, 50% (v/v) ethanol	SDS-PAGE analysis (4.2.1.7)
SDS-PAGE running	25 mM Tris-HCl (pH 6.8), 192 mM glycine, 0.1% (w/v) SDS	SDS-PAGE analysis (4.2.1.7)
SEC mobile phase	70% (v/v) water, 30% (v/v) acetonitrile, 0.1% (v/v) TFA	Enrichment of tryptic peptides (4.2.4.3)
Snf2H Elution	25 mM Hepes-HCl (pH 7.0), 300 mM KCl, 400 mM imidazole (pH 7.4), 1 mM DTT	Purification of Snf2H (4.2.2.3)
Snf2H Lysis	25 mM Hepes-KOH (pH 8.0), 300 mM KCl, 7.5 mM imidazole (pH 7.4), 10% (v/v) glycerol, 1 mM DTT	Purification of Snf2H (4.2.2.3)
Snf2H-SEC	25 mM Hepes-KOH (pH 7.5), 300 mM KCl, 1 mM DTT	Purification of Snf2H (4.2.2.3)
Snf2H-storage	25 mM Hepes-KOH (pH 7.5), 210 mM KCl, 15% (v/v) glycerol, 1 mM DTT	Purification of Snf2H (4.2.2.3)
SPE elution	50% (v/v) water, 50% (v/v) acetonitrile, 0.1% (v/v) formic acid	Solid-phase extraction of tryptic peptides (4.2.4.3)
SPE wash	95% (v/v) water, 5% (v/v) acetonitrile, 0.1% (v/v) formic acid	Solid-phase extraction of tryptic peptides (4.2.4.3)
TE	10 mM Tris-KOH (pH 8.0), 0.1 mM EDTA (pH 8.0)	Preparation of DNA fragments (4.2.3.1)
TLC developer	0.3 M NaH_2PO_4, 1 M LiCl	TLC-based ATPase assay (4.2.7.2.1)
TLC quench	2 mM EDTA (pH 8.0), 1 M LiCl, 0.3 M NaH_2PO_4	TLC-based ATPase assay (4.2.7.2.1)
TLC reaction	25 mM Hepes-KOH (pH 7.6), 1.5 mM $Mg(OAc)_2$, 0.1 mM EDTA (pH 8.0), 10% (v/v) glycerol, 100 mM KOAc, 0.2 g/L BSA, 1 mM DTT	TLC-based ATPase assay (4.2.7.2.1)
Urea loading	9 M urea, 25 mM Tris-HCl (pH 6.8), 1% (w/v) SDS, 1 mM EDTA (pH 8.0), 0.02% (w/v) bromophenol blue, 100 mM DTT	SDS-PAGE analysis (4.2.1.7)
UV-XL	25 mM Hepes-KOH (pH 7.6), 0.1 mM EDTA (pH 8.0), 10% (v/v) glycerol, 100 mM KOAc, 1.5 mM $MgCl_2$, 1 mM DTT	UV cross-linking (4.2.4.1.1)

* *continues next page* *

UZ-10% glycerol	20 mM Hepes-KOH (pH 7.4), 0.005% (v/v) Igepal CA-630, 0.1 mM EDTA (pH 8.0), 10% (v/v) glycerol	Nucleosome reconstitution (4.2.3.3)
UZ-30% glycerol	20 mM Hepes-KOH (pH 7.4), 0.005% (v/v) Igepal CA-630, 0.1 mM EDTA (pH 8.0), 30% (v/v) glycerol	Nucleosome reconstitution (4.2.3.3)
XL-denaturation	6 M urea, 2 M thiourea, 10 mM Hepes-KOH (pH 8.0), 200 mM NH_4HCO_3	In-solution tryptic digestion (4.2.4.2.2)

4.2. Methods

4.2.1. Molecular biology methods

4.2.1.1. Cloning of ISWI constructs

Point mutations were introduced into DmISWI$_{WT}$ (i.e., ISWI$_{K337D}$, ISWI$_{D485K}$, and ISWI$_{K337D\ D485K}$) using the Gibson assembly cloning method (281).

Each polymerase chain reaction (PCR) sample comprised the following components: 50 ng of the template plasmid (pFMP210, pFMP383 or pFMP384, cf. Table 10), 5 µL of 5x HF reaction buffer, 0.5 µL of 10 mM deoxynucleotide triphosphates (dNTPs) solution mix, 1.3 µL of 10 µM forward and reverse primers (cf. Table 11), and 0.5 µL of 2 U/µL Phusion High-Fidelity DNA polymerase. The components were mixed on ice and the volume of the reaction mixture adjusted to 25 µL with H_2O. The PCR was performed using a thermocycler and relied on the following thermal cycling protocol: Initialization at 98 °C for 3 min followed by 25 cycles of DNA denaturation (98 °C for 30 s), primer annealing (63 °C for 30 s), and DNA elongation (72 °C for 120 s).

To digest the parental plasmid, 1 µL of the DpnI restriction enzyme (10 U/µL) was added to the PCR product and the sample was incubated at 37 °C for 1 h. The restriction enzyme was subsequently inactivated by heat (80 °C for 20 min).

The assembly of amplified DNA fragments was initiated by mixing 5 µL of the digested PCR product with 15 µL of the Gibson master mix [117 mM Tris-HCl (pH 7.5), 6.5% (v/v) polyethylene glycol (PEG) 8000, 13 mM $MgCl_2$, 13 mM DTT, 0.26 mM dNTPs, 1.3 mM nicotinamide adenine dinucleotide (NAD), 0.005 U/µL T5 exonuclease, 0.033 U/µL Phusion polymerase, and 5.3 U/µL Taq ligase]. Following incubation of the reaction mixture at 50 °C for 1 h, the assembled DNA was transformed into competent *E. coli* cells (cf. section 4.2.1.2) and the sequence verified by DNA sequencing (cf. section 4.2.1.4).

4.2.1.2. Transformation in *E. coli*

The competent *E. coli* strains BL21-Gold(DE3), Rosetta^{TM} 2(DE3) or DH5α (cf. Table 9) were transformed with plasmid DNA using the heat shock method (282). That is, approximately 100 µL *E. coli* cells were thawed on ice and 40−100 ng of purified plasmid DNA was added. After 10 min of incubation on ice, the *E. coli* cells were heat shocked at 42 °C for 45 s and the suspension was immediately placed back on ice for another 10 min. Following addition of 1 mL lysogeny broth (LB) medium (cf. Table 12), the cell suspension was incubated at 37 °C for 10 to 60 min under gentle shaking (600 rpm, Thermomixer comfort). In a last step, the *E. coli* cells were plated on LB agar plates containing the appropriate antibiotics for the plasmid vector (cf. section 4.2.1.3).

4.2.1.3. Culture of *E. coli*

The different *E. coli* strains were grown at 37 °C either on LB agar plates [1.5% (w/v) LB agar] or in liquid LB medium (cf. Table 12) under constant shaking. The LB agar plates and the LB medium were supplemented with 100 µg/mL ampicillin and/or 34 µg/mL chloramphenicol depending on the plasmid vector. In the case of the ISWI$_{M578B}$ construct, the transformed bacteria culture was grown in LB medium supplemented with 200 µg/mL ampicillin, 34 µg/mL chloramphenicol, and 1 mM Bpa (0.2 M Bpa stock solution, dissolved in 1 M NaOH).

4.2.1.4. Isolation of plasmid DNA and sequencing

Single colonies of DH5α cells, which had been transformed with plasmid DNA (cf. section 4.2.1.2), were picked from LB agar plates and used for inoculation in LB medium supplemented with the appropriate antibiotics (cf. section 4.2.1.3). The *E. coli* cells were incubated overnight at 37 °C and harvested by centrifugation (4000 rpm, Sorvall SLA3000 rotor). The amplified plasmid DNA was extracted from cells using a commercially available kit (NucleoSpin Plasmid EasyPure, Plasmid Mini, Midi or Giga, cf. Table 8) according to the manufacturer’s protocol. To verify the correct DNA sequence, purified plasmids were sent for DNA sequencing to Eurofins Genomics in Munich.

4.2.1.5. Agarose gel electrophoresis

DNA fragments were separated according to size by agarose gel electrophoresis. Agarose gels were casted by dissolving 0.8 to 1.2% (w/v) agarose in either TAE buffer or in 0.5x TBE buffer (cf. Table 12) supplemented with 5 µg/mL ethidium bromide. DNA samples were mixed with an appropriate volume of 6x Gel Loading Dye and then run alongside a DNA ladder (100 bp and/or 1 kb ladder, cf. Table 8) by applying a constant voltage of 140 V. In a last step, agarose gels were digitized using the ChemiDoc imaging system.

4.2.1.6. Native polyacrylamide gel electrophoresis

For native polyacrylamide gel electrophoresis (PAGE), 4.5% polyacrylamide gels were casted using a 30% acrylamide/bisacrylamide stock solution, 0.6% (v/v) tetramethylethylenediamine (TEMED), and 0.4% (w/v) ammonium persulfate (APS) in 0.2 to 1.0x TBE buffer. Each gel was run at 4 °C and 100 V for 60 min prior to sample loading. Samples were mixed with an appropriate volume of 6x Orange G-based loading dye supplemented with 5% (v/v) glycerol and were separated at 4 °C by applying a constant voltage ranging from 100 to 140 V. DNA detection was accomplished by measuring the intrinsic fluorescence of DNA with an UV lamp at 254 nm wavelength. Alternatively, polyacrylamide gels were stained with 50 µg/mL ethidium bromide in TBE buffer at room temperature for 60 min, rinsed with water, and digitized employing the ChemiDoc gel documentation instrument.

4.2.1.7. SDS-PAGE analysis

Proteins were separated according to size by SDS-PAGE (283). The sample preparation procedure for SDS-PAGE analysis of whole cell extracts and purified protein samples slightly differed. In the case of whole cell extracts, pelleted samples were resuspended in urea loading buffer [100 µl loading buffer per optical density at 600 nm (OD_{600}) value, Table 12]. The resuspended cells were heated at 65 °C for 15 min and were well mixed to shear genomic DNA. For purified proteins, pelleted samples were resuspended in an appropriate volume of 5x Laemmli loading buffer (cf. Table 12) and boiled at 95 °C for 5 min. Individual samples were loaded onto precast SDS-PAGE gels and were separated alongside PeqGOLD protein marker IV or V by applying a constant current of 25 mA and using SDS-PAGE running buffer (cf. Table 12). Subsequent to electrophoresis, gels were fixed with SDS-PAGE fixing solution and proteins were stained with Coomassie Blue staining solution (Table 12). Excess of dye was removed with water and the gel was digitized using the ChemiDoc gel documentation instrument.

4.2.1.8. Protein precipitation

Proteins were precipitated either to reduce the sample volume required for SDS-PAGE analysis or to exchange the sample buffer. The volume of the sample was adjusted to 100 µL using a matching sample buffer and trichloroacetic acid (TCA) was added to a final concentration of 15% (v/v). Following an incubation period of 20 min on ice, the precipitated proteins were separated by centrifugation (13000 rpm, SS34 rotor, Sorvall RC 6 Plus) at 4 °C for 30 min. The supernatant was discarded and the pellet was washed two times with 300 µl of cold acetone. The air-dried pellet was resuspended in the corresponding buffer needed for downstream application.

4.2.2. Protein expression and purification

4.2.2.1. Protein expression in *E. coli*

For the expression of *Drosophila* core histones and several ISWI constructs (i.e., ISWI_{WT}, $\text{ISWI}_{\Delta\text{HSS}}$, HSS_{ISWI}, $\text{ISWI}_{\text{K337D}}$, $\text{ISWI}_{\text{D485K}}$, and $\text{ISWI}_{\text{K337D D485K}}$), BL21-Gold(DE3) cells were transformed with the corresponding expression plasmid (cf. section 4.2.1.2 and Table 10) and were subsequently plated on selective LB agar plates (cf. section 4.2.1.3). A single colony was used to inoculate approximately 15–150 mL of LB medium supplemented with 100 µg/mL ampicillin and the pre-culture was incubated overnight at 37 °C under constant shaking. The main culture encompassed 2 L of LB medium supplemented with 100 µg/mL ampicillin, which was inoculated to an OD_{600} value of approximately 0.005 or 0.01 using an Ultrospec 2000 spectrophotometer. Following incubation at 37 °C under constant shaking, protein expression was induced at an OD_{600} value of 0.6 to 0.8 using 1 mM isopropyl-β-D-thiogalactopyranosid (IPTG) and the cell suspension was incubated overnight at 18 °C. The *E. coli* cells were harvested by centrifugation (4000 rpm, Sorvall SLA3000 rotor) at 4 °C for 10 min. The cell pellet was washed with either water or the first purification buffer, flash frozen in liquid nitrogen, and stored at -80 °C until further use.

For the expression of the $\text{His}_6\text{-ISWI}_{\text{M578B}}$ variant, the corresponding plasmid DNA was transformed into BL21-Gold(DE3) cells that already contained a plasmid (pFMP153, Table 10) encoding for both a Bpa-comprising mutant tRNA as well as a Bpa-specific aminoacyl-tRNA synthetase. The anticodon of the mutant tRNA was complementary to the TAG stop codon in order to facilitate the site-specific incorporation of the photo-reactive amino acid Bpa during translation. A single colony from chloramphenicol/ampicillin-selective LB agar plates was used to inoculate approximately 15 mL of LB medium supplemented with 34 µg/mL chloramphenicol and 200 µg/mL ampicillin and the pre-culture was incubated overnight at 37 °C under constant shaking. The main culture encompassed 2 L of LB medium supplemented with 34 µg/mL chloramphenicol, 200 µg/mL ampicillin, and 1 mM Bpa. Protein expression was induced at an OD_{600} value of 0.6 to 0.8 using 0.2 mM IPTG and cells were allowed to grow overnight at 18 °C under constant shaking. Subsequent preparatory steps were identical to the ones described above for *Drosophila* proteins.

For the expression of the Snf2H enzyme, I transformed Rosetta$^{\text{TM}}$ 2 (DE3) cells with the corresponding expression plasmid (cf. Table 10). A single colony from chloramphenicol/ampicillin-selective LB agar plates was used to inoculate approximately 15–150 mL of LB medium supplemented with 34 µg/mL chloramphenicol and 100 µg/mL ampicillin and the pre-culture was incubated overnight at 37 °C under constant shaking. The main culture encompassed 2 L of “rich” LB medium (cf. Table 12) supplemented with 34 µg/mL chloramphenicol and 100 µg/mL ampicillin. Protein expression was induced at an OD_{600} value of 0.6 to 0.8 using 0.4 mM IPTG. Subsequent preparatory steps were identical to the ones described above.

The overexpression of proteins was generally monitored by SDS-PAGE analysis. That is, during each protein expression, 1 mL of the cell culture prior to IPTG-induced overexpression and cell harvesting were removed, pelleted, and processed as described in section 4.2.1.7.

4.2.2.2. Purification of ISWI constructs

4.2.2.2.1. Purification of DmISWI$_{WT}$ and additional point mutation constructs

Pellets of *E. coli* cells expressing either His$_6$-tagged DmISWI$_{WT}$ or point-mutant constructs (i.e., ISWI$_{K337D}$, ISWI$_{D485K}$, and ISWI$_{K337D\ D485K}$) were resuspended in 30 mL ISWI His-A buffer (cf. Table 12). The ISWI His-A buffer was supplemented with 1 mg/L aprotinin, 1 mg/L leupeptin, 0.7 mg/L pepstatin, 1 mM phenylmethylsulfonyl fluoride (PMSF), and 1 Complete Protease Inhibitor Cocktail tablet to prevent protein proteolysis. The bacteria cells were lysed by passing the suspension three times through a French Press (1500 psi, French Pressure Cell Press Model FA-078) followed by sonication (Sonifier S-250 D) for a total time of 1 min at an amplitude of 25% on ice. Alternatively, *E. coli* cells were lysed employing a microfluidizer instrument (5 runs at 1000 bar, Microfluidizer LM10). Following addition of benzonase (1000 U/L cell culture) to degrade DNA and RNA, the cell lysate was centrifuged for 30 min at 19000 rpm and 4 °C (SS34 rotor, Sorvall RC 6 Plus) and the soluble fraction was filtered using 0.45 µm Rotilabo-syringe filters.

The His$_6$-tagged ISWI constructs were subsequently purified by nickel affinity chromatography (1 or 5 mL HisTrap HP columns) using an ÄKTA FPLC system. That is, the instrument was pre-equilibrated with ISWI-His-A buffer supplemented with 20 mM imidazole and the clarified lysate was loaded onto the HisTrap HP column. Unwanted protein species were washed off the column using ISWI-His-B buffer (cf. Table 12) and the following step imidazole gradient: 10 column volumes (CVs) of 20 mM imidazole, 6 CVs of 40 mM imidazole, and 1 CV of 80 mM imidazole. The flow-rate for the 1 and 5 mL HisTrap HP columns during the wash procedure was set to 1.5 and 2.5 mL/min, respectively. The full-length ISWI proteins were subsequently eluted by applying a linear gradient from 80 to 400 mM imidazole over 10 CVs at a flow rate of 1 mL/min or 2 mL/min. ISWI fractions were pooled and the combined sample supplemented with His-tagged TEV protease (prepared inhouse) to a final concentration of 0.06 mg/mL. The sample was subsequently dialyzed against ISWI dialysis buffer (1 L for at least 1 h, 1 L overnight, cf. Table 12) using 6000–8000 Da molecular weight cut-off (MWCO) Spectra/Por dialysis tubing. TEV-cleaved ISWI proteins were separated from unwanted protein species and reaction products by means of nickel affinity chromatography. The collected flow-through was subsequently diluted four-fold with buffer [10 mM Tris-HCl (pH 7.6), 10% (v/v) glycerol, and 1 mM DTT] to lower the salt concentration prior to cation exchange chromatography and the sample was filtered using 0.2 µm syringe filters. ISWI proteins were immobilized on a Mono S 5/50 GL ion exchange column, which had been pre-equilibrated with ISWI MonoS-A buffer (cf. Table 12) supplemented with 40 mM NaCl. Unwanted protein species were washed off the column with 17 CVs of ISWI MonoS-A buffer supplemented with 40 mM NaCl. ISWI proteins were eluted by applying a 6.67 min linear gradient at a constant flow-rate of 1.5 mL/min and increasing concentrations (40 to 600 mM) of NaCl. ISWI fractions were pooled and the combined sample concentrated using Amicon Ultra-4 centrifugal filter units (30 kDa MWCO). In a final step, ISWI samples were subjected to size-exclusion chromatography. The sample was loaded onto a Superdex 200 column (i.e., Superdex 200 HiLoad 16/60, Superdex 200 Increase 10/300 GL, or Superdex 200 10/300 GL) that had been pre-equilibrated with ISWI SEC buffer (cf. Table 12). Fractions that contained ISWI proteins were pooled and concentrated to 1–10 mg/mL using 30 kDa MWCO Amicon Ultra-4 centrifugal filter units. Small aliquots of the purified protein were flash frozen in liquid nitrogen and stored at -80 °C until further use. The yield for DmISWI$_{\mathrm{WT}}$ was between 0.5 and 3.1 mg per liter cell culture (n = 4). Purification of ISWI point-mutant constructs (i.e., ISWI$_{\mathrm{K337D}}$, ISWI$_{\mathrm{D485K}}$, and ISWI$_{\mathrm{K337D\ D485K}}$) typically yielded between 0.2 to 0.5 mg of protein per liter cell culture (n = 1).

4.2.2.2.2. Purification of ISWI$_{\mathrm{M578B}}$

Pellets of *E. coli* cells expressing the His$_6$-tagged ISWI$_{\mathrm{M578B}}$ construct were resuspended in an identical manner as described for DmISWI$_{\mathrm{WT}}$ in section 4.2.2.2.1. Cell lysis was achieved by passing the suspension five times through a microfluidizer instrument (1000 bar, Microfluidizer LM10). Following addition of benzonase (1000 U/L cell culture), the cell lysate was cleared by centrifugation and filtration and the sample was subjected to nickel affinity chromatography in an identical manner as specified for DmISWI$_{\mathrm{WT}}$ in section 4.2.2.2.1. Notably, the UV light of the FPLC instrument was switched off during the purification procedure to prevent unwanted cross-linking reactions of the ISWI$_{\mathrm{M578B}}$ variant. Following TEV-mediated cleavage of the His$_6$-tag, ISWI$_{\mathrm{M578B}}$ samples were further purified by nickel affinity and size-exclusion chromatography as described for DmISWI$_{\mathrm{WT}}$ in section 4.2.2.2.1. The yield was 0.4 mg per liter cell culture (n = 1).

4.2.2.2.3. Purification of $\mathrm{ISWI}_{\Delta\mathrm{HSS}}$

Cells expressing His_6-$\mathrm{ISWI}_{\Delta\mathrm{HSS}}$ were resuspended in 35 mL of $\mathrm{ISWI}_{\Delta\mathrm{HSS}}$ lysis buffer (cf. Table 12). The lysis buffer was supplemented with 1 mM PMSF, 20 mM imidazole, 1 mM DTT, and 1 Complete Protease Inhibitor Cocktail tablet. The bacterial cells were lysed by passing the suspension five times through a microfluidizer instrument (1000 bar, Microfluidizer LM10). Following addition of benzonase (1000 U/L cell culture), the cell lysate was cleared by centrifugation and filtration as specified for $\mathrm{DmISWI}_{\mathrm{WT}}$ in section 4.2.2.2.1. The sample was subsequently subjected to nickel affinity chromatography and thus was loaded onto a 1 mL HisTrap HP column, which had been pre-equilibrated with ISWI ΔHSS-A buffer (cf. Table 12) supplemented with 20 mM imidazole. Most sample impurities were efficiently removed at a constant flow-rate of 1 mL/min using ISWI ΔHSS-B buffer (cf. Table 12) and the following step imidazole gradient: 7 CVs of 40 mM imidazole, followed by 5 CVs of 80 mM imidazole, and 2.5 CVs of 120 mM imidazole. The final wash step encompassed a 1 min linear gradient at a constant flow-rate of 1 mL/min and increasing concentrations (120−160 mM) of imidazole. Prior to elution of the $\mathrm{ISWI}_{\Delta\mathrm{HSS}}$ protein with 400 mM imidazole, a pre-equilibrated 5 mL HiTrap Q HP anion exchange column was mounted down-stream to the nickel affinity column in order to remove negatively charged contaminants. $\mathrm{ISWI}_{\Delta\mathrm{HSS}}$ fractions were pooled and the combined sample was subjected to size-exclusion chromatography. That is, $\mathrm{ISWI}_{\Delta\mathrm{HSS}}$ samples were loaded onto a 120 mL Superdex 200 HiLoad 16/60 column, which had been pre-equilibrated with ISWI ΔHSS SEC buffer (cf. Table 12). Individual $\mathrm{ISWI}_{\Delta\mathrm{HSS}}$ fractions were pooled and concentrated to approximately 7 mg/mL using 30 kDa MWCO Amicon Ultra-4 centrifugal filter units before being flash frozen in liquid nitrogen and stored as small aliquots at -80 °C. The yield was 6.3 mg of protein per liter cell culture (n = 1).

4.2.2.2.4. Purification of $\mathrm{HSS}_{\mathrm{ISWI}}$

Pellets of *E. coli* cells expressing the His_6-tagged $\mathrm{HSS}_{\mathrm{ISWI}}$ protein were resuspended in 30 mL HSS-NiA buffer (cf. Table 12). The HSS-NiA buffer was supplemented with 1 mg/L aprotinin, 1 mg/L leupeptin, 0.7 mg/L pepstatin, 1 mM PMSF, 0.5 mM DTT, and 1 Complete Protease Inhibitor Cocktail tablet. Bacterial cells were lysed as described for $\mathrm{DmISWI}_{\mathrm{WT}}$ in section 4.2.2.2.1. Following addition of benzonase (1000 U/L cell culture), the cell lysate was cleared by centrifugation and filtration as described in section 4.2.2.2.1. The His_6-tagged $\mathrm{HSS}_{\mathrm{ISWI}}$ protein was subsequently purified by nickel affinity chromatography. The cleared cell lysate was loaded onto a 5 mL HisTrap HP column, which had been pre-equilibrated with HSS-NiA buffer (cf. Table 12). Contaminating protein species were washed off the column using HSS-NiB buffer (cf. Table 12) and the following step imidazole gradient: 8 CVs of HSS-NiA buffer followed by 4 CVs of 20 mM imidazole. The $\mathrm{HSS}_{\mathrm{ISWI}}$ protein was eluted by applying a linear gradient over 13 CVs at a flow-rate of 1 mL/min and increasing (20–500 mM) imidazole concentrations. HSS_{ISWI} fractions were pooled and the sample was supplemented with TEV protease to a final concentration of 0.06 mg/mL. The sample was subsequently dialyzed overnight against 1 L HSS-Dialysis buffer (cf. Table 12) using 6000–8000 Da MWCO Spectra/Por dialysis tubing. The TEV-cleaved HSS_{ISWI} protein was further purified by means of nickel affinity chromatography and the flow-through was collected and was subsequently concentrated to 0.5–1 mL using Amicon Ultra-4 centrifugal filter units (10 kDa MWCO). The protein sample was further purified by size-exclusion chromatography. Thereby, the sample was loaded onto either a Superdex 200 Increase 10/300 GL or a Superdex 200 10/300 GL column, which had been pre-equilibrated with HSS-SEC buffer (cf. Table 12). In a final step, the eluted HSS_{ISWI} protein was pooled and concentrated to 2–5 mg/mL before being flash frozen in liquid nitrogen and stored as small aliquots at -80 °C. The yields were 0.4 and 6.5 mg of protein per liter cell culture (n = 2).

4.2.2.3. Purification of Snf2H

Pellets of *E. coli* cells overexpressing His_6-tagged Snf2H were resuspended in Snf2H lysis buffer (20 mL/L cell culture, cf. Table 12). The Snf2H lysis buffer was supplemented with 1 mg/L aprotinin, 1 mg/L leupeptin, 0.7 mg/L pepstatin, 1 mM PMSF, and 1 Complete Protease Inhibitor Cocktail tablet. Cell lysis was accomplished as described in section 4.2.2.2.1 by passing the suspension through a French Press followed by sonication or by employing a Microfluidizer LM10 instrument. Following addition of benzonase (1000 U/L cell culture), the cell lysate was cleared by centrifugation and filtration as specified in section 4.2.2.2.1. The His_6-tagged Snf2H protein was subsequently purified by nickel affinity chromatography. The sample was loaded onto a 5 mL HisTrap HP column, which had been pre-equilibrated with Snf2H lysis buffer, at a flow rate of 1.0 mL/min. Unwanted protein species were washed off the column using 8 CVs of Snf2H lysis buffer at a flow-rate of 1.5 mL/min. The Snf2H enzyme was eluted by applying a linear gradient over 8 CVs from 0 to 100% Snf2H elution buffer (cf. Table 12) at a constant flow-rate of 1.5 mL/min. Enzyme fractions were subsequently pooled and subjected to anion exchange chromatography in order to separate Snf2H molecules from contaminating DNA. The protein sample was loaded onto a Mono Q 5/50 GL column, which had been pre-equilibrated with Snf2H-SEC buffer (cf. Table 12). The flow-through was collected and concentrated to 0.5–1 mL per liter cell culture using Amicon Ultra-4 centrifugal filter units (30 kDa MWCO). Following addition of TEV protease to a final concentration of 0.075–0.15 mg/mL, the protein sample was dialyzed overnight against 1 L of Snf2H-SEC buffer using Spectra/Por dialysis tubing (6000–8000 Da MWCO). The purity of the Snf2H sample was further enhanced using size-exclusion chromatography. The filtered sample (0.2 µm syringe filter) was loaded onto a 120 mL Superdex 200 HiLoad 16/60 column, which had been pre-equilibrated with Snf2H-SEC buffer. Snf2H fractions were pooled and concentrated (Amicon Ultra-4 centrifugal filter unit, 30 kDa MWCO) before being dialyzed against 0.5 L of Snf2H-storage buffer (cf. Table 12) for at least 16 hours. Small aliquots of purified Snf2H were flash frozen in liquid nitrogen and stored at -80 °C. The purification yielded 3.0 and 4.4 mg of protein per liter cell culture (n = 2).

4.2.2.4. Purification of core histones

4.2.2.4.1. Histone purification according to the IBP protocol

Pellets of *E. coli* cells overexpressing a *Drosophila* core histone protein (i.e., H2A, H2B, H3, or H4) were resuspended in 35 mL of histone-wash buffer (cf. Table 12). The histone-wash buffer was supplemented with 1 mg/L aprotinin, 1 mg/L leupeptin, and 0.7 mg/L pepstatin. The bacterial cells were lysed by sonication (Digital Sonifier S-250 D) for a total time of 2 min at an amplitude of 30% followed by passing the suspension three times through a French Press (1500 psi, French Pressure Cell Press Model FA-078). The cell lysate was pelleted by centrifugation for 30 min at 19000 rpm and 4 °C (SS34 rotor, Sorvall RC 6 Plus). Inclusion bodies were purified by a series of washing steps, in which the insoluble fraction of the lysate was repeatedly resuspended in buffer and pelleted by centrifugation. During the first washing step, the pelleted lysate was resuspended in histone-wash buffer, which was supplemented with 1% (v/v) of the Triton X-100 surfactant. During the following two cycles, the insoluble fraction was washed with histone-wash buffer without any additives. Extraction of histone proteins was accomplished by suspension of the inclusion bodies in histone-unfolding buffer (cf. Table 12) and incubation of the sample for 1 hour under constant rotation. The sample was subsequently dialyzed overnight against 1 L of SAU buffer supplemented with 200 mM NaCl (cf. Table 12, the buffer was exchanged three times) using Spectra/Por dialysis tubing (6000–8000 Da MWCO). Following filtration of the sample using 0.45 µm syringe filters, histone proteins were purified by means of cation exchange chromatography. The sample was loaded onto a 5 mL HiTrap SP column, which had been pre-equilibrated with SAU buffer supplemented with 200 mM NaCl. Unwanted protein species were washed off the column using SAU buffer and the following step NaCl gradient: 5 CVs of 200 mM NaCl, followed by 3 CVs of 250 mM NaCl, and 3 CVs of 300 mM NaCl. Histone proteins were eluted by applying a nonlinear gradient from 300 to 800 mM NaCl (increase to 350 mM NaCl over 5 CVs followed by an increase to 800 mM NaCl over 7 CVs) at a constant flow-rate of 1.7 mL/min. Histone fractions were pooled and dialyzed overnight against 3 L of deionized water (water was exchanged three times) using Spectra/Por dialysis tubing (6000–8000 Da MWCO). The concentration of individual histone proteins was determined by UV absorption measurements at 280 nm using a NanoDrop spectrophotometer and taking into account the respective extinction coefficient (Table 13). Sample purity was calculated as described by Glasel (229). Small aliquots of purified histone proteins were flash frozen in liquid nitrogen and stored at -80 °C until further use.

Table 13: Histone extinction coefficients. Extinction coefficients of individual *Drosophila* core histones are listed according to Klinker *et al.* (227).

Histone	MW [Da]	ε_{280} [M^{-1} cm^{-1}]
H2A	13232	4470
H2B	13565	7450
H3	15257	4470
H4	11250	5960

4.2.2.4.2. Histone purification according to the RHP protocol

Pellets of *E. coli* cells overexpressing a *Drosophila* core histone protein (i.e., H2A, H2B, H3, or H4) were resuspended in 35 mL of SAU buffer (cf. Table 12). The SAU buffer was supplemented with 200 mM NaCl, 1 mg/L aprotinin, 1 mg/L leupeptin, 0.7 mg/L pepstatin, and 1 mM PMSF. Bacterial cells were lysed by sonication (Digital Sonifier S-250 D) for a total time of 2 min at an amplitude of 30% followed by passing the suspension three times through a French Press (1500 psi, French Pressure Cell Press Model FA-078). The lysate was pelleted by centrifugation for 30 min at 19000 rpm and 4 °C (SS34 rotor, Sorvall RC 6 Plus) and the supernatant was filtered using HPF Millex syringe filters.

In the RHP "Variant 1" protocol (cf. Figure 8B), histone proteins were subsequently purified by cation exchange chromatography in an identical manner as described in section 4.2.2.4.1. Histone fractions were pooled and dialyzed overnight against 1.5 L of deionized water (the dialysate was exchanged three times) using Spectra/Por dialysis tubing (6000–8000 Da MWCO). Protein samples were supplemented with 15 mM Tris-HCl (pH 8.0), filtered using 0.45 µm syringe filters, and subjected to anion exchange chromatography in order to remove contaminating DNA. The sample was loaded onto a 5 mL HiTrap Q HP column, which had been pre-equilibrated with 15 mM Tris-HCl (pH 8.0). Following collection of the flow-through, protein concentration and sample purity were determined as specified in section 4.2.2.4.1. Small aliquots of purified histone proteins were flash frozen in liquid nitrogen and stored at -80 °C until further use.

In the RHP “Variant 2” protocol (cf. Figure 8B), removal of contaminating DNA was coupled to cation exchange chromatography by placing the HiTrap Q HP column upstream of the HiTrap SP HP column during histone purification. Once the protein sample bound to the cation exchange column, the HiTrap Q HP column was simply detached from the FPLC system and the purification procedure proceeded as described above for “Variant 1” of the RHP protocol.

4.2.3. Reconstitution of nucleosomes

4.2.3.1. DNA digestion and purification

DNA that was used during nucleosome reconstitution (cf. section 4.2.3.3) was prepared from plasmid DNA harboring the 601 positioning sequence (235) using restriction enzyme-mediated digestion in combination with size separation by native PAGE.

The corresponding plasmid (i.e., pFMP109 or pFMP151, cf. Table 10) was transformed into DH5α *E. coli* cells for amplification (cf. section 4.2.1.2). The plasmid DNA was subsequently isolated and purified as described in section 4.2.1.4.

Restriction enzyme-mediated digestion of the plasmid DNA was initiated by diluting the DNA to a final concentration of 1 mg/mL in 1x Buffer 4 supplemented with 70 U/mL of SmaI. The reaction mixture was subsequently incubated at 37 °C for 18 to 20 h. Notably, digestion of plasmid pFMP151 with the SmaI enzyme results in four identical DNA fragments of 187 bp length with terminal nucleosome positioning sequence. Following precipitation of DNA with 1/10 volume of 3 M sodium acetate (pH 5.2) and 2.5-times the initial volume of ethanol, the sample was centrifuged for 30 min at 19000 rpm and 4 °C (SS34 rotor, Sorvall RC 6 Plus). DNA fragments were subsequently dissolved in approximately 500 µL TE buffer (cf. Table 12) at room temperature and the sample was separated by native PAGE (cf. section 4.2.1.6). UV shadowing using an UV lamp (Ultra Violet Products) at 254 nm allowed the localization and isolation of the target DNA fragments. The DNA fragments were subsequently eluted from the polyacrylamide slices using the Whatman Elutrap electroelution system according to the manufacturer’s guidelines at 100−140 V for at least 3 h. The eluted DNA was precipitated as described above and then resuspended in TE buffer. DNA concentration was determined by UV measurements at 254 nm employing a NanoDrop ND1000 spectrophotometer.

4.2.3.2. Octamer reconstitution

Each of the purified core histones was lyophilized overnight (Alpha 1–2 and RZ 2.5) and solubilized in octamer unfolding buffer (cf. Table 12) to a concentration of approximately 4 mg/mL. Following incubation for 30 min under constant rotation at room temperature, the concentration of each histone was determined as described in section 4.2.2.4.1. The four core histones H2A, H2B, H3, and H4 were subsequently mixed in a molar ratio of 1.6:1.4:1:1, respectively, and histone stoichiometry was evaluated by SDS-PAGE analysis (cf. section 4.2.1.7). The sample was dialyzed overnight at 4 °C against octamer refolding buffer (cf. Table 12) using Spectra/Por dialysis tubing (3500 Da MWCO). Following centrifugation of the sample at 19000 rpm (SS34 rotor, Sorvall RC 6 Plus) for 30 min, the supernatant was concentrated to 2–4 mL using 30 kDa MWCO Amicon Ultra-4 centrifugal filter units.

Assembled octamers were separated from different protein species by means of size-exclusion chromatography. The sample was therefore loaded onto a 120 mL Superdex 200 HiLoad 16/60 column, which had been pre-equilibrated with octamer refolding buffer. Histone octamers exhibiting correct subunit stoichiometry typically eluted at approximately 60 mL. The respective fractions were pooled and octamer concentration was determined using a NanoDrop ND1000 spectrophotometer and assuming an extinction coefficient of 44700 $M^{-1}cm^{-1}$. Small aliquots of purified core histone octamers were flash frozen in liquid nitrogen and stored at -80 °C.

4.2.3.3. Nucleosome reconstitution

Mononucleosomes were reconstituted by salt gradient dialysis using purified histone octamers (cf. 4.2.2.4) and defined DNA fragments of 187 bp length (cf. section 4.2.3.1) in a 300 µL reaction volume.

To find an optimal molar ratio between DNA and histone octamers in preliminary experiments, increasing amounts of histone octamers were mixed with 0.3 µg/µL DNA in buffer [20 mM Tris-HCl (pH 7.7), 2 M KCl, and 10 mM DTT] and nucleosome formation was evaluated by native PAGE analysis (cf. section 4.2.1.6). Nucleosome reconstitution was typically found to be most efficient at a molar DNA:octamer ratio of approximately 1 (i.e., 0.93 ± 0.14, n = 25).

Salt gradient dialysis was performed at 4 °C using either Slide-A-Lyzer MINI dialysis devices (7000 Da MWCO) or a custom-built dialysis chamber equipped with 7000 Da MWCO Spectra/Por dialysis tubing. Salt gradient dialysis was initiated by dialyzing the sample against 100 mL of Mononuc-2000 buffer (cf. Table 12). The salt concentration of the buffer was lowered over time using Mononuc-0 buffer (cf. Table 12) and a peristaltic pump (MINIPULS Evolution). The flow-rate of the peristaltic pump was thereby set to 0.35 rpm for the initial 24 hours and was then increased to 0.8 rpm for at least another 3 h. The volume of the dialysate was kept constant throughout dialysis procedure.

Following centrifugation for 15 min at 13000 rpm (Eppendorf 5417C centrifuge) and 4 °C, nucleosome concentration was estimated by UV measurements at 254 nm using a NanoDrop ND1000 spectrophotometer and the quality of the sample assessed by native PAGE analysis (cf. section 4.2.1.6).

Samples subjected to XL-MS analysis, mononucleosomes were further purified by glycerol gradient ultracentrifugation. The gradient ranging from 10 to 30% glycerol was prepared in polypropylene tubes (14 x 89 mm) by mixing UZ-10% and UZ-30% solutions (cf. Table 12) with the help of the Gradient Master instrument and the following settings: 2.25 min, 81.5°, 11 rpm, and UP rotation. The nucleosome sample ($V \leq 500$ µL) was layered on top of the glycerol gradient and centrifuged for 19 hours at 34000 rpm (SW 41 Ti rotor) and 4 °C. Drop fractions of 200–300 µL were collected from the bottom of the glycerol gradient by the use of a 20-gauge needle and the quality of the sample was evaluated by native PAGE analysis (cf. section 4.2.1.6). Qualitatively satisfying nucleosome fractions (i.e., high nucleosome concentrations, low concentration of unbound DNA) were pooled and concentrated to 2–5 µM using 30 kDa MWCO Amicon Ultra-4 centrifugal filter units. Nucleosome concentration was estimated by UV measurements at 254 nm using a NanoDrop spectrophotometer and the quality of the sample assessed by native PAGE analysis. Purified mononucleosomes were stored up to six weeks in the fridge at approximately 8 °C.

4.2.4. Protein cross-linking coupled to mass spectrometry

4.2.4.1. Protein cross-linking

4.2.4.1.1. UV cross-linking

UV cross-linking was performed essentially as described previously by Forné *et al.* (157). Briefly, 100 µL samples comprising 1.0 µM of purified $ISWI_{M578B}$ protein and UV-XL buffer (cf. Table 12) were exposed to long-wave UV light (365 nm) in a Bio-Link 365 UV-Crosslinker system on ice. Following UV irradiation for various time intervals (i.e., 0, 30, and 120 min), 30 µL of the sample was removed and subjected to SDS-PAGE analysis (cf. section 4.2.1.7) and in-gel tryptic digestion (cf. section 4.2.4.2.1).

4.2.4.1.2. Chemical cross-linking

Enzyme-nucleosome and enzyme-ADP-BeF_x complexes were formed by incubating the respective molecules for 10 min on ice in the respective c-XL buffer (cf. Table 12) in order to allow binding to equilibrate. The ADP-BeF_x solution was prepared by mixing equal volumes of a 50 mM ADP-Mg^{2+} stock solution (prepared by dissolving ADP and $MgCl_2$ in an equimolar ratio in water at pH 7) with a premixed solution containing 50 mM $BeSO_4$ and 150 mM NaF. Following centrifugation of protein samples for 10 min at 13000 rpm and 4 °C (Eppendorf 5417C centrifuge), chemical cross-linking was initiated by addition of either the BS^{2}G or the BS^3 cross-linking agent (dissolved in DMSO). Table 14 summarizes the distinct cross-linking conditions for the DmISWI and Snf2H enzymes that resulted in productive XL-MS data for different functional states of the catalytic cycle (cf. STable 1–STable 5).

Table 14: Chemical cross-linking conditions for the DmISWI and Snf2H enzymes. The specific cross-linking conditions that resulted in productive XL-MS data are summarized for each protein state. The cross-linking buffers c-XL #1–5 are specified in Table 12.

Protein state	Enzyme [µM]	Nucleotide [mM]	Nucleosome [µM]	BS^{2}G [mM]	or	BS^3 [mM]	Buffer
DmISWI - Apo	1.0–1.5	0	0	0.5–3.0		1.0	c-XL #1
Snf2H - Apo	1.0–8.0	0	0	0		0.7–1.4	c-XL #2 / #3
Snf2H - ADP-BeF$_x$	1.0–1.5	3.0	0	0		1.0	c-XL #2 / #4
Snf2H - Nucleosome	1.5	3.0	0.8 or 1.5	0		1.0	c-XL #5

Following incubation of the sample for 30 min on ice or at 30 °C, the cross-linking reaction was quenched by adding NH_4HCO_3 to a final concentration of 200 mM and the sample was incubated for another 20 min on ice. Potential protein aggregates were removed by centrifugation for 10 min at 13000 rpm and 4 °C (Eppendorf 5417C centrifuge). Notably, each XL-MS experiment also included a DMSO-treated negative control sample, in which target protein(s) were processed in an identical manner in the absence of a chemical cross-linker.

Cross-linked proteins were subsequently precipitated by TCA (cf. section 4.2.1.8) and subjected to in-solution tryptic digestion (cf. section 4.2.4.2.2). Alternatively, selected samples (cf. column “Size selection” in STable 1–STable 5) were subjected to size-exclusion chromatography prior to in-solution digestion. Size-exclusion chromatography was performed by loading the sample onto either a Superdex 200 Increase 10/300 GL or a Superdex 200 10/300 GL column, which had been pre-equilibrated with ISWI SEC or c-XL #2 buffer for DmISWI and Snf2H samples, respectively. Enzyme fractions were pooled, proteins were precipitated by TCA, and the sample was subjected to in-solution tryptic digestion (cf. section 4.2.4.2.2).

4.2.4.2. Protein proteolysis

4.2.4.2.1. In-gel tryptic digestion

Cross-linked $ISWI_{M578B}$ samples (cf. section 4.2.4.1.1) were separated by SDS-PAGE analysis and stained with Coomassie Blue. Bands corresponding to $ISWI_{M578B}$ were excised from the polyacrylamide gel and each gel slice was thoroughly washed with water and 40 mM NH_4HCO_3 at room temperature. The gel slices were subsequently shrunken by submerging them in acetonitrile (ACN) for 20 min at room temperature. The gel slices were air-dried for 2 min and then rehydrated under reducing solution conditions (10 mM DTT in 40 mM NH_4HCO_3). Following incubation of the sample for 1 hour at room temperature, thiol groups were alkylated with 55 mM iodoacetamide (IAA) in the absence of light for another 30 min at room temperature. Each gel slide was subsequently washed three times with 40 mM NH_4HCO_3 and ACN before being air-dried for 5 min. Tryptic digestion was initiated by rehydrating each gel slice with 10 µL digestion buffer (200 ng sequencing grade modified trypsin, 5 mM acetic acid, and 36 mM NH_4HCO_3). Following an initial incubation period of 2–3 min on ice, the volume of the reaction mixture was adjusted to 50 µL using 40 mM NH_4HCO_3 and the sample incubated for another 5 min. Following addition of another 40 µL of 40 mM NH_4HCO_3, the sample was incubated overnight at 37 °C under constant shaking (600 rpm, Thermomixer comfort). The solution was transferred to a new tube and the sample was acidified by addition of trifluoroacetic acid (TFA) to a final concentration of 0.1% (v/v). The tryptic peptide mixture was subsequently desalted and concentrated by solid-phase extraction (SPE) as described in section 4.2.4.3.

4.2.4.2.2. In-solution tryptic digestion

Chemically cross-linked protein samples, which had been precipitated by TCA (cf. section 4.2.4.1.2), were solubilized in XL-denaturation buffer (cf. Table 12) to a final protein concentration of approximately 1 mg/mL. Disulfide bonds were reduced by addition of DTT to a final concentration of 5 mM and incubation of the sample for 1 hour at room temperature. Reactive thiol groups were subsequently alkylated in the presence of 10 mM IAA for 30 min in the dark at room temperature. Following dilution of the sample with 25 mM NH_4HCO_3 to a final concentration of 1 M urea, protein proteolysis was initiated by addition of trypsin (200 ng/µL sequencing grade modified trypsin in 50 mM acetic acid) in a 1:50 enzyme to substrate ratio. Tryptic digestion was allowed to proceed overnight at 37 °C under constant shaking (600 rpm, Thermomixer comfort). Trypsin was inactivated by lowering pH to 2–3 using formic acid and the sample was subsequently desalted and concentrated by SPE as described in section 4.2.4.3.

4.2.4.3. Solid-phase extraction and enrichment of tryptic peptides

The tryptic peptide mixture was subjected to SPE using either OMIX C18 pipette tips (10–100 µL) or Sep-Pak tC18 cartridges.

In the case of the OMIX C18 pipette tips, the chromatography resin was activated and equilibrated by flushing the pipette tips three times with 100 µL of 50% (v/v) ACN and 100 µL of 0.1% (v/v) TFA, respectively. The acidified tryptic digest was loaded onto the C18 resin and was washed five times with 100 µL of 0.1% (v/v) TFA. Tryptic peptides were eluted in 50 µL of 60% (v/v) ACN supplemented with 0.25% (v/v) TFA.

In the case of the Sep-Pak tC18 cartridges, the chromatography resin was activated and equilibrated by flushing the cartridges with 700 µL ACN and two times 700 µL of SPE wash solution (cf. Table 12), respectively. Following acidification of the tryptic digest to pH 2−3 with formic acid, the sample was loaded onto the resin and the cartridge was washed twice with 700 µL SPE wash solution. Tryptic peptides were eluted in 500 µL of SPE elution solution (cf. Table 12).

Following SPE by either OMIX C18 pipette tips or Sep-Pak tC18 cartridges, samples were evaporated to dryness in a vacuum centrifuge at 30 °C. Tryptic peptides were subsequently resuspended in either 10−20 µL of 0.1% (v/v) TFA and the sample subjected to LC-MS/MS analysis (cf. section 4.2.4.4) or in 25 µL of SEC mobile phase (cf. Table 12) for size-exclusion chromatography.

Selected samples were subjected to size-exclusion chromatography in order to enrich cross-linked peptides as described previously by Leitner *et al.* (284). The peptide mixture was loaded onto a Superdex Peptide PC 3.2/300 column, which had been pre-equilibrated with 30% (v/v) ACN supplemented with 0.1% (v/v) TFA. Fractions were collected every 2 min at a flow-rate of 50 µL/min in 96-well MultiScreen HTS plates. Samples were subsequently evaporated to dryness as described above and were resuspended in 10−20 µL of 0.1% (v/v) TFA before being subjected to LC-MS/MS analysis.

4.2.4.4. LC-MS/MS analysis

LC-MS/MS analysis was kindly performed by Dr. I. Forné (LMU, Munich). Samples were injected into an UltiMate 3000 or RSLCnano HPLC system, which had been equipped with a 15 cm analytical C18 nano column (75 µm ID, packed with ReproSil-Pur C18-AQ 2.4 µm). Peptides were gradually eluted by applying a 40−60 min linear gradient and increasing concentrations (i.e., 5−60%) of ACN in 0.1% formic acid. The effluent was directly electrosprayed into the ion source of either a LTQ-Orbitrap XL or Q-Exactive HF mass spectrometer. Both instruments were operated in positive ionization mode with precursor and fragment ions being detected in data-dependent acquisition mode with high resolution and accuracy.

In the case of the LTQ-Orbitrap XL instrument, ionization was accomplished by applying a constant spray voltage of 1.4 kV and a capillary temperature of 200 °C in the absence of any sheath or auxiliary gas flow. Precursor ions were detected in survey full-scan MS mode ranging from 300−2000 m/z with a resolution of 60000 at m/z 400. The six most abundant peptide ions with charge states between 2+ and 5+ were sequentially isolated to a target value of 10000 and fragmented in the linear ion trap by collision-induced dissociation (CID, 35% normalized collision energy). The collision voltage and activation time was set to q = 0.25 and 30 ms, respectively. The ion selection threshold was set to 10000 counts for MS/MS. Fragment ion spectra were recorded with the Orbitrap detector. Internal calibration was achieved as described previously by Forné *et al.* (157) using a total of three lock mass ions from ambient air (m/z = 371.10123, 445.12002, and 519.13882).

In the case of the Q-Exactive HF mass spectrometer, spray voltage and capillary temperature were set to 1.5 kV and 250 °C, respectively. Sheath and auxiliary gas flow were turned off. Precursor ions were detected in survey full-scan MS mode ranging from 375−1600 m/z with high resolution as specified above. The ten most intense peptide ions with charge states between 3+ and 5+ were sequentially isolated to a target value of 100000 and subjected to CID fragmentation at 27% normalized collision energy. The ion selection threshold was set to 33000 counts for MS/MS.

Thermo binary raw files were converted into mzXML or mgf format using msconvert (ProteoWizard Tools, http://proteowizard.sourceforge.net/tools.shtml) and Proteome Discoverer 1.4-PostSearch Recalibrator Node (ThermoFisher Scientific), respectively.

4.2.4.5. Data analysis and identification of cross-linked peptides

Cross-linked peptides were identified using the Crossfinder software (157, 200). In the case of chemical cross-linking data, only lysine residues of the target protein(s) were considered as potential cross-linking sites. In contrast, all residues of the ISWI$_{M578B}$ variant were considered to facilitate the Bpa-mediated formation of cross-links upon UV irradiation. The number of missed trypsin cleavage sites was set to 2 or 3. Oxidation of methionine and carbamidomethylation of cysteine residues were defined as variable and fixed modifications, respectively. Peptide hits for individual steady-state conditions were subsequently filtered according to the Crossfinder score, fragmentation quality, and peptide length as specified in Table 15. Precursor and fragment ion mass accuracy was set to 9 and 12.5 parts per million (ppm), respectively. The FDR did not exceed 7% for any functional state when applying these filtering criteria.

Table 15: Peptide identification criteria.

Protein	**ISWI$_{WT}$**	**ISWI$_{M578B}$**	**Snf2H**	**Snf2H**	**Snf2H-nucleosome**
Cross-linker	BS^{2}G, BS^3	UV	BS^3	BS^3	BS^3
Ligand	none	none	none	ADP-BeF$_x$	ADP-BeF$_x$
Score	$\geq$ 800	$\geq$ 400	$\geq$ 1000	$\geq$ 700	$\geq$ 1200
Relative filter score	100	100	100	100	100
Number of fragment ions per spectrum	$\geq$ 6	$\geq$ 5	$\geq$ 5	$\geq$ 5	$\geq$ 6
Number of fragment ions per peptide	$\geq$ 2	$\geq$ 2	$\geq$ 2	$\geq$ 2	$\geq$ 3
Fractional intensity of assigned MS2 peaks	$\geq$ 0.05	$\geq$ 0.05	$\geq$ 0.05	$\geq$ 0.05	$\geq$ 0.05
Minimal peptide length	1	1	1	1	3
False-discovery rate (FDR)	$\leq$ 0.05	$\leq$ 0.05	$\leq$ 0.07	$\leq$ 0.05	$\leq$ 0.03

Peptide hits were manually discarded from further analysis if one of the following was true: (i) the same candidate was identified in the negative (i.e., DMSO-treated or unirradiated) control sample, (ii) the spacing between cross-linked residues of intra-domain linkages was below ten, and (iii) the cross-linked lysine residue was at the C-terminal end of the peptide (285).

Sequence assignments were subsequently manually verified by assessing the correct assignment of precursor and fragment ions in MS/MS spectra. A tabular overview of identified cross-links for the DmISWI and Snf2H remodeling enzymes across different functional states is provided in STable 1–STable 5. Notably, STable 1 furthermore includes previously published Bpa-mediated cross-links for ISWI$_{M578B}$ (157) and ISWI$_{H483B}$ (115) that were used during computational modeling and data interpretation of the DmISWI enzyme as well as an unpublished data set, which was kindly provided by Dr. Felix Müller-Planitz (LMU, Munich).

4.2.4.6. Relative quantification of cross-linked peptides

The relative quantification of cross-linked peptides relied on the use of isotopically labeled BS^3-H$_4$ and BS^3-D$_4$ cross-linking agents. The Snf2H enzyme was chemically cross-linked in the apo, ADP-BeF$_x$-, and nucleosome-bound state with either BS^3-H$_4$ or BS^3-D$_4$ as described in section 4.2.4.1.2. Following quenching of the cross-linking reaction, heavy and light cross-linked samples were mixed in an equimolar ratio and then subjected to in-solution tryptic digestion (cf. section 4.2.4.2.2), size-exclusion chromatography (cf. section 4.2.4.3), and LC-MS/MS analysis (cf. section 4.2.4.4). Identification of cross-linked peptides was accomplished using the Crossfinder software as detailed in section 4.2.4.5. Individual pairs of heavy and light cross-linked peptides were further analyzed with the Skyline software package (version 3.5.0.9319; https://skyline.ms/) (286). In the Skyline software, the sequence of identified cross-links was linearized and included customized modifications to account for the BS^3-H_4 cross-linker (156.078644 Da) and the mass difference between the isotopically labeled cross-linking agents (4.025107 Da). The elution peaks of these linearized cross-links were subsequently found in Thermo binary raw files and integrated in a semi-automated manner in the Skyline software. Each peak assignment was manually verified on the basis of the following criteria: (i) correct retention time (tolerance: 2 min), (ii) correct and appropriate elution peak boundaries, (iii) correct charge state of the precursor ion, (iv) transition items for the precursor ion > 0.75, and (v) precursor mass accuracy < 7.5 ppm. Peak assignments that did not meet the aforementioned criteria were discarded from further analysis. The average BS^3-H_4/BS^3-D_4 ratio for individual cross-links was obtained as described in section 2.5.3.

4.2.5. SAXS

4.2.5.1. Sample preparation

Freshly purified protein samples (V = 0.3−1.1 mL) were dialyzed against 500 mL SAXS buffer (cf. Table 12, the dialysate was exchanged three times) for approximately 24 hours at 4 °C using 3000–6000 Da MWCO Spectra/Por dialysis tubing. Following centrifugation for 10 min at 13000 rpm and 4 °C (Eppendorf 5417C centrifuge), samples were concentrated to 1−7 mg/mL (cf. Table 16) using Amicon Ultra-4 centrifugal filter units (10 or 30 kDa MWCO). Protein concentrations were determined by measuring the UV absorption at 280 nm employing a NanoDrop ND1000 spectrophotometer. Extinction coefficients for DmISWI and Snf2H proteins were obtained using the ProtParam tool from the ExPASy Proteomics server (http://web.expasy.org/protparam/). Sample purity was evaluated by SDS-PAGE analysis (cf. section 4.2.1.7). Finally, small aliquots of the purified proteins as well as respective buffer samples were flash frozen in liquid nitrogen and stored at -80 °C until further use.

Table 16: Prepared protein samples for SAXS measurements.

#	Enzyme	Enzyme concentration [g/l]	ADP-BeF_x [mM]	#	Enzyme	Enzyme concentration [g/l]	ADP-BeF_x [mM]
1	$ISWI_{WT}$	1.00	0	11	His_6-$ISWI_{\Delta HSS}$	3.34	3
2	$ISWI_{WT}$	2.00	0	12	His_6-$ISWI_{\Delta HSS}$	6.67	3
3	$ISWI_{WT}$	4.00	0	13	HSS_{ISWI}	1.83	0
4	$ISWI_{WT}$	1.00	3	14	HSS_{ISWI}	4.58	0
5	$ISWI_{WT}$	2.00	3	15	Snf2H	1.00	0
6	$ISWI_{WT}$	4.00	3	16	Snf2H	2.00	0
7	His_6-$ISWI_{\Delta HSS}$	1.50	0	17	Snf2H	4.00	0
8	His_6-$ISWI_{\Delta HSS}$	3.34	0	18	Snf2H	1.00	3
9	His_6-$ISWI_{\Delta HSS}$	7.00	0	19	Snf2H	2.00	3
10	His_6-$ISWI_{\Delta HSS}$	1.50	3	20	Snf2H	4.00	3

4.2.5.2. Data acquisition and analysis

SAXS measurements of different ISWI and Snf2H samples (cf. Table 16) as well as data analysis were kindly performed by Dr. L. Brützel (LMU, Munich) as described in (1). Briefly, data were collected at beamline BM29, ESRF, Grenoble (287) at an X-ray wavelength (λ) of 0.99 Å using a sample-to-detector distance of 2.87 m and a Pilatus 1M detector. This experimental setup resulted in an acceptable q-range of approximately 0.1−3.5 nm^{-1} [$q = 4\pi\cdot\sin(\theta)/\lambda$, where θ is defined as the total scattering angle]. Following syringe filtration (0.22 µm) and centrifugation for 10 min at 13500 rpm (tabletop centrifuge from Eppendorf), each protein sample listed in Table 16 was measured 10 times using an exposure time of 4 s in 'flow' mode at room temperature. Matching buffer samples were measured in an identical manner before and after each protein sample. Neither protein nor buffer samples exhibited signs of radiation damage.

The collected SAXS data were processed by means of a custom-written MATLAB script (The MathWorks Inc.). That is, matching protein sample profiles were averaged and then background corrected by subtracting the averaged profiles of the respective buffer. In a final step, SAXS data of the lowest and highest concentrated protein sample were scaled and merged for the low- and high q-region, respectively.

Radii of gyration were calculated for each protein construct and condition by Guinier analyses using a custom-written MATLAB script. That is, the logarithm of the scattering intensity was fitted as a function of q^2 to a straight line for small values of q (288). The respective mean and standard deviation for each protein construct were obtained by repeating Guinier analysis ten times for varying fitting ranges between $1.0 < q_{max}\cdot R_g < 1.3$.

Low-resolution density maps for individual protein constructs and conditions were generated by applying a simulated annealing protocol in the DAMMIF software (289). For each scattering profile, 20 independent runs in the "slow" mode were performed with default parameters and assuming no symmetry. The low-resolution structures of each molecule were subsequently aligned using a normalized spatial discrepancy (NSD) criterion (290) and averaged in the DAMAVER software (291). Notably, models for each protein and condition were structurally similar as indicated by pairwise NSD values between zero and one. The aligned bead models were averaged and loosely connected beads were removed by filtering. These models were subsequently converted into electron density maps using the pdb2vol program from the SITUS package (version 2.7.2) (292) and aligned to the respective atomic structures. The nominal resolution of the scattering data may be expressed on the basis of the highest measured q-values (i.e., 3.5 nm^{-1}) as $2\pi/q_{max}$ (293). According to this equation, we obtained a nominal resolution of approximately 2 nm. However, the resolution assessment for *ab-initio* shape reconstructions is not clearly defined; the resolution of individual models determined from the SAXS scattering data is estimated to be in the range of 2–3 nm (Prof. Dr.

Jan Lipfert, LMU, personal communication). Finally, molecular envelope shapes with aligned structures were prepared using visual molecular dynamics (294).

4.2.6. Computational modeling

XL-MS-driven modeling of all DmISWI and Snf2H structures was kindly performed by Dr. C. Schindler (TUM, Munich).

4.2.6.1. Structure preparation

The input structures for rigid body docking were prepared by homology modeling of individual DmISWI and Snf2H domains based on available X-ray structures of related remodeling enzymes using the MODELLER software (295). The ATPase modules of DmISWI and Snf2H were homology modeled from the X-ray structure of ScChd1 (pdb 3MWY) (141). Residues N- and C-terminal to residue 116 and 637, respectively, were excluded from the final models due to poor sequence conservation and structure dissimilarities in these regions between different experimental structures. The ATPase domain was subsequently cleaved at a predicted hinge region (i.e., residues 351–352 in DmISWI) (Emekli et al., 2008) that connects both ATPase lobes. Consequently, the two rigid bodies of the ATPase domain used for docking of the DmISWI enzyme comprised residues 116–351 and 352–637. Likewise, the two lobes used for docking of the Snf2H enzyme comprised residues 120–403 and 404–689. There was no need to homology model the HSS domain of the DmISWI enzyme because the structure of the DNA-binding domain has been successfully determined by X-ray crystallography (116). The HSS domain of Snf2H in turn was homology modeled from the HSS structure of the DmISWI enzyme (pdb 1OFC). In a final step, protein structures were transformed into the ATTRACT coarse-grained (296, 297) and all-atom representation (298, 299) using the ATTRACT tools ‘reduce’ and ‘aareduce’. Missing atoms were reconstructed with PDB2PQR (300, 301). Protonation states were assigned with PropKa (302).

4.2.6.2. Rigid body docking

Rigid body docking was performed using a custom-modified ATTRACT protein-protein docking protocol (303) that enabled the implementation of XL-MS-derived distance restraints between pairs of Cα atoms. The distance between Cα atoms of selected cross-linked residue pairs was restrained by an upper harmonic potential with a maximum distance of 25 and 29 Å for chemical BS^2G and BS^3 cross-links, respectively. Likewise, the maximum distance for Bpa-mediated cross-links was set to 20 Å. Cross-links that were implemented in the docking protocol yielded excellent fragmentation data during MS/MS analysis (cf. Figure 19, Figure 44A, and SFigure 5–SFigure 7) and are marked in STable 1–STable 5. In addition, the distance between residues of the predicted hinge region of the ATPase domain (i.e., residues 351–352 and 403–404 in DmISWI and Snf2H, respectively) was restrained in order to keep these adjacent residues within a maximum distance of 10 Å during computational docking.

In the case of the DmISWI enzyme, integrative modeling of the ATPase domain was initiated by generating 100000 starting configurations with both rigid bodies being placed at random positions and orientations. For each starting configuration, the center-of-mass translation and orientation of rigid bodies was optimized in a potential energy minimization using the ATTRACT coarse-grained force field (296, 297) and XL-MS-derived distance restraints for the ATPase domain (cf. STable 1). Notably, *ab-initio* docking of the ATPase domain was performed in an identical manner in the absence of XL-MS-derived distance restraints. The different structures were ranked on the basis of their ATTRACT score evaluated within a squared cutoff of 50 $Å^2$ and the restraint potentials. The top-ranked 200 ATPase structures were considered for further refinement with the flexible interface refinement method iATTRACT (304). The XL-MS-derived distance restraints were also implemented during flexible refinement. The convergence of individual structures was assessed by calculating the model precision as the minimal average pair-wise Cα RMSD (305) between the respective 200 final models.

To model the full-length DmISWI enzyme, the ten best models of the ATPase domain were docked against the crystal structure of the HSS domain (pdb 1OFC) (116) in an ensemble docking approach. The above described modeling procedure was repeated with 100000 starting configurations for each of the ten ATPase structures. The computational docking was guided by selected, XL-MS-derived distance restraints between the ATPase domain and the HSS domain as further specified in STable 2.

In the case of the Snf2H enzyme, the modeling strategy had to be slightly adapted compared to the one described for the DmISWI enzyme in order to overcome the limited number of identified cross-links between both rigid bodies of the ATPase domain. That is, integrative modeling of the full-length Snf2H protein was initiated by placing individual Snf2H domains (i.e., both rigid bodies of the ATPase domain and the HSS homology model) at random positions and orientations ($1x10^5$ starting configurations). Using a three-body docking protocol, the arrangement of both ATPase lobes in the modeled Snf2H structures would primarily depend on their relative orientation towards the HSS domain. Optimization of each starting configuration in terms of potential energy minimization and flexible refinement was identical as described above and was guided by selected XL-MS-derived distance restraints (cf. STable 3and STable 4) between individual structural bodies.

Individual enzyme models were compared against SAXS data using FoXS with defaults settings. The calculated values are reported as reduced χ-values (306). The model with the best

χ-fit to the SAXS data was typically selected as representative structural model. Finally, DmISWI and Snf2H models were visualized with the PyMOL software (versions 1.1eval and 1.30) and identified cross-links mapped onto the structures for the evaluation of Cα-Cα distances (cf. STable 1–STable 5).

4.2.7. Functional assays

4.2.7.1. Electrophoretic mobility shift assay

The formation of enzyme-nucleosome complexes was investigated by an electrophoretic mobility shift assay (EMSA). That is, increasing amounts of either DmISWI or Snf2H were titrated to a constant amount of 0N40 mononucleosomes in EMSA buffer #1–5 (cf. Table 12). Protein concentrations and buffer conditions that were used during EMSA analysis are specified in Figure 40 and SFigure 3. In addition, selected samples contained 3 mM of a particular nucleotide (i.e., ADP, ADP-BeF_x, and AMP-PNP) and/or 0N0 instead of 0N40 mononucleosomes. Following incubation for 10 min on ice, the sample was separated by native PAGE/0.2x TBE as described in section 4.2.1.6. To evaluate the impact of chemical cross-linking on complex formation, the sample was supplemented with either the BS^2G or BS^3 cross-linking agent. Following incubation for 20 min on ice, the cross-linking reaction was quenched with 200 mM NH_4HCO_3 and the sample was separated by native PAGE/0.2x TBE.

4.2.7.2. ATPase assays

4.2.7.2.1. Thin-layer chromatography ATPase assay

ATP hydrolysis of DmISWI and Snf2H was assessed by means of a thin-layer chromatography (TLC)-based ATPase assay as described previously (140). Briefly, individual samples were prepared by mixing the remodeling enzyme, salmon sperm DNA, and increasing concentrations of ADP-BeF_x according to Table 17 in TLC reaction buffer (cf. Table 12).

Table 17: Prepared protein samples for TLC ATPase assay.

#	Enzyme	Enzyme concentration [nM]	Salmon sperm DNA [g/L]	ADP-BeF_x [mM]
1	Snf2H	300	0.2	0, 0.5 or 5.0
2	Snf2H	1000	0	0, 0.5 or 5.0
3	Snf2H	6000	0	0, 0.5 or 5.0
4	$ISWI_{WT}$	80	0.2	0, 0.5 or 5.0
5	$ISWI_{WT}$	6000	0	0, 0.5 or 5.0
6	$ISWI_{WT}$	1000	0	0, 0.5 or 5.0
7	$ISWI_{\Delta HSS}$	6000	0	0, 0.5 or 5.0

ATP hydrolysis was initiated by addition of 1 µM Mg^{2+}-ATP and 0.2 µCi [γ-^{32}P]ATP (3000 Ci/mmol) and the sample was incubated for various time intervals at 28 °C. Data for the 0 min time point were collected in the absence of the respective remodeling enzyme. The enzymatic reaction was quenched by diluting the sample into 3 volumes of TLC quench solution (cf. Table 12). A total of 0.5 µL of the quenched sample was subsequently spotted onto TLC PEI cellulose F plates, which were developed in TLC developer solution (cf. Table 12) for approximately 20 min. Air-dried plates were exposed for approximately four hours to an imaging plate, which was read out by a Fluorescent Image Analyzer FLA-3000 instrument. The signals corresponding to unhydrolyzed ATP and free phosphate were quantified using the AIDA Image Analyzer software (Elysia-Raytest GmbH). The percentage of hydrolyzed ATP was calculated for each time point and condition. These values were plotted as a function of time and were fitted to a linear function to deduce the slope that corresponds to the percentage of hydrolyzed ATP per minute. Finally, results from the TLC-based ATPase assay were normalized for enzyme concentration and the number of ATP molecules hydrolyzed per enzyme per minute was plotted as a function of ADP-BeF_x concentration.

4.2.7.2.2. NADH-coupled ATPase assay

ATP hydrolysis of DmISWI and individual point-mutant constructs (i.e., $ISWI_{K337D}$, $ISWI_{D485K}$, and $ISWI_{K337D\ D485K}$) was measured using a NADH-coupled ATPase assay as described previously (140). Individual samples were prepared by mixing the enzyme (300 nM), pyruvate kinase (15.5 U/mL), phosphoenolpyruvate (6 mM), lactate dehydrogenase (15.5 U/mL), reduced nicotinamide adenine dinucleotide (NADH, 1.2 mM), and varying amounts of salmon sperm DNA (0–1.3 g/L) in ATPase assay buffer (cf. Table 12). ATP hydrolysis was subsequently initiated by addition of 3 mM ATP-Mg^{2+}. The ATPase assay was performed in flat bottom 384 well plates at 26 °C using a final reaction volume of 30 µL. The concentration of NADH was monitored by absorption measurements for 30 min employing a PowerWave HT 384 well plate reader. ATPase activities were calculated from linear fits to the data. To determine the maximal turnover rate of individual remodeling enzymes at saturating DNA concentrations, the ATPase activities were subsequently fitted to the Michaelis-Menten equation using the KaleidaGraph software (version 4.03). To ensure equal enzyme amounts during the NADH-coupled ATPase assay, a fraction of each reaction mixture was analyzed by SDS-PAGE and Coomassie Blue staining. Bands corresponding to DmISWI were quantified with the Bio-Rad Image Lab 5.2.1 software (cf. Figure 17D).

5. References

1. Harrer N, Schindler CEM, Bruetzel LK, Forne I, Ludwigsen J, Imhof A, et al. Structural Architecture of the Nucleosome Remodeler ISWI Determined from Cross-Linking, Mass Spectrometry, SAXS, and Modeling. Structure. 2018;26(2):282-94 e6.

2. International Human Genome Sequencing C. Finishing the euchromatic sequence of the human genome. Nature. 2004;431(7011):931-45.

3. Swygert SG, Peterson CL. Chromatin dynamics: interplay between remodeling enzymes and histone modifications. Biochim Biophys Acta. 2014;1839(8):728-36.

4. Wang J, Jia ST, Jia S. New Insights into the Regulation of Heterochromatin. Trends Genet. 2016;32(5):284-94.

5. Rosa S, Shaw P. Insights into chromatin structure and dynamics in plants. Biology (Basel). 2013;2(4):1378-410.

6. Kouzarides T. Chromatin Modifications and Their Function. Cell. 2007;128(4):693-705.

7. Margueron R, Reinberg D. Chromatin structure and the inheritance of epigenetic information. Nature Reviews Genetics. 2010;11:285.

8. McGhee JD, Felsenfeld G. Nucleosome structure. Annu Rev Biochem. 1980;49:1115-56.

9. Kornberg RD. Chromatin structure: a repeating unit of histones and DNA. Science. 1974;184(4139):868-71.

10. Luger K, Mader AW, Richmond RK, Sargent DF, Richmond TJ. Crystal structure of the nucleosome core particle at 2.8 A resolution. Nature. 1997;389(6648):251-60.

11. Richmond TJ, Finch JT, Rushton B, Rhodes D, Klug A. Structure of the nucleosome core particle at 7 A resolution. Nature. 1984;311(5986):532-7.

12. Arents G, Burlingame RW, Wang BC, Love WE, Moudrianakis EN. The nucleosomal core histone octamer at 3.1 A resolution: a tripartite protein assembly and a left-handed superhelix. Proc Natl Acad Sci U S A. 1991;88(22):10148-52.

13. Thomas JO, Kornberg RD. An octamer of histones in chromatin and free in solution. Proc Natl Acad Sci U S A. 1975;72(7):2626-30.

14. Thatcher TH, Gorovsky MA. Phylogenetic analysis of the core histones H2A, H2B, H3, and H4. Nucleic Acids Res. 1994;22(2):174-9.

15. Arents G, Moudrianakis EN. The histone fold: a ubiquitous architectural motif utilized in DNA compaction and protein dimerization. Proc Natl Acad Sci U S A. 1995;92(24):11170-4.

16. Peterson CL, Laniel MA. Histones and histone modifications. Curr Biol. 2004;14(14):R546-51.

17. Jenuwein T, Allis CD. Translating the histone code. Science. 2001;293(5532):1074-80.

18. Davey CA, Sargent DF, Luger K, Maeder AW, Richmond TJ. Solvent mediated interactions in the structure of the nucleosome core particle at 1.9 a resolution. J Mol Biol. 2002;319(5):1097-113.

19. Hall MA, Shundrovsky A, Bai L, Fulbright RM, Lis JT, Wang MD. High-resolution dynamic mapping of histone-DNA interactions in a nucleosome. Nat Struct Mol Biol. 2009;16(2):124-9.

20. Kono H, Sakuraba S, Ishida H. Free energy profiles for unwrapping the outer superhelical turn of nucleosomal DNA. PLoS Comput Biol. 2018;14(3):e1006024.

21. Liu X, Li M, Xia X, Li X, Chen Z. Mechanism of chromatin remodelling revealed by the Snf2-nucleosome structure. Nature. 2017;544(7651):440-5.

22. Kagalwala MN, Glaus BJ, Dang W, Zofall M, Bartholomew B. Topography of the ISW2-nucleosome complex: insights into nucleosome spacing and chromatin remodeling. EMBO J. 2004;23(10):2092-104.

23. Dang W, Bartholomew B. Domain architecture of the catalytic subunit in the ISW2-nucleosome complex. Molecular and cellular biology. 2007;27(23):8306-17.

24. Farnung L, Vos SM, Wigge C, Cramer P. Nucleosome-Chd1 structure and implications for chromatin remodelling. Nature. 2017;550(7677):539-42.

25. Zofall M, Persinger J, Kassabov SR, Bartholomew B. Chromatin remodeling by ISW2 and SWI/SNF requires DNA translocation inside the nucleosome. Nat Struct Mol Biol. 2006;13(4):339-46.

26. Kalashnikova AA, Porter-Goff ME, Muthurajan UM, Luger K, Hansen JC. The role of the nucleosome acidic patch in modulating higher order chromatin structure. J R Soc Interface. 2013;10(82):20121022.

27. Dann GP, Liszczak GP, Bagert JD, Muller MM, Nguyen UTT, Wojcik F, et al. ISWI chromatin remodellers sense nucleosome modifications to determine substrate preference. Nature. 2017;548(7669):607-11.

28. Gamarra N, Johnson SL, Trnka MJ, Burlingame AL, Narlikar GJ. The nucleosomal acidic patch relieves auto-inhibition by the ISWI remodeler SNF2h. Elife. 2018;7.

29. Olins AL, Olins DE. Spheroid chromatin units (v bodies). Science. 1974;183(4122):330-2.

30. Woodcock C, editor Ultrastructure of inactive chromatin. Journal of Cell Biology; 1973: ROCKEFELLER UNIV PRESS 1114 FIRST AVE, 4TH FL, NEW YORK, NY 10021.

31. Fletcher TM, Hansen JC. The nucleosomal array: structure/function relationships. Crit Rev Eukaryot Gene Expr. 1996;6(2-3):149-88.

32. Hergeth SP, Schneider R. The H1 linker histones: multifunctional proteins beyond the nucleosomal core particle. EMBO Rep. 2015;16(11):1439-53.

33. Harshman SW, Young NL, Parthun MR, Freitas MA. H1 histones: current perspectives and challenges. Nucleic Acids Res. 2013;41(21):9593-609.

34. Marsden MP, Laemmli UK. Metaphase chromosome structure: evidence for a radial loop model. Cell. 1979;17(4):849-58.

35. Langmore JP, Schutt C. The higher order structure of chicken erythrocyte chromosomes in vivo. Nature. 1980;288(5791):620-2.

36. Song F, Chen P, Sun D, Wang M, Dong L, Liang D, et al. Cryo-EM study of the chromatin fiber reveals a double helix twisted by tetranucleosomal units. Science. 2014;344(6182):376-80.

37. Tremethick DJ. Higher-order structures of chromatin: the elusive 30 nm fiber. Cell. 2007;128(4):651-4.

38. Finch JT, Klug A. Solenoidal model for superstructure in chromatin. Proc Natl Acad Sci U S A. 1976;73(6):1897-901.

39. Williams SP, Athey BD, Muglia LJ, Schappe RS, Gough AH, Langmore JP. Chromatin fibers are left-handed double helices with diameter and mass per unit length that depend on linker length. Biophys J. 1986;49(1):233-48.

40. Maeshima K, Hihara S, Eltsov M. Chromatin structure: does the 30-nm fibre exist in vivo? Current opinion in cell biology. 2010;22(3):291-7.

41. Fussner E, Ching RW, Bazett-Jones DP. Living without 30 nm chromatin fibers. Trends in biochemical sciences. 2011;36(1):1-6.

42. Eltsov M, Maclellan KM, Maeshima K, Frangakis AS, Dubochet J. Analysis of cryo-electron microscopy images does not support the existence of 30-nm chromatin fibers in mitotic chromosomes in situ. Proc Natl Acad Sci U S A. 2008;105(50):19732-7.

43. Luger K, Dechassa ML, Tremethick DJ. New insights into nucleosome and chromatin structure: an ordered state or a disordered affair? Nature reviews Molecular cell biology. 2012;13(7):436.

44. Zhou BR, Jiang J, Ghirlando R, Norouzi D, Sathish Yadav KN, Feng H, et al. Revisit of Reconstituted 30-Nm Nucleosome Arrays Reveals an Ensemble of Dynamic Structures. J Mol Biol. 2018.

45. Maeshima K, Imai R, Tamura S, Nozaki T. Chromatin as dynamic 10-nm fibers. Chromosoma. 2014;123(3):225-37.

46. Maeshima K, Rogge R, Tamura S, Joti Y, Hikima T, Szerlong H, et al. Nucleosomal arrays self-assemble into supramolecular globular structures lacking 30-nm fibers. EMBO J. 2016;35(10):1115-32.

47. Chakravarthy S, Park YJ, Chodaparambil J, Edayathumangalam RS, Luger K. Structure and dynamic properties of nucleosome core particles. FEBS Lett. 2005;579(4):895-8.

48. Zlatanova J, Bishop TC, Victor JM, Jackson V, van Holde K. The nucleosome family: dynamic and growing. Structure. 2009;17(2):160-71.

49. Melters DP, Nye J, Zhao H, Dalal Y. Chromatin Dynamics in Vivo: A Game of Musical Chairs. Genes (Basel). 2015;6(3):751-76.

50. Talbert PB, Henikoff S. Histone variants on the move: substrates for chromatin dynamics. Nat Rev Mol Cell Biol. 2017;18(2):115-26.

51. Gautier T, Abbott DW, Molla A, Verdel A, Ausio J, Dimitrov S. Histone variant H2ABbd confers lower stability to the nucleosome. EMBO Rep. 2004;5(7):715-20.

52. Jin C, Felsenfeld G. Nucleosome stability mediated by histone variants H3.3 and H2A.Z. Genes Dev. 2007;21(12):1519-29.

53. Fan JY, Rangasamy D, Luger K, Tremethick DJ. H2A.Z alters the nucleosome surface to promote HP1alpha-mediated chromatin fiber folding. Molecular cell. 2004;16(4):655-61.

54. Henikoff S, Smith MM. Histone variants and epigenetics. Cold Spring Harb Perspect Biol. 2015;7(1):a019364.

55. Georgoulis A, Vorgias CE, Chrousos GP, Rogakou EP. Genome Instability and gammaH2AX. Int J Mol Sci. 2017;18(9).

56. Bannister AJ, Kouzarides T. Regulation of chromatin by histone modifications. Cell Res. 2011;21(3):381-95.

57. Bowman GD, Poirier MG. Post-translational modifications of histones that influence nucleosome dynamics. Chem Rev. 2015;115(6):2274-95.

58. Olsen CA. Expansion of the lysine acylation landscape. Angew Chem Int Ed Engl. 2012;51(16):3755-6.

59. Kebede AF, Schneider R, Daujat S. Novel types and sites of histone modifications emerge as players in the transcriptional regulation contest. FEBS J. 2015;282(9):1658-74.

60. Allfrey VG, Faulkner R, Mirsky AE. Acetylation and Methylation of Histones and Their Possible Role in the Regulation of Rna Synthesis. Proc Natl Acad Sci U S A. 1964;51:786-94.

61. Pogo BG, Allfrey VG, Mirsky AE. RNA synthesis and histone acetylation during the course of gene activation in lymphocytes. Proc Natl Acad Sci U S A. 1966;55(4):805-12.

62. Galvani A, Thiriet C. Nucleosome Dancing at the Tempo of Histone Tail Acetylation. Genes (Basel). 2015;6(3):607-21.

63. Millar CB, Kurdistani SK, Grunstein M. Acetylation of yeast histone H4 lysine 16: a switch for protein interactions in heterochromatin and euchromatin. Cold Spring Harb Symp Quant Biol. 2004;69:193-200.

64. Shia WJ, Pattenden SG, Workman JL. Histone H4 lysine 16 acetylation breaks the genome's silence. Genome Biol. 2006;7(5):217.

65. Shogren-Knaak M, Ishii H, Sun JM, Pazin MJ, Davie JR, Peterson CL. Histone H4-K16 acetylation controls chromatin structure and protein interactions. Science. 2006;311(5762):844-7.

66. Robinson PJ, An W, Routh A, Martino F, Chapman L, Roeder RG, et al. 30 nm chromatin fibre decompaction requires both H4-K16 acetylation and linker histone eviction. J Mol Biol. 2008;381(4):816-25.

67. Liu Y, Lu C, Yang Y, Fan Y, Yang R, Liu CF, et al. Influence of histone tails and H4 tail acetylations on nucleosome-nucleosome interactions. J Mol Biol. 2011;414(5):749-64.

68. Klinker H, Mueller-Planitz F, Yang R, Forne I, Liu CF, Nordenskiold L, et al. ISWI remodelling of physiological chromatin fibres acetylated at lysine 16 of histone H4. PLoS One. 2014;9(2):e88411.

69. Ferreira H, Flaus A, Owen-Hughes T. Histone modifications influence the action of Snf2 family remodelling enzymes by different mechanisms. J Mol Biol. 2007;374(3):563-79.

70. Corona DF, Clapier CR, Becker PB, Tamkun JW. Modulation of ISWI function by site-specific histone acetylation. EMBO Rep. 2002;3(3):242-7.

71. Clapier CR, Nightingale KP, Becker PB. A critical epitope for substrate recognition by the nucleosome remodeling ATPase ISWI. Nucleic Acids Res. 2002;30(3):649-55.

72. Mani U, S AS, Goutham RNA, Mohan SS. SWI/SNF Infobase-An exclusive information portal for SWI/SNF remodeling complex subunits. PLoS One. 2017;12(9):e0184445.

73. Zeng L, Zhou MM. Bromodomain: an acetyl-lysine binding domain. FEBS Lett. 2002;513(1):124-8.

74. Strahl BD, Allis CD. The language of covalent histone modifications. Nature. 2000;403(6765):41-5.

75. Soshnev AA, Josefowicz SZ, Allis CD. Greater Than the Sum of Parts: Complexity of the Dynamic Epigenome. Molecular cell. 2016;62(5):681-94.

76. Prakash K, Fournier D. Evidence for the implication of the histone code in building the genome structure. Biosystems. 2018;164:49-59.

77. Holoch D, Moazed D. RNA-mediated epigenetic regulation of gene expression. Nat Rev Genet. 2015;16(2):71-84.

78. Bergmann JH, Spector DL. Long non-coding RNAs: modulators of nuclear structure and function. Curr Opin Cell Biol. 2014;26:10-8.

79. McBryant SJ, Adams VH, Hansen JC. Chromatin architectural proteins. Chromosome Res. 2006;14(1):39-51.

80. Smith ZD, Meissner A. DNA methylation: roles in mammalian development. Nat Rev Genet. 2013;14(3):204-20.

81. Becker PB, Workman JL. Nucleosome remodeling and epigenetics. Cold Spring Harb Perspect Biol. 2013;5(9).

82. Workman JL, Abmayr SM. Fundamentals of chromatin. New York: Springer; 2014. xiii, 587 pages p.

83. Clapier CR, Cairns BR. The biology of chromatin remodeling complexes. Annu Rev Biochem. 2009;78:273-304.

84. Yang JG, Madrid TS, Sevastopoulos E, Narlikar GJ. The chromatin-remodeling enzyme ACF is an ATP-dependent DNA length sensor that regulates nucleosome spacing. Nat Struct Mol Biol. 2006;13(12):1078-83.

85. Ito T, Bulger M, Pazin MJ, Kobayashi R, Kadonaga JT. ACF, an ISWI-containing and ATP-utilizing chromatin assembly and remodeling factor. Cell. 1997;90(1):145-55.

86. Bruno M, Flaus A, Stockdale C, Rencurel C, Ferreira H, Owen-Hughes T. Histone H2A/H2B dimer exchange by ATP-dependent chromatin remodeling activities. Molecular cell. 2003;12(6):1599-606.

87. Walfridsson J, Khorosjutina O, Matikainen P, Gustafsson CM, Ekwall K. A genome-wide role for CHD remodelling factors and Nap1 in nucleosome disassembly. EMBO J. 2007;26(12):2868-79.

88. Jaskelioff M, Gavin IM, Peterson CL, Logie C. SWI-SNF-mediated nucleosome remodeling: role of histone octamer mobility in the persistence of the remodeled state. Molecular and cellular biology. 2000;20(9):3058-68.

89. Narlikar GJ, Sundaramoorthy R, Owen-Hughes T. Mechanisms and functions of ATP-dependent chromatin-remodeling enzymes. Cell. 2013;154(3):490-503.

90. Kumar R, Li DQ, Muller S, Knapp S. Epigenomic regulation of oncogenesis by chromatin remodeling. Oncogene. 2016;35(34):4423-36.

91. Langst G, Manelyte L. Chromatin Remodelers: From Function to Dysfunction. Genes (Basel). 2015;6(2):299-324.

92. Tsukiyama T, Wu C. Purification and properties of an ATP-dependent nucleosome remodeling factor. Cell. 1995;83(6):1011-20.

93. Tsukiyama T, Daniel C, Tamkun J, Wu C. ISWI, a member of the SWl2/SNF2 ATPase family, encodes the 140 kDa subunit of the nucleosome remodeling factor. Cell. 1995;83(6):1021-6.

94. Aihara T, Miyoshi Y, Koyama K, Suzuki M, Takahashi E, Monden M, et al. Cloning and mapping of SMARCA5 encoding hSNF2H, a novel human homologue of Drosophila ISWI. Cytogenetic and Genome Research. 1998;81(3-4):191-3.

95. Lazzaro MA, Picketts DJ. Cloning and characterization of the murine Imitation Switch (ISWI) genes: differential expression patterns suggest distinct developmental roles for Snf2h and Snf2l. Journal of neurochemistry. 2001;77(4):1145-56.

96. Poot RA, Dellaire G, Hülsmann BB, Grimaldi MA, Corona DF, Becker PB, et al. HuCHRAC, a human ISWI chromatin remodelling complex contains hACF1 and two novel histone- fold proteins. The EMBO journal. 2000;19(13):3377-87.

97. Varga-Weisz PD, Wilm M, Bonte E, Dumas K, Mann M, Becker PB. Chromatin-remodelling factor CHRAC contains the ATPases ISWI and topoisomerase II. Nature. 1997;388(6642):598.

98. LeRoy G, Orphanides G, Lane WS, Reinberg D. Requirement of RSF and FACT for transcription of chromatin templates in vitro. Science. 1998;282(5395):1900-4.

99. Loyola A, Huang J-Y, LeRoy G, Hu S, Wang Y-H, Donnelly RJ, et al. Functional analysis of the subunits of the chromatin assembly factor RSF. Molecular and cellular biology. 2003;23(19):6759-68.

100. Strohner R, Nemeth A, Jansa P, Hofmann- Rohrer U, Santoro R, Längst G, et al. NoRC—a novel member of mammalian ISWI- containing chromatin remodeling machines. The EMBO journal. 2001;20(17):4892-900.

101. Bozhenok L, Wade PA, Varga- Weisz P. WSTF–ISWI chromatin remodeling complex targets heterochromatic replication foci. The EMBO journal. 2002;21(9):2231-41.

102. Banting GS, Barak O, Ames TM, Burnham AC, Kardel MD, Cooch NS, et al. CECR2, a protein involved in neurulation, forms a novel chromatin remodeling complex with SNF2L. Human molecular genetics. 2005;14(4):513-24.

103. Oppikofer M, Bai T, Gan Y, Haley B, Liu P, Sandoval W, et al. Expansion of the ISWI chromatin remodeler family with new active complexes. EMBO reports. 2017:e201744011.

104. Hakimi M-A, Bochar DA, Schmiesing JA, Dong Y, Barak OG, Speicher DW, et al. A chromatin remodelling complex that loads cohesin onto human chromosomes. Nature. 2002;418(6901):994.

105. Eberharter A, Vetter I, Ferreira R, Becker PB. ACF1 improves the effectiveness of nucleosome mobilization by ISWI through PHD-histone contacts. EMBO J. 2004;23(20):4029-39.

106. Ruthenburg AJ, Li H, Milne TA, Dewell S, McGinty RK, Yuen M, et al. Recognition of a mononucleosomal histone modification pattern by BPTF via multivalent interactions. Cell. 2011;145(5):692-706.

107. Singleton MR, Wigley DB. Modularity and specialization in superfamily 1 and 2 helicases. J Bacteriol. 2002;184(7):1819-26.

108. Flaus A, Martin DM, Barton GJ, Owen-Hughes T. Identification of multiple distinct Snf2 subfamilies with conserved structural motifs. Nucleic Acids Res. 2006;34(10):2887-905.

109. Thoma NH, Czyzewski BK, Alexeev AA, Mazin AV, Kowalczykowski SC, Pavletich NP. Structure of the SWI2/SNF2 chromatin-remodeling domain of eukaryotic Rad54. Nat Struct Mol Biol. 2005;12(4):350-6.

110. Hall MC, Matson SW. Helicase motifs: the engine that powers DNA unwinding. Mol Microbiol. 1999;34(5):867-77.

111. De la Rosa MB, Nelson SW. An interaction between the Walker A and D-loop motifs is critical to ATP hydrolysis and cooperativity in bacteriophage T4 Rad50. J Biol Chem. 2011;286(29):26258-66.

112. Elles LM, Uhlenbeck OC. Mutation of the arginine finger in the active site of Escherichia coli DbpA abolishes ATPase and helicase activity and confers a dominant slow growth phenotype. Nucleic Acids Res. 2008;36(1):41-50.

113. Nagy GN, Suardiaz R, Lopata A, Ozohanics O, Vekey K, Brooks BR, et al. Structural Characterization of Arginine Fingers: Identification of an Arginine Finger for the Pyrophosphatase dUTPases. J Am Chem Soc. 2016;138(45):15035-45.

114. Clapier CR, Cairns BR. Regulation of ISWI involves inhibitory modules antagonized by nucleosomal epitopes. Nature. 2012;492(7428):280-4.

115. Ludwigsen J, Pfennig S, Singh AK, Schindler C, Harrer N, Forne I, et al. Concerted regulation of ISWI by an autoinhibitory domain and the H4 N-terminal tail. Elife. 2017;6:e21477.

116. Grune T, Brzeski J, Eberharter A, Clapier CR, Corona DF, Becker PB, et al. Crystal structure and functional analysis of a nucleosome recognition module of the remodeling factor ISWI. Molecular cell. 2003;12(2):449-60.

117. Ogata K, Morikawa S, Nakamura H, Sekikawa A, Inoue T, Kanai H, et al. Solution structure of a specific DNA complex of the Myb DNA-binding domain with cooperative recognition helices. Cell. 1994;79(4):639-48.

118. Sharma A, Jenkins KR, Heroux A, Bowman GD. Crystal structure of the chromodomain helicase DNA-binding protein 1 (Chd1) DNA-binding domain in complex with DNA. J Biol Chem. 2011;286(49):42099-104.

119. Schwanbeck R, Xiao H, Wu C. Spatial contacts and nucleosome step movements induced by the NURF chromatin remodeling complex. J Biol Chem. 2004;279(38):39933-41.

120. Dechassa ML, Zhang B, Horowitz-Scherer R, Persinger J, Woodcock CL, Peterson CL, et al. Architecture of the SWI/SNF-nucleosome complex. Molecular and cellular biology. 2008;28(19):6010-21.

121. Dechassa ML, Hota SK, Sen P, Chatterjee N, Prasad P, Bartholomew B. Disparity in the DNA translocase domains of SWI/SNF and ISW2. Nucleic Acids Res. 2012;40(10):4412-21.

122. Saha A, Wittmeyer J, Cairns BR. Chromatin remodeling through directional DNA translocation from an internal nucleosomal site. Nat Struct Mol Biol. 2005;12(9):747-55.

123. Nodelman IM, Bleichert F, Patel A, Ren R, Horvath KC, Berger JM, et al. Interdomain Communication of the Chd1 Chromatin Remodeler across the DNA Gyres of the Nucleosome. Molecular cell. 2017;65(3):447-59 e6.

124. Clapier CR, Langst G, Corona DF, Becker PB, Nightingale KP. Critical role for the histone H4 N terminus in nucleosome remodeling by ISWI. Molecular and cellular biology. 2001;21(3):875-83.

125. Dang W, Kagalwala MN, Bartholomew B. Regulation of ISW2 by concerted action of histone H4 tail and extranucleosomal DNA. Molecular and cellular biology. 2006;26(20):7388-96.

126. Eustermann S, Schall K, Kostrewa D, Lakomek K, Strauss M, Moldt M, et al. Structural basis for ATP-dependent chromatin remodelling by the INO80 complex. Nature. 2018;556(7701):386-90.

127. Hota SK, Bhardwaj SK, Deindl S, Lin YC, Zhuang X, Bartholomew B. Nucleosome mobilization by ISW2 requires the concerted action of the ATPase and SLIDE domains. Nat Struct Mol Biol. 2013;20(2):222-9.

128. Ryan DP, Sundaramoorthy R, Martin D, Singh V, Owen-Hughes T. The DNA-binding domain of the Chd1 chromatin-remodelling enzyme contains SANT and SLIDE domains. EMBO J. 2011;30(13):2596-609.

129. Leonard JD, Narlikar GJ. A Nucleotide-Driven Switch Regulates Flanking DNA Length Sensing by a Dimeric Chromatin Remodeler. Molecular cell. 2015.

130. Flaus A, Owen-Hughes T. Mechanisms for nucleosome mobilization. Biopolymers. 2003;68(4):563-78.

131. Kulić I, Schiessel H. Chromatin dynamics: nucleosomes go mobile through twist defects. Physical review letters. 2003;91(14):148103.

132. Kulic IM, Schiessel H. Nucleosome repositioning via loop formation. Biophys J. 2003;84(5):3197-211.

133. Lorch Y, Davis B, Kornberg RD. Chromatin remodeling by DNA bending, not twisting. Proc Natl Acad Sci U S A. 2005;102(5):1329-32.

134. Lequieu J, Schwartz DC, de Pablo JJ. In silico evidence for sequence-dependent nucleosome sliding. Proceedings of the National Academy of Sciences. 2017;114(44):E9197-E205.

135. Eslami-Mossallam B, Schiessel H, van Noort J. Nucleosome dynamics: Sequence matters. Adv Colloid Interface Sci. 2016;232:101-13.

136. Blosser TR, Yang JG, Stone MD, Narlikar GJ, Zhuang X. Dynamics of nucleosome remodelling by individual ACF complexes. Nature. 2009;462(7276):1022.

137. Sirinakis G, Clapier CR, Gao Y, Viswanathan R, Cairns BR, Zhang Y. The RSC chromatin remodelling ATPase translocates DNA with high force and small step size. EMBO J. 2011;30(12):2364-72.

138. Deindl S, Hwang WL, Hota SK, Blosser TR, Prasad P, Bartholomew B, et al. ISWI remodelers slide nucleosomes with coordinated multi-base-pair entry steps and single-base-pair exit steps. Cell. 2013;152(3):442-52.

139. Brandani GB, Niina T, Tan C, Takada S. DNA sliding in nucleosomes via twist defect propagation revealed by molecular simulations. Nucleic Acids Research. 2018:gky158-gky.

140. Mueller-Planitz F, Klinker H, Ludwigsen J, Becker PB. The ATPase domain of ISWI is an autonomous nucleosome remodeling machine. Nat Struct Mol Biol. 2013;20(1):82-9.

141. Hauk G, McKnight JN, Nodelman IM, Bowman GD. The chromodomains of the Chd1 chromatin remodeler regulate DNA access to the ATPase motor. Molecular cell. 2010;39(5):711-23.

142. Hamiche A, Kang JG, Dennis C, Xiao H, Wu C. Histone tails modulate nucleosome mobility and regulate ATP-dependent nucleosome sliding by NURF. Proc Natl Acad Sci U S A. 2001;98(25):14316-21.

143. Fazzio TG, Gelbart ME, Tsukiyama T. Two distinct mechanisms of chromatin interaction by the Isw2 chromatin remodeling complex in vivo. Molecular and cellular biology. 2005;25(21):9165-74.

144. Zofall M, Persinger J, Bartholomew B. Functional role of extranucleosomal DNA and the entry site of the nucleosome in chromatin remodeling by ISW2. Molecular and cellular biology. 2004;24(22):10047-57.

145. McKnight JN, Jenkins KR, Nodelman IM, Escobar T, Bowman GD. Extranucleosomal DNA binding directs nucleosome sliding by Chd1. Molecular and cellular biology. 2011;31(23):4746-59.

146. Yan L, Wang L, Tian Y, Xia X, Chen Z. Structure and regulation of the chromatin remodeller ISWI. Nature. 2016;540(7633):466-9.

147. Hwang WL, Deindl S, Harada BT, Zhuang X. Histone H4 tail mediates allosteric regulation of nucleosome remodelling by linker DNA. Nature. 2014;512(7513):213-7.

148. Qiu Y, Levendosky RF, Chakravarthy S, Patel A, Bowman GD, Myong S. The Chd1 Chromatin Remodeler Shifts Nucleosomal DNA Bidirectionally as a Monomer. Molecular cell. 2017;68(1):76-88 e6.

149. Lusser A, Urwin DL, Kadonaga JT. Distinct activities of CHD1 and ACF in ATP-dependent chromatin assembly. Nat Struct Mol Biol. 2005;12(2):160-6.

150. Racki LR, Yang JG, Naber N, Partensky PD, Acevedo A, Purcell TJ, et al. The chromatin remodeller ACF acts as a dimeric motor to space nucleosomes. Nature. 2009;462(7276):1016-21.

151. Yamada K, Frouws TD, Angst B, Fitzgerald DJ, DeLuca C, Schimmele K, et al. Structure and mechanism of the chromatin remodelling factor ISW1a. Nature. 2011;472(7344):448-53.

152. Shaw G, Gan J, Zhou YN, Zhi H, Subburaman P, Zhang R, et al. Structure of RapA, a Swi2/Snf2 protein that recycles RNA polymerase during transcription. Structure. 2008;16(9):1417-27.

153. Xia X, Liu X, Li T, Fang X, Chen Z. Structure of chromatin remodeler Swi2/Snf2 in the resting state. Nat Struct Mol Biol. 2016;23(8):722-9.

154. Durr H, Korner C, Muller M, Hickmann V, Hopfner KP. X-ray structures of the Sulfolobus solfataricus SWI2/SNF2 ATPase core and its complex with DNA. Cell. 2005;121(3):363-73.

155. Sundaramoorthy R, Hughes AL, Singh V, Wiechens N, Ryan DP, El-Mkami H, et al. Structural reorganization of the chromatin remodeling enzyme Chd1 upon engagement with nucleosomes. Elife. 2017;6.

156. Tosi A, Haas C, Herzog F, Gilmozzi A, Berninghausen O, Ungewickell C, et al. Structure and subunit topology of the INO80 chromatin remodeler and its nucleosome complex. Cell. 2013;154(6):1207-19.

157. Forne I, Ludwigsen J, Imhof A, Becker PB, Mueller-Planitz F. Probing the conformation of the ISWI ATPase domain with genetically encoded photoreactive crosslinkers and mass spectrometry. Mol Cell Proteomics. 2012;11(4):M111 012088.

158. Lewis R, Durr H, Hopfner KP, Michaelis J. Conformational changes of a Swi2/Snf2 ATPase during its mechano-chemical cycle. Nucleic Acids Res. 2008;36(6):1881-90.

159. Racki LR, Naber N, Pate E, Leonard JD, Cooke R, Narlikar GJ. The histone H4 tail regulates the conformation of the ATP-binding pocket in the SNF2h chromatin remodeling enzyme. J Mol Biol. 2014;426(10):2034-44.

160. Graewert MA, Svergun DI. Impact and progress in small and wide angle X-ray scattering (SAXS and WAXS). Curr Opin Struct Biol. 2013;23(5):748-54.

161. Tuukkanen AT, Spilotros A, Svergun DI. Progress in small-angle scattering from biological solutions at high-brilliance synchrotrons. IUCrJ. 2017;4(Pt 5):518-28.

162. Patel TR, Chojnowski G, Astha, Koul A, McKenna SA, Bujnicki JM. Structural studies of RNA-protein complexes: A hybrid approach involving hydrodynamics, scattering, and computational methods. Methods. 2017;118-119:146-62.

163. Boldon L, Laliberte F, Liu L. Review of the fundamental theories behind small angle X-ray scattering, molecular dynamics simulations, and relevant integrated application. Nano Rev. 2015;6:25661.

164. Guinier A, Fournet Gr. Small-angle scattering of X-rays. New York,: Wiley; 1955. 268 p. p.

165. Rambo RP, Tainer JA. Accurate assessment of mass, models and resolution by small-angle scattering. Nature. 2013;496(7446):477-81.

166. Koch MH, Vachette P, Svergun DI. Small-angle scattering: a view on the properties, structures and structural changes of biological macromolecules in solution. Q Rev Biophys. 2003;36(2):147-227.

167. Stoddard CD, Montange RK, Hennelly SP, Rambo RP, Sanbonmatsu KY, Batey RT. Free state conformational sampling of the SAM-I riboswitch aptamer domain. Structure. 2010;18(7):787-97.

168. Lawson MR, Dyer K, Berger JM. Ligand-induced and small-molecule control of substrate loading in a hexameric helicase. Proc Natl Acad Sci U S A. 2016;113(48):13714-9.

169. Riek U, Scholz R, Konarev P, Rufer A, Suter M, Nazabal A, et al. Structural properties of AMP-activated protein kinase: dimerization, molecular shape, and changes upon ligand binding. J Biol Chem. 2008;283(26):18331-43.

170. Petoukhov MV, Svergun DI. Applications of small-angle X-ray scattering to biomacromolecular solutions. Int J Biochem Cell Biol. 2013;45(2):429-37.

171. Franke D, Jeffries CM, Svergun DI. Correlation Map, a goodness-of-fit test for one-dimensional X-ray scattering spectra. Nat Methods. 2015;12(5):419-22.

172. Ullman JB. Structural equation modeling: reviewing the basics and moving forward. J Pers Assess. 2006;87(1):35-50.

173. Schumacker RE, Lomax RG. A beginner's guide to structural equation modeling. 2004.

174. Watson AA, Mahajan P, Mertens HD, Deery MJ, Zhang W, Pham P, et al. The PHD and chromo domains regulate the ATPase activity of the human chromatin remodeler CHD4. J Mol Biol. 2012;422(1):3-17.

175. Schindler CEM, de Vries SJ, Sasse A, Zacharias M. SAXS Data Alone can Generate High-Quality Models of Protein-Protein Complexes. Structure. 2016;24(8):1387-97.

176. Young MM, Tang N, Hempel JC, Oshiro CM, Taylor EW, Kuntz ID, et al. High throughput protein fold identification by using experimental constraints derived from intramolecular cross-links and mass spectrometry. Proc Natl Acad Sci U S A. 2000;97(11):5802-6.

177. Leitner A, Walzthoeni T, Kahraman A, Herzog F, Rinner O, Beck M, et al. Probing native protein structures by chemical cross-linking, mass spectrometry, and bioinformatics. Mol Cell Proteomics. 2010;9(8):1634-49.

178. Hofmann T, Fischer AW, Meiler J, Kalkhof S. Protein structure prediction guided by crosslinking restraints--A systematic evaluation of the impact of the crosslinking spacer length. Methods. 2015;89:79-90.

179. Sinz A. Cross-Linking/Mass Spectrometry for Studying Protein Structures and Protein-Protein Interactions: Where Are We Now and Where Should We Go From Here? Angew Chem Int Ed Engl. 2018.

180. Leitner A, Reischl R, Walzthoeni T, Herzog F, Bohn S, Forster F, et al. Expanding the chemical cross-linking toolbox by the use of multiple proteases and enrichment by size exclusion chromatography. Mol Cell Proteomics. 2012;11(3):M111 014126.

181. Chin JW, Martin AB, King DS, Wang L, Schultz PG. Addition of a photocrosslinking amino acid to the genetic code of Escherichiacoli. Proc Natl Acad Sci U S A. 2002;99(17):11020-4.

182. Wittelsberger A, Thomas BE, Mierke DF, Rosenblatt M. Methionine acts as a "magnet" in photoaffinity crosslinking experiments. FEBS Lett. 2006;580(7):1872-6.

183. Kalkhof S, Sinz A. Chances and pitfalls of chemical cross-linking with amine-reactive N-hydroxysuccinimide esters. Anal Bioanal Chem. 2008;392(1-2):305-12.

184. Madler S, Bich C, Touboul D, Zenobi R. Chemical cross-linking with NHS esters: a systematic study on amino acid reactivities. J Mass Spectrom. 2009;44(5):694-706.

185. Muller DR, Schindler P, Towbin H, Wirth U, Voshol H, Hoving S, et al. Isotope-tagged cross-linking reagents. A new tool in mass spectrometric protein interaction analysis. Anal Chem. 2001;73(9):1927-34.

186. Walzthoeni T, Claassen M, Leitner A, Herzog F, Bohn S, Forster F, et al. False discovery rate estimation for cross-linked peptides identified by mass spectrometry. Nat Methods. 2012;9(9):901-3.

187. Bohn S, Beck F, Sakata E, Walzthoeni T, Beck M, Aebersold R, et al. Structure of the 26S proteasome from Schizosaccharomyces pombe at subnanometer resolution. Proc Natl Acad Sci U S A. 2010;107(49):20992-7.

188. Fischer L, Chen ZA, Rappsilber J. Quantitative cross-linking/mass spectrometry using isotope-labelled cross-linkers. J Proteomics. 2013;88:120-8.

189. Chen Z, Fischer L, Tahir S, Bukowski-Wills JC, Barlow P, Rappsilber J. Quantitative cross-linking/mass spectrometry reveals subtle protein conformational changes. Wellcome Open Res. 2016;1:5.

190. Leitner A, Faini M, Stengel F, Aebersold R. Crosslinking and Mass Spectrometry: An Integrated Technology to Understand the Structure and Function of Molecular Machines. Trends Biochem Sci. 2016;41(1):20-32.

191. Olsen JV, Ong SE, Mann M. Trypsin cleaves exclusively C-terminal to arginine and lysine residues. Mol Cell Proteomics. 2004;3(6):608-14.

192. Schilling B, Row RH, Gibson BW, Guo X, Young MM. MS2Assign, automated assignment and nomenclature of tandem mass spectra of chemically crosslinked peptides. J Am Soc Mass Spectrom. 2003;14(8):834-50.

193. Sinz A. Chemical cross-linking and mass spectrometry for mapping three-dimensional structures of proteins and protein complexes. J Mass Spectrom. 2003;38(12):1225-37.

194. Dorman G, Prestwich GD. Benzophenone photophores in biochemistry. Biochemistry. 1994;33(19):5661-73.

195. Roepstorff P, Fohlman J. Proposal for a common nomenclature for sequence ions in mass spectra of peptides. Biomed Mass Spectrom. 1984;11(11):601.

196. Fenn JB, Mann M, Meng CK, Wong SF, Whitehouse CM. Electrospray ionization for mass spectrometry of large biomolecules. Science. 1989;246(4926):64-71.

197. Banerjee S, Mazumdar S. Electrospray ionization mass spectrometry: a technique to access the information beyond the molecular weight of the analyte. Int J Anal Chem. 2012;2012:282574.

198. Wells JM, McLuckey SA. Collision-induced dissociation (CID) of peptides and proteins. Methods Enzymol. 2005;402:148-85.

199. Seidler J, Zinn N, Boehm ME, Lehmann WD. De novo sequencing of peptides by MS/MS. Proteomics. 2010;10(4):634-49.

200. Mueller-Planitz F. Crossfinder-assisted mapping of protein crosslinks formed by site-specifically incorporated crosslinkers. Bioinformatics. 2015;31(12):2043-5.

201. Yilmaz S, Shiferaw GA, Rayo J, Economou A, Martens L, Vandermarliere E. Cross-linked peptide identification: A computational forest of algorithms. Mass Spectrom Rev. 2018.

202. Leitner A. Cross-linking and other structural proteomics techniques: how chemistry is enabling mass spectrometry applications in structural biology. Chemical Science. 2016;7(8):4792-803.

203. Annesley TM. Ion suppression in mass spectrometry. Clin Chem. 2003;49(7):1041-4.

204. Rinner O, Seebacher J, Walzthoeni T, Mueller LN, Beck M, Schmidt A, et al. Identification of cross-linked peptides from large sequence databases. Nat Methods. 2008;5(4):315-8.

205. Maiolica A, Cittaro D, Borsotti D, Sennels L, Ciferri C, Tarricone C, et al. Structural analysis of multiprotein complexes by cross-linking, mass spectrometry, and database searching. Mol Cell Proteomics. 2007;6(12):2200-11.

206. Leitner A, Joachimiak LA, Unverdorben P, Walzthoeni T, Frydman J, Forster F, et al. Chemical cross-linking/mass spectrometry targeting acidic residues in proteins and protein complexes. Proc Natl Acad Sci U S A. 2014;111(26):9455-60.

207. Rozbesky D, Rosulek M, Kukacka Z, Chmelik J, Man P, Novak P. Impact of Chemical Cross-Linking on Protein Structure and Function. Anal Chem. 2018;90(2):1104-13.

208. Nguyen VQ, Ranjan A, Stengel F, Wei D, Aebersold R, Wu C, et al. Molecular architecture of the ATP-dependent chromatin-remodeling complex SWR1. Cell. 2013;154(6):1220-31.

209. Murakami K, Elmlund H, Kalisman N, Bushnell DA, Adams CM, Azubel M, et al. Architecture of an RNA polymerase II transcription pre-initiation complex. Science. 2013;342(6159):1238724.

210. Plaschka C, Lariviere L, Wenzeck L, Seizl M, Hemann M, Tegunov D, et al. Architecture of the RNA polymerase II-Mediator core initiation complex. Nature. 2015;518(7539):376-80.

211. Martinez-Rucobo FW, Kohler R, van de Waterbeemd M, Heck AJ, Hemann M, Herzog F, et al. Molecular Basis of Transcription-Coupled Pre-mRNA Capping. Molecular cell. 2015;58(6):1079-89.

212. Xu Y, Bernecky C, Lee CT, Maier KC, Schwalb B, Tegunov D, et al. Architecture of the RNA polymerase II-Paf1C-TFIIS transcription elongation complex. Nat Commun. 2017;8:15741.

213. Erzberger JP, Stengel F, Pellarin R, Zhang S, Schaefer T, Aylett CHS, et al. Molecular architecture of the 40SeIF1eIF3 translation initiation complex. Cell. 2014;158(5):1123-35.

214. Greber BJ, Bieri P, Leibundgut M, Leitner A, Aebersold R, Boehringer D, et al. Ribosome. The complete structure of the 55S mammalian mitochondrial ribosome. Science. 2015;348(6232):303-8.

215. Joachimiak LA, Walzthoeni T, Liu CW, Aebersold R, Frydman J. The structural basis of substrate recognition by the eukaryotic chaperonin TRiC/CCT. Cell. 2014;159(5):1042-55.

216. Kock M, Nunes MM, Hemann M, Kube S, Dohmen RJ, Herzog F, et al. Proteasome assembly from 15S precursors involves major conformational changes and recycling of the Pba1-Pba2 chaperone. Nat Commun. 2015;6:6123.

217. Heuck A, Schitter-Sollner S, Suskiewicz MJ, Kurzbauer R, Kley J, Schleiffer A, et al. Structural basis for the disaggregase activity and regulation of Hsp104. Elife. 2016;5.

218. Bui KH, von Appen A, DiGuilio AL, Ori A, Sparks L, Mackmull MT, et al. Integrated structural analysis of the human nuclear pore complex scaffold. Cell. 2013;155(6):1233-43.

219. Mei K, Li Y, Wang S, Shao G, Wang J, Ding Y, et al. Cryo-EM structure of the exocyst complex. Nat Struct Mol Biol. 2018.

220. Politis A, Borysik AJ. Assembling the pieces of macromolecular complexes: Hybrid structural biology approaches. Proteomics. 2015;15(16):2792-803.

221. Herzog F, Kahraman A, Boehringer D, Mak R, Bracher A, Walzthoeni T, et al. Structural probing of a protein phosphatase 2A network by chemical cross-linking and mass spectrometry. Science. 2012;337(6100):1348-52.

222. Lossl P, Kolbel K, Tanzler D, Nannemann D, Ihling CH, Keller MV, et al. Analysis of nidogen-1/laminin gamma1 interaction by cross-linking, mass spectrometry, and computational modeling reveals multiple binding modes. PLoS One. 2014;9(11):e112886.

223. Merkley ED, Rysavy S, Kahraman A, Hafen RP, Daggett V, Adkins JN. Distance restraints from crosslinking mass spectrometry: mining a molecular dynamics simulation database to evaluate lysine-lysine distances. Protein Sci. 2014;23(6):747-59.

224. Taylor AF, Amundsen SK, Guttman M, Lee KK, Luo J, Ranish J, et al. Control of RecBCD enzyme activity by DNA binding- and Chi hotspot-dependent conformational changes. J Mol Biol. 2014;426(21):3479-99.

225. Luger K, Rechsteiner TJ, Richmond TJ. Expression and purification of recombinant histones and nucleosome reconstitution. Methods Mol Biol. 1999;119:1-16.

226. Luger K, Rechsteiner TJ, Richmond TJ. Preparation of nucleosome core particle from recombinant histones. Methods Enzymol. 1999;304:3-19.

227. Klinker H, Haas C, Harrer N, Becker PB, Mueller-Planitz F. Rapid purification of recombinant histones. PLoS One. 2014;9(8):e104029.

228. Dick C, Johns EW. Histone from Drosophila melanogaster. Comp Biochem Physiol. 1969;31(3):529-33.

229. Glasel JA. Validity of nucleic acid purities monitored by 260nm/280nm absorbance ratios. Biotechniques. 1995;18(1):62-3.

230. Schmidt C, Robinson CV. A comparative cross-linking strategy to probe conformational changes in protein complexes. Nat Protoc. 2014;9(9):2224-36.

231. Grishaev A. Sample preparation, data collection, and preliminary data analysis in biomolecular solution X-ray scattering. Curr Protoc Protein Sci. 2012;Chapter 17:Unit17 4.

232. Durr H, Flaus A, Owen-Hughes T, Hopfner KP. Snf2 family ATPases and DExx box helicases: differences and unifying concepts from high-resolution crystal structures. Nucleic Acids Res. 2006;34(15):4160-7.

233. Barlow DJ, Thornton JM. Ion-pairs in proteins. J Mol Biol. 1983;168(4):867-85.

234. Kikhney AG, Svergun DI. A practical guide to small angle X-ray scattering (SAXS) of flexible and intrinsically disordered proteins. FEBS Lett. 2015;589(19 Pt A):2570-7.

235. Lowary PT, Widom J. New DNA sequence rules for high affinity binding to histone octamer and sequence-directed nucleosome positioning. J Mol Biol. 1998;276(1):19-42.

236. Haas C. Structural Analysis of Chromatin Remodeler by Electron Microscopy [Dissertation]: Ludwig-Maximilians-Universität München; 2013.

237. Al-Ani G, Briggs K, Malik SS, Conner M, Azuma Y, Fischer CJ. Quantitative determination of binding of ISWI to nucleosomes and DNA shows allosteric regulation of DNA binding by nucleotides. Biochemistry. 2014;53(27):4334-45.

238. Sinha KK, Gross JD, Narlikar GJ. Distortion of histone octamer core promotes nucleosome mobilization by a chromatin remodeler. Science. 2017;355(6322).

239. Chavez JD, Eng JK, Schweppe DK, Cilia M, Rivera K, Zhong X, et al. A General Method for Targeted Quantitative Cross-Linking Mass Spectrometry. PLoS One. 2016;11(12):e0167547.

240. Clapier CR, Iwasa J, Cairns BR, Peterson CL. Mechanisms of action and regulation of ATP-dependent chromatin-remodelling complexes. Nat Rev Mol Cell Biol. 2017;18(7):407-22.

241. Zhou CY, Johnson SL, Gamarra NI, Narlikar GJ. Mechanisms of ATP-Dependent Chromatin Remodeling Motors. Annu Rev Biophys. 2016;45:153-81.

242. Wilson BG, Roberts CW. SWI/SNF nucleosome remodellers and cancer. Nat Rev Cancer. 2011;11(7):481-92.

243. Kadoch C, Crabtree GR. Mammalian SWI/SNF chromatin remodeling complexes and cancer: Mechanistic insights gained from human genomics. Sci Adv. 2015;1(5):e1500447.

244. Garraway LA, Lander ES. Lessons from the cancer genome. Cell. 2013;153(1):17-37.

245. Hamiche A, Sandaltzopoulos R, Gdula DA, Wu C. ATP-dependent histone octamer sliding mediated by the chromatin remodeling complex NURF. Cell. 1999;97(7):833-42.

246. Langst G, Bonte EJ, Corona DF, Becker PB. Nucleosome movement by CHRAC and ISWI without disruption or trans-displacement of the histone octamer. Cell. 1999;97(7):843-52.

247. Krishnan VV, Rupp B. Macromolecular Structure Determination: Comparison of X-ray Crystallography and NMR Spectroscopy. eLS: John Wiley & Sons, Ltd; 2001.

248. Faini M, Stengel F, Aebersold R. The Evolving Contribution of Mass Spectrometry to Integrative Structural Biology. J Am Soc Mass Spectrom. 2016;27(6):966-74.

249. Kay LE. New Views of Functionally Dynamic Proteins by Solution NMR Spectroscopy. J Mol Biol. 2016;428(2 Pt A):323-31.

250. Acharya KR, Lloyd MD. The advantages and limitations of protein crystal structures. Trends Pharmacol Sci. 2005;26(1):10-4.

251. Karaca E, Bonvin AM. Advances in integrative modeling of biomolecular complexes. Methods. 2013;59(3):372-81.

252. Kahraman A, Malmstrom L, Aebersold R. Xwalk: computing and visualizing distances in cross-linking experiments. Bioinformatics. 2011;27(15):2163-4.

253. Ferber M, Kosinski J, Ori A, Rashid UJ, Moreno-Morcillo M, Simon B, et al. Automated structure modeling of large protein assemblies using crosslinks as distance restraints. Nat Methods. 2016;13(6):515-20.

254. Guaitoli G, Raimondi F, Gilsbach BK, Gomez-Llorente Y, Deyaert E, Renzi F, et al. Structural model of the dimeric Parkinson's protein LRRK2 reveals a compact architecture involving distant interdomain contacts. Proc Natl Acad Sci U S A. 2016;113(30):E4357-66.

255. Ding YH, Gong Z, Dong X, Liu K, Liu Z, Liu C, et al. Modeling Protein Excited-state Structures from "Over-length" Chemical Cross-links. J Biol Chem. 2017;292(4):1187-96.

256. Sali A, Berman HM, Schwede T, Trewhella J, Kleywegt G, Burley SK, et al. Outcome of the First wwPDB Hybrid/Integrative Methods Task Force Workshop. Structure. 2015;23(7):1156-67.

257. Kosloff M, Kolodny R. Sequence-similar, structure-dissimilar protein pairs in the PDB. Proteins. 2008;71(2):891-902.

258. Sengoku T, Nureki O, Nakamura A, Kobayashi S, Yokoyama S. Structural basis for RNA unwinding by the DEAD-box protein Drosophila Vasa. Cell. 2006;125(2):287-300.

259. Lieleg C, Ketterer P, Nuebler J, Ludwigsen J, Gerland U, Dietz H, et al. Nucleosome spacing generated by ISWI and CHD1 remodelers is constant regardless of nucleosome density. Molecular and cellular biology. 2015;35(9):1588-605.

260. Belsom A, Mudd G, Giese S, Auer M, Rappsilber J. Complementary Benzophenone Cross-Linking/Mass Spectrometry Photochemistry. Anal Chem. 2017;89(10):5319-24.

261. Cormann KU, Moller M, Nowaczyk MM. Critical Assessment of Protein Cross-Linking and Molecular Docking: An Updated Model for the Interaction Between Photosystem II and Psb27. Front Plant Sci. 2016;7:157.

262. Schmidt C, Zhou M, Marriott H, Morgner N, Politis A, Robinson CV. Comparative cross-linking and mass spectrometry of an intact F-type ATPase suggest a role for phosphorylation. Nat Commun. 2013;4:1985.

263. Lehmann LC, Hewitt G, Aibara S, Leitner A, Marklund E, Maslen SL, et al. Mechanistic Insights into Autoinhibition of the Oncogenic Chromatin Remodeler ALC1. Molecular cell. 2017;68(5):847-59 e7.

264. Del Campo M, Lambowitz AM. Structure of the Yeast DEAD box protein Mss116p reveals two wedges that crimp RNA. Molecular cell. 2009;35(5):598-609.

265. Fitzgerald DJ, DeLuca C, Berger I, Gaillard H, Sigrist R, Schimmele K, et al. Reaction cycle of the yeast Isw2 chromatin remodeling complex. EMBO J. 2004;23(19):3836-43.

266. Erdel F, Schubert T, Marth C, Langst G, Rippe K. Human ISWI chromatin-remodeling complexes sample nucleosomes via transient binding reactions and become immobilized at active sites. Proc Natl Acad Sci U S A. 2010;107(46):19873-8.

267. Weidemann T, Wachsmuth M, Knoch TA, Muller G, Waldeck W, Langowski J. Counting nucleosomes in living cells with a combination of fluorescence correlation spectroscopy and confocal imaging. J Mol Biol. 2003;334(2):229-40.

268. Gallego LD, Ghodgaonkar Steger M, Polyansky AA, Schubert T, Zagrovic B, Zheng N, et al. Structural mechanism for the recognition and ubiquitination of a single nucleosome residue by Rad6-Bre1. Proc Natl Acad Sci U S A. 2016;113(38):10553-8.

269. Makde RD, England JR, Yennawar HP, Tan S. Structure of RCC1 chromatin factor bound to the nucleosome core particle. Nature. 2010;467(7315):562-6.

270. Armache KJ, Garlick JD, Canzio D, Narlikar GJ, Kingston RE. Structural basis of silencing: Sir3 BAH domain in complex with a nucleosome at 3.0 A resolution. Science. 2011;334(6058):977-82.

271. McGinty RK, Henrici RC, Tan S. Crystal structure of the PRC1 ubiquitylation module bound to the nucleosome. Nature. 2014;514(7524):591-6.

272. Barbera AJ, Chodaparambil JV, Kelley-Clarke B, Joukov V, Walter JC, Luger K, et al. The nucleosomal surface as a docking station for Kaposi's sarcoma herpesvirus LANA. Science. 2006;311(5762):856-61.

273. Kato H, Jiang J, Zhou BR, Rozendaal M, Feng H, Ghirlando R, et al. A conserved mechanism for centromeric nucleosome recognition by centromere protein CENP-C. Science. 2013;340(6136):1110-3.

274. Skinner JJ, Lim WK, Bedard S, Black BE, Englander SW. Protein hydrogen exchange: testing current models. Protein Sci. 2012;21(7):987-95.

275. Skinner JJ, Lim WK, Bedard S, Black BE, Englander SW. Protein dynamics viewed by hydrogen exchange. Protein Sci. 2012;21(7):996-1005.

276. Wales TE, Engen JR. Hydrogen exchange mass spectrometry for the analysis of protein dynamics. Mass Spectrom Rev. 2006;25(1):158-70.

277. Zhang Z, Smith DL. Determination of amide hydrogen exchange by mass spectrometry: a new tool for protein structure elucidation. Protein Sci. 1993;2(4):522-31.

278. Engen JR. Analysis of protein conformation and dynamics by hydrogen/deuterium exchange MS. Anal Chem. 2009;81(19):7870-5.

279. Chalmers MJ, Busby SA, Pascal BD, West GM, Griffin PR. Differential hydrogen/deuterium exchange mass spectrometry analysis of protein-ligand interactions. Expert Rev Proteomics. 2011;8(1):43-59.

280. Konermann L, Pan J, Liu YH. Hydrogen exchange mass spectrometry for studying protein structure and dynamics. Chem Soc Rev. 2011;40(3):1224-34.

281. Gibson DG, Young L, Chuang RY, Venter JC, Hutchison CA, 3rd, Smith HO. Enzymatic assembly of DNA molecules up to several hundred kilobases. Nat Methods. 2009;6(5):343-5.

282. Froger A, Hall JE. Transformation of plasmid DNA into E. coli using the heat shock method. J Vis Exp. 2007(6):253.

283. Laemmli UK. Cleavage of structural proteins during the assembly of the head of bacteriophage T4. Nature. 1970;227(5259):680-5.

284. Leitner A, Walzthoeni T, Aebersold R. Lysine-specific chemical cross-linking of protein complexes and identification of cross-linking sites using LC-MS/MS and the xQuest/xProphet software pipeline. Nat Protoc. 2014;9(1):120-37.

285. Holding AN. XL-MS: Protein cross-linking coupled with mass spectrometry. Methods. 2015;89:54-63.

286. MacLean B, Tomazela DM, Shulman N, Chambers M, Finney GL, Frewen B, et al. Skyline: an open source document editor for creating and analyzing targeted proteomics experiments. Bioinformatics. 2010;26(7):966-8.

287. Pernot P, Round A, Barrett R, De Maria Antolinos A, Gobbo A, Gordon E, et al. Upgraded ESRF BM29 beamline for SAXS on macromolecules in solution. J Synchrotron Radiat. 2013;20(Pt 4):660-4.

288. Guinier A. La diffraction des rayons X aux tres petits angles: applications a l'etude de phenomenes ultramicroscopiques. Annales de Physiques. 1939;12:161-237.

289. Franke D, Svergun DI. DAMMIF, a program for rapid ab-initio shape determination in small-angle scattering. J Appl Crystallogr. 2009;42(Pt 2):342-6.

290. Kozin MB, Svergun DI. Automated matching of high-and low-resolution structural models. Journal of applied crystallography. 2001;34(1):33-41.

291. Volkov VV, Svergun DI. Uniqueness of ab initio shape determination in small-angle scattering. Journal of applied crystallography. 2003;36(3):860-4.

292. Wriggers W, Milligan RA, McCammon JA. Situs: A package for docking crystal structures into low-resolution maps from electron microscopy. J Struct Biol. 1999;125(2-3):185-95.

293. Svergun DI, Koch MHJ, Timmins PA, May RP. Small Angle X-Ray and Neutron Scattering from Solutions of Biological Macromolecules: OUP Oxford; 2013.

294. Humphrey W, Dalke A, Schulten K. VMD: visual molecular dynamics. J Mol Graph. 1996;14(1):33-8, 27-8.

295. Webb B, Sali A. Comparative Protein Structure Modeling Using MODELLER. Curr Protoc Protein Sci. 2016;86:2 9 1-2 9 37.

296. Zacharias M. Protein-protein docking with a reduced protein model accounting for side-chain flexibility. Protein Sci. 2003;12(6):1271-82.

297. Fiorucci S, Zacharias M. Binding site prediction and improved scoring during flexible protein-protein docking with ATTRACT. Proteins. 2010;78(15):3131-9.

298. Jorgensen WL, Tirado-Rives J. The OPLS [optimized potentials for liquid simulations] potential functions for proteins, energy minimizations for crystals of cyclic peptides and crambin. J Am Chem Soc. 1988;110(6):1657-66.

299. Linge JP, Nilges M. Influence of non-bonded parameters on the quality of NMR structures: a new force field for NMR structure calculation. J Biomol NMR. 1999;13(1):51-9.

300. Dolinsky TJ, Nielsen JE, McCammon JA, Baker NA. PDB2PQR: an automated pipeline for the setup of Poisson-Boltzmann electrostatics calculations. Nucleic Acids Res. 2004;32(Web Server issue):W665-7.

301. Dolinsky TJ, Czodrowski P, Li H, Nielsen JE, Jensen JH, Klebe G, et al. PDB2PQR: expanding and upgrading automated preparation of biomolecular structures for molecular simulations. Nucleic Acids Res. 2007;35(Web Server issue):W522-5.

302. Li H, Robertson AD, Jensen JH. Very fast empirical prediction and rationalization of protein pKa values. Proteins. 2005;61(4):704-21.

303. de Vries SJ, Schindler CE, Chauvot de Beauchene I, Zacharias M. A web interface for easy flexible protein-protein docking with ATTRACT. Biophys J. 2015;108(3):462-5.

304. Schindler CE, de Vries SJ, Zacharias M. iATTRACT: simultaneous global and local interface optimization for protein-protein docking refinement. Proteins. 2015;83(2):248-58.

305. Schneidman-Duhovny D, Pellarin R, Sali A. Uncertainty in integrative structural modeling. Curr Opin Struct Biol. 2014;28:96-104.

306. Schneidman-Duhovny D, Hammel M, Tainer JA, Sali A. Accurate SAXS profile computation and its assessment by contrast variation experiments. Biophys J. 2013;105(4):962-74.

6. Appendix

6.1. Enrichment of cross-linked peptides by size-exclusion chromatography

I optimized the chemical cross-linking workflow by implementing an additional enrichment step for cross-linked peptides, in a similar manner as described previously (284). Briefly, following chemical cross-linking of the remodeling enzyme using either the BS^2G or the BS^3 agent (SFigure 1A), the sample was subjected to size-exclusion chromatography (SFigure 1B) and in-solution tryptic digestion. The tryptic digest was subsequently separated by size-exclusion chromatography (SFigure 1C), which resulted in an enrichment of cross-linked peptides relative to the input sample (SFigure 1D). The enrichment of cross-linked peptides was beneficial in terms of number of identified cross-links that could be used as distance restraints during computational modeling.

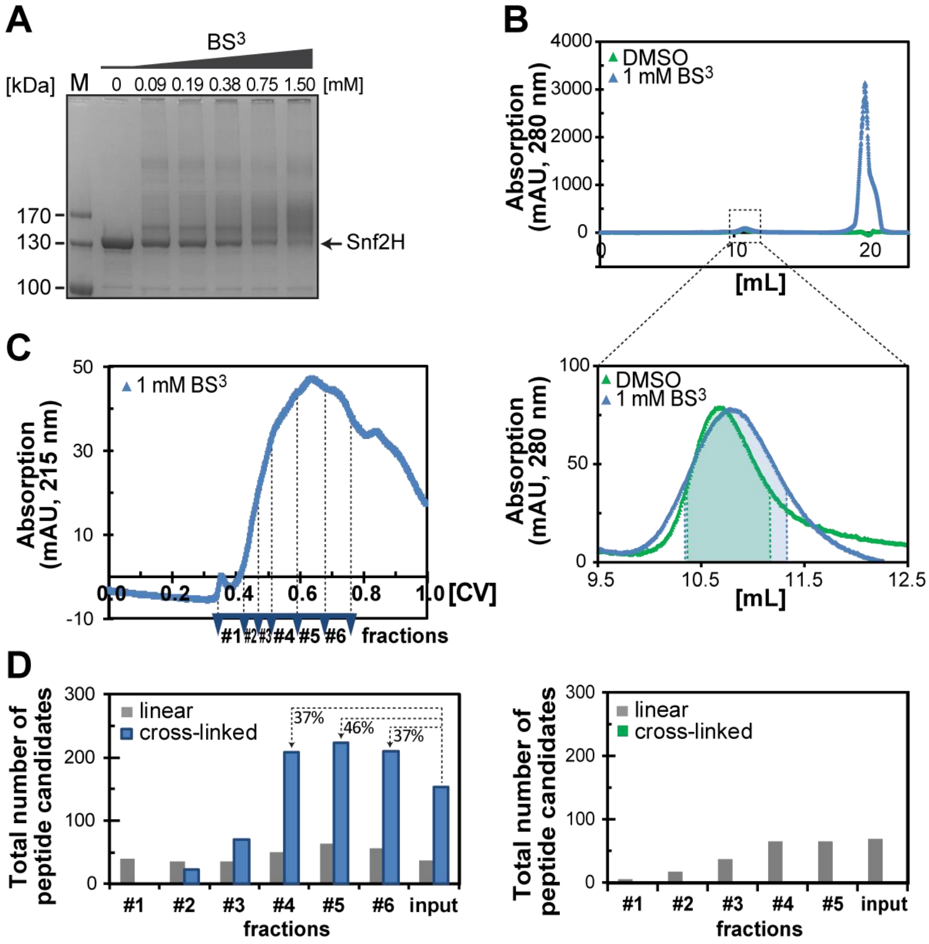

SFigure 1: Enrichment of cross-linked peptides by size-exclusion chromatography. (A) Chemical cross-linking of the Snf2H enzyme using increasing concentrations of the BS^3 cross-linker viewed by SDS-PAGE analysis. **(B)** The results from size-exclusion chromatography of cross-linked and DMSO-treated Snf2H samples are shown. Notably, the elution profiles for the Snf2H enzyme (1 µM) in the presence of either

** continues next page **

DMSO (green) or 1 mM BS^3 (blue) did not provide evidence for protein di- or multimerization under the tested conditions. Fractions corresponding to the colored peak areas were pooled and subjected to in-solution tryptic digestion. **(C)** The results from the separation of the tryptic peptide mixture by size-exclusion chromatography are shown. Fractions #1–6 were subsequently analyzed by LC-MS/MS measurements. **(D)** The total number of identified cross-linked (blue) and linear peptides (grey) for BS^3- (left) and DMSO-treated (right) samples are presented. The enrichment of cross-linked peptides prior to LC-MS/MS analysis resulted in more cross-link identifications for fractions #4–6 relative to the input sample, which was not subjected to size-exclusion chromatography. Peptides were identified using the Crossfinder software using comparable identification criteria as specified in Table 15.

Dr. I. Forné (LMU, Munich) performed the LC-MS/MS analysis.

6.2. Studying the impact of ADP-BeF$_x$-binding on ATP hydrolysis of ISWI-type remodeling enzymes

I determined the impact of the non-hydrolysable ADP-BeF$_x$ analog on ATP turnover rate of Snf2H, DmISWI, and DmISWI$_{\Delta HSS}$ using a TLC-based ATPase assay as described in section 4.2.7.2.1. Increasing concentrations of ADP-BeF$_x$ readily inhibited ATP hydrolysis of the studied ISWI-type remodeling enzymes in a dose-dependent manner (SFigure 2). Results should be considered as preliminary as the assay was only performed once.

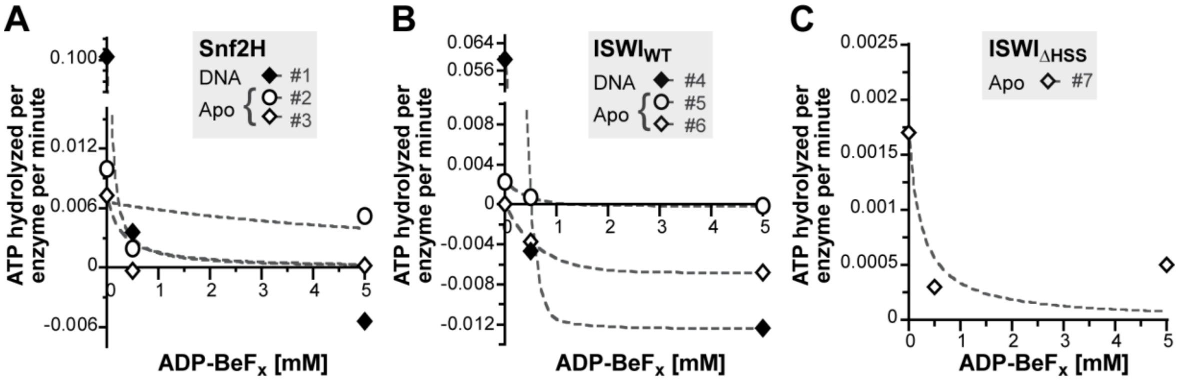

SFigure 2: Preliminary results from the TLC-based ATPase assay for individual ISWI-type enzymes. The number of ATP molecules that were hydrolyzed per enzyme per minute is plotted against increasing concentrations of ADP-BeF$_x$ for **(A)** Snf2H, **(B)** DmISWI, and **(C)** DmISWI$_{\Delta HSS}$. Unfilled and filled symbols refer to data collected in the absence and presence of 0.2 g/L salmon sperm DNA (n = 1). Individual sample conditions #1–7 are specified in Table 17. The results from the TLC-based ATPase assay collectively suggested that ATP hydrolysis of the studied Snf2H and DmISWI constructs is inhibited at > 0.5 mM ADP-BeF$_x$.

6.3. Studying the formation of enzyme-nucleosome complexes by EMSA

SFigure 3 summarizes my efforts on finding optimal solution conditions to chemically cross-link the Snf2H and DmISWI remodeling enzymes in complex with the nucleosomal substrate. The formation of enzyme-nucleosome complexes was monitored by EMSA as further specified in section 4.2.7.1. Notably, SFigure 3 is related to Figure 40 of the main text and thus includes replicate measurements as well as data for additionally tested conditions for the DmISWI and Snf2H remodeling enzymes.

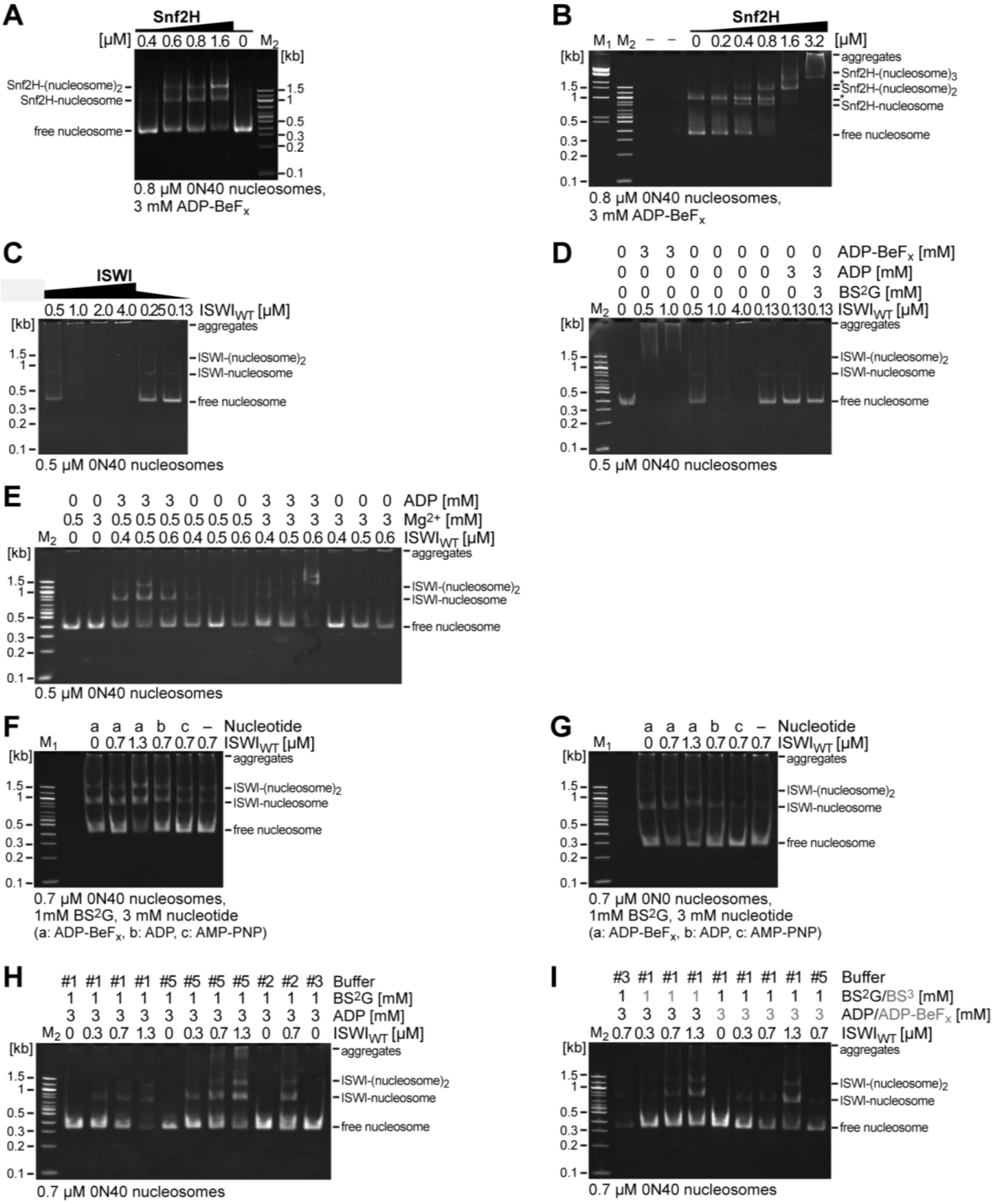

** continues next page **

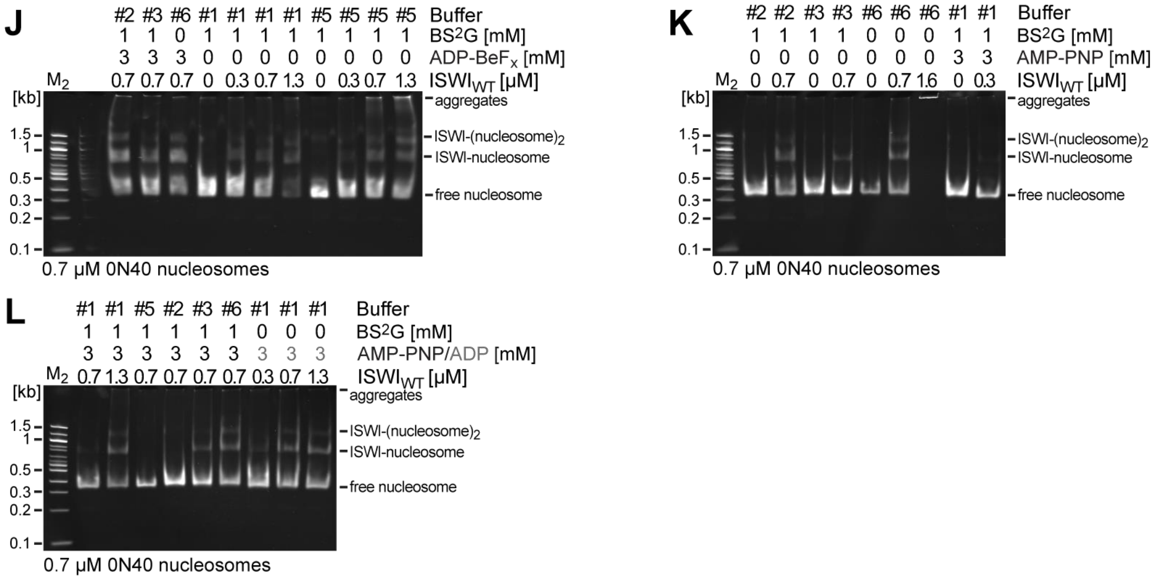

SFigure 3: Monitoring the formation of enzyme-nucleosome complexes by EMSA. The interaction of either Snf2H or DmISWI with mononucleosomes was studied for different solution conditions by EMSA. Protein species were separated by a 4.5% native PAGE/0.2x TBE approach and were stained with ethidium bromide (cf. section 4.2.1.6). The composition of individual EMSA buffers #1–6 is specified in Table 12. DNA ladders are denoted as 'M_1' and 'M_2'. Asterisks (*) indicate overassembled nucleosomes. **(A, B)** Increasing concentrations of the Snf2H enzyme were incubated with a constant amount of 0N40 mononucleosomes and ADP-BeF_x in EMSA buffer #4. **(C)** Increasing concentrations of the DmISWI enzyme were incubated with a constant amount of 0N40 nucleosomes in EMSA buffer #1. **(D)** The DmISWI enzyme was incubated in the presence or absence of the indicated nucleotide (ADP or ADP-BeF_x) with a constant amount of 0N40 nucleosomes in EMSA buffer #1. **(E)** The DmISWI enzyme was incubated in the presence or absence of ADP with a constant amount of 0N40 nucleosomes in EMSA buffer #1 containing different concentrations of Mg^{2+}. **(F, G)** The DmISWI protein was incubated in the presence of the indicated nucleotide (ADP, ADP-BeF_x or AMP-PNP) with a constant amount of either 0N40 or 0N0 nucleosomes in EMSA buffer #5. The enzyme-nucleosome complex was chemically cross-linked using 1 mM of the BS^2G cross-linking agent. **(H–L)** In order to evaluate the impact of the different EMSA buffers on complex formation, DmISWI was incubated with a constant amount 0N40 nucleosomes in distinct buffers. Notably, the samples were supplemented with the indicated nucleotide and/or chemical cross-linking agent.

6.4. Sequence alignments of remodeling enzymes

SFigure 4: Sequence alignments of remodeling enzymes. The protein sequences of DmISWI, Snf2H, MtISWI, and ScChd1were aligned using the Clustal Omega webserver (https://www.ebi.ac.uk/Tools/msa/clustalo/). Numbers and colored bars below the sequence alignments specify the range of enzyme domains, i.e. NTR (cyan), ATPase lobe 1 (yellow), ATPase lobe 2 (red), and HSS (green), for the Snf2H enzyme. Grey and black arrows indicate the positions of Bpa-substituted amino acids and positions of point mutations, respectively, which were introduced into full-length DmISWI. Rectangles indicate structural motifs I, II, and VI.

6.5. Tabular overview of identified cross-links for DmISWI and Snf2H

STable 1: Cross-links within the ATPase module of the DmISWI enzyme under apo state conditions. Cross-linked peptides are listed in an ordered manner according to their cross-link identification number (XL_{ISWI} 1–30) together with information about the cross-linked residues and MS-related identification parameters (e.g., precursor mass and charge state). Cross-linked sites are color-coded according to the domain architecture in Figure 12 with respective residues being underlined in the peptide sequences (B signifies Bpa). Data derive from four independent XL-MS experiments using either BS^{2}G or BS^3 as well as from additional data sources as specified in table footnotes. Accordingly, each cross-link was categorized into one of the following 'reproducibility groups': (I) the cross-linked peptide was independently reproduced, (II) the cross-linked residue pair was independently reproduced, (III) the cross-linked residue pair was repoduced in technical replicates, and (IV) not reproduced. The Cα-Cα distances of individual cross-links were measured in the indicated structures using PyMOL. Orange and red values signify Cα-Cα distances that violated the defined distance threshold by ≤ 5 Å and > 5 Å, respectively. The table was adapted from (1) in accordance with Elsevier's policies.

													Cα-Cα distances (Å)					
XL ISWI	Vari-ant	Site 1	Site 2	Peptide 1 sequence	Peptide 2 sequence	Mass (Da)	Charge	Error (ppm)	DmISWI protein	Cross-linker	Repro-ducibility group	Size selec-tion	cf. model in Figure 14A	cf. model in Figure 14E	cf. model in Figure 16	cf. model in Figure 23B	cf. model in Figure 26D	[Cross-linking sites 1, 2 in pdb 5JXR] cf. structure in Figure 26C
1[‡]	a	578	172	BVIQGGR	HFK	1309.693	3	0.1	M578B	Bpa	I	In-gel	13.8[x]	13.8[x]	45.9	13.3[x]	16.8	16.9 [637, 230]
1[‡]	b	578	172	BVIQGGR	TLQTISLLGYLKHFK	2640.479	4	9.0	M578B	Bpa	I	In-gel	13.8[x]	13.8[x]	45.9	13.3[x]	16.8	16.9 [637, 230]
2[‡]		578	120	LDKBVIQGGR	FDASPAYIK	2246.174	3	8.3	M578B	Bpa	I	In-gel	11.2[x]	10.0[x]	39.4	10.6[x]	12.4	12.3 [637, 179]
3[‡]		338	483	LHAVLKPFLLR	LDGQTPBEDR	2586.396	4	8.0	H483B	Bpa	I	In-gel	12.8[x]	10.2[x]	23.9	20.7[x]	18.1	18.1 [395, 542]
4	a	547	350	IGQKKQVR	LKAEVEKR	2065.237	4	0.1	WT	BS^3	II	SEC	10.2	11.4[x]	21.4	17.0	9.8	9.7 [606, 407]
4	b	547	350	IGQKK	LKAEVEKR	1682.009	3	0.3	WT	BS^3	I	SEC	10.2	11.4[x]	21.4	17.0	9.8	9.7 [606, 407]
4	c	547	350	IGQKKQVR	LKAEVEKR	2065.237	4	0.1	WT	BS^3	II	SEC	10.2	11.4[x]	21.4	17.0	9.8	9.7 [606, 407]
5		337	547	LHAVLKPFLLRR	IGQKK	2172.363	4	-0.1	WT	BS^3	IV	none	28.9	23.9[x]	29.8	17.7	20.7	21.0 [395, 606]
6	a	350	353	LKAEVEKR	LKPKKEMK	2110.255	5	-0.8	WT	BS^3	II	SEC	10.9	9.0[x]	16.7	12.5	9.7	9.6 [407, 410]
6[†]	b	350	353	AEVEKR	LKPK	1310.756	4	1.4	WT	BS^{2}G	II	SEC	10.9	9.0[x]	16.7	12.5	9.7	9.6 [407, 410]
6[†]	c	350	353	LKAEVEKR	LKPK	1551.935	3	4.1	WT	BS^{2}G	I	SEC	10.9	9.0[x]	16.7	12.5	9.7	9.6 [407, 410]
7		169	578	TLQTISLLGYLKHFK	LDKBVIQGGR	2996.685	4	5.1	M578B	Bpa	I	In-gel	11.9	12.0[x]	41.0	13.3	18.4	18.4 [227, 637]
8		637	345	TAEQKAALDSLGESSLR	LKAEVEKR	2884.551	4	1.9	WT	BS^3	IV	none	34.1	30.9[x]	20.8	27.1	51.7	51.2 (34.2[$]) [705, 402]
9	a	637	577	TAEQKAALDSLGESSLR	LDKMVIQGGR	3028.587	3	2.2	WT	BS^3	I	SEC	13.7	13.9	13.9	13.9	26.8	26.5 (12.4[$]) [705, 636]
9	b	637	577	GEAKTAEQKAALDSLGESSLR	LDKMVIQGGR	3413.783	4	1.1	WT	BS^3	II	SEC	13.7	13.9	13.9	13.9	26.8	26.5 (12.4[$]) [705, 636]
9	c	637	577	GEAKTAEQKAALDSLGESSLR	LRLDKMVIQGGR	3682.968	5	1.2	WT	BS^3	II	SEC	13.7	13.9	13.9	13.9	26.8	26.5 (12.4[$]) [705, 636]
9[†]	d	637	577	TAEQKAALDSLGESSLR	LDKMVIQGGR	2986.540	3	3.9	WT	BS$_2$G	II	SEC	13.7	13.9	13.9	13.9	26.8	26.5 (12.4[$]) [705, 636]
9[†]	e	637	577	TAEQKAALDSLGESSLR	LRLDKMVIQGGR	3271.720	4	6.0	WT	BS$_2$G	II	SEC	13.7	13.9	13.9	13.9	26.8	26.5 (12.4[$]) [705, 636]
10[†]	a	637	356	TAEQKAALDSLGESSLR	KEMK	2405.211	3	6.6	WT	BS$_2$G	II	SEC	16.8	16.8	16.8	16.8	44.7	43.9 (13.2[$]) [705, 413]
10	b	637	356	TAEQKAALDSLGESSLR	KEMKIFVGLSK	3191.711	4	2.8	WT	BS^3	II	SEC	16.8	16.8	16.8	16.8	44.7	43.9 (13.2[$]) [705, 413]
11	a	391	595	DIDVVNGAGKVEKMR	SNQLNKDEMLNIIR	3454.792	4	1.4	WT	BS^3	I	SEC	4.8	4.8	4.8	4.8	53.0	54.8 (6.1[$]) [450, 654]
11[†]	b	391	595	VEKMR	SNQLNKDEMLNIIR	2444.252	4	6.0	WT	BS^{2}G	II	SEC	4.8	4.8	4.8	4.8	53.0	54.8 (6.1[$]) [450, 654]
11[†]	c	391	595	DIDVVNGAGKVEKMR	SNQLNKDEMLNIIR	3412.745	3	7.2	WT	BS^{2}G	I	SEC	4.8	4.8	4.8	4.8	53.0	54.8 (6.1[$]) [450, 654]
11[†]	d	391	595	DIDVVNGAGKVEKMR	SNQLNKDEMLNIIR	3870.101	4	9.6	WT	BS^{2}G	I	SEC	4.8	4.8	4.8	4.8	53.0	54.8 (6.1[$]) [450, 654]
12	a	388	595	VLLKDIDVVNGAGKVEK	SNQLNKDEMLNIIR	3620.981	4	-0.7	WT	BS^3	I	SEC	9.4	9.4	9.5	9.4	55.9	60.3 (11.8[$]) [445, 654]
12	b	388	595	DIDVVNGAGKVEK	SNQLNKDEMLNIIR	3167.650	3	0.8	WT	BS^3	II	SEC	9.4	9.4	9.5	9.4	55.9	60.3 (11.8[$]) [445, 654]
12	c	388	595	VLLKDIDVVNGAGKVEK	LVDNRSNQLNKDEMLNIIR	4218.305	5	1.5	WT	BS^3	II	SEC	9.4	9.4	9.5	9.4	55.9	60.3 (11.8[$]) [445, 654]
12[†]	d	388	595	VLLKDIDVVNGAGKVEKMR	SNQLNKDEMLNIIR	3870.101	4	7.8	WT	BS^{2}G	I	SEC	9.4	9.4	9.5	9.4	55.9	60.3 (11.8[$]) [445, 654]
13[†]		337	70	LHAVLKPFLLR	SPTKPK	2058.236	4	6.0	WT	BS^{2}G	IV	SEC	N/A	N/A	N/A	N/A	25.4	25.3 [394, 119]
14		52	70	RFDFLLKQTEIFTHFMTNSAK	SPTKPK	3329.742	4	4.5	WT	BS^{2}G	I	SEC	N/A	N/A	N/A	N/A	17.2	17.6 [101, 119]
15		276	247	EFKTANR	KFNWR	1751.911	3	0.7	WT	BS^3	III	none	8.1	8.1	8.1	8.1	8.6	8.5 [334, 305]

* continues next page *

16[†]		276	246	EFKTANR	SVFKK	1567.836	3	1.8	WT	BS^{2}G	I	SEC	7.4	7.4	7.4	7.4	7.1	7.1 [334, 304]
17[†]		186	267	NQAGPHIVIVPKSTLQNWVNEFK	SKLSEILR	3658.984	3	7.9	WT	BS^{2}G	III	SEC	17.7	17.7	17.7	17.7	15.9	16.2 [244, 325]
18[†]		267	242	SKLSEILR	EKSVFK	1776.999	3	4.5	WT	BS^{2}G	I	SEC	10.4	10.4	10.4	10.4	12.5	12.5 [325, 300]
19	a	564	577	LITESTVEEKIVER	LDKMVIQGGR	2898.574	4	-0.3	WT	BS^3	III	none	22.6	22.6	22.6	22.9	20.4	20.2 [623, 636]
19	b	564	577	LITESTVEEKIVERAEVK	LRLDKMVIQGGR	3595.002	4	0.6	WT	BS^3	III	none	22.6	22.6	22.6	22.9	20.4	20.2 [623, 636]
20		356	548	KEMKIFVGLSK	IGQKKQVR	2372.398	5	0.9	WT	BS^3	III	none	11.8	11.8	11.8	11.8	11.3	11.3 [413, 607]
21		353	547	LKPKKEMK	IGQKK	1711.043	3	-0.7	WT	BS^3	I	SEC	6.9	6.9	6.9	6.9	7.9	7.8 [410, 606]
22[†]		353	548	LKPKKEMK	KQVR	1629.990	4	1.4	WT	BS^{2}G	I	SEC	6.7	6.7	6.7	6.7	7.9	7.1 [410, 607]
23[†]		391	675	VEKMR	EKQK	1288.681	3	4.1	WT	BS^{2}G	IV	SEC	N/A	N/A	N/A	N/A	N/A	N/A [450, 735]
24[‡]	a	578	664	BVIQGGR	AALDSLGESSLR	2097.086	3	6.3	M578B	Bpa	II	SEC	N/A	N/A	N/A	N/A	N/A	10.3 [637, 712]
24[‡]	b	578	664	LDKBVIQGGR	AALDSLGESSLR	2453.292	3	9.0	M578B	Bpa	II	SEC	N/A	N/A	N/A	N/A	N/A	10.3 [637, 712]
24[‡]	c	578	664	LRLDKBVIQGGR	AALDSLGESSLR	2722.477	4	5.0	M578B	Bpa	II	SEC	N/A	N/A	N/A	N/A	N/A	10.3 [637, 712]
25[‡]		578	665	BVIQGGR	AALDSLGESSLR	2097.086	3	6.3	M578B	Bpa	II	SEC	N/A	N/A	N/A	N/A	N/A	8.6 [637, 713]
26	a	693	577	KANYAVDAYFREALR	LRLDKMVIQGGR	3308.782	5	-0.8	WT	BS^3	IV	none	N/A	N/A	N/A	N/A	N/A	N/A [752, 638]
26	b	693	577	KANYAVDAYFR	LDKMVIQGGR	2570.332	4	0.9	WT	BS^3	IV	none	N/A	N/A	N/A	N/A	N/A	N/A [752, 638]
27	a	693	564	KANYAVDAYFR	LITESTVEEKIVER	3099.613	4	1.4	WT	BS^3	III	none	N/A	N/A	N/A	N/A	N/A	N/A [623, 752]
27	b	693	564	KANYAVDAYFREALR	LITESTVEEKIVER	3568.878	5	2.7	WT	BS^3	III	none	N/A	N/A	N/A	N/A	N/A	N/A [752, 623]
28	a	613	693	FGANQVFSSKETDITDEDIDVILER GEAK	KANYAVDAYFR	4680.288	5	4.0	WT	BS^3	III	none	N/A	N/A	N/A	N/A	N/A	N/A [672, 752]
28	b	613	693	FGANQVFSSKETDITDEDIDVILER	KANYAVDAYFR	4295.091	4	3.6	WT	BS^3	III	none	N/A	N/A	N/A	N/A	N/A	N/A [672, 752]
29		637	693	TAEQKAALDSLGESSLR	KANYAVDAYFR	3229.626	4	1.1	WT	BS^3	IV	none	N/A	N/A	N/A	N/A	N/A	N/A [705, 752]
30	a	595	693	LVDNRSNQLNKDEMLNIIR	KANYAVDAYFREALR	4208.180	5	-3.7	WT	BS^3	III	none	N/A	N/A	N/A	N/A	N/A	N/A [654, 752]
30	b	595	693	SNQLNKDEMLNIIR	KANYAVDAYFR	3141.592	3	1.1	WT	BS^3	III	none	N/A	N/A	N/A	N/A	N/A	N/A [654, 752]
30	c	595	693	LVDNRSNQLNKDEMLNIIR	KANYAVDAYFR	3754.910	5	1.8	WT	BS^3	III	none	N/A	N/A	N/A	N/A	N/A	N/A [654, 752]
30	d	595	693	SNQLNKDEMLNIIR	KANYAVDAYFREALR	3626.852	5	-0.3	WT	BS^3	III	none	N/A	N/A	N/A	N/A	N/A	N/A [752, 654]

[‡] Cross-link was described in either Forné *et al.* (157) or Ludwigsen *et al.* (115).

[†] Cross-link was identified in an unpublished data set provided by Dr. F. Müller-Planitz (LMU, Munich).

[x] Cross-link was used as distance restraint during rigid body docking.

[$] Cα-Cα distance between two protomers in the crystal structure.

N/A = Not available, at least one amino acid is missing in the structure.

STable 2: Cross-links originating from the HSS domain of the DmISWI enzyme under apo state conditions. Cross-linked peptides are listed in an ordered manner according to their cross-link identification number (XL_{ISWI} 31–61). The table is structured in an identical manner as described for STable 1. Data derive from five independent UV-induced or chemical cross-linking experiments as well as from an additional data source as specified in table footnotes. The table was adapted from (1) in accordance with Elsevier’s policies.

XL_{ISWI}	Variant	Site 1	Site 2	Peptide 1 sequence	Peptide 2 sequence	Mass (Da)	Charge	Error (ppm)	DmISWI protein	Cross-linker	Reproducibility group	Size selection	Cα-Cα distances (Å)				
													cf. model in Figure 21	cf. model in Figure 23A	cf. model in Figure 23B	cf. model in Figure 25	cf. model in Figure 26D
31[†□]	a	391	900	VEKMR	GKNYTEIEDR	1980.958	3	5.2	WT	BS^2G	I	SEC	25.7[x]	39.8[x]	23.9[x]	25.6[x]	33.3[x]
31[†]	b	391	900	DIDVVNGAGKVEKMR	GKNYTEIEDR	2949.450	3	8.4	WT	BS^2G	I	SEC	25.7[x]	39.8[x]	23.9[x]	25.6[x]	33.3[x]
32[□]	a	595	810	LVDNRSNQLNKDEMLNIIR	DFNQFIKANEK	3774.937	4	-2.0	WT	BS^3	II	SEC	31.7[x]	32.6[x]	29.0[x]	N/A	37.2[x]
32[†]	b	595	810	SNQLNKDEMLNIIR	DFNQFIKANEK	3135.566	3	6.4	WT	BS^2G	II	SEC	31.7	32.6[x]	29.0	N/A	37.2
32	c	595	810	SNQLNKDEMLNIIR	DFNQFIKANEK	3177.613	3	1.8	WT	BS^3	I	SEC	31.7[x]	32.6[x]	29.0[x]	N/A	37.2[x]
33[†□]		388	810	DIDVVNGAGKVEK	DFNQFIKANEK	2791.403	3	6.6	WT	BS^2G	II	SEC	23.7[x]	26.0[x]	22.6[x]	34.5[x]	33.8[x]
34[†◊]		124	900	FDASPAYIKSGEMR	GKNYTEIEDR	2890.345	3	5.4	WT	BS^2G	IV	SEC	19.4[x]	33.0[x]	21.4[x]	18.6[x]	27.0[x]
35[†□]		124	945	FDASPAYIKSGEMR	FDWFIKSR	2764.332	3	7.5	WT	BS^2G	I	SEC	29.1[x]	31.8[x]	25.8[x]	33.3[x]	33.9[x]
36		865	391	GEGKIQR	VEKMR	1585.861	3	1.1	WT	BS^3	II	SEC	26.2	30.1[x]	23.3	32.4	34.5
37		945	247	ASPQFRFDWFIKSR	KFNWR	2671.381	4	0.2	WT	BS^3	IV	none	49.6	32.7[x]	52.2	31.7	54.2
38		973	353	RCNTLITLIERENIELEEKER	LKPKK	3369.859	3	-3.2	WT	BS^2G	II	SEC	59.6	46.2[x]	63.9	31.4	52.7
39	a	564	945	LITESTVEEKIVERAEVK	FDWFIKSR	3307.771	4	2.3	WT	BS^3	II	SEC	25.7	34.7[x]	17.8	28.4	7.9
39[†]	b	564	945	LITESTVEEKIVER	FDWFIKSR	2838.481	3	5.8	WT	BS^2G	I	SEC	25.7	34.7[x]	17.8	28.4	7.9
40		359	874	EMKIFVGLSK	KALDQK	2006.112	3	3.3	WT	BS^3	IV	none	53.7	32.4[x]	49.9	35.1	44.0
41		578	942	BVIQGGR	FDWFIK	1733.893	3	-2.2	M578B	Bpa	IV	In-gel	18.6	27.1	15.2	31.0	20.8
42	a	595	865	SNQLNKDEMLNIIR	GEGKIQR	2611.375	4	0.5	WT	BS^3	I	SEC	24.9	27.7[x]	22.2	N/A	31.5
42	b	595	865	LVDNRSNQLNKDEMLNIIR	GEGKIQR	3208.699	5	-0.1	WT	BS^3	II	SEC	24.9	27.7[x]	22.2	N/A	31.5
43		595	874	SNQLNKDEMLNIIR	KALDQK	2526.348	4	0.0	WT	BS^3	III	none	33.3	21.8[x]	30.2	N/A	40.1
44		595	879	SNQLNKDEMLNIIR	ALDQKMSR	2772.426	4	0.3	WT	BS^3	III	none	34.5	22.1[x]	31.3	N/A	43.2
45		595	900	SNQLNKDEMLNIIR	GKNYTEIEDR	3048.519	4	3.6	WT	BS^3	IV	none	22.0	36.1[x]	20.2	N/A	37.7
46[†]		900	70	GKNYTEIEDR	SPTKPK	1975.985	3	5.2	WT	BS^2G	IV	SEC	N/A	N/A	N/A	33.2[x]	57.6
47[†]		900	72	GKNYTEIEDR	SPTKPKGRPK	2414.256	4	4.4	WT	BS^2G	IV	SEC	N/A	N/A	N/A	29.2[x]	53.1
48		898	70	LQYGNNKGK	SPTKPK	1772.942	4	2.0	WT	BS^2G	I	SEC	N/A	N/A	N/A	39.2[x]	62.1
49		810	865	DFNQFIKANEK	GEGKIQR	2277.176	3	-0.5	WT	BS^3	I	SEC	13.6	13.6	13.6	13.6	13.6
50		810	825	DFNQFIKANEKYGR	DDIDNIAKDVEGK	3297.616	5	0.0	WT	BS^3	IV	none	12.2	12.2	12.2	12.2	12.2
51	a	879	945	ALDQKMSR	FDWFIKSR	2183.120	3	0.2	WT	BS^3	III	none	25.2	25.2	25.2	25.2	25.2
51	b	879	945	ALDQKMSR	ASPQFRFDWFIKSR	2869.470	4	1.1	WT	BS^3	III	none	25.2	25.2	25.2	25.2	25.2
52[†]		756	712	VPKNTELGSDATK	VSEPKAPK	2309.212	3	5.8	WT	BS^2G	I	SEC	N/A	N/A	N/A	N/A	N/A
53[†]		814	865	ANEKYGRDDIDNIAK	GEGKIQR	2603.294	3	4.8	WT	BS^2G	IV	SEC	9.0	9.0	9.0	9.0	9.0
54		830	810	DDIDNIAKDVEGKTPEEVIEYNAVFWER	DFNQFIKANEKYGR	5118.453	5	7.2	WT	BS^2G	I	SEC	14.3	14.3	14.3	14.3	14.3
55		898	945	LQYGNNKGK	FDWFIKSR	2256.169	3	7.5	WT	BS^3	IV	none	19.0	19.0	19.0	19.0	19.0
56	a	945	874	FDWFIKSR	KALDQK	1937.041	4	0.5	WT	BS^3	III	none	28.5	28.5	28.5	28.5	28.5
56	b	945	874	ASPQFRFDWFIKSR	KALDQK	2623.391	5	0.6	WT	BS^3	III	none	28.5	28.5	28.5	28.5	28.5
57	a	756	693	TVGYKVPKNTELGSDATK	KANYAVDAYFR	3361.720	4	-0.1	WT	BS^3	III	none	N/A	N/A	N/A	N/A	N/A
57	b	756	693	TVGYKVPKNTELGSDATK	KANYAVDAYFREALR	3830.985	5	0.4	WT	BS^3	III	none	N/A	N/A	N/A	N/A	N/A
58		693	874	KANYAVDAYFR	KALDQK	2156.127	3	1.0	WT	BS^3	III	none	N/A	N/A	N/A	N/A	N/A
59[†]		677	865	QKLNALGNWIEPPKR	GEGKIQR	2645.440	5	5.3	WT	BS^2G	IV	SEC	N/A	N/A	N/A	N/A	N/A
60[†]		865	675	GEGKIQR	EKQK	1413.758	3	5.6	WT	BS^2G	IV	SEC	N/A	N/A	N/A	N/A	N/A
61[†]		1023	1010	KSEVVATSSNSKK	ASQKR	2048.086	4	6.1	WT	BS^2G	I	SEC	N/A	N/A	N/A	N/A	N/A

[†] Cross-link was identified in an unpublished data set provided by Dr. F. Müller-Planitz (LMU, Munich).

[◊], [□] MS/MS spectra are provided in Figure 19 and SFigure 5, respectively.

[x] Cross-link was used as distance restraint during rigid body docking.

N/A = Not available, at least one amino acid is missing from the structure.

STable 3: Cross-links for the Snf2H enzyme under apo state conditions. Cross-linked peptides are listed in an ordered manner according to their cross-link identification number (XL$_{\text{Snf2H}}$ 1–84). The table is structured in an indentical manner as described for STable 1 with cross-linked sites being color-coded according to the domain architecture in Figure 27. Data derive from two independent XL-MS experiments.

XL$_{\text{Snf2H}}$	Variant	Site 1[#]	Site 2	Peptide 1 sequence	Peptide 2 sequence	Mass (Da)	Charge	Error (ppm)	Cross-linker	Reproducibility group	Size selection	Peptide enrichment	Cα-Cα distances (Å) cf. model #1 in Figure 31A
1		899	176	CNELQDIEKIMAQIER	FEDSPSYVKWGK	3568.7221	3	4.8	BS^3	IV	SEC	+	42.5
2		929	314	YKAPFHQLR	IKNEK	1927.0681	5	-0.8	BS^3	IV	SEC	+	24.3
3		929	328	YKAPFHQLR	EFKTTNR	2191.1540	3	0	BS^3	III	SEC	+	30.5
4		397	758	RIKADVEK	VSEPKAPK	1950.1152	3	0.5	BS^3	IV	SEC	+	56.4
5	a	397	799	RIKADVEK	TIGYKVPR	2028.1734	3	0.5	BS^3	III	SEC	+	64.4
5	b	799	397	TIGYKVPR	IKADVEK	1872.0722	3	-0.1	BS^3	III	SEC	+	64.4
6	a	990	397	FDWFLKSR	IKADVEK	2037.0937	3	0.9	BS^3	II	none	+	43.2
6	b	990	397	FDWFLKSR	RIKADVEK	2193.1948	3	2.3	BS^3	II	SEC	+	43.2
7	a	929	397	YKAPFHQLR	IKADVEK	2098.1577	3	1.1	BS^3	III	SEC	+	28.8[x]
7[□]	b	929	397	YKAPFHQLR	RIKADVEK	2254.2588	3	3.0	BS^3	III	SEC	+	28.8[x]
8[□]		264	929	SVCLIGDKEQR	YKAPFHQLR	2600.3536	4	0.7	BS^3	III	SEC	+	19.1[x]
9[□]		176	855	FEDSPSYVKWGK	DFNQFIKANEK	2932.4285	3	2.0	BS^3	IV	SEC	+	31.3[x]
10[□]		223	929	TLQTISLLGYMKHYR	YKAPFHQLR	3119.6745	4	2.1	BS^3	III	SEC	+	31.8[x]
11[□]	a	264	990	SVCLIGDKEQR	FDWFLKSR	2539.2896	3	-1.1	BS^3	I	SEC	+	33.7[x]
11	b	264	990	SVCLIGDKEQR	FDWFLKSR	2543.3147	3	-0.8	BS^3	I	none	+	33.7[x]
12[□]		176	929	FEDSPSYVKWGK	YKAPFHQLR	2738.3859	3	0.4	BS^3	IV	SEC	+	29.2[x]
13		160	929	RTEQEEDEELLTESSKATNVCTR	YKAPFHQLR	4020.9490	5	3.1	BS^3	III	SEC	+	39.9
14[□]	a	176	990	FEDSPSYVKWGK	FDWFLKSR	2677.3219	3	2.0	BS^3	I	SEC	+	31.3[x]
14	b	176	990	FEDSPSYVKWGK	FDWFLKSR	2681.3470	4	0.4	BS^3	I	none	+	31.3[x]
15		160	990	TEQEEDEELLTESSKATNVCTR	FDWFLKSR	3803.7839	3	2.9	BS^3	III	SEC	+	51.1
16		847	264	LLTQGFTNWNKR	SVCLIGDKEQR	2918.5075	3	3.1	BS^3	III	SEC	+	69.7
17		990	408	FDWFLKSR	KEVK	1737.9456	3	0.3	BS^3	IV	none	+	45.3
18	a	929	408	YKAPFHQLR	KEVK	1803.0347	4	-1.0	BS^3	IV	none	+	41.8
18	b	408	929	SLPPKKEVK	YKAPFHQLR	2321.3262	5	1.7	BS^3	II	SEC	+	41.8
19		855	418	DFNQFIKANEK	IYVGLSKMQR	2684.3998	3	2.0	BS^3	III	SEC	+	33.0
20		929	494	YKAPFHQLR	LLPKLK	2007.2035	3	0.3	BS^3	IV	SEC	+	43.3
21		990	600	FDWFLKSR	IGQTKTVR	2137.1686	3	-1.6	BS^3	IV	SEC	+	49.6
22		929	600	YKAPFHQLR	IGQTKTVR	2198.2326	3	1.1	BS^3	II	SEC	+	51.1
23		418	758	IYVGLSKMQR	VSEPKAPK	2202.2084	3	1.1	BS^3	II	SEC	+	51.1
24		430	855	ILMKDIDILNSAGK	DFNQFIKANEK	3020.5895	3	-1.6	BS^3	III	SEC	+	48.5
25[Δ]		430	929	ILMKDIDILNSAGK	YKAPFHQLR	2826.5468	4	-2.8	BS^3	IV	SEC	+	48.4
26[□]		418	929	IYVGLSKMQR	YKAPFHQLR	2490.3571	3	1.8	BS^3	III	SEC	+	38.4[x]
27		407	929	SLPPKKEVK	YKAPFHQLR	2321.3262	5	1.7	BS^3	IV	SEC	+	45.2
28[□]		430	990	ILMKDIDILNSAGK	FDWFLKSR	2765.4828	3	1.3	BS^3	III	SEC	+	31.5[x]
29[□]		418	990	IYVGLSKMQR	FDWFLKSR	2429.2932	3	-0.3	BS^3	I	SEC	+	19.1[x]
30[◊]	a	647	929	IGKDEMLQMIR	YKAPFHQLR	2629.3875	4	-3.3	BS^3	IV	SEC	+	51.7
30	b	647	929	YKAPFHQLR	IKKDEK	2056.1471	5	-0.4	BS^3	III	SEC	+	51.7
31[◊]		665	990	HGATHVFASKESEITDEDIDGILER	FDWFLKSR	4003.9595	5	3.0	BS^3	I	none	+	13.5
32		694	990	LSKMGESSLR	FDWFLKSR	2358.2044	4	-1.8	BS^3	IV	SEC	+	N/A
33[◊]		990	128	FDWFLKSR	IKKDEK	1995.0831	3	0.6	BS^3	IV	SEC	+	23.7
34[◊]		990	121	FDWFLKSR	MKPGRPR	2076.1093	5	-0.3	BS^3	III	SEC	+	25.0
35[◊]	a	132	990	DEKQNLLSVGDYR	FDWFLKSR	2771.3921	4	0.9	BS^3	III	SEC	+	20.5
35	b	132	990	KDEKQNLLSVGDYR	FDWFLKSR	2899.4871	4	-0.3	BS^3	III	SEC	+	20.5
36		97	990	ANRFEYLLKQTELFAHFIQPAAQK	FDWFLKSR	4098.1522	5	0.6	BS^3	III	SEC	+	N/A
37		71	990	QKEIQEPDPTYEEK	FDWFLKSR	2968.4497	3	0	BS^3	IV	SEC	+	N/A

** continues next page **

38		71	299	QKEIQEPDPTYEEK	KFNWR	2620.2811	4	-1.6	BS^3	III	SEC	+	N/A
39		71	328	QKEIQEPDPTYEEK	EFKTTNR	2765.3398	4	-0.3	BS^3	III	SEC	+	N/A
40	a	160	121	RTEQEEDEELLTESSKATNVCTR	MKPGRPR	3702.7944	5	-0.7	BS^3	III	SEC	+	32.5
40	b	160	121	TEQEEDEELLTESSKATNVCTR	MKPGRPR	3546.6933	4	1.6	BS^3	III	SEC	+	32.5
41	a	160	128	RTEQEEDEELLTESSKATNVCTR	IKKDEK	3621.7683	5	-0.5	BS^3	III	SEC	+	35.4
41	b	160	128	TEQEEDEELLTESSKATNVCTR	IKKDEK	3465.6671	5	0.5	BS^3	III	SEC	+	35.4
42	a	160	129	RTEQEEDEELLTESSKATNVCTR	IKKDEK	3621.7683	4	2.5	BS^3	III	SEC	+	33.6
42	b	160	129	TEQEEDEELLTESSKATNVCTR	IKKDEK	3465.6671	5	1.4	BS^3	III	SEC	+	33.6
43		397	624	IKADVEK	AEMKLR	1701.9337	3	0.6	BS^3	II	SEC	+	35.3
44[□]		160	644	TEQEEDEELLTESSKATNVCTR	LVDQNLNKIGKDEMLQMIR	4963.4104	5	2.8	BS^3	IV	SEC	+	37.2[x]
45[◊]		440	647	DIDILNSAGKMDK	IGKDEMLQMIR	2889.4652	3	-1.8	BS^3	II	SEC	+	8.8
46	a	644	443	LVDQNLNKIGKDEMLQMIR	MDKMR	3078.6002	4	-0.9	BS^3	I	none	+	16.8
46[◊]	b	644	443	LVDQNLNKIGK	MDKMR	2058.0967	3	3.1	BS^3	II	SEC	+	16.8
47[◊]		647	443	IGKDEMLQMIR	MDKMR	2150.0722	3	0.7	BS^3	II	SEC	+	8.0
48[◊]	a	665	418	HGATHVFASKESEITDEDIDGILER	IYVGLSKMQR	4100.0527	4	3.5	BS^3	I	SEC	+	21.5
48	b	665	418	HGATHVFASK	IYVGLSKMQR	2385.2629	3	-0.2	BS^3	IV	SEC	+	21.5
49[◊]		665	430	HGATHVFASKESEITDEDIDGILER	ILMKDIDILNSAGK	4436.2424	4	2.2	BS^3	III	SEC	+	21.5
50[Δ]		684	408	KTAEMNEK	KEVK	1593.8587	3	0.1	BS^3	I	none	+	9.1
51	a	665	683	HGATHVFASKESEITDEDIDGILER	GAKK	3308.6527	3	3.3	BS^3	II	SEC	+	28.3
51	b	665	683	HGATHVFASK	GAKK	1593.8629	4	-1.1	BS^3	II	SEC	+	28.3
52	a	665	684	HGATHVFASKESEITDEDIDGILER	KTAEMNEK	3855.8475	4	-0.2	BS^3	III	SEC	+	29.4
52	b	665	684	HGATHVFASK	KTAEMNEK	2141.0577	3	1.2	BS^3	III	SEC	+	29.4
53		407	494	SLPPKKEVK	LLPKLK	1873.2018	3	0.8	BS^3	I	SEC	+	19.5
54		407	600	SLPPKKEVK	IGQTKTVR	2068.2560	4	0.6	BS^3	I	none	+	9.2
55		408	494	SLPPKKEVK	LLPKLK	1873.2018	3	-0.5	BS^3	I	SEC	+	17.9
56	a	408	600	SLPPKKEVK	IGQTKTVR	2064.2309	3	-1.0	BS^3	I	SEC	+	11.8
56	b	600	408	IGQTKTVR	KEVK	1545.9394	3	0.7	BS^3	I	none	+	11.8
57		430	418	ILMKDIDILNSAGK	IYVGLSKMQR	2861.5761	4	3.2	BS^3	III	SEC	+	18.8
58		494	407	MVVLDKLLPKLK	SLPPKKEVK	2558.5851	3	1.4	BS^3	II	SEC	+	19.5
59	a	494	408	MVVLDKLLPKLK	KEVK	2036.2685	3	1.3	BS^3	II	SEC	+	17.9
59	b	494	408	LLPKLK	KEVK	1350.8852	3	-0.6	BS^3	I	SEC	+	17.9
59	c	494	408	MVVLDKLLPKLK	SLPPKKEVK	2574.5800	4	0.5	BS^3	II	SEC	+	17.9
59	d	494	408	LLPKLKEQGSR	KEVK	1908.1410	4	-0.2	BS^3	II	SEC	+	17.9
59	e	494	408	MVVLDKLLPKLK	SLPPKKEVK	2558.5851	3	1.4	BS^3	II	SEC	+	17.9
60	a	494	411	MVVLDKLLPKLK	KEVK	2036.2685	4	0.8	BS^3	III	SEC	+	17.7
60	b	494	411	LLPKLK	KEVK	1350.8852	3	-0.7	BS^3	III	SEC	+	17.7
60	c	494	411	LLPKLKEQGSR	KEVK	1908.1410	3	0.6	BS^3	III	SEC	+	17.7
61	a	494	600	MVVLDKLLPKLK	IGQTKTVR	2435.4915	4	-0.1	BS^3	III	SEC	+	17.9
61	b	600	494	IGQTKTVR	LLPKLK	1750.1082	3	0.7	BS^3	III	SEC	+	17.9
62	a	600	496	IGQTKTVR	LKEQGSR	1860.0732	4	0.8	BS^3	I	SEC	+	15.5
63		600	624	IGQTKTVR	AEMKLR	1790.0388	3	-0.4	BS^3	I	none	+	29.3
64		264	294	SVCLIGDKEQR	EKSVFK	2178.1357	3	0.1	BS^3	III	SEC	+	13.9
65		264	298	SVCLIGDKEQR	EKSVFKK	2306.2307	3	0.1	BS^3	IV	SEC	+	17.7
66		264	299	SVCLIGDKEQR	KFNWR	2195.1461	4	-0.3	BS^3	I	none	+	19.1
67		264	314	SVCLIGDKEQR	IKNEK	2072.0938	4	0.1	BS^3	III	SEC	+	29.4
68		264	317	SVCLIGDKEQR	IKNEKSK	2287.2208	4	0	BS^3	IV	SEC	+	26.7
69	a	264	319	SVCLIGDKEQR	SKLSEIVR	2372.2736	3	-0.1	BS^3	III	SEC	+	20.5
69	b	264	319	WVPTLRSVCLIGDKEQR	SKLSEIVR	3124.7070	3	4.7	BS^3	III	SEC	+	20.5
70		767	847	APRPPKQPNVQDFQFFPPR	LLTQGFTNWNKR	3880.0328	5	2.1	BS^3	III	SEC	+	20.6
71		929	990	YKAPFHQLR	FDWFLKSR	2394.2639	3	5.5	BS^3	III	SEC	+	26.8
72		847	761	LLTQGFTNWNKR	APKAPRPPK	2575.4389	3	-1.1	BS^3	III	SEC	+	22.3
73		899	847	CNELQDIEKIMAQIER	LLTQGFTNWNKR	3603.8180	3	-0.8	BS^3	III	SEC	+	15.2
74	a	814	799	NPELPNAAQAQKEEQLK	KTIGYKVPR	3105.6825	4	-0.8	BS^3	II	SEC	+	10.0

** continues next page **

74	b	814	799	NPELPNAAQAQKEEQLK	TIGYKVPR	2977.5875	3	2.2	BS^3	II	SEC	+	10.0
75	a	799	758	TIGYKVPR	VSEPKAPK	1925.0988	3	0.2	BS^3	I	SEC	+	20.2
75	b	799	758	KTIGYKVPR	VSEPKAPK	2053.1937	3	0.5	BS^3	II	SEC	+	20.2
76	a	71	121	QKEIQEPDPTYEEK	MKPGRPR	2711.3591	5	-0.6	BS^3	III	SEC	+	N/A
76	b	71	121	QKEIQEPDPTYEEK	TPTSPLKMKPGRPR	3435.7710	5	-2.9	BS^3	IV	SEC	+	N/A
77		71	128	QKEIQEPDPTYEEK	IKKDEK	2630.3329	4	-2.8	BS^3	III	SEC	+	N/A
78		71	129	QKEIQEPDPTYEEK	IKKDEK	2630.3329	4	0.6	BS^3	IV	SEC	+	N/A
79	a	83	121	EIQEPDPTYEEKMQTDR	MKPGRPR	3086.4804	4	-2.8	BS^3	III	SEC	+	N/A
79	b	83	121	EIQEPDPTYEEKMQTDRANR	MKPGRPRIKK	3812.9304	4	-7.9	BS^3	IV	SEC	+	N/A
80		97	121	ANRFEYLLKQTELFAHFIQPAAQK	MKPGRPR	3841.0616	5	3.8	BS^3	II	SEC	+	N/A
81	a	97	128	ANRFEYLLKQTELFAHFIQPAAQK	IKKDEK	3760.0355	4	2.2	BS^3	III	SEC	+	N/A
81	b	97	128	FEYLLKQTELFAHFIQPAAQK	IKKDEK	3418.8543	5	-0.7	BS^3	III	SEC	+	N/A
82	a	97	129	ANRFEYLLKQTELFAHFIQPAAQK	KDEK	3518.8564	4	-3.8	BS^3	III	SEC	+	N/A
82	b	97	129	FEYLLKQTELFAHFIQPAAQK	IKKDEK	3418.8543	5	3.4	BS^3	III	SEC	+	N/A
83	a	855	739	DFNQFIKANEK	KANYAVDAYFR	2807.3921	3	2.1	BS^3	I	none	+	N/A
83	b	855	739	RDFNQFIKANEK	KANYAVDAYFR	2963.4932	4	0.9	BS^3	II	SEC	+	N/A
84		919	1020	KALDTK	EKAEK	1415.7873	4	0.8	BS^3	I	none	+	N/A

[□], [◊], [Δ] MS/MS spectra are provided in SFigure 6, SFigure 9A, and SFigure 10A, respectively.
[x] Cross-link was used as distance restraint during rigid body docking.
N/A = Not available, at least one amino acid is missing in the structure. N/D = Not determined.

STable 4: Cross-links for the Snf2H enzyme in the presence of ADP-BeF$_x$. Cross-linked peptides are listed in an ordered manner according to their cross-link identification number (XL$_{Snf2H,nt}$ 1–154). The table is structured in an indentical manner as described for STable 1 with cross-linked sites being color-coded according to the domain architecture in Figure 27. Data derive from three independent XL-MS experiments.

XL$_{Snf2H,nt}$	Variant	Site 1	Site 2	Peptide 1 sequence	Peptide 2 sequence	Mass (Da)	Charge	Error (ppm)	Cross-linker	Reproducibility group	Size selection	Peptide enrichment	Cα-Cα distances (Å) cf. model #1 in Figure 37A
1[Δ]		176	847	FEDSPSYVKWGK	LLTQGFTNWNKR	3056.5398	3	2.3	BS^3	III	none	+	54.5
2[□]		176	855	FEDSPSYVKWGK	DFNQFIKANEK	2932.4285	3	0.2	BS^3	I	SEC	+	43.8[x]
3[□]		176	929	FEDSPSYVKWGK	YKAPFHQLR	2738.3859	3	1.9	BS^3	I	SEC	+	18.3[x]
4[□]		176	990	FEDSPSYVKWGK	FDWFLKSR	2677.3219	3	3.5	BS^3	I	SEC	+	40.8[x]
5		223	855	TLQTISLLGYMKHYR	DFNQFIKANEK	3313.7171	3	3.4	BS^3	IV	none	+	45.5
6[□]		223	929	TLQTISLLGYMKHYR	YKAPFHQLR	3119.6745	4	-1.1	BS^3	I	SEC	+	26.5[x]
7		264	758	SVCLIGDKEQR	VSEPKAPK	2296.2099	3	-6.0	BS^3	IV	SEC	+	47.8
8[□]		264	929	SVCLIGDKEQR	YKAPFHQLR	2600.3536	4	-1.6	BS^3	III	SEC	+	32.3[x]
9[□]		264	990	SVCLIGDKEQR	FDWFLKSR	2539.2896	3	3.8	BS^3	III	SEC	+	25.2[x]
10		758	397	VSEPKAPK	IKADVEK	1794.0140	3	0.9	BS^3	IV	SEC	+	86.4
11[□]		847	264	LLTQGFTNWNKR	SVCLIGDKEQR	2918.5075	3	2.9	BS^3	IV	SEC	+	32.8[x]
12[□]		855	299	DFNQFIKANEK	KFNWR	2240.1380	3	1.1	BS^3	I	SEC	+	40.1[x]
13[□]		929	299	YKAPFHQLR	KFNWR	2046.0954	3	-3.0	BS^3	I	SEC	+	35.9[x]
14		929	328	YKAPFHQLR	EFKTTNR	2191.1540	3	-1.0	BS^3	I	SEC	+	32.8
15[□]	a	929	397	YKAPFHQLR	IKADVEK	2098.1577	3	1.2	BS^3	I	SEC	+	15.6[x]
15	b	929	397	YKAPFHQLR	RIKADVEK	2254.2588	5	-0.3	BS^3	I	SEC	+	15.6
16[□]		990	299	FDWFLKSR	KFNWR	1985.0314	4	-2.2	BS^3	I	SEC	+	33.7[x]
17[□]		990	328	FDWFLKSR	EFKTTNR	2130.0900	3	1.1	BS^3	I	none	+	33.4[x]

** continues next page **

18[□]	a	990	397	FDWFLKSR	IKADVEK	2037.0937	3	0.2	BS^3	I	none	+	33.4[x]
18	b	990	397	FDWFLKSR	RIKADVEK	2193.1948	3	0.3	BS^3	II	none	+	33.4
18	c	990	397	NSPQFRFDWFLKSR	IKADVEK	2766.4496	4	3.1	BS^3	II	none	+	33.4
18	d	990	397	NSPQFRFDWFLKSR	RIKADVEK	2922.5507	4	2.3	BS^3	II	none	+	33.4
19		176	1036	FEDSPSYVKWGK	KMDGAPDGR	2525.1899	4	4.1	BS^3	I	none	+	N/A
20		264	1036	SVCLIGDKEQR	KMDGAPDGR	2403.1525	4	2.8	BS^3	III	SEC	+	N/A
21		223	739	TLQTISLLGYMKHYR	KANYAVDAYFR	3277.6960	3	1.1	BS^3	I	none	+	N/A
22		176	739	FEDSPSYVKWGK	KANYAVDAYFR	2896.4074	3	2.2	BS^3	I	none	+	N/A
23		418	929	IYVGLSKMQR	YKAPFHQLR	2490.3571	3	2.4	BS^3	I	none	+	38.1
24[□]		418	990	IYVGLSKMQR	FDWFLKSR	2429.2932	3	2.1	BS^3	I	none	+	24.8[x]
25		430	855	ILMKDIDILNSAGK	DFNQFIKANEK	3020.5895	3	3.1	BS^3	I	none	+	73.4
26[□]	a	430	990	ILMKDIDILNSAGK	FDWFLKSR	2765.4828	3	4.7	BS^3	I	SEC	+	36.2[x]
26	b	430	990	ILMKDIDILNSAGKMDK	FDWFLKSR	3139.6452	4	0.1	BS^3	II	none	+	36.2
26	c	430	990	ILMKDIDILNSAGK	NSPQFRFDWFLKSR	3494.8387	4	3.6	BS^3	III	none	+	36.2
27		440	990	ILMKDIDILNSAGKMDK	FDWFLKSR	3139.6452	4	1.7	BS^3	IV	none	+	43.9
28		990	624	FDWFLKSR	AEMKLR	1982.0450	3	-1.0	BS^3	I	SEC	+	40.4
29		990	496	FDWFLKSR	LKEQGSR	2052.0794	3	0.3	BS^3	IV	SEC	+	39.8
30		418	1036	IYVGLSKMQR	KMDGAPDGR	2277.1612	3	3.4	BS^3	I	none	+	N/A
31		430	739	ILMKDIDILNSAGK	KANYAVDAYFR	2984.5684	4	-0.3	BS^3	I	SEC	+	N/A
32		71	684	QKEIQEPDPTYEEK	KTAEMNEK	2820.3377	3	1.8	BS^3	I	SEC	+	N/A
33		160	644	TEQEEDEELLTESSKATNVCTR	LVDQNLNKIGKDEMLQMIR	4963.4104	5	-1.1	BS^3	III	SEC	+	72.3
34		496	129	LKEQGSR	IKKDEK	1713.9627	3	-1.4	BS^3	IV	SEC	+	54.3
35		83	328	EIQEPDPTYEEKMQTDR	EFKTTNR	3140.4610	3	-0.2	BS^3	IV	SEC	+	N/A
36		97	328	ANRFEYLLKQTELFAHFIQPAAQK	EFKTTNR	3895.0423	5	4.1	BS^3	IV	SEC	+	N/A
37		71	929	QKEIQEPDPTYEEK	YKAPFHQLR	3029.5137	4	1.6	BS^3	I	SEC	+	N/A
38		71	990	QKEIQEPDPTYEEK	FDWFLKSR	2968.4497	3	0.1	BS^3	I	SEC	+	N/A
39		83	929	EIQEPDPTYEEKMQTDR	YKAPFHQLR	3404.6349	4	1.0	BS^3	IV	SEC	+	N/A
40		97	990	ANRFEYLLKQTELFAHFIQPAAQK	FDWFLKSR	4098.1522	5	-4.3	BS^3	IV	SEC	+	N/A
41[Δ]		132	990	DEKQNLLSVGDYR	FDWFLKSR	2771.3921	3	-0.7	BS^3	IV	SEC	+	36.9
42	a	160	929	RTEQEEDEELLTESSKATNVCTR	YKAPFHQLR	4020.9490	5	-1.4	BS^3	III	SEC	+	36.4
42	b	160	929	TEQEEDEELLTESSKATNVCTR	YKAPFHQLR	3864.8479	4	4.0	BS^3	III	SEC	+	36.4
43[Δ]		929	128	YKAPFHQLR	IKKDEK	2056.1471	3	0.6	BS^3	IV	SEC	+	24.9
44[Δ]		990	129	FDWFLKSR	IKKDEK	1995.0831	3	-0.9	BS^3	I	SEC	+	27.9
45[Δ]	a	990	128	FDWFLKSR	IKKDEK	1995.0831	3	1.2	BS^3	II	SEC	+	25.2
45	b	990	128	NSPQFRFDWFLKSR	IKKDEK	2724.4390	4	4.8	BS^3	II	none	+	25.2
46[Δ]	a	990	121	FDWFLKSR	MKPGRPR	2076.1093	4	-0.5	BS^3	I	SEC	+	36.6
46	b	990	121	NSPQFRFDWFLKSR	MKPGRPR	2805.4652	5	1.3	BS^3	II	none	+	36.6
47		97	128	ANRFEYLLKQTELFAHFIQPAAQK	IKKDEK	3760.0355	5	0.8	BS^3	I	none	+	N/A
48	a	160	128	RTEQEEDEELLTESSKATNVCTR	IKKDEK	3621.7683	5	1.6	BS^3	II	SEC	+	35.7
48	b	160	128	TEQEEDEELLTESSKATNVCTR	IKKDEK	3465.6671	3	1.0	BS^3	II	SEC	+	35.7
49		83	121	EIQEPDPTYEEKMQTDR	MKPGRPR	3086.4804	5	2.9	BS^3	II	none	+	N/A
50[Δ]	a	647	443	LVDQNLNKIGKDEMLQMIR	MDKMR	3074.5751	3	2.4	BS^3	II	none	+	8.0
50	b	647	443	IGKDEMLQMIR	MDKMR	2150.0722	3	1.1	BS^3	I	none	+	8.0
51[Δ]	a	440	647	DIDILNSAGKMDK	IGKDEMLQMIR	2889.4652	3	2.5	BS^3	I	SEC	+	8.8
51	b	440	647	ILMKDIDILNSAGKMDK	IGKDEMLQMIR	3374.7688	5	2.6	BS^3	II	SEC	+	8.8
51	c	440	647	DIDILNSAGKMDKMR	IGKDEMLQMIR	3176.6068	4	3.6	BS^3	II	none	+	8.8
52[Δ]		665	430	HGATHVFASKESEITDEDIDGILER	ILMKDIDILNSAGK	4436.2424	4	2.0	BS^3	I	SEC	+	21.5
53[Δ]		665	418	HGATHVFASKESEITDEDIDGILER	IYVGLSKMQR	4100.0527	4	1.2	BS^3	I	none	+	5.6
54[Δ]		647	929	LVDQNLNKIGKDEMLQMIR	YKAPFHQLR	3553.8904	4	1.0	BS^3	I	none	+	45.5
55[Δ]	a	647	990	LVDQNLNKIGKDEMLQMIR	FDWFLKSR	3492.8264	4	1.8	BS^3		none	+	43.1
55	b	647	990	IGKDEMLQMIR	FDWFLKSR	2568.3235	3	0.4	BS^3	I	none	+	43.1
56[□]		665	929	HGATHVFASKESEITDEDIDGILER	YKAPFHQLR	4065.0235	5	1.4	BS^3	I	none	+	36.8[x]

** continues next page **

57$^{\Delta}$		665	990	HGATHVFASKESEITDEDIDGILER	FDWFLKSR	4003.9595	4	-1.3	BS^3	I	none	+	20.1
58		990	684	FDWFLKSR	KTAEMNEK	2185.0880	3	5.5	BS^3	IV	SEC	+	32.5
59		665	684	HGATHVFASKESEITDEDIDGILER	KTAEMNEK	3855.8475	4	1.4	BS^3	I	SEC	+	29.4
60		665	724	HGATHVFASKESEITDEDIDGILER	QKIAFTEWIEPPKR	4648.3452	5	5.7	BS^3	IV	SEC	+	N/A
61		665	735	HGATHVFASKESEITDEDIDGILER	IAFTEWIEPPKR	4392.1917	5	3.3	BS^3	IV	none	+	N/A
62	a	665	739	HGATHVFASKESEITDEDIDGILER	KANYAVDAYFR	4223.0450	4	-1.8	BS^3	I	SEC	+	N/A
62	b	665	739	HGATHVFASKESEITDEDIDGILER	ERKANYAVDAYFR	4508.1887	5	1.2	BS^3	IV	SEC	+	N/A
63		647	739	IGKDEMLQMIR	KANYAVDAYFR	2787.4090	3	-0.8	BS^3	I	none	+	N/A
64		665	1036	HGATHVFASKESEITDEDIDGILER	KMDGAPDGR	3851.8275	4	0.2	BS^3	I	SEC	+	N/A
65		694	683	TAEMNEKLSKMGESSLR	GAKK	2450.2511	3	1.5	BS^3	III	none	+	N/A
66		694	758	LSKMGESSLR	VSEPKAPK	2115.1247	3	1.3	BS^3	IV	SEC	+	N/A
67		223	176	TLQTISLLGYMKHYR	FEDSPSYVKWGK	3402.7325	3	0.2	BS^3	IV	none	+	14.4
68		249	298	STLHNWMSEFK	SVFKK	2140.0665	3	-6.6	BS^3	IV	none	+	26.8
69		264	294	SVCLIGDKEQR	EKSVFK	2178.1357	4	1.1	BS^3	III	SEC	+	13.9
70	a	264	299	SVCLIGDKEQR	KFNWR	2191.1210	3	0.5	BS^3	III	none	+	19.1
70	b	264	299	SVCLIGDKEQR	SVFKKFNWR	2652.3849	3	3.9	BS^3	IV	SEC	+	19.1
71		264	317	SVCLIGDKEQR	IKNEKSK	2287.2208	4	1.2	BS^3	IV	SEC	+	26.7
72		264	319	SVCLIGDKEQR	SKLSEIVR	2372.2736	3	1.4	BS^3	IV	SEC	+	20.5
73		292	319	DVLLPGEWDVCVTSYEMLIKEK	SKLSEIVR	3691.9096	3	5.8	BS^3	IV	SEC	+	11.1
74		319	298	SKLSEIVR	SVFKK	1675.9874	3	0.3	BS^3	IV	SEC	+	13.0
75		319	294	SKLSEIVR	EKSVFK	1805.0300	3	0.3	BS^3	IV	SEC	+	10.3
76	a	328	299	EFKTTNR	KFNWR	1781.9215	4	2.7	BS^3	I	none	+	8.2
76	b	328	299	LSEIVREFKTTNR	KFNWR	2479.3338	4	0.6	BS^3	II	none	+	8.2
77	a	328	298	EFKTTNR	SVFKK	1639.8935	3	-1.0	BS^3	I	SEC	+	7.6
77	b	328	298	LSEIVREFKTTNR	SVFKK	2337.3058	4	-4.0	BS^3	III	none	+	7.6
78	a	397	314	IKADVEK	IKNEK	1573.9230	3	-0.8	BS^3	I	none	+	26.1
78	b	397	314	RIKADVEK	IKNEK	1725.9991	3	-0.7	BS^3	I	SEC	+	26.1
79		694	397	LSKMGESSLR	IKADVEK	2046.1033	3	-0.1	BS^3	I	SEC	+	N/A
80		724	176	QKIAFTEWIEPPKR	FEDSPSYVKWGK	3321.7076	5	3.7	BS^3	IV	SEC	+	N/A
81	a	739	397	KANYAVDAYFR	IKADVEK	2256.1792	3	0.4	BS^3	I	none	+	N/A
81	b	739	397	KANYAVDAYFR	RIKADVEK	2412.2804	3	-1.8	BS^3	III	none	+	N/A
82		739	328	KANYAVDAYFR	EFKTTNR	2349.1755	3	0.9	BS^3	IV	SEC	+	N/A
83		739	299	KANYAVDAYFR	KFNWR	2204.1169	3	3.9	BS^3	I	none	+	N/A
84	a	402	600	ADVEKSLPPK	IGQTKTVR	2122.2000	3	-0.1	BS^3	II	SEC	+	15.8
84	b	402	600	IKADVEKSLPPK	IGQTKTVR	2363.3790	3	-3.1	BS^3	II	SEC	+	15.8
85		407	600	SLPPKKEVK	IGQTKTVR	2064.2309	3	1.1	BS^3	I	none	+	9.2
86	a	494	408	MVVLDKLLPKLK	KEVK	2036.2685	3	2.0	BS^3	III	none	+	17.9
86	b	494	408	LLPKLKEQGSR	KEVK	1908.1410	3	-0.3	BS^3	III	none	+	17.9
86	c	494	408	LLPKLK	KEVK	1350.8852	3	-2.2	BS^3	III	none	+	17.9
86	d	494	408	LLPKLKEQGSR	SLPPKKEVK	2430.4576	3	3.4	BS^3	III	none	+	17.9
86	e	494	408	MVVLDKLLPKLK	SLPPKKEVK	2558.5851	4	1.8	BS^3	III	none	+	17.9
87		494	600	MVVLDKLLPKLK	IGQTKTVR	2435.4915	4	2.0	BS^3	III	none	+	17.9
88	a	600	496	IGQTKTVR	LKEQGSR	1856.0481	3	-1.3	BS^3	IV	SEC	+	15.5
88	b	600	494	IGQTKTVR	LLPKLK	1750.1082	3	0.8	BS^3	I	SEC	+	15.5
89	a	408	600	SLPPKKEVK	IGQTKTVR	2064.2309	3	0.2	BS^3	I	none	+	11.7
89	b	600	408	IGQTKTVR	KEVK	1545.9394	3	-0.5	BS^3	I	none	+	11.7
89	c	600	408	AHRIGQTKTVR	KEVK	1906.1114	4	-1.1	BS^3	II	none	+	11.7
90		624	443	AEMKLR	MDKMR	1563.7937	3	3.3	BS^3	IV	none	+	24.7
91		739	600	KANYAVDAYFR	IGQTKTVR	2356.2541	3	3.4	BS^3	I	SEC	+	N/A
92		739	496	KANYAVDAYFR	LKEQGSR	2271.1650	3	-0.3	BS^3	II	SEC	+	N/A
93		739	418	KANYAVDAYFR	IYVGLSKMQR	2648.3787	3	1.4	BS^3	I	none	+	N/A
94	a	761	799	APKAPRPPK	TIGYKVPR	2031.1995	3	0.6	BS^3	I	SEC	+	12.0
94	b	761	799	APKAPRPPK	KTIGYKVPR	2159.2945	4	-1.6	BS^3	I	none	+	12.0

** continues next page **

94	c	761	799	APKAPRPPKQPNVQDFQFFPPR	TIGYKVPR	3631.9782	5	0.3	BS^3	II	SEC	+	12.0
95		767	847	APRPPKQPNVQDFQFFPPR	LLTQGFTNWNKR	3880.0328	5	3.3	BS^3	IV	SEC	+	20.6
96		794	758	KTIGYKVPR	VSEPKAPK	2053.1937	4	1.3	BS^3	IV	SEC	+	23.6
97	a	799	758	KTIGYKVPR	VSEPKAPK	2053.1937	3	-0.8	BS^3	I	SEC	+	20.2
97	b	799	758	TIGYKVPR	VSEPKAPK	1925.0988	3	0.3	BS^3	I	none	+	20.2
98	a	814	799	NPELPNAAQAQKEEQLK	KTIGYKVPR	3105.6825	5	2.5	BS^3	I	SEC	+	10.0
98	b	814	799	NPELPNAAQAQKEEQLK	TIGYKVPR	2977.5875	3	2.6	BS^3	III	none	+	10.0
99		847	761	LLTQGFTNWNKR	APKAPRPPK	2575.4389	3	-0.8	BS^3	I	SEC	+	22.3
100		847	758	LLTQGFTNWNKR	VSEPKAPK	2469.3382	3	1.3	BS^3	I	none	+	21.6
101	a	859	918	ANEKWGRDDIENIAR	ISIKK	2511.3448	4	1.9	BS^3	III	none	+	18.0
101	b	859	918	ANEKWGRDDIENIAR	RISIKK	2667.4459	4	0.1	BS^3	III	none	+	18.0
102	a	899	855	CNELQDIEKIMAQIER	DFNQFIKANEK	3479.7068	3	-1.8	BS^3	III	SEC	+	12.4
102	b	899	855	CNELQDIEKIMAQIER	RDFNQFIKANEK	3635.8079	5	-0.5	BS^3	III	SEC	+	12.4
103		899	847	CNELQDIEKIMAQIER	LLTQGFTNWNKR	3603.8180	3	0.4	BS^3	I	SEC	+	15.2
104	a	929	918	YKAPFHQLR	ISIKK	1884.0987	4	-4.9	BS^3	I	SEC	+	18.6
104	b	929	918	YKAPFHQLR	RISIKK	2040.1998	5	-1.6	BS^3	II	SEC	+	18.6
105		929	990	YKAPFHQLR	FDWFLKSR	2394.2639	3	-3.8	BS^3	IV	SEC	+	26.8
106		990	919	FDWFLKSR	KALDTK	1910.0304	3	4.3	BS^3	IV	SEC	+	28.2
107		990	918	FDWFLKSR	ISIKK	1823.0347	3	1.0	BS^3	IV	none	+	25.9
108		1020	919	ENMELEEKEKAEK	KALDTK	2418.2202	3	2.2	BS^3	I	none	+	N/A
109	a	691	943	TAEMNEKLSK	ISYGTNKGK	2254.1517	3	0.8	BS^3	III	none	+	N/A
109	b	691	943	KTAEMNEKLSK	ISYGTNKGK	2382.2467	3	-1.7	BS^3	III	none	+	N/A
110	a	691	990	TAEMNEKLSK	FDWFLKSR	2385.2041	3	-1.8	BS^3	I	SEC	+	N/A
110	b	691	990	KTAEMNEKLSK	FDWFLKSR	2513.2990	3	-3.2	BS^3	II	none	+	N/A
111		694	758	LSKMGESSLR	VSEPKAPK	2099.1298	3	-1.7	BS^3	III	none	+	N/A
112		694	929	LSKMGESSLR	YKAPFHQLR	2403.2735	3	3.5	BS^3	IV	SEC	+	N/A
113		694	943	LSKMGESSLR	ISYGTNKGK	2211.1571	3	-0.1	BS^3	I	SEC	+	N/A
114		694	990	LSKMGESSLR	FDWFLKSR	2342.2095	3	1.1	BS^3	I	none	+	N/A
115		724	919	QKIAFTEWIEPPKR	KALDTK	2554.4161	5	-1.0	BS^3	IV	SEC	+	N/A
116		724	929	QKIAFTEWIEPPKR	YKAPFHQLR	3038.6497	5	-3.5	BS^3	IV	SEC	+	N/A
117		724	990	QKIAFTEWIEPPKR	FDWFLKSR	2977.5857	4	2.7	BS^3	IV	SEC	+	N/A
118		735	761	IAFTEWIEPPKR	APKAPRPPK	2584.4532	4	1.2	BS^3	IV	SEC	+	N/A
119		735	855	IAFTEWIEPPKR	DFNQFIKANEK	2976.5388	3	3.5	BS^3	IV	SEC	+	N/A
120		735	919	IAFTEWIEPPKR	KALDTK	2298.2626	4	1.8	BS^3	IV	SEC	+	N/A
121	a	739	758	KANYAVDAYFR	VSEPKAPK	2309.2058	3	0.3	BS^3	I	none	+	N/A
121	b	739	758	KANYAVDAYFREALR	VSEPKAPK	2778.4707	4	2.2	BS^3	II	none	+	N/A
122		739	761	KANYAVDAYFR	APKAPRPPK	2415.3065	3	-2.1	BS^3	I	SEC	+	N/A
123	a	739	799	KANYAVDAYFR	TIGYKVPR	2387.2640	3	-2.6	BS^3		SEC	+	N/A
123	b	739	799	KANYAVDAYFR	KTIGYKVPR	2515.3589	4	1.6	BS^3	IV	SEC	+	N/A
124		739	918	KANYAVDAYFR	ISIKK	2042.1202	3	-0.9	BS^3	I	none	+	N/A
125		739	919	KANYAVDAYFR	KALDTK	2129.1159	3	2.3	BS^3	I	none	+	N/A
126		739	929	KANYAVDAYFR	YKAPFHQLR	2613.3494	3	-2.3	BS^3	III	none	+	N/A
127		739	943	KANYAVDAYFR	ISYGTNKGK	2421.2330	3	0.9	BS^3	IV	SEC	+	N/A
128		739	990	KANYAVDAYFR	FDWFLKSR	2552.2854	3	3.8	BS^3	I	SEC	+	N/A
129		767	739	APRPPKQPNVQDFQFFPPR	KANYAVDAYFR	3719.9004	4	0.5	BS^3	IV	SEC	+	N/A
130		847	739	LLTQGFTNWNKR	KANYAVDAYFR	2931.5034	3	-0.2	BS^3	I	SEC	+	N/A
131		855	739	DFNQFIKANEK	KANYAVDAYFR	2807.3921	3	2.5	BS^3	I	SEC	+	N/A
132		855	694	DFNQFIKANEK	LSKMGESSLR	2597.3161	3	1.3	BS^3	I	SEC	+	N/A
133		859	739	ANEKWGRDDIENIAR	KANYAVDAYFR	3240.5955	5	0.3	BS^3	IV	SEC	+	N/A
134		875	724	EVEGKTPEEVIEYSAVFWER	QKIAFTEWIEPPK	4120.0724	5	4.1	BS^3	IV	none	+	N/A
135	a	899	739	CNELQDIEKIMAQIER	KANYAVDAYFR	3443.6856	4	1.3	BS^3	III	SEC	+	N/A
135	b	899	739	CNELQDIEKIMAQIERGEAR	KANYAVDAYFR	3856.8879	5	0.9	BS^3	III	SEC	+	N/A
136	a	1029	919	RGPKPSTQKR	KALDTK	1966.1325	4	0.3	BS^3	II	none	+	N/A

** continues next page **

136	b	1029	919	GPKPSTQKR	KALDTK	1810.0314	4	-0.6	BS^3	I	SEC	+	N/A
136	c	1029	919	GPKPSTQK	KALDTK	1653.9303	4	-2.0	BS^3	II	SEC	+	N/A
137	a	1034	919	GPKPSTQKR	KALDTK	1810.0314	3	-3.6	BS^3	I	SEC	+	N/A
137	b	1034	919	RGPKPSTQKR	KALDTK	1966.1325	4	-0.8	BS^3	I	SEC	+	N/A
138	a	1036	929	KMDGAPDGR	YKAPFHQLR	2242.1319	3	-0.8	BS^3	I	none	+	N/A
138	b	1036	929	KMDGAPDGRGR	YKAPFHQLR	2455.2545	4	1.2	BS^3	II	none	+	N/A
139	a	1036	919	KMDGAPDGR	KALDTK	1757.8984	3	-0.4	BS^3	II	none	+	N/A
139	b	1036	919	RKMDGAPDGR	KALDTK	1929.9944	4	1.1	BS^3	II	SEC	+	N/A
139	c	1036	919	KMDGAPDGRGR	KALDTK	1971.0210	3	2.4	BS^3	II	none	+	N/A
140	a	1036	918	KMDGAPDGR	RISIKK	1827.0038	4	0	BS^3	II	none	+	N/A
140	b	1036	918	KMDGAPDGR	ISIKK	1670.9027	3	2.4	BS^3	II	none	+	N/A
140	c	1036	918	KMDGAPDGRGR	ISIKK	1884.0253	4	1.3	BS^3	II	none	+	N/A
141	a	694	1036	LSKMGESSLR	KMDGAPDGR	2190.0775	3	-0.7	BS^3	I	none	+	N/A
141	b	694	1036	TAEMNEKLSKMGESSLR	KMDGAPDGR	2993.4259	3	1.7	BS^3	II	none	+	N/A
142		722	694	NFTMDTESSVYNFEGEDYREKQK	LSKMGESSLR	4060.8673	5	4.7	BS^3	I	SEC	+	N/A
143		722	691	NFTMDTESSVYNFEGEDYREKQK	TAEMNEKLSK	4103.8619	4	0.2	BS^3	III	none	+	N/A
144		722	1036	NFTMDTESSVYNFEGEDYREKQK	KMDGAPDGR	3899.7257	4	1.7	BS^3	III	none	+	N/A
145		724	739	QKIAFTEWIEPPKR	KANYAVDAYFR	3196.6712	5	0.4	BS^3	I	SEC	+	N/A
146		724	694	QKIAFTEWIEPPKR	LSKMGESSLR	2986.5952	4	1.0	BS^3	IV	SEC	+	N/A
147		735	694	IAFTEWIEPPKR	LSKMGESSLR	2730.4417	3	-2.5	BS^3	IV	SEC	+	N/A
148		735	1036	IAFTEWIEPPKR	KMDGAPDGR	2569.3001	4	-1.1	BS^3	IV	SEC	+	N/A
149		739	694	KANYAVDAYFR	LSKMGESSLR	2577.2899	3	2.6	BS^3	I	SEC	+	N/A
150		739	691	KANYAVDAYFR	KTAEMNEKLSK	2732.3846	3	2.5	BS^3	I	SEC	+	N/A
151		739	691	KANYAVDAYFR	TAEMNEKLSK	2604.2896	3	1.4	BS^3	I	none	+	N/A
152	a	739	1036	KANYAVDAYFR	KMDGAPDGR	2400.1534	4	-4.7	BS^3	III	none	+	N/A
152	b	739	1036	KANYAVDAYFR	KMDGAPDGRGR	2613.2760	4	-3.3	BS^3	III	none	+	N/A
152	c	739	1036	ERKANYAVDAYFR	KMDGAPDGR	2685.2972	3	-5.6	BS^3	III	none	+	N/A
153		739	1051	KANYAVDAYFR	LKL	1826.9932	3	3.0	BS^3	III	none	+	N/A
154		1020	1036	ENMELEEKEKAEK	KMDGAPDGR	2689.2577	3	0	BS^3	I	SEC	+	N/A

□, Δ MS/MS spectra are provided in SFigure 7 and SFigure 9B, respectively.

x Cross-link was used as distance restraint during rigid body docking.

N/A = Not available, at least one amino acid is missing in the structure.

STable 5: Cross-links for the Snf2H enzyme in the presence of nucleosomes. Cross-linked peptides are listed in an ordered manner according to their cross-link identification number (XL$_{\text{Snf2H,c}}$ 1–181). The table is structured in an indentical manner as described for STable 1 with cross-linked sites being color-coded according to the domain architecture in Figure 41. Data derive from two independent XL-MS experiments.

XL$_{\text{Snf2H,c}}$	Vari-ant	Site 1	Site 2	Pro-tein 1	Pro-tein 2	Peptide 1 sequence	Peptide 2 sequence	Mass (Da)	Charge	Error (ppm)	Cross-linker	Repro-ducibility group	Size selec-tion	Peptide enrich-ment	Cα-Cα distances (Å) cf. structure (pdb 2PYO) in Figure 42A
1		17	7	H2B	H2B	AQKNITK	TSGKAAK	1604.9401	3	0	BS^3	III	none	+	N/A
2		31	82	H2B	H2B	KESYAIYIYK	LAHYNKR	2319.2567	4	-0.5	BS^3	IV	none	+	13.3; 13.7
3		14	4	H3	H3	KSTGGKAPR	TKQTAR	1746.0052	4	-2.8	BS^3	III	none	+	N/A
4		14	37	H3	H3	KSTGGKAPR	KPHR	1578.9258	4	-1.6	BS^3	II	none	+	N/A
5		18	4	H3	H3	KQLATK	TKQTAR	1532.9189	3	-0.2	BS^3	I	none	+	N/A
6	a	23	4	H3	H3	KQLATKAAR	TKQTAR	1831.0943	4	-0.2	BS^3	I	none	+	N/A
6	b	23	4	H3	H3	KQLATKAAR	TKQTARK	1959.1893	5	-2.0	BS^3	II	none	+	N/A
7	a	23	9	H3	H3	KQLATKAAR	KSTGGKAPR	2028.2108	4	-0.6	BS^3	I	none	+	N/A
7	b	23	9	H3	H3	KQLATKAAR	KSTGGK	1704.0197	4	-2.7	BS^3	I	none	+	N/A
8		23	37	H3	H3	KQLATKAAR	KPHR	1664.0149	4	-0.4	BS^3	I	none	+	N/A
9	a	27	4	H3	H3	KSAPATGGVKKPHR	TKQTAR	2278.3173	5	-1.4	BS^3	I	none	+	N/A
9	b	27	4	H3	H3	KSAPATGGVK	TKQTAR	1760.0096	3	0.9	BS^3	I	none	+	N/A
10	a	27	9	H3	H3	KSAPATGGVK	KSTGGKAPR	1957.1260	4	-1.3	BS^3	I	none	+	N/A
10	b	27	9	H3	H3	KSAPATGGVK	KSTGGK	1632.9350	3	-4.9	BS^3	II	none	+	N/A
11	a	27	14	H3	H3	KSAPATGGVKKPHR	KSTGGKAPR	2475.4338	5	1.1	BS^3	II	none	+	N/A
11	b	27	14	H3	H3	KSAPATGGVKKPHR	STGGKAPR	2347.3388	5	-0.5	BS^3	I	none	+	N/A
11	c	27	14	H3	H3	KSAPATGGVK	KSTGGKAPR	1957.1260	4	2.5	BS^3	I	none	+	N/A
11	d	27	14	H3	H3	KSAPATGGVK	STGGKAPR	1829.0311	3	3.7	BS^3	I	none	+	N/A
12		36	18	H3	H3	KSAPATGGVKKPHR	KQLATK	2262.3476	4	-1.0	BS^3	I	none	+	N/A
13	a	36	23	H3	H3	SAPATGGVKKPHR	KQLATKAAR	2432.4280	5	-2.2	BS^3	II	none	+	N/A
13	b	36	23	H3	H3	KSAPATGGVKKPHR	KQLATKAAR	2560.5229	5	-0.9	BS^3	I	none	+	N/A
14		37	14	H3	H3	SAPATGGVKKPHR	KSTGGKAPR	2347.3388	4	-0.6	BS^3	IV	none	+	N/A
15	a	56	18	H3	H3	YQKSTELLIR	KQLATK	2079.2243	3	-1.2	BS^3	I	none	+	N/A
15	b	56	18	H3	H3	RYQKSTELLIR	KQLATK	2235.3254	4	3.7	BS^3	II	none	+	N/A
16		8	20	H4	H4	GKGGKGLGK	KVLR	1456.9393	3	-1.4	BS^3	IV	none	+	N/A
17		20	8	H4	H4	KVLRDNIQGITKPAIR	GKGGKGLGK	2763.6751	5	0.2	BS^3	IV	none	+	N/A
18		31	35	H2B	H2A	RKESYAIYIYK	KGNYAER	2411.2789	4	-1.7	BS^3	III	none	+	15.5; 15.9
19		12	23	H4	H3	GLGKGGAKR	KQLATKAAR	1970.2053	4	1.8	BS^3	III	none	+	N/A
20		8	23	H4	H3	GKGGKGLGK	KQLATKAAR	1928.1835	4	0.2	BS^3	IV	none	+	N/A
21		56	73	H3	H2A	RYQKSTELLIR	DNKK	2051.1679	3	0.8	BS^3	IV	none	+	15.3; 15.7
22	a	56	74	H3	H2A	YQKSTELLIR	DNKKTR	2152.2155	3	0	BS^3	II	none	+	15.5;15.9
22	b	56	74	H3	H2A	RYQKSTELLIR	DNKKTR	2308.3167	4	-0.9	BS^3	II	none	+	15.5;15.9
23		27	8	H3	H4	KSAPATGGVK	GKGGKGLGK	1857.0987	3	0.4	BS^3	III	none	+	N/A
24		105	79	H2B	H3	LLLPGELAKHAVSEGTK	EIAQDFKTDLR	3238.7753	3	1.5	BS^3	I	none	+	16.3; 16.6
25		35	7	H2A	H2B	KGNYAER	TSGKAAK	1639.8833	3	0.4	BS^3	IV	none	+	N/A
26		35	82	H2A	H2B	KGNYAER	LAHYNKR	1879.0004	4	1.8	BS^3	I	none	+	19.9; 20.3
27		91	35	H4	H2A	TVTAMDVVYALKR	KGNYAER	2444.3037	4	2.1	BS^3	IV	none	+	25.6; 25.7
28		23	118	H3	H2A	KQLATKAAR	KTEK	1631.9874	3	-1.5	BS^3	IV	none	+	N/A
29	a	117	14	H2B	H2A	AVTKYTSSK	GKAKSR	1771.0143	3	0.2	BS^3	I	none	+	13.4; 14.0
29	b	117	14	H2B	H2A	HAVSEGTKAVTKYTSSK	AKSR	2395.3011	5	-0.2	BS^3	I	none	+	13.4; 14.0
29	c	117	14	H2B	H2A	HAVSEGTKAVTKYTSSK	GKAKSR	2580.4175	5	0.1	BS^3	I	none	+	13.4; 14.0
29	d	117	14	H2B	H2A	AVTKYTSSK	AKSR	1585.8979	3	0.2	BS^3	IV	none	+	13.4; 14.0
30	a	117	10	H2B	H2A	HAVSEGTKAVTKYTSSK	VKGK	2365.3157	4	0.2	BS^3	IV	none	+	N/A
30	b	117	10	H2B	H2A	AVTKYTSSK	GGKVKGK	1798.0504	3	0.6	BS^3	IV	none	+	N/A
30	c	117	10	H2B	H2A	HAVSEGTKAVTKYTSSK	GGKVKGK	2607.4536	5	-1.2	BS^3	IV	none	+	N/A

** continues next page **

31		117	8	H2B	H2A	AVTKYTSSK	GKGGKVK	1798.0504	3	-0.7	BS^3	I	none	+	N/A
32$^{\lozenge}$		176	847	Snf2H	Snf2H	FEDSPSYVKWGK	LLTQGFTNWNKR	3060.5649	3	1.7	BS^3	IV	none	+	N/D
33$^{\lozenge}$		176	929	Snf2H	Snf2H	FEDSPSYVKWGK	YKAPFHQLR	2742.4110	3	-2	BS^3	III	none	+	N/D
34$^{\lozenge}$		176	990	Snf2H	Snf2H	FEDSPSYVKWGK	FDWFLKSR	2681.3470	3	0.4	BS^3	III	none	+	N/D
35$^{\lozenge}$		929	264	Snf2H	Snf2H	YKAPFHQLR	SVCLIGDK	2191.1764	4	-6.5	BS^3	IV	none	+	N/D
36$^{\lozenge}$		929	299	Snf2H	Snf2H	YKAPFHQLR	KFNWR	2050.1204	4	1.4	BS^3	IV	none	+	N/D
37$^{\lozenge}$		990	299	Snf2H	Snf2H	FDWFLKSR	KFNWR	1989.0565	4	1.2	BS^3	III	none	+	N/D
38		176	739	Snf2H	Snf2H	FEDSPSYVKWGK	KANYAVDAYFR	2900.4325	3	0.8	BS^3	I	none	+	N/A
39$^{\square}$		176	758	Snf2H	Snf2H	FEDSPSYVKWGK	VSEPKAPK	2438.2673	3	1.9	BS^3	III	none	+	N/D
40$^{\square}$		176	799	Snf2H	Snf2H	FEDSPSYVKWGK	TIGYKVPR	2516.3255	3	-0.8	BS^3	III	none	+	N/D
41		176	1036	Snf2H	Snf2H	FEDSPSYVKWGK	KMDGAPDGR	2529.2150	3	-1.8	BS^3	IV	none	+	N/A
42		724	176	Snf2H	Snf2H	QKIAFTEWIEPPKR	FEDSPSYVKWGK	3325.7327	5	-1.7	BS^3	IV	none	+	N/A
43$^{\lozenge}$		418	990	Snf2H	Snf2H	IYVGLSKMQR	FDWFLKSR	2433.3182	3	0.3	BS^3	IV	none	+	N/D
44$^{\square}$		430	929	Snf2H	Snf2H	ILMKDIDILNSAGK	YKAPFHQLR	2830.5719	4	0.9	BS^3	IV	none	+	N/D
45$^{\lozenge}$		430	990	Snf2H	Snf2H	ILMKDIDILNSAGK	FDWFLKSR	2769.5079	3	-0.8	BS^3	III	none	+	N/D
46		418	1036	Snf2H	Snf2H	IYVGLSKMQR	KMDGAPDGR	2281.1863	3	-3.2	BS^3	IV	none	+	N/A
47		430	739	Snf2H	Snf2H	ILMKDIDILNSAGK	KANYAVDAYFR	2988.5935	3	-1.4	BS^3	III	none	+	N/A
48		739	418	Snf2H	Snf2H	KANYAVDAYFR	IYVGLSKMQR	2652.4038	3	2.1	BS^3	III	none	+	N/A
49		440	739	Snf2H	Snf2H	ILMKDIDILNSAGKMDK	KANYAVDAYFR	3362.7559	4	-0.5	BS^3	III	none	+	N/A
50$^{\square}$		119	328	Snf2H	Snf2H	TPTSPLKMKPGRPR	EFKTTNR	2601.4365	4	-1.2	BS^3	IV	none	+	N/A
51$^{\square}$		319	121	Snf2H	Snf2H	SKLSEIVREFK	MKPGRPR	2333.3193	3	-2.9	BS^3	IV	none	+	N/D
52$^{\square}$		176	121	Snf2H	Snf2H	FEDSPSYVKWGK	MKPGRPR	2424.2564	3	0.4	BS^3	III	none	+	N/D
53$^{\square}$	a	83	990	Snf2H	Snf2H	EIQEPDPTYEEKMQTDR	FDWFLKSR	3347.5960	4	-4.2	BS^3	III	none	+	N/A
53	b	83	990	Snf2H	Snf2H	EIQEPDPTYEEKMQTDR	NSPQFRFDWFLKSR	4076.9519	4	1.8	BS^3	III	none	+	N/A
54$^{\square}$		112	814	Snf2H	Snf2H	QTELFAHFIQPAAQKTPTSPLK	VPRNPELPNAAQAQKEEQLK	4853.6021	5	0.5	BS^3	IV	none	+	N/A
55$^{\lozenge}$		119	990	Snf2H	Snf2H	TPTSPLKMKPGRPR	FDWFLKSR	2804.5464	4	-1.6	BS^3	III	none	+	N/A
56$^{\lozenge}$		121	990	Snf2H	Snf2H	TPTSPLKMKPGRPR	FDWFLKSR	2804.5464	4	-1.6	BS^3	III	none	+	N/A
57$^{\lozenge}$		929	121	Snf2H	Snf2H	YKAPFHQLR	MKPGRPR	2141.1984	5	-3.4	BS^3	IV	none	+	N/A
58$^{\lozenge}$		990	129	Snf2H	Snf2H	FDWFLKSR	IKKDEK	1999.1082	4	-1.9	BS^3	III	none	+	N/D
59$^{\square}$	a	647	490	Snf2H	Snf2H	LVDQNLNKIGKDEMLQMIR	MVVLDKLLPK	3553.9954	4	3.5	BS^3	III	none	+	N/D
59	b	647	490	Snf2H	Snf2H	IGKDEMLQMIR	MVVLDKLLPK	2629.4925	3	2.8	BS^3	III	none	+	N/D
60$^{\square}$		665	490	Snf2H	Snf2H	HGATHVFASKESEITDEDIDGILER	MVVLDKLLPK	4065.1285	4	-3.9	BS^3	III	none	+	N/D
61$^{\square}$		490	684	Snf2H	Snf2H	MVVLDKLLPK	KTAEMNEK	2246.2570	3	2.5	BS^3	IV	none	+	N/D
62$^{\lozenge}$	a	644	443	Snf2H	Snf2H	LVDQNLNKIGKDEMLQMIR	MDKMR	3078.6002	3	-1.5	BS^3	III	none	+	N/D
62	b	644	443	Snf2H	Snf2H	LVDQNLNKIGKDEMLQMIR	DIDILNSAGKMDKMR	4105.1348	4	2.2	BS^3	III	none	+	N/D
63$^{\lozenge}$	a	443	647	Snf2H	Snf2H	DIDILNSAGKMDKMR	IGKDEMLQMIR	3180.6319	3	1.8	BS^3	III	none	+	N/D
63	b	647	443	Snf2H	Snf2H	IGKDEMLQMIR	MDKMR	2154.0973	3	1.1	BS^3	III	none	+	N/D
63	c	647	443	Snf2H	Snf2H	LVDQNLNKIGKDEMLQMIR	DIDILNSAGKMDKMR	4105.1348	5	0.1	BS^3	III	none	+	N/D
64$^{\lozenge}$	a	440	647	Snf2H	Snf2H	DIDILNSAGKMDK	IGKDEMLQMIR	2893.4903	3	6.4	BS^3	III	none	+	N/D
64	b	440	647	Snf2H	Snf2H	DIDILNSAGKMDKMR	IGKDEMLQMIR	3180.6319	4	1.3	BS^3	III	none	+	N/D
64	c	440	647	Snf2H	Snf2H	ILMKDIDILNSAGKMDK	IGKDEMLQMIR	3378.7939	4	0.9	BS^3	III	none	+	N/D
64	d	647	440	Snf2H	Snf2H	LVDQNLNKIGKDEMLQMIR	DIDILNSAGKMDK	3817.9932	4	6.6	BS^3	III	none	+	N/D
64	e	647	440	Snf2H	Snf2H	LVDQNLNKIGKDEMLQMIR	DIDILNSAGKMDKMR	4105.1348	5	-4.8	BS^3	III	none	+	N/D
65$^{\square}$	a	430	647	Snf2H	Snf2H	ILMKDIDILNSAGK	IGKDEMLQMIR	3004.6315	3	-1.2	BS^3	III	none	+	N/D
65	b	647	430	Snf2H	Snf2H	LVDQNLNKIGKDEMLQMIR	ILMKDIDILNSAGK	3929.1344	4	0.9	BS^3	III	none	+	N/D
66$^{\lozenge}$		665	430	Snf2H	Snf2H	HGATHVFASKESEITDEDIDGILER	ILMKDIDILNSAGKMDK	4814.4299	5	-2.9	BS^3	IV	none	+	N/D
67$^{\lozenge}$		665	418	Snf2H	Snf2H	HGATHVFASKESEITDEDIDGILER	IYVGLSKMQR	4104.0778	4	-2.9	BS^3	III	none	+	N/D
68$^{\square}$		418	684	Snf2H	Snf2H	IYVGLSKMQR	KTAEMNEK	2285.2063	3	-1.9	BS^3	III	none	+	N/D
69$^{\square}$		408	684	Snf2H	Snf2H	SLPPKKEVK	KTAEMNEK	2116.1753	4	0.3	BS^3	IV	none	+	N/D
70$^{\square}$		407	684	Snf2H	Snf2H	SLPPKKEVK	KTAEMNEK	2116.1753	4	0.3	BS^3	III	none	+	N/D
71$^{\lozenge}$		665	929	Snf2H	Snf2H	HGATHVFASKESEITDEDIDGILER	YKAPFHQLR	4069.0486	5	-0.1	BS^3	I	none	+	N/D
72$^{\lozenge}$		647	929	Snf2H	Snf2H	IGKDEMLQMIR	YKAPFHQLR	2633.4126	4	0.1	BS^3	IV	none	+	N/D
73$^{\lozenge}$		665	990	Snf2H	Snf2H	HGATHVFASKESEITDEDIDGILER	FDWFLKSR	4007.9846	4	-0.4	BS^3	III	none	+	N/D

** continues next page **

74	a	990	647	Snf2H	Snf2H	NSPQFRFDWFLKSR	IGKDEMLQMIR	3301.7044	4	4.4	BS^3	III	none	+	N/D
74$^{\diamond}$	b	647	990	Snf2H	Snf2H	LVDQNLNKIGKDEMLQMIR	FDWFLKSR	3496.8515	4	0.5	BS^3	III	none	+	N/D
74	c	647	990	Snf2H	Snf2H	LVDQNLNKIGKDEMLQMIR	NSPQFRFDWFLKSR	4226.2073	5	-0.4	BS^3	III	none	+	N/D
74	d	647	990	Snf2H	Snf2H	IGKDEMLQMIR	FDWFLKSR	2572.3486	4	0.7	BS^3	III	none	+	N/D
75		694	684	Snf2H	Snf2H	LSKMGESSLR	KTAEMNEK	2198.1226	4	0.7	BS^3	III	none	+	N/A
76		694	683	Snf2H	Snf2H	LSKMGESSLR	GAKK	1650.9278	3	1.2	BS^3	IV	none	+	N/A
77		665	694	Snf2H	Snf2H	HGATHVFASKESEITDEDIDGILER	LSKMGESSLR	4016.9942	4	-3.0	BS^3	IV	none	+	N/A
78	a	647	691	Snf2H	Snf2H	LVDQNLNKIGKDEMLQMIR	TAEMNEKLSK	3548.8557	4	-1.6	BS^3	III	none	+	N/A
78	b	647	691	Snf2H	Snf2H	IGKDEMLQMIR	TAEMNEKLSK	2624.3527	3	2.6	BS^3	III	none	+	N/A
79	a	647	694	Snf2H	Snf2H	LVDQNLNKIGKDEMLQMIR	LSKMGESSLR	3505.8611	5	2.5	BS^3	III	none	+	N/A
79	b	647	694	Snf2H	Snf2H	IGKDEMLQMIR	LSKMGESSLR	2581.3582	3	1.4	BS^3	III	none	+	N/A
79	c	644	694	Snf2H	Snf2H	LVDQNLNKIGKDEMLQMIR	LSKMGESSLR	3505.8611	4	2.6	BS^3	III	none	+	N/A
80	a	665	735	Snf2H	Snf2H	HGATHVFASKESEITDEDIDGILER	IAFTEWIEPPKRER	4681.3605	4	-1.3	BS^3	III	none	+	N/A
80	b	665	735	Snf2H	Snf2H	HGATHVFASKESEITDEDIDGILER	IAFTEWIEPPKR	4396.2168	4	4.8	BS^3	III	none	+	N/A
81	a	647	739	Snf2H	Snf2H	IGKDEMLQMIR	KANYAVDAYFR	2791.4341	3	-0.7	BS^3	II	none	+	N/A
81	b	647	739	Snf2H	Snf2H	LVDQNLNKIGKDEMLQMIR	KANYAVDAYFR	3715.9370	3	1.4	BS^3	II	none	+	N/A
81	c	739	647	Snf2H	Snf2H	ERKANYAVDAYFR	IGKDEMLQMIR	3076.5778	5	0.8	BS^3	II	none	+	N/A
82		644	739	Snf2H	Snf2H	LVDQNLNKIGKDEMLQMIR	KANYAVDAYFR	3715.937	4	0.4	BS^3	I	none	+	N/A
83		665	1036	Snf2H	Snf2H	HGATHVFASKESEITDEDIDGILER	KMDGAPDGR	3855.8526	4	5.5	BS^3	IV	none	+	N/A
84	a	647	684	Snf2H	Snf2H	IGKDEMLQMIR	KTAEMNEK	2424.2366	3	-0.3	BS^3	III	none	+	N/A
84	b	647	684	Snf2H	Snf2H	LVDQNLNKIGKDEMLQMIR	KTAEMNEK	3348.7396	4	1.0	BS^3	III	none	+	N/A
85		665	683	Snf2H	Snf2H	HGATHVFASKESEITDEDIDGILER	GAKK	3312.6778	3	0.8	BS^3	IV	none	+	N/A
86	a	665	684	Snf2H	Snf2H	HGATHVFASKESEITDEDIDGILER	KTAEMNEKLSK	4188.0837	5	3.4	BS^3	II	none	+	N/A
86	b	665	684	Snf2H	Snf2H	HGATHVFASKESEITDEDIDGILER	KTAEMNEK	3859.8726	5	-2.4	BS^3	I	none	+	N/A
87		97	121	Snf2H	Snf2H	ANRFEYLLKQTELFAHFIQPAAQK	MKPGRPR	3845.0867	5	-3.5	BS^3	IV	none	+	N/A
88		97	128	Snf2H	Snf2H	ANRFEYLLKQTELFAHFIQPAAQK	IKKDEK	3764.0606	4	0.3	BS^3	III	none	+	N/A
89		112	128	Snf2H	Snf2H	QTELFAHFIQPAAQKTPTSPLK	IKKDEK	3353.8539	4	1.1	BS^3	IV	none	+	N/A
90	a	160	176	Snf2H	Snf2H	RTEQEEDEELLTESSK	FEDSPSYVKWGK	3505.6565	4	1.0	BS^3	III	none	+	N/D
90$^{\square}$	b	160	176	Snf2H	Snf2H	TEQEEDEELLTESSK	FEDSPSYVKWGK	3349.5553	3	3.4	BS^3	III	none	+	N/D
91$^{\square}$		176	128	Snf2H	Snf2H	FEDSPSYVKWGK	IKKDEK	2343.2302	3	2.1	BS^3	IV	none	+	N/D
92	a	176	249	Snf2H	Snf2H	FEDSPSYVKWGK	STLHNWMSEFKR	3118.5162	3	2.1	BS^3	I	none	+	N/D
92	b	176	249	Snf2H	Snf2H	FEDSPSYVKWGKLR	STLHNWMSEFKR	3387.7014	4	2.1	BS^3	II	none	+	N/D
93		176	397	Snf2H	Snf2H	FEDSPSYVKWGK	IKADVEK	2385.2408	3	-2.0	BS^3	IV	none	+	N/D
94		223	176	Snf2H	Snf2H	TLQTISLLGYMKHYR	FEDSPSYVKWGK	3406.7576	4	-0.4	BS^3	IV	none	+	N/D
95		319	298	Snf2H	Snf2H	SKLSEIVREFK	SVFKK	2084.2185	4	1.4	BS^3	III	none	+	N/D
96		328	298	Snf2H	Snf2H	EFKTTNR	SVFKK	1643.9186	3	-0.2	BS^3	IV	none	+	N/D
97		328	299	Snf2H	Snf2H	EFKTTNR	KFNWR	1785.9466	4	0.9	BS^3	IV	none	+	N/D
98		397	314	Snf2H	Snf2H	IKADVEK	IKNEK	1573.9230	3	-0.2	BS^3	IV	none	+	N/D
99		407	600	Snf2H	Snf2H	SLPPKKEVK	IGQTKTVR	2068.2560	4	-1.6	BS^3	III	none	+	N/D
100	a	600	408	Snf2H	Snf2H	IGQTKTVR	KEVK	1545.9394	3	2.3	BS^3	III	none	+	N/D
100	b	408	600	Snf2H	Snf2H	SLPPKKEVK	IGQTKTVR	2068.2560	4	-1.6	BS^3	III	none	+	N/D
101		411	490	Snf2H	Snf2H	KEVKIYVGLSK	MVVLDK	2108.2470	3	-0.7	BS^3	IV	none	+	N/D
102		494	407	Snf2H	Snf2H	MVVLDKLLPKLK	SLPPKKEVK	2562.6102	3	-1.1	BS^3	IV	none	+	N/D
103	a	494	408	Snf2H	Snf2H	LLPKLKEQGSR	SLPPKKEVK	2434.4827	3	-0.5	BS^3	III	none	+	N/D
103	b	494	408	Snf2H	Snf2H	LLPKLKEQGSR	KEVK	1912.1661	4	-1.4	BS^3	III	none	+	N/D
103	c	494	408	Snf2H	Snf2H	MVVLDKLLPKLK	KEVK	2040.2936	3	-1.4	BS^3	III	none	+	N/D
103	d	494	408	Snf2H	Snf2H	MVVLDKLLPKLK	SLPPKKEVK	2562.6102	3	-1.1	BS^3	III	none	+	N/D
104		929	919	Snf2H	Snf2H	YKAPFHQLR	KALDTK	1975.1195	3	4.2	BS^3	I	none	+	N/D
105	a	929	918	Snf2H	Snf2H	IGRYKAPFHQLR	ISIKK	2214.3305	4	0.5	BS^3	I	none	+	N/D
105	b	929	918	Snf2H	Snf2H	YKAPFHQLR	ISIKK	1888.1238	3	3.7	BS^3	I	none	+	N/D
105	c	929	918	Snf2H	Snf2H	YKAPFHQLR	RISIKK	2044.2249	5	-2.3	BS^3	I	none	+	N/D
106		847	859	Snf2H	Snf2H	LLTQGFTNWNKRDFNQFIK	ANEKWGRDDIENIAR	4297.1973	5	0.5	BS^3	IV	none	+	N/D
107		943	929	Snf2H	Snf2H	ISYGTNKGK	YKAPFHQLR	2267.2366	5	-3.0	BS^3	IV	none	+	N/D

** continues next page **

108		814	799	Snf2H	Snf2H	NPELPNAAQAQKEEQLK	TIGYKVPR	2981.6126	4	-2.4	BS^3	I	none	+	N/D
109	a	761	799	Snf2H	Snf2H	APKAPRPPK	KTIGYKVPR	2163.3196	4	-1.7	BS^3	III	none	+	N/D
109	b	761	799	Snf2H	Snf2H	APKAPRPPK	TIGYKVPR	2035.2246	3	1.1	BS^3	III	none	+	N/D
110		758	799	Snf2H	Snf2H	EALRVSEPKAPK	TIGYKVPR	2398.3888	3	-0.1	BS^3	III	none	+	N/D
111	a	799	758	Snf2H	Snf2H	TIGYKVPR	VSEPKAPK	1929.1239	3	1.1	BS^3	III	none	+	N/D
111	b	799	758	Snf2H	Snf2H	KTIGYKVPR	VSEPKAPK	2057.2188	3	0	BS^3	III	none	+	N/D
112		943	990	Snf2H	Snf2H	ISYGTNKGK	FDWFLKSR	2206.1726	3	3.2	BS^3	IV	none	+	N/D
113	a	929	990	Snf2H	Snf2H	IGRYKAPFHQLR	FDWFLKSR	2724.4956	5	-0.3	BS^3	II	none	+	N/D
113	b	990	929	Snf2H	Snf2H	NSPQFRFDWFLKSR	YKAPFHQLR	3127.6448	4	1.2	BS^3	II	none	+	N/D
113	c	929	990	Snf2H	Snf2H	YKAPFHQLR	FDWFLKSR	2398.289	3	2.7	BS^3	I	none	+	N/D
114	a	990	919	Snf2H	Snf2H	FDWFLKSR	KALDTK	1914.0555	4	-1.4	BS^3	II	none	+	N/D
114	b	990	919	Snf2H	Snf2H	NSPQFRFDWFLKSR	KALDTK	2643.4113	4	2.4	BS^3	I	none	+	N/D
115		847	761	Snf2H	Snf2H	LLTQGFTNWNKR	APKAPRPPK	2579.4640	3	-2.7	BS^3	III	none	+	N/D
116	a	758	847	Snf2H	Snf2H	EALRVSEPKAPK	LLTQGFTNWNKR	2942.6282	4	2.5	BS^3	III	none	+	N/D
116	b	847	758	Snf2H	Snf2H	LLTQGFTNWNKR	VSEPKAPK	2473.3633	3	0.2	BS^3	III	none	+	N/D
116	c	847	758	Snf2H	Snf2H	LLTQGFTNWNKRDFNQFIK	VSEPKAPK	3365.8076	3	1.3	BS^3	III	none	+	N/D
117▸		929	799	Snf2H	Snf2H	YKAPFHQLR	TIGYKVPR	2233.2675	3	0.7	BS^3	IV	none	+	N/D
118▸		990	799	Snf2H	Snf2H	FDWFLKSR	TIGYKVPR	2172.2035	3	1.5	BS^3	IV	none	+	N/D
119▸		990	758	Snf2H	Snf2H	NSPQFRFDWFLKSR	VSEPKAPK	2823.5012	4	0.5	BS^3	IV	none	+	N/D
120		847	739	Snf2H	Snf2H	LLTQGFTNWNKR	KANYAVDAYFR	2935.5285	3	-0.2	BS^3	IV	none	+	N/A
121		739	758	Snf2H	Snf2H	KANYAVDAYFR	VSEPKAPK	2313.2309	3	1.3	BS^3	I	none	+	N/A
122		1036	990	Snf2H	Snf2H	KMDGAPDGR	FDWFLKSR	2185.0930	3	1.5	BS^3	I	none	+	N/A
123		990	1049	Snf2H	Snf2H	FDWFLKSR	KLKL	1740.0278	3	0.3	BS^3	IV	none	+	N/A
124		739	799	Snf2H	Snf2H	KANYAVDAYFR	TIGYKVPR	2391.2891	3	-0.5	BS^3	I	none	+	N/A
125		990	1051	Snf2H	Snf2H	FDWFLKSR	KLKL	1740.0278	3	-0.4	BS^3	III	none	+	N/A
126		694	758	Snf2H	Snf2H	LSKMGESSLR	VSEPKAPK	2103.1549	4	-0.3	BS^3	IV	none	+	N/A
127		1034	943	Snf2H	Snf2H	GPKPSTQKR	ISYGTNKGK	2106.1737	3	0.7	BS^3	III	none	+	N/A
128		943	1036	Snf2H	Snf2H	ISYGTNKGK	KMDGAPDGR	2054.0406	3	0.4	BS^3	III	none	+	N/A
129		1018	919	Snf2H	Snf2H	ENMELEEKEKAEK	KALDTK	2422.2453	3	0.1	BS^3	III	none	+	N/A
130	a	919	1020	Snf2H	Snf2H	KALDTK	EKAEK	1419.8124	3	1.2	BS^3	IV	none	+	N/A
130	b	1020	919	Snf2H	Snf2H	ENMELEEKEKAEK	KALDTK	2422.2453	3	1.1	BS^3	IV	none	+	N/A
131	a	929	1034	Snf2H	Snf2H	IGRYKAPFHQLR	GPKPSTQKR	2624.4967	5	-4.0	BS^3	II	none	+	N/A
131	b	1034	929	Snf2H	Snf2H	GPKPSTQKR	YKAPFHQLR	2298.2901	5	-0.9	BS^3	I	none	+	N/A
131	c	1034	929	Snf2H	Snf2H	RGPKPSTQKR	YKAPFHQLR	2454.3912	5	1.8	BS^3	I	none	+	N/A
132	a	929	1036	Snf2H	Snf2H	IGRYKAPFHQLR	KMDGAPDGR	2572.3637	5	2.5	BS^3	I	none	+	N/A
132	b	929	1036	Snf2H	Snf2H	IGRYKAPFHQLR	KMDGAPDGRGR	2801.4811	5	2.0	BS^3	II	none	+	N/A
132	c	1036	929	Snf2H	Snf2H	KMDGAPDGRGR	YKAPFHQLR	2475.2745	5	1.1	BS^3	II	none	+	N/A
132	d	1036	929	Snf2H	Snf2H	KMDGAPDGR	YKAPFHQLR	2246.1570	4	-0.5	BS^3	I	none	+	N/A
133		1029	919	Snf2H	Snf2H	GPKPSTQKR	KALDTK	1814.0565	4	-0.3	BS^3	I	none	+	N/A
134	a	1034	919	Snf2H	Snf2H	GPKPSTQKR	KALDTK	1814.0565	4	0.4	BS^3	II	none	+	N/A
134	b	1034	919	Snf2H	Snf2H	RGPKPSTQKR	KALDTK	1970.1576	4	-1.9	BS^3	I	none	+	N/A
135		855	739	Snf2H	Snf2H	DFNQFIKANEK	KANYAVDAYFR	2811.4172	3	-1.9	BS^3	IV	none	+	N/A
136	a	919	1036	Snf2H	Snf2H	ISIKKALDTK	KMDGAPDGR	2219.2135	4	-1.0	BS^3	II	none	+	N/A
136	b	919	1036	Snf2H	Snf2H	KALDTKIGR	KMDGAPDGR	2104.1250	4	-0.3	BS^3	II	none	+	N/A
136	c	1036	919	Snf2H	Snf2H	KMDGAPDGRGR	KALDTK	1975.0461	4	-0.5	BS^3	II	none	+	N/A
136	d	1036	919	Snf2H	Snf2H	KMDGAPDGR	KALDTK	1761.9235	3	-0.5	BS^3	II	none	+	N/A
137		1036	918	Snf2H	Snf2H	KMDGAPDGR	ISIKK	1674.9278	3	0.8	BS^3	IV	none	+	N/A
138	a	929	1051	Snf2H	Snf2H	YKAPFHQLR	LKL	1672.9968	3	0	BS^3	III	none	+	N/A
138	b	929	1051	Snf2H	Snf2H	YKAPFHQLR	KLKL	1801.0918	4	0.5	BS^3	III	none	+	N/A
139		739	929	Snf2H	Snf2H	KANYAVDAYFR	YKAPFHQLR	2617.3745	4	-0.2	BS^3	I	none	+	N/A
140		694	943	Snf2H	Snf2H	LSKMGESSLR	ISYGTNKGK	2215.1822	3	-1.5	BS^3	III	none	+	N/A
141		739	990	Snf2H	Snf2H	KANYAVDAYFR	FDWFLKSR	2556.3105	3	1.5	BS^3	IV	none	+	N/A
142		691	990	Snf2H	Snf2H	TAEMNEKLSK	FDWFLKSR	2389.2292	3	2.7	BS^3	III	none	+	N/A
143		1036	1049	Snf2H	Snf2H	KMDGAPDGR	KLKL	1587.8958	3	-4.3	BS^3	I	none	+	N/A

** continues next page **

144		1036	1051	Snf2H	Snf2H	KMDGAPDGR	KLKL	1587.8958	4	-3.7	BS^3	I	none	+	N/A
145		722	694	Snf2H	Snf2H	NFTMDTESSVYNFEGEDYREKQK	LSKMGESSLR	4064.8924	4	-4.6	BS^3	II	none	+	N/A
146		694	739	Snf2H	Snf2H	TAEMNEKLSKMGESSLR	KANYAVDAYFR	3368.6685	4	-2.1	BS^3	III	none	+	N/A
147		739	691	Snf2H	Snf2H	KANYAVDAYFR	TAEMNEKLSK	2608.3147	3	-2.0	BS^3	III	none	+	N/A
148		1036	758	Snf2H	Snf2H	KMDGAPDGR	VSEPKAPK	1942.0134	4	0.1	BS^3	III	none	+	N/A
149	a	739	1036	Snf2H	Snf2H	KANYAVDAYFR	KMDGAPDGR	2404.1785	3	-5.1	BS^3	I	none	+	N/A
149	b	739	1036	Snf2H	Snf2H	KANYAVDAYFR	KMDGAPDGRGR	2633.2960	4	2.5	BS^3	II	none	+	N/A
149	c	694	1036	Snf2H	Snf2H	LSKMGESSLR	KMDGAPDGR	2194.1026	4	-1.2	BS^3	I	none	+	N/A
															Cα-Cα distances (Å) cf. model in Figure 44B
150°		990	118	Snf2H	H2A	FDWFLKSR	KTEK	1743.9499	3	4.8	BS^3	III	none	+	42.4
151°		105	739	H2B	Snf2H	LLLPGELAKHAVSEGTK	KANYAVDAYFR	3220.7436	3	2.5	BS^3	I	none	+	N/A
152°		105	758	H2B	Snf2H	LLLPGELAKHAVSEGTK	VSEPKAPK	2758.5785	3	3.9	BS^3	IV	none	+	N/A
153°		990	117	Snf2H	H2B	NSPQFRFDWFLKSR	AVTKYTSSK	2952.5438	4	1.9	BS^3	IV	none	+	27.0
154▼		105	929	H2B	Snf2H	LLLPGELAKHAVSEGTK	YKAPFHQLR	3062.7221	5	0.8	BS^3	III	none	+	14.7^x
155°		105	990	H2B	Snf2H	LLLPGELAKHAVSEGTK	FDWFLKSR	3001.6581	3	4.8	BS^3	III	none	+	19.8
156°		105	1036	H2B	Snf2H	LLLPGELAKHAVSEGTK	KMDGAPDGR	2849.5261	3	-5.3	BS^3	I	none	+	N/A
157°		105	1049	H2B	Snf2H	LLLPGELAKHAVSEGTK	KLKL	2404.4609	3	1.8	BS^3	III	none	+	N/A
158°		117	1036	H2B	Snf2H	AVTKYTSSK	KMDGAPDGR	2071.0559	3	4.9	BS^3	III	none	+	N/A
159°		739	11	Snf2H	H2B	KANYAVDAYFR	KAGK	1861.0038	3	2.5	BS^3	IV	none	+	N/A
160°		739	117	Snf2H	H2B	KANYAVDAYFR	AVTKYTSSK	2442.2735	3	1.7	BS^3	III	none	+	N/A
161°		739	122	Snf2H	H2B	KANYAVDAYFR	AVTKYTSSK	2442.2735	3	1.2	BS^3	IV	none	+	N/A
162°		249	4	Snf2H	H3	STLHNWMSEFKR	TKQTAR	2380.2261	4	1.3	BS^3	IV	none	+	N/A
163°		739	4	Snf2H	H3	KANYAVDAYFR	TKQTAR	2162.1424	3	0.2	BS^3	IV	none	+	N/A
164°		929	4	Snf2H	H3	YKAPFHQLR	TKQTAR	2004.1208	3	0.5	BS^3	I	none	+	N/A
165°	a	990	4	Snf2H	H3	NSPQFRFDWFLKSR	TKQTAR	2672.4127	4	1.5	BS^3	III	none	+	N/A
165	b	990	4	Snf2H	H3	FDWFLKSR	TKQTAR	1943.0569	3	2.5	BS^3	III	none	+	N/A
166°		9	929	H3	Snf2H	KSTGGKAPR	YKAPFHQLR	2201.2373	5	-0.1	BS^3	III	none	+	N/A
167°	a	929	14	Snf2H	H3	YKAPFHQLR	STGGKAPR	2073.1423	3	-1.1	BS^3	II	none	+	N/A
167	b	14	929	H3	Snf2H	KSTGGKAPR	YKAPFHQLR	2201.2373	5	-0.6	BS^3	I	none	+	N/A
168°		919	18	Snf2H	H3	KALDTK	KQLATK	1503.9175	3	-0.2	BS^3	III	none	+	N/A
169°		929	18	Snf2H	H3	YKAPFHQLR	KQLATK	1988.1511	3	0.6	BS^3	I	none	+	N/A
170°	a	990	18	Snf2H	H3	FDWFLKSR	KQLATK	1927.0871	4	-0.9	BS^3	I	none	+	N/A
170	b	990	18	Snf2H	H3	NSPQFRFDWFLKSR	KQLATK	2656.4429	5	1.3	BS^3	I	none	+	N/A
171°		1036	18	Snf2H	H3	KMDGAPDGRGR	KQLATK	2004.0726	5	-1.4	BS^3	IV	none	+	N/A
172°		23	919	H3	Snf2H	KQLATKAAR	KALDTK	1802.0929	3	-0.4	BS^3	IV	none	+	N/A
173°		23	929	H3	Snf2H	KQLATKAAR	YKAPFHQLR	2286.3264	4	-0.5	BS^3	I	none	+	N/A
174°		27	929	H3	Snf2H	KSAPATGGVK	YKAPFHQLR	2215.2417	4	-0.5	BS^3	I	none	+	N/A
175°		27	943	H3	Snf2H	KSAPATGGVK	ISYGTNKGK	2023.1253	3	2.8	BS^3	IV	none	+	N/A
176°	a	990	27	Snf2H	H3	NSPQFRFDWFLKSR	KSAPATGGVK	2883.5336	4	2.2	BS^3	I	none	+	N/A
176	b	27	990	H3	Snf2H	KSAPATGGVK	FDWFLKSR	2154.1777	3	-3.5	BS^3	II	none	+	N/A
177°		27	1036	H3	Snf2H	KSAPATGGVKKPHR	KMDGAPDGR	2536.3484	5	-3.6	BS^3	II	none	+	N/A
178°		56	758	H3	Snf2H	YQKSTELLIR	VSEPKAPK	2246.2826	3	7.8	BS^3	IV	none	+	N/A
179°	a	929	8	Snf2H	H4	YKAPFHQLR	GGKGLGK	1916.0936	4	0.1	BS^3	III	none	+	N/A
179	b	8	929	H4	Snf2H	GKGGKGLGK	YKAPFHQLR	2101.2100	5	-1.2	BS^3	III	none	+	N/A
180°	a	12	929	H4	Snf2H	GLGKGGAKR	YKAPFHQLR	2143.2318	4	1.5	BS^3	III	none	+	N/A
180	b	929	12	Snf2H	H4	YKAPFHQLR	GLGKGGAK	1987.1307	3	-0.2	BS^3	III	none	+	N/A
181	a	16	929	H4	Snf2H	GLGKGGAKR	YKAPFHQLR	2143.2318	5	-0.9	BS^3	I	none	+	N/A
181°	b	929	16	Snf2H	H4	YKAPFHQLR	GGAKR	1788.0098	4	-1.0	BS^3	II	none	+	N/A
181	c	929	16	Snf2H	H4	IGRYKAPFHQLR	GGAKR	2114.2165	5	-0.4	BS^3	II	none	+	N/A

▼, ►, ◊, □, ° MS/MS spectra are provided in Figure 44A, SFigure 8, SFigure 9C, SFigure 10B, and SFigure 11, respectively.

[x] Cross-link was used as distance restraint during rigid body docking.

N/A = Not available, at least one amino acid is missing in the structure. N/D = Not determined.

6.6. MS/MS spectra of cross-linked peptides

6.6.1. Additional MS/MS spectra of cross-links used for modeling

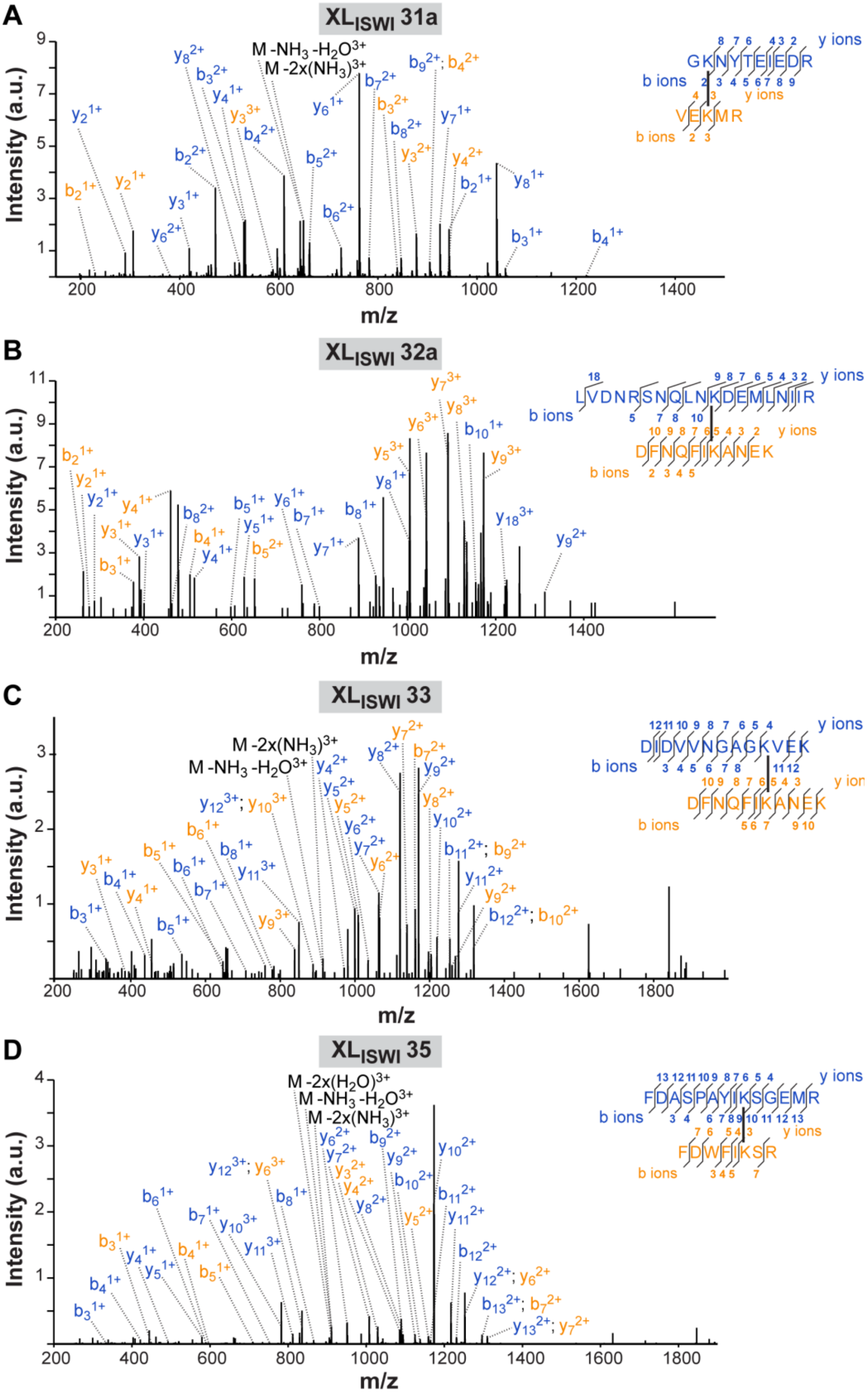

SFigure 5: Additional MS/MS spectra of cross-links used to model the full-length DmISWI enzyme. Related to Figure 21. Cross-links **(A)–(D)** are denoted according to their XL_{ISWI} identification number provided in STable 2. Adapted and reprinted from (1) in accordance with Elsevier's policies.

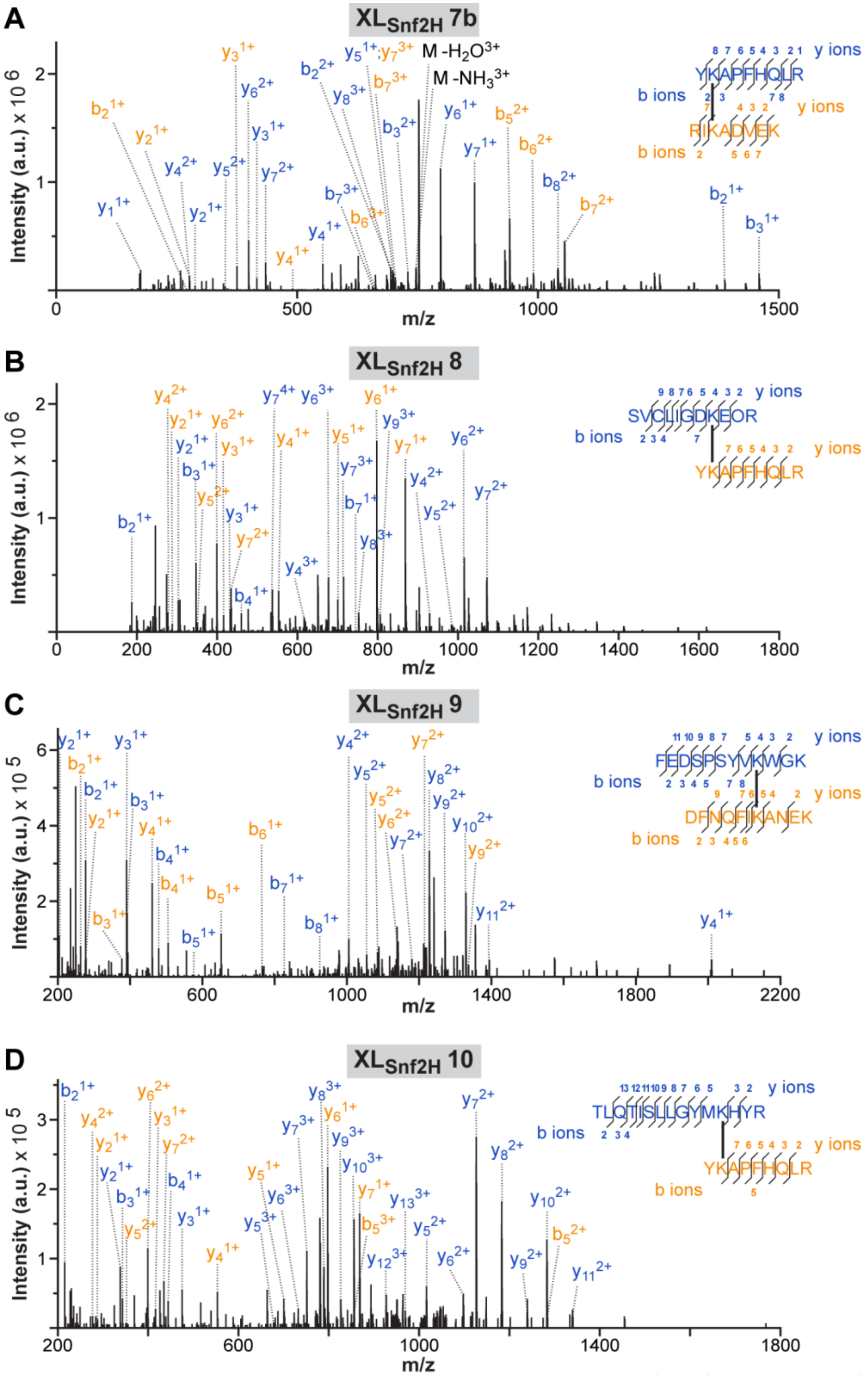

* continues next page*

E

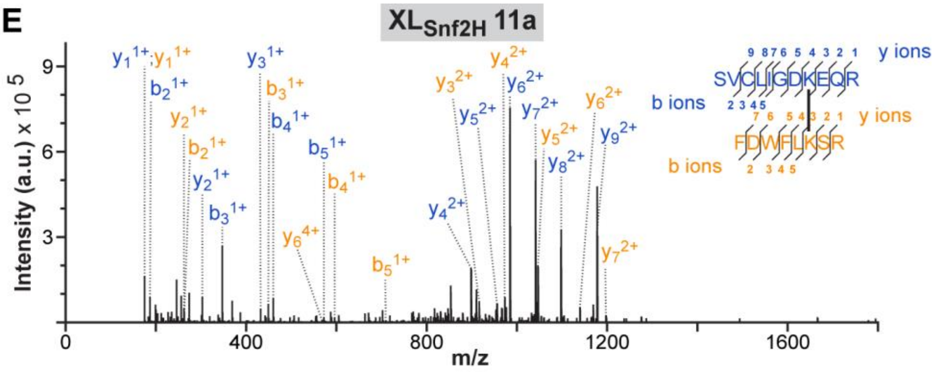

F

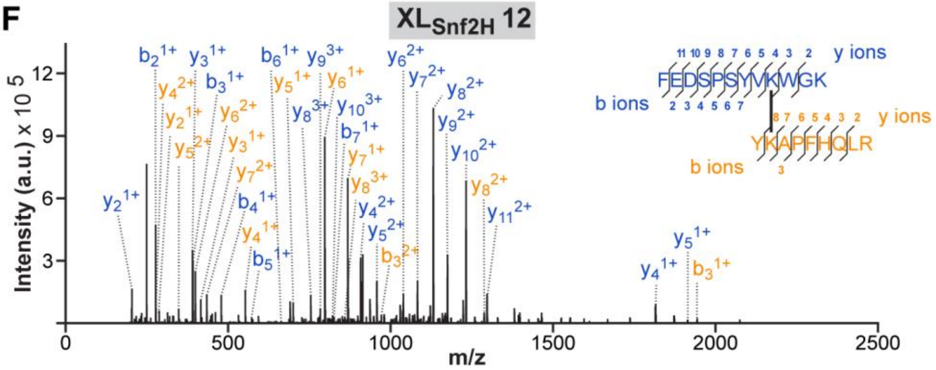

G

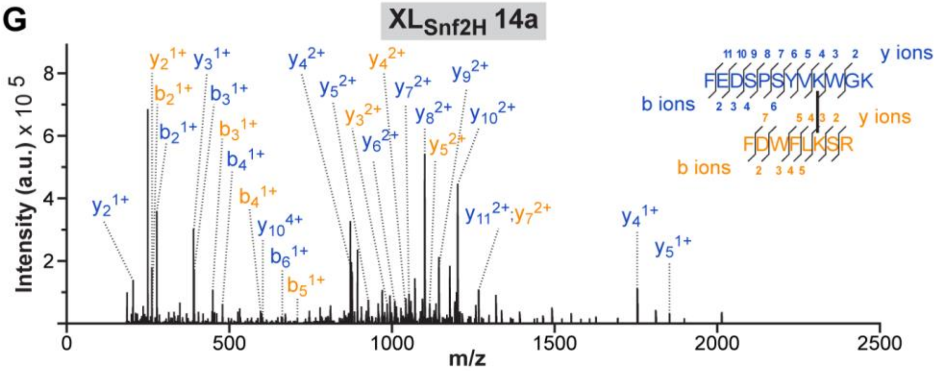

H

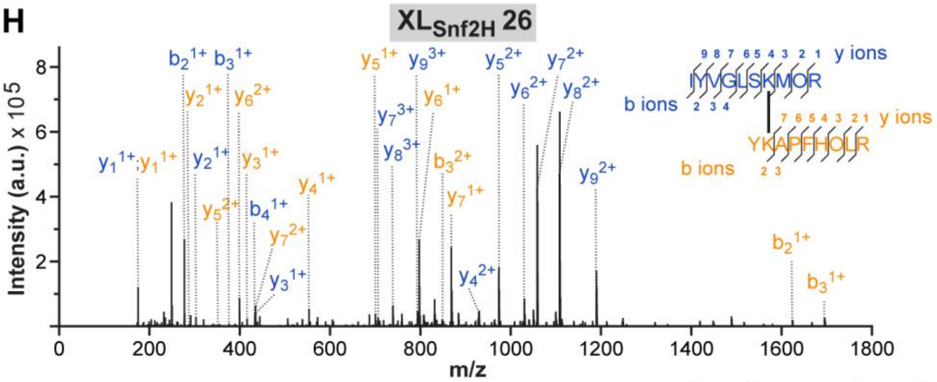

* continues next page*

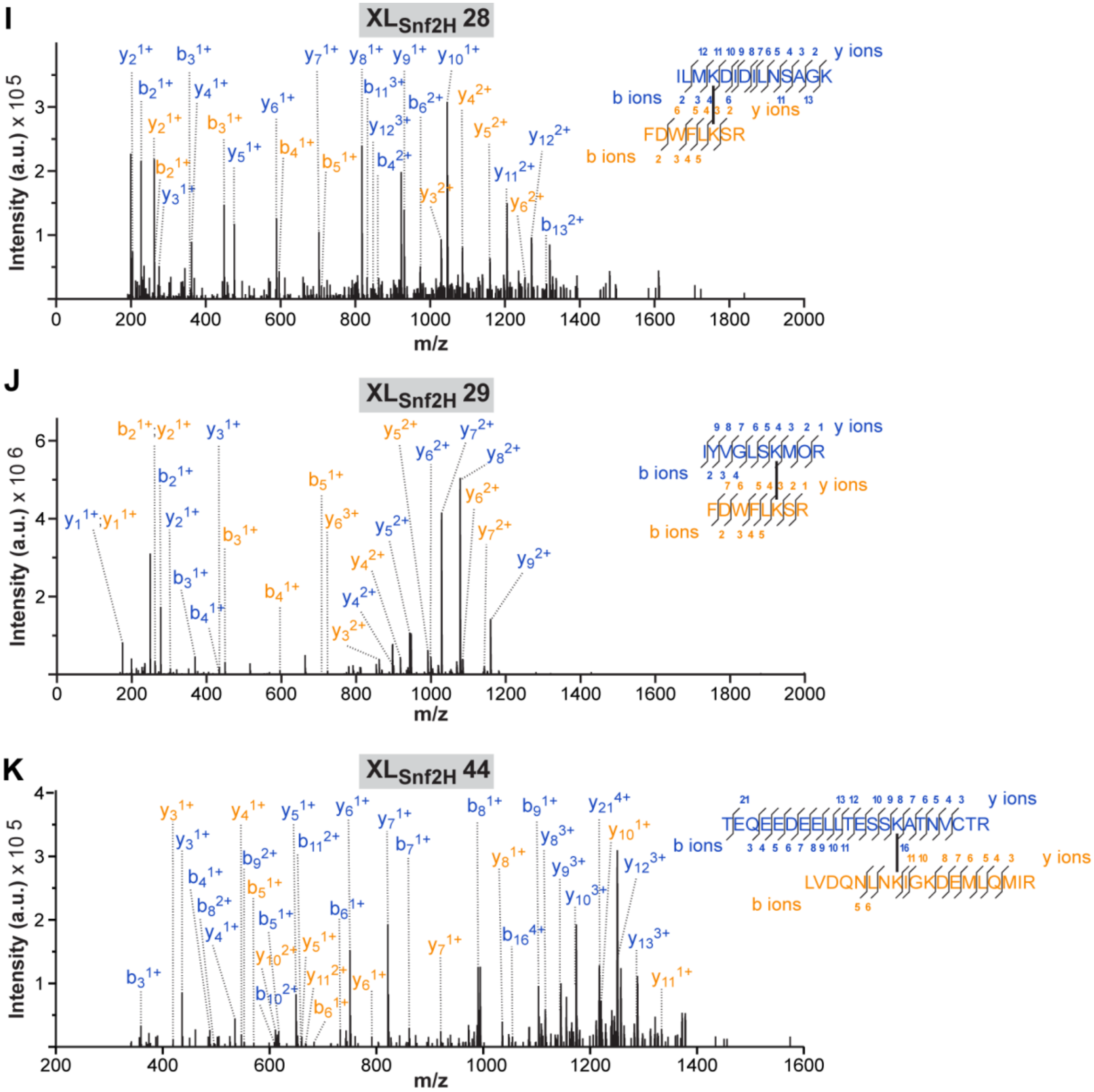

SFigure 6: MS/MS spectra of cross-links used to model the structure of Snf2H under apo state conditions. Related to Figure 31A. Cross-links **(A)–(K)** are denoted according to their XL$_{Snf2H}$ identification number provided in STable 3.

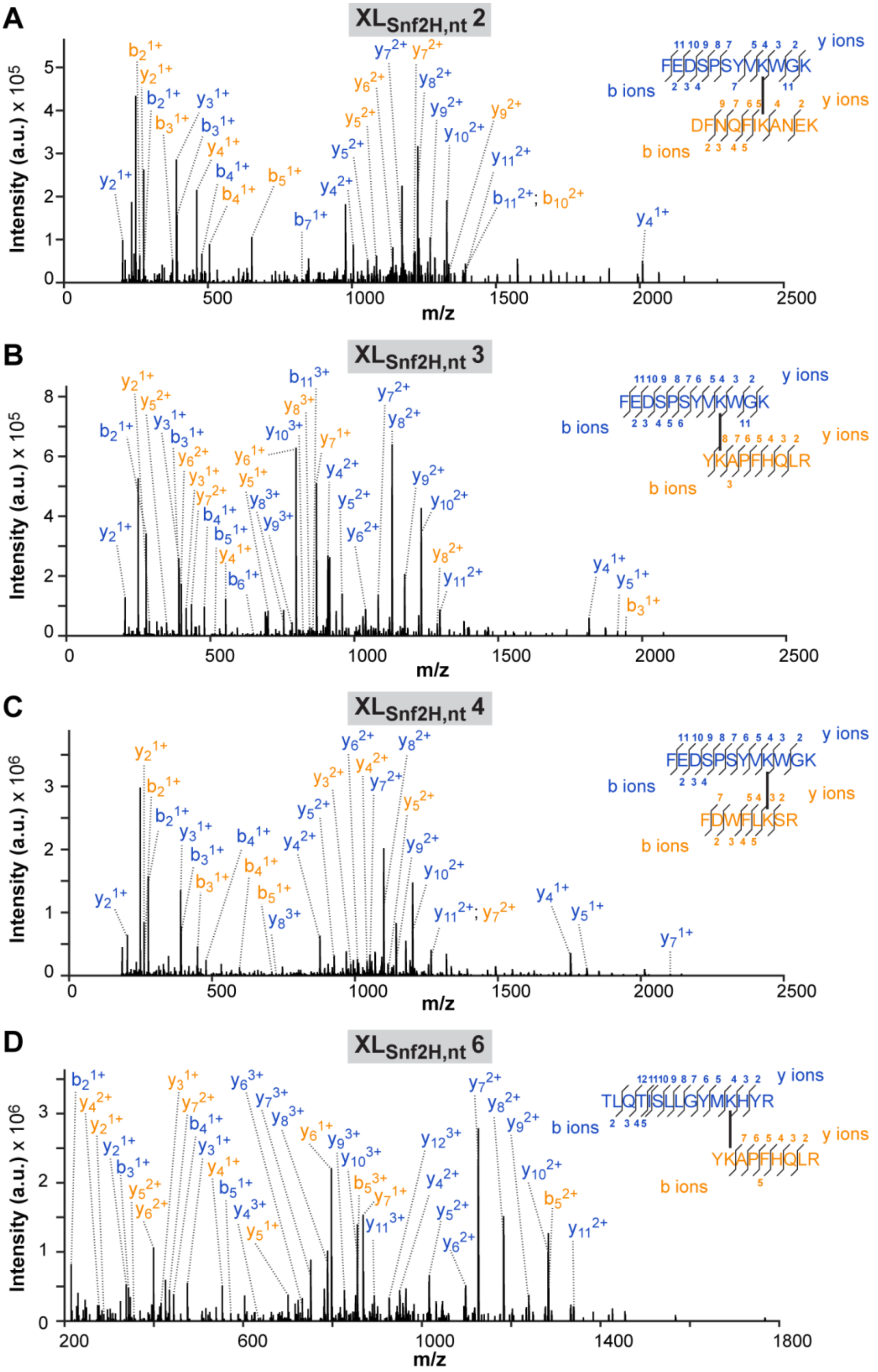

* continues next page*

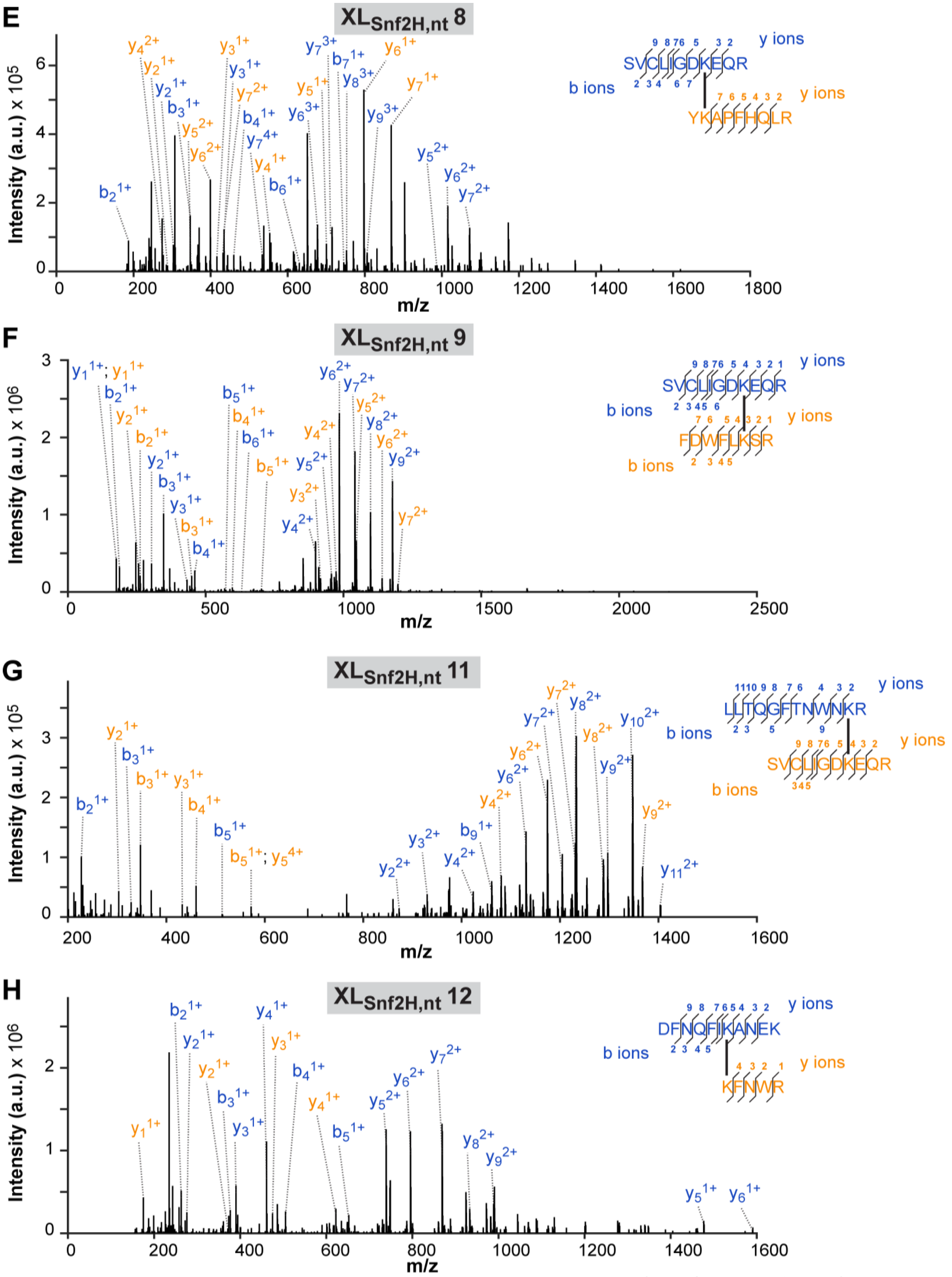

* continues next page*

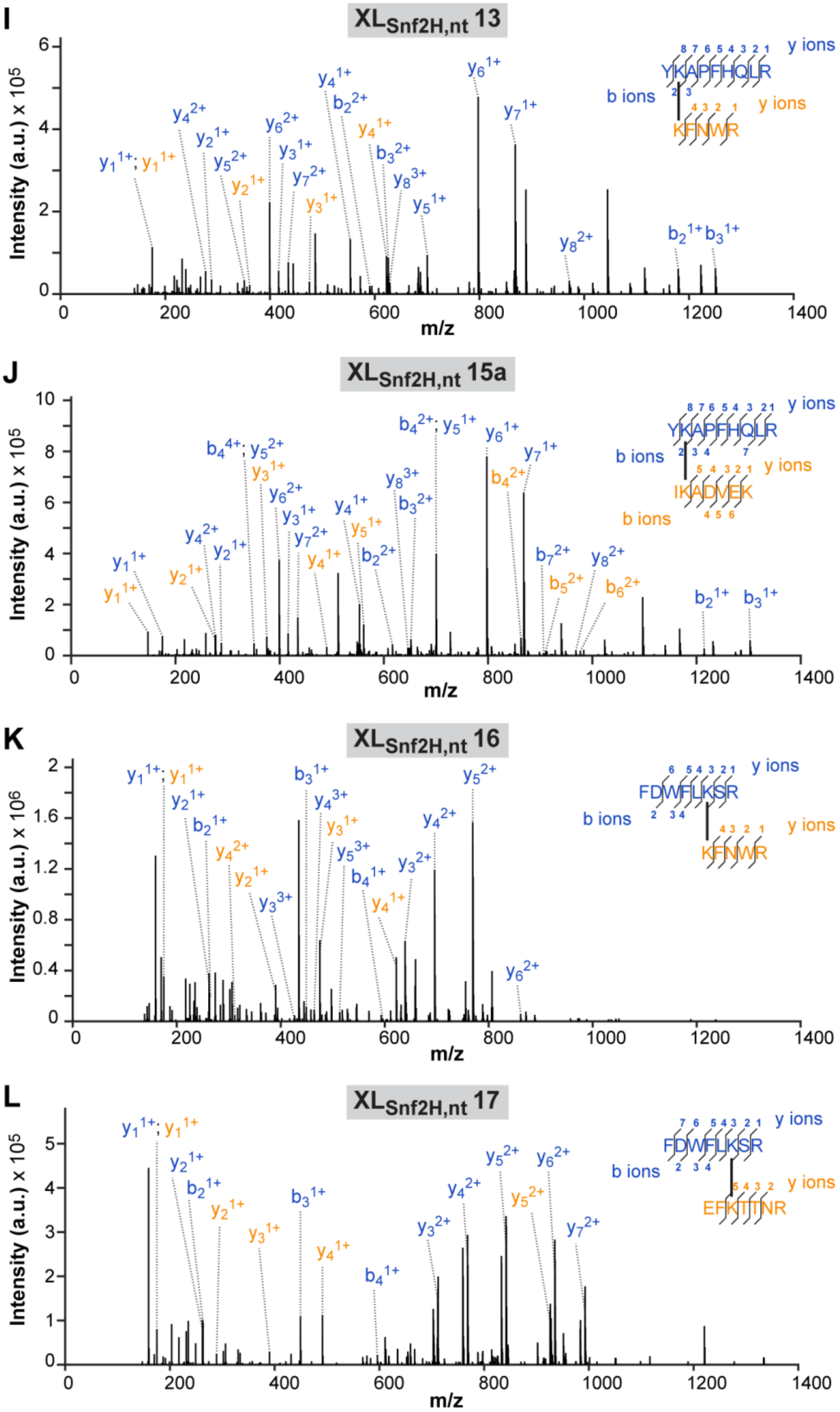

* continues next page*

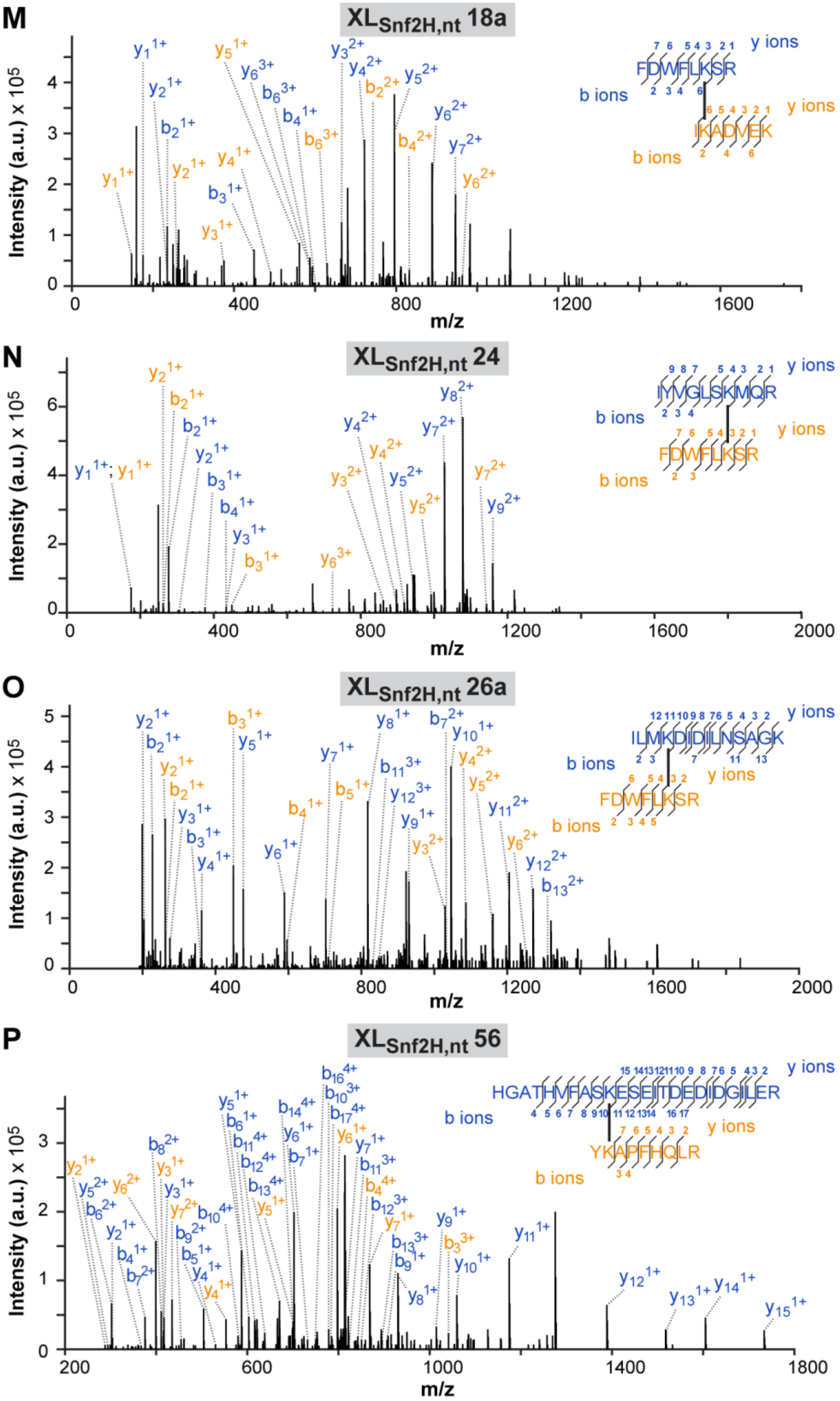

SFigure 7: MS/MS spectra of cross-links used to model the structure of Snf2H in the presence of ADP-BeF$_x$. Related to Figure 37A. Cross-links **(A)–(P)** are denoted according to their XL$_{\mathrm{Snf2H,nt}}$ identification number provided in STable 4.

6.6.2. Additional MS/MS spectra of cross-links for the Snf2H enzyme

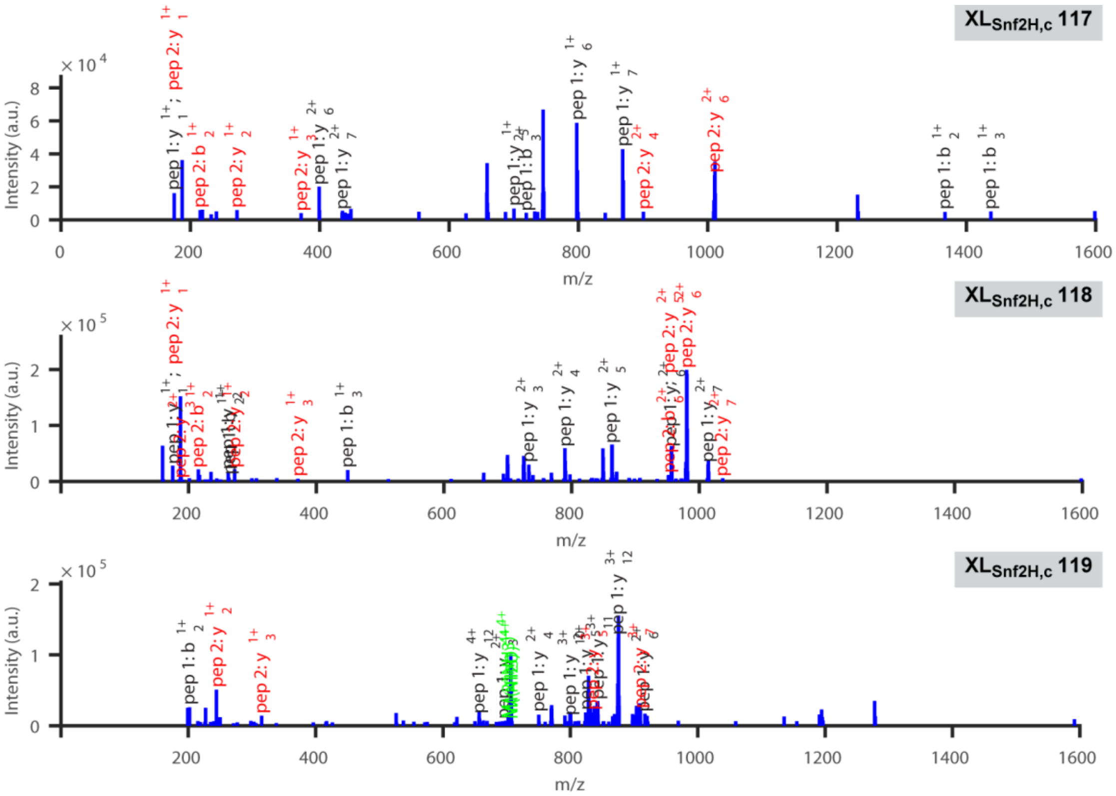

SFigure 8: MS/MS spectra of identified cross-links XL$_{\text{Snf2H,c}}$ 117–119. Related to Figure 42C. These cross-links connect residues within the HSS domain of the Snf2H enzyme in the presence of nucleosomes and exceed the BS^3 distance threshold in the respective homology model. Cross-links are denoted according to their XL$_{\text{Snf2H,c}}$ identification number provided in STable 5.

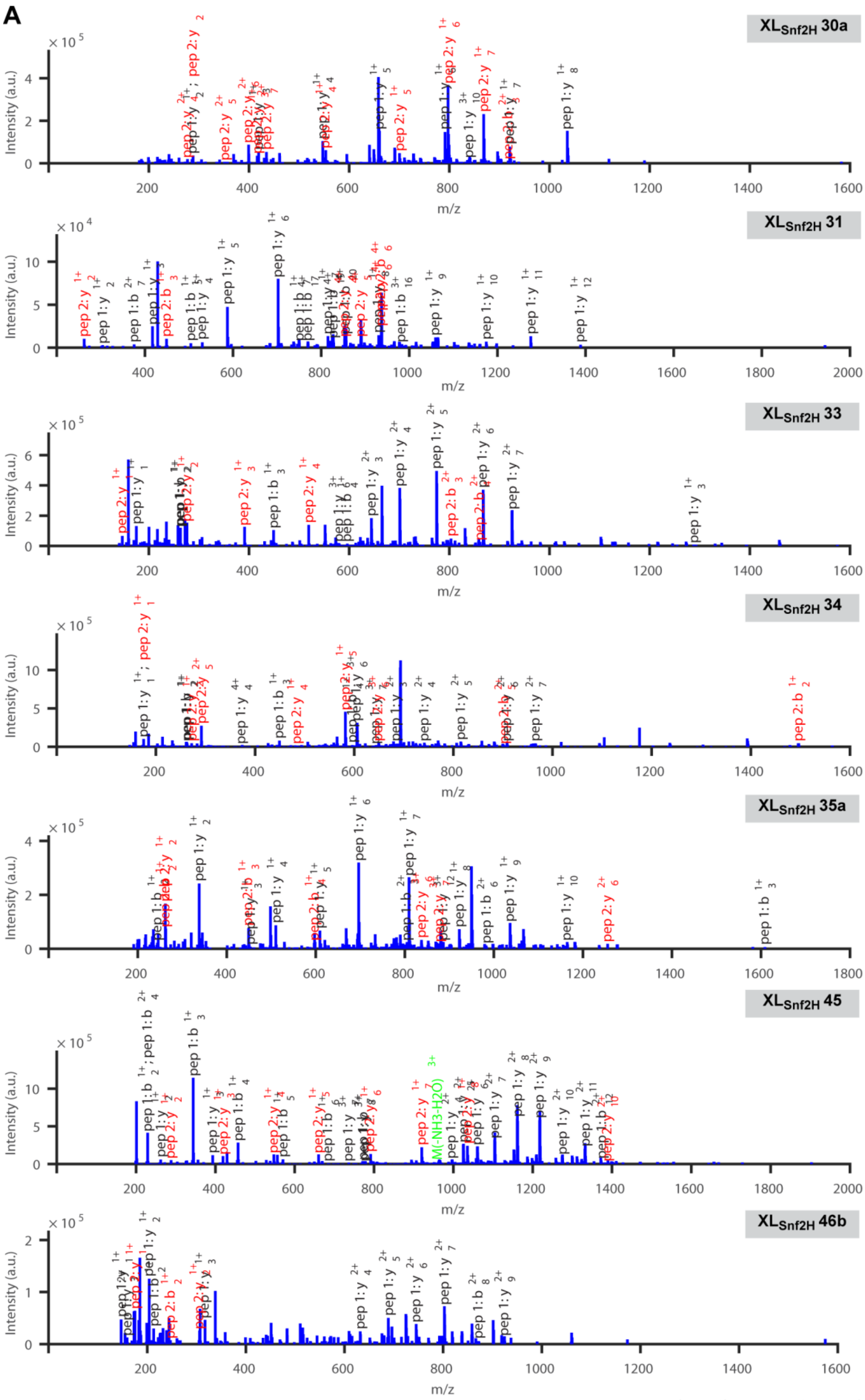

* continues next page *

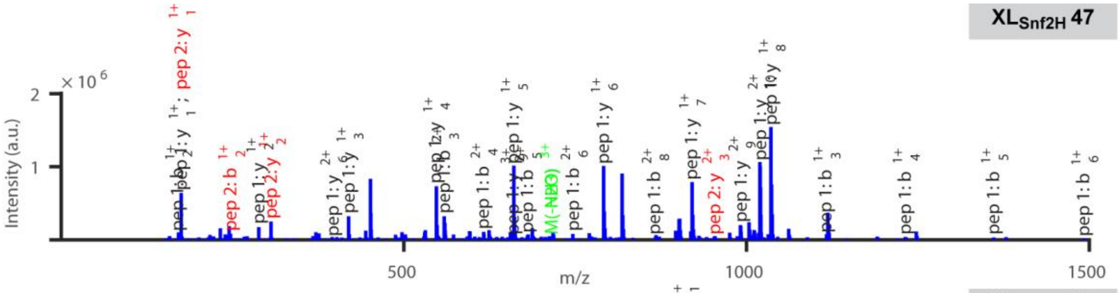

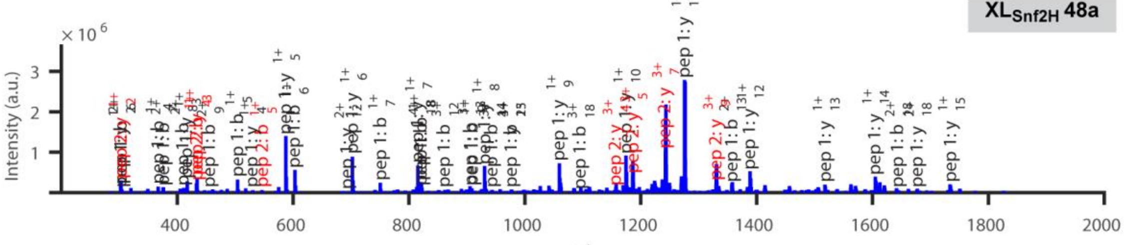

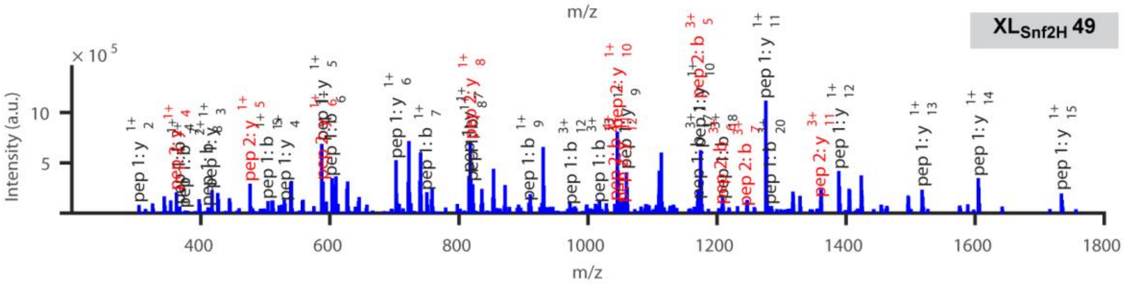

B

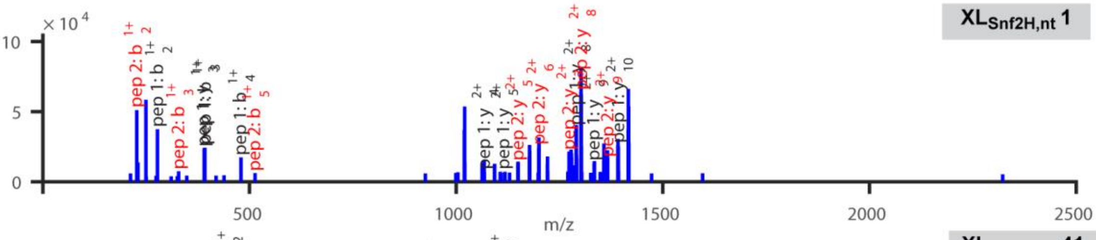

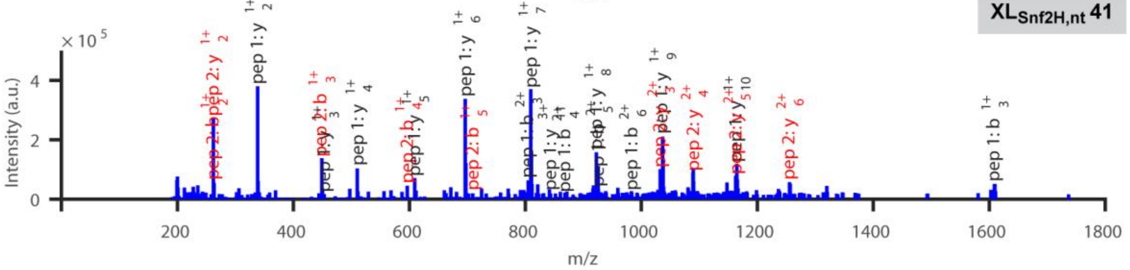

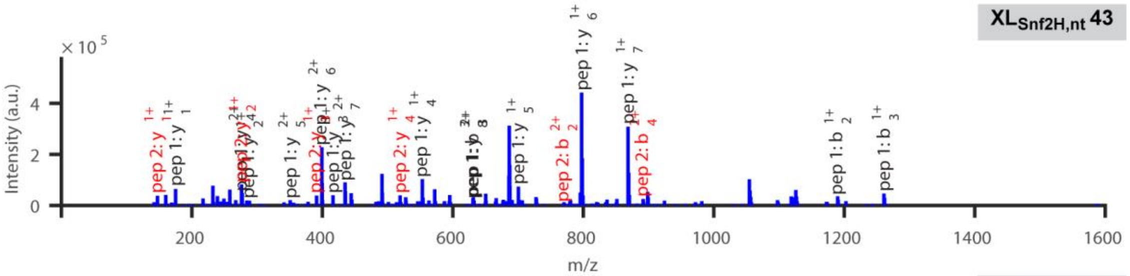

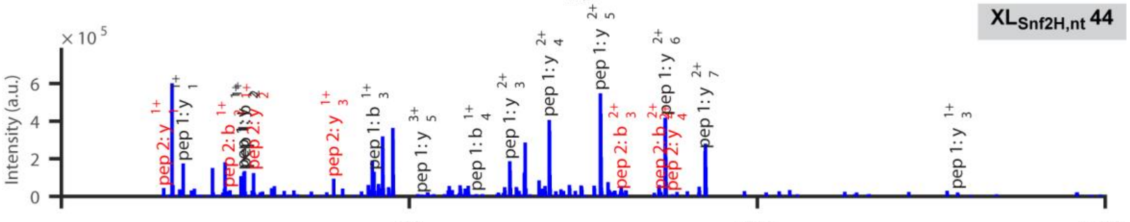

* continues next page *

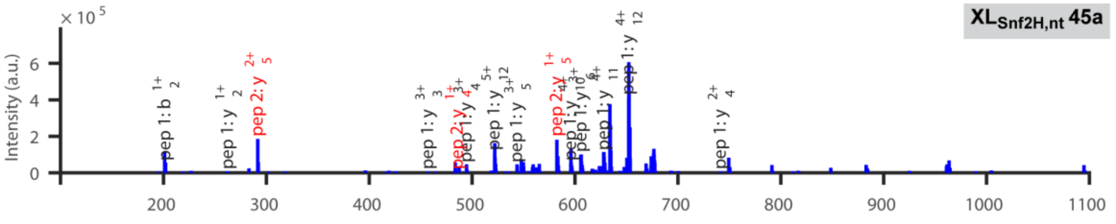
XL$_{Snf2H,nt}$ 45a

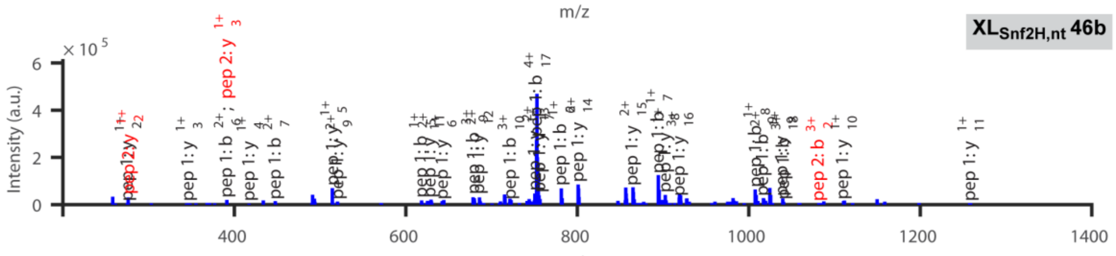
XL$_{Snf2H,nt}$ 46b

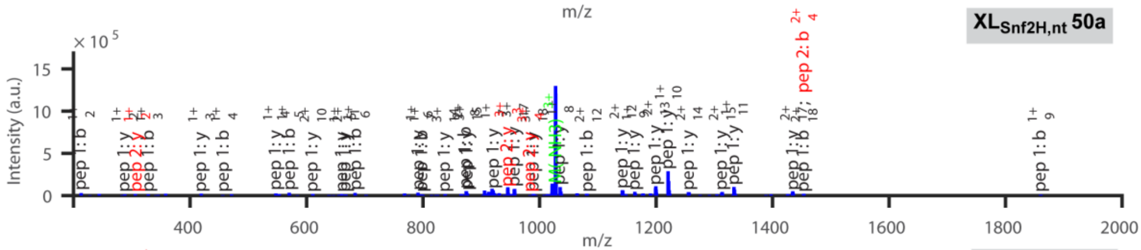
XL$_{Snf2H,nt}$ 50a

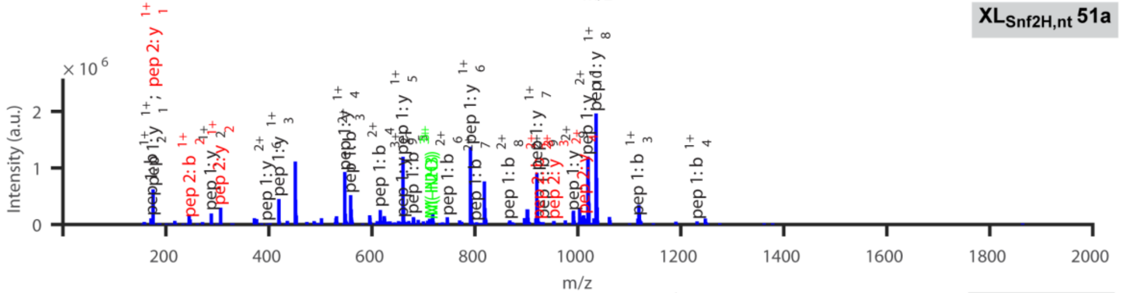
XL$_{Snf2H,nt}$ 51a

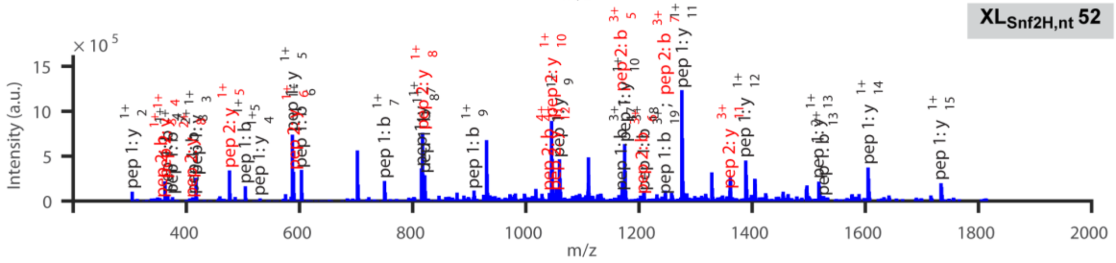
XL$_{Snf2H,nt}$ 52

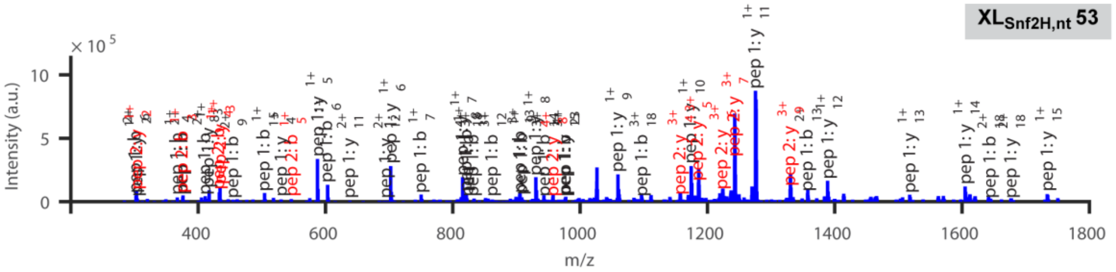
XL$_{Snf2H,nt}$ 53

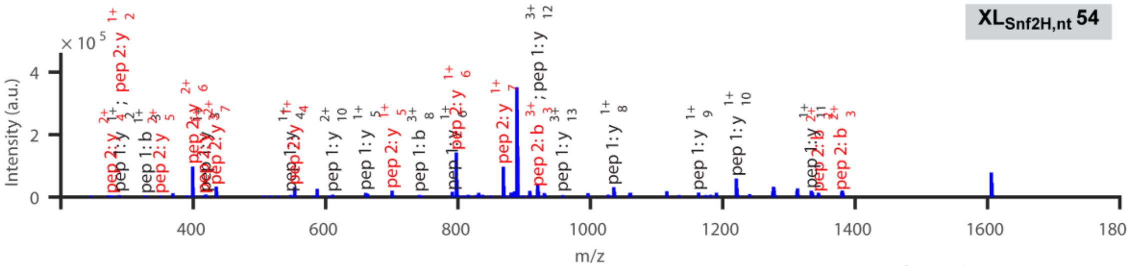
XL$_{Snf2H,nt}$ 54

* continues next page *

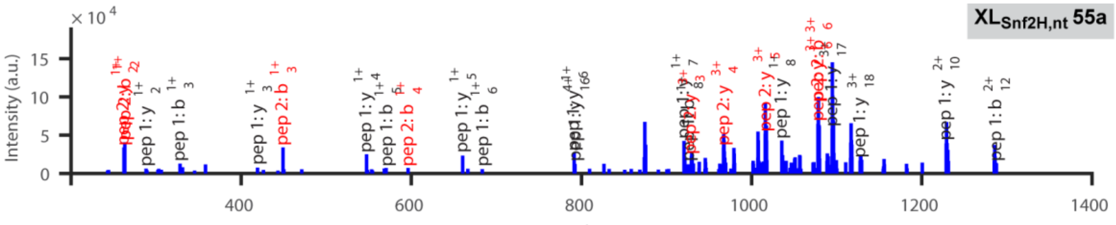

XL$_{Snf2H,nt}$ 55a

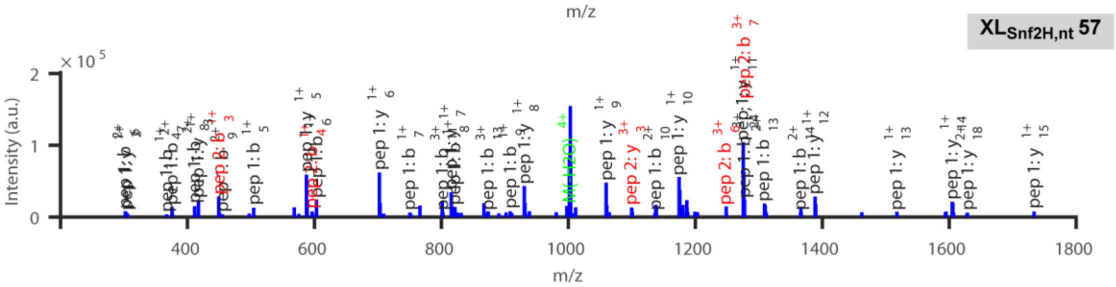

XL$_{Snf2H,nt}$ 57

C

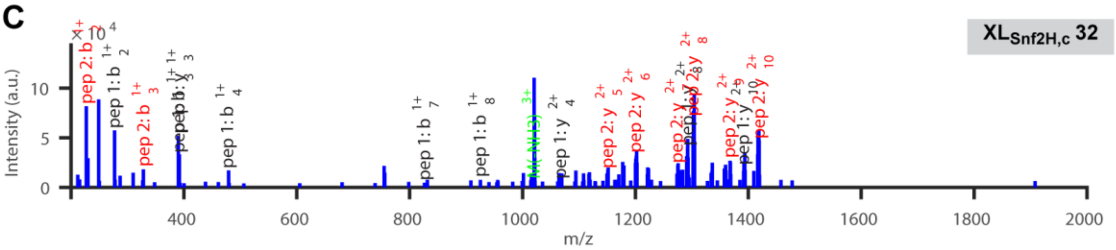

XL$_{Snf2H,c}$ 32

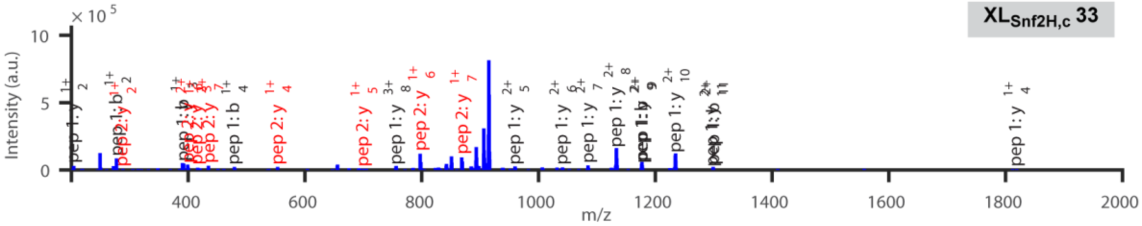

XL$_{Snf2H,c}$ 33

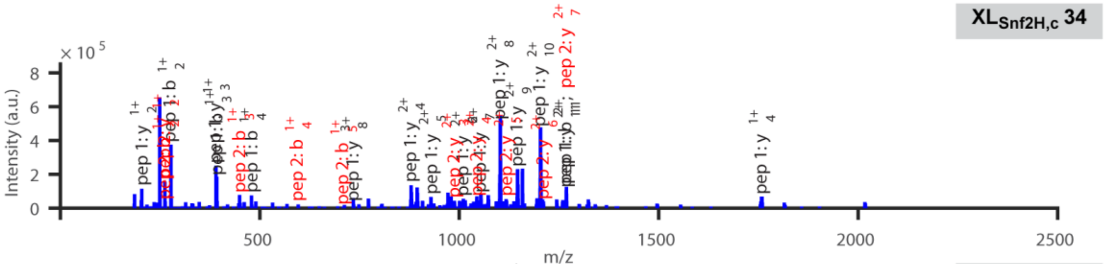

XL$_{Snf2H,c}$ 34

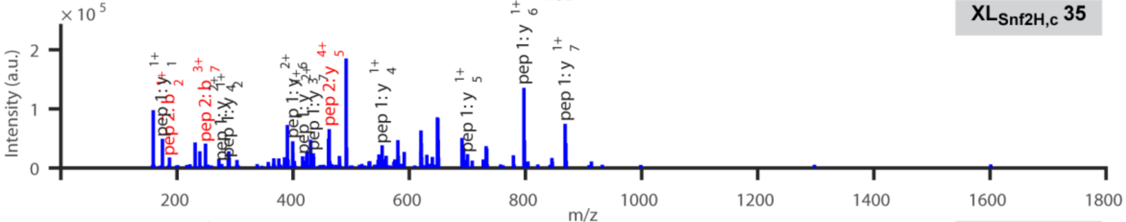

XL$_{Snf2H,c}$ 35

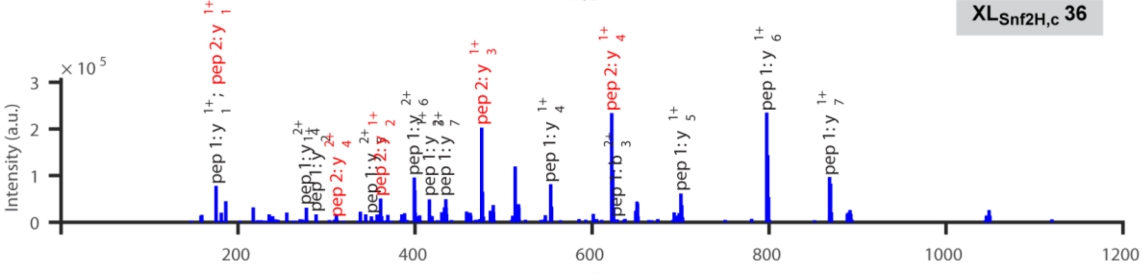

XL$_{Snf2H,c}$ 36

* continues next page *

XL$_{Snf2H,c}$ 37

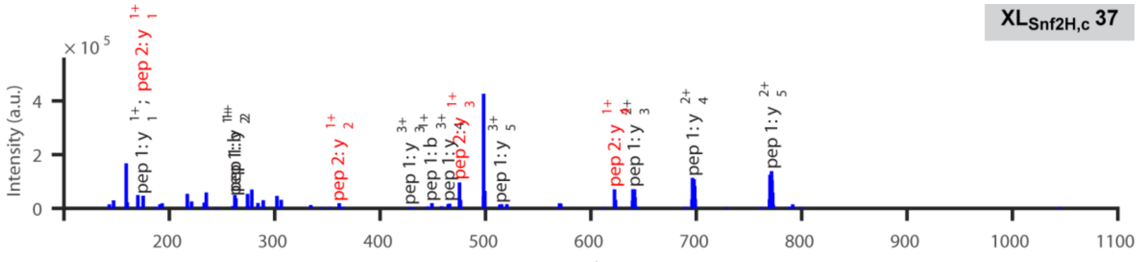

XL$_{Snf2H,c}$ 43

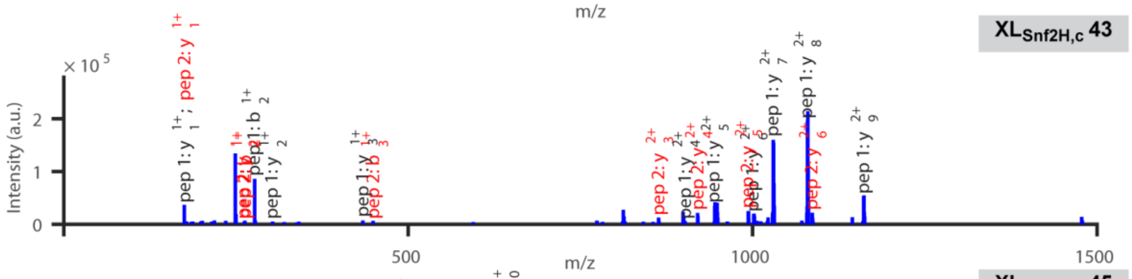

XL$_{Snf2H,c}$ 45

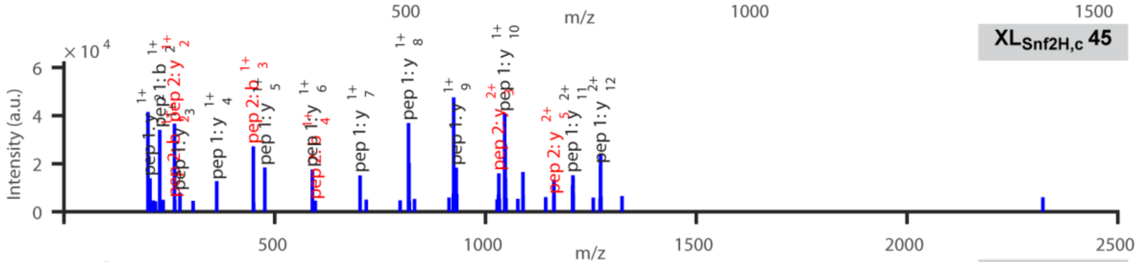

XL$_{Snf2H,c}$ 55

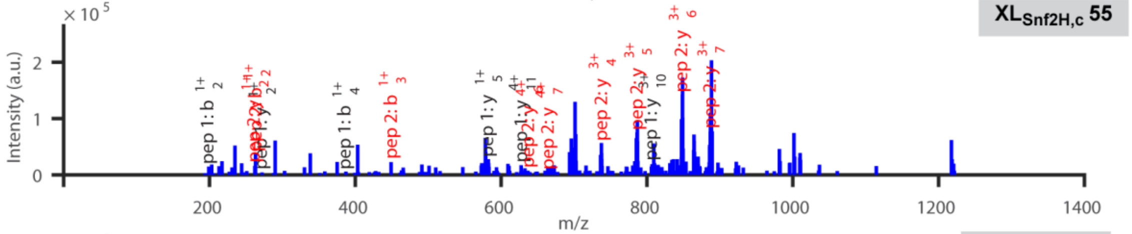

XL$_{Snf2H,c}$ 56

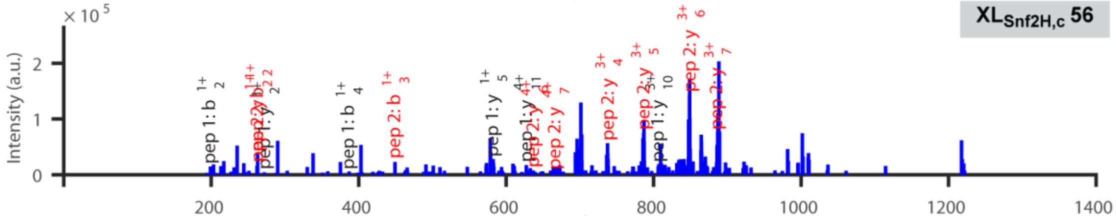

XL$_{Snf2H,c}$ 57

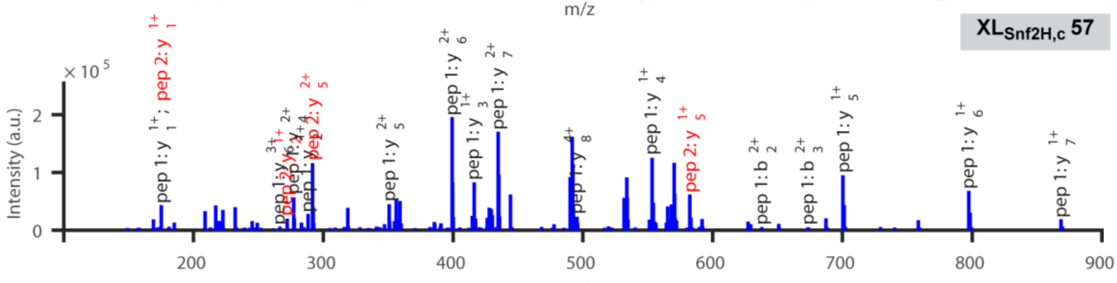

XL$_{Snf2H,c}$ 58

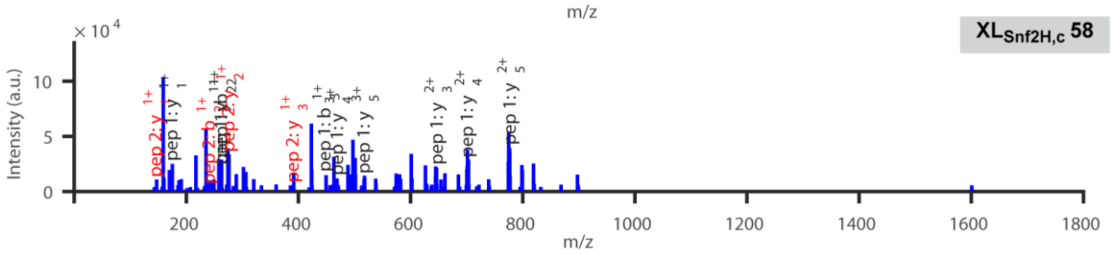

* continues next page *

XL$_{Snf2H,c}$ 62a

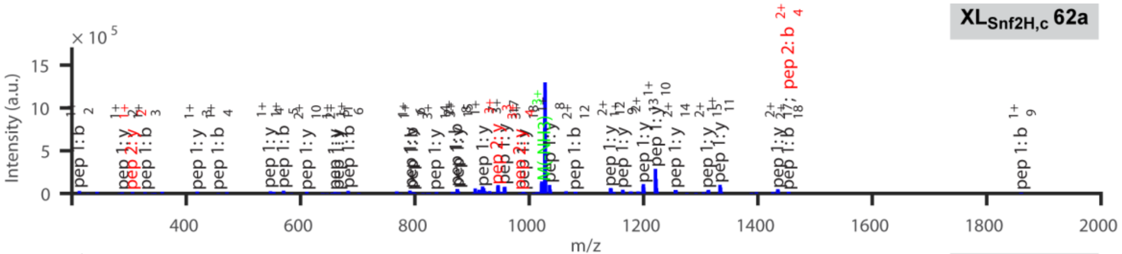

XL$_{Snf2H,c}$ 63a

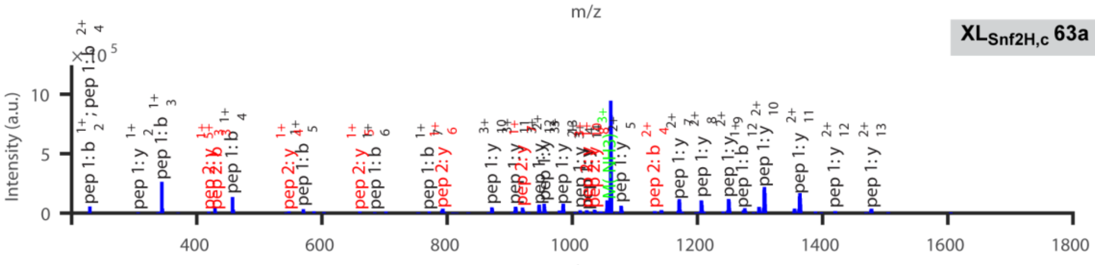

XL$_{Snf2H,c}$ 64a

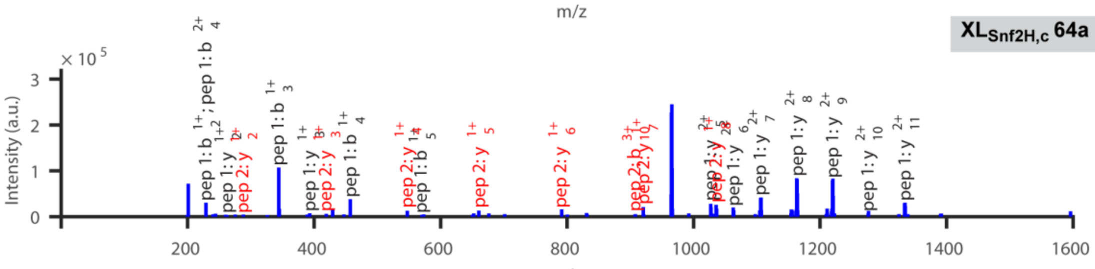

XL$_{Snf2H,c}$ 66

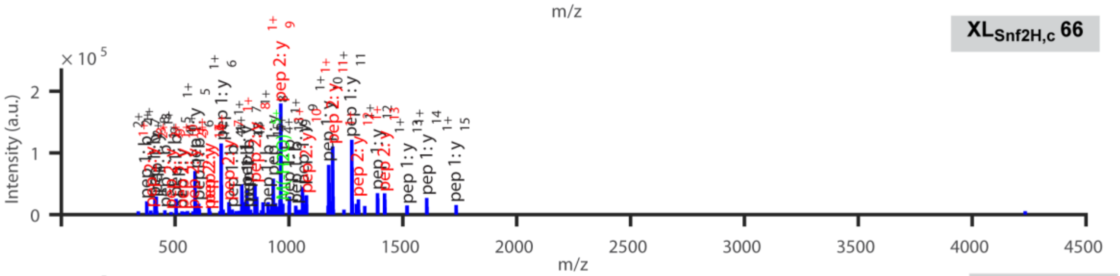

XL$_{Snf2H,c}$ 67

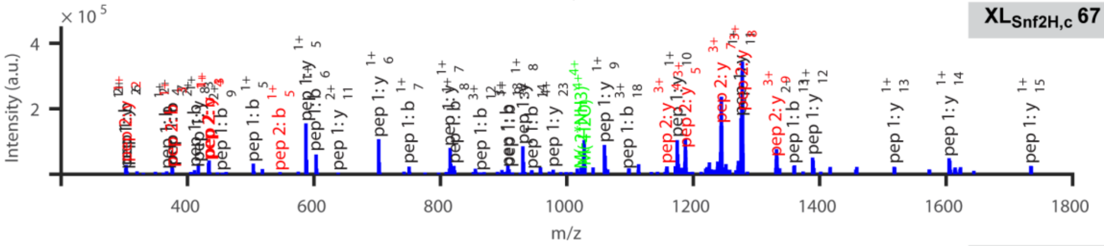

XL$_{Snf2H,c}$ 71

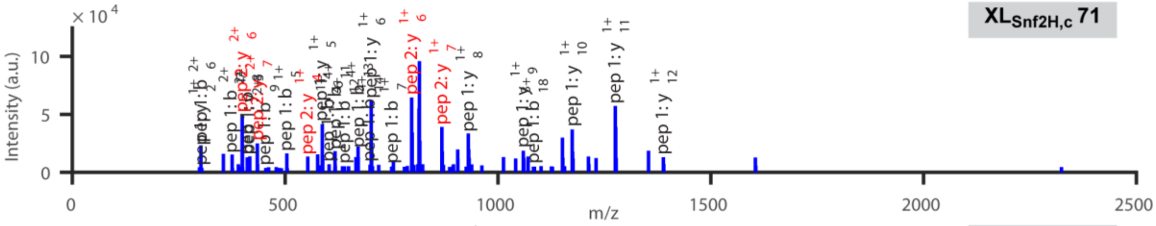

XL$_{Snf2H,c}$ 72

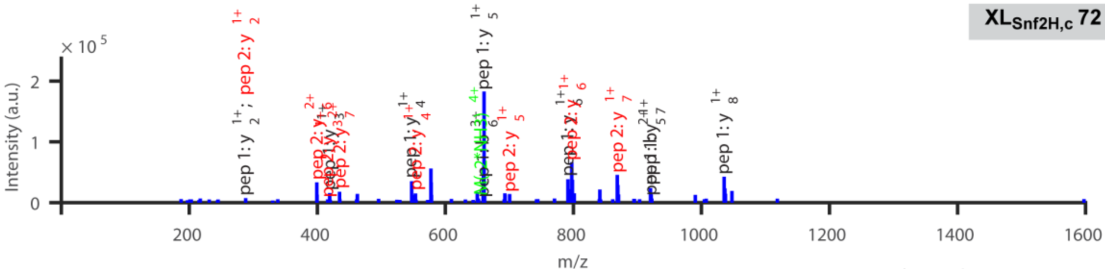

* continues next page *

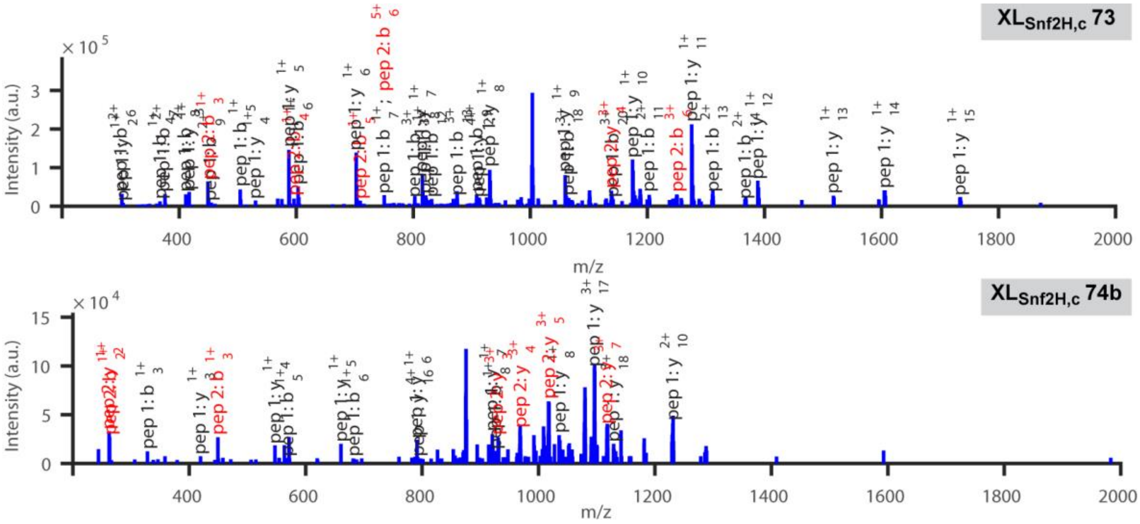

SFigure 9: MS/MS spectra of Snf2H cross-links that are listed in Table 4. Identical and similar inter-domain cross-links for the Snf2H enzyme in the **(A)** apo, **(B)** ADP-BeF$_x$, and **(C)** nucleosome state. Cross-links are denoted according to their XL identification number provided in STable 3–STable 5. Individual cross-links listed in Table 4 were implemented during computation modeling and thus the MS/MS spectra for these cross-linked peptides (i.e., XL$_{\text{Snf2H}}$ 8, 12, 14, 28, 29 and XL$_{\text{Snf2H,nt}}$ 3, 4, 8, 13, 16, 24, 26, 56) can be found in either SFigure 6 or SFigure 7.

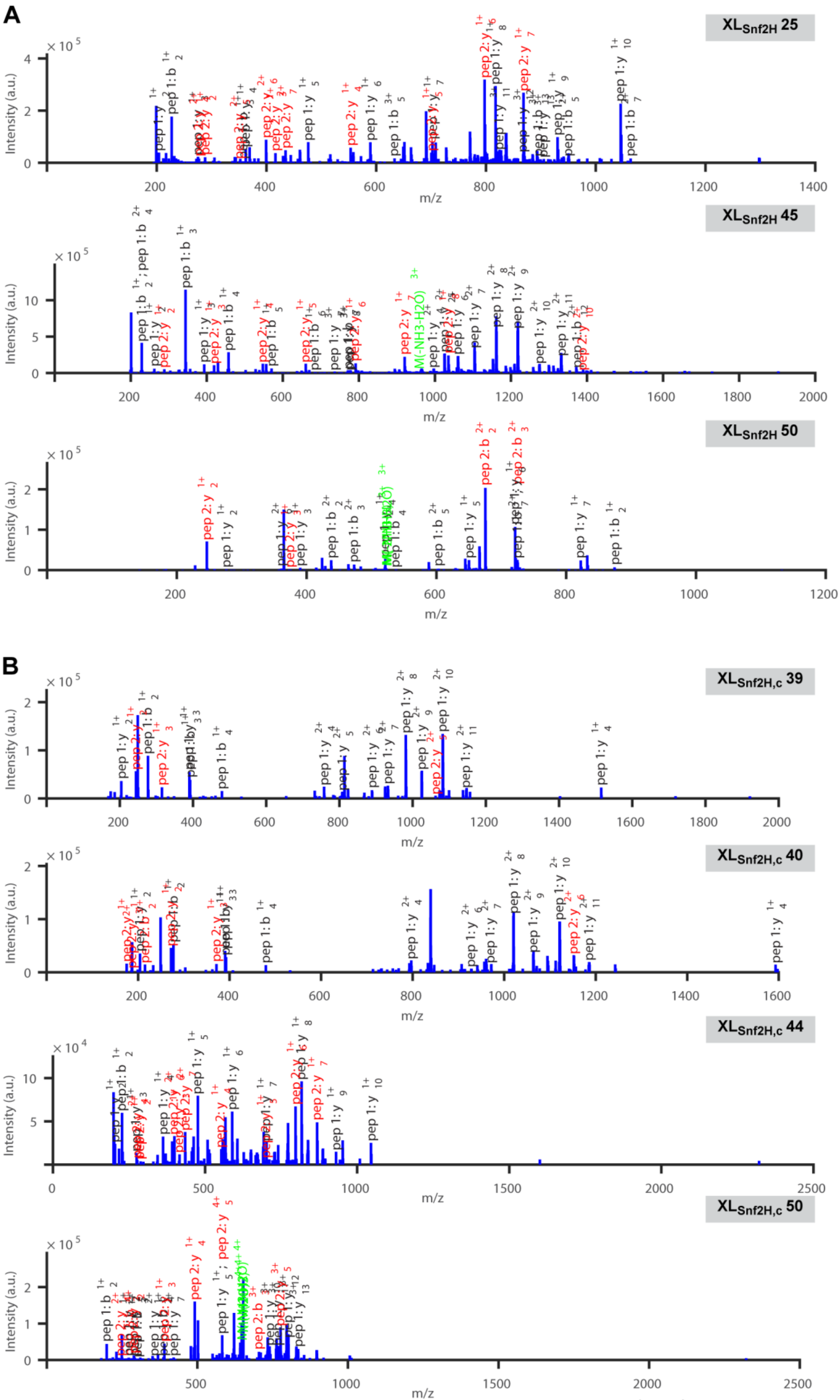

* continues next page *

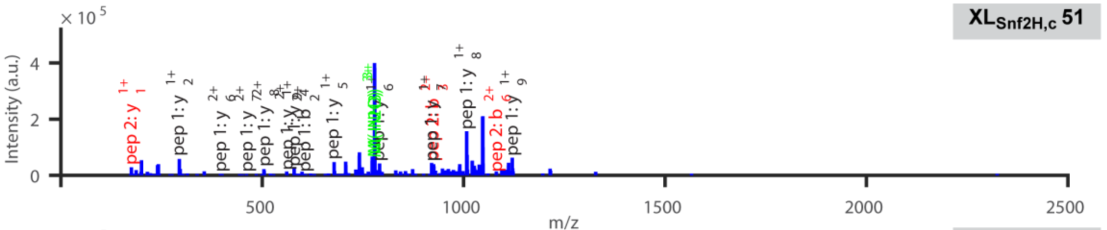
XL$_{Snf2H,c}$ 51

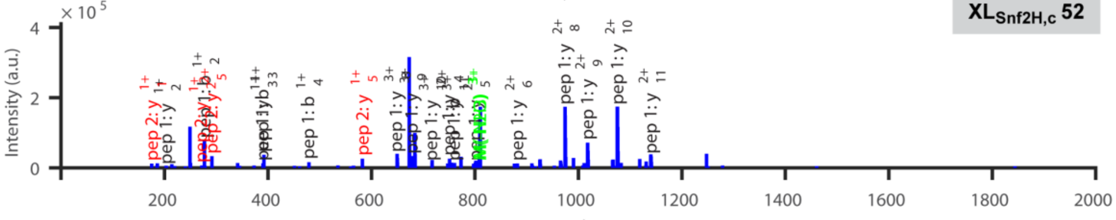
XL$_{Snf2H,c}$ 52

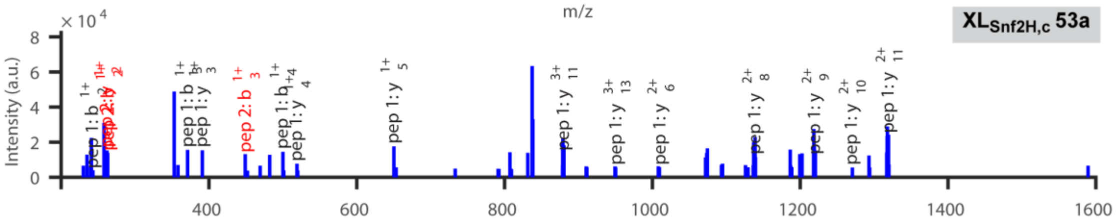
XL$_{Snf2H,c}$ 53a

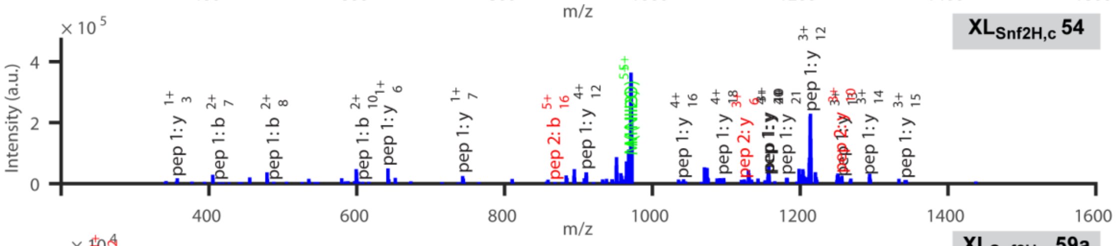
XL$_{Snf2H,c}$ 54

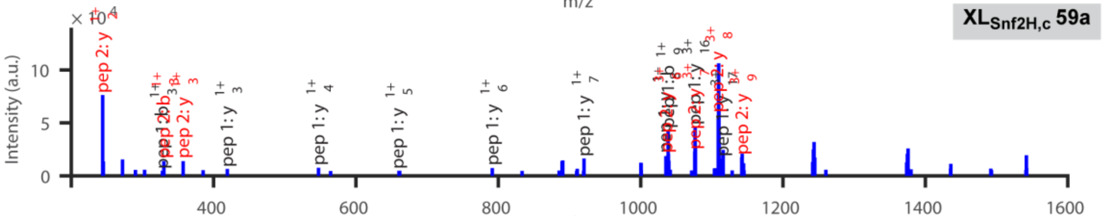
XL$_{Snf2H,c}$ 59a

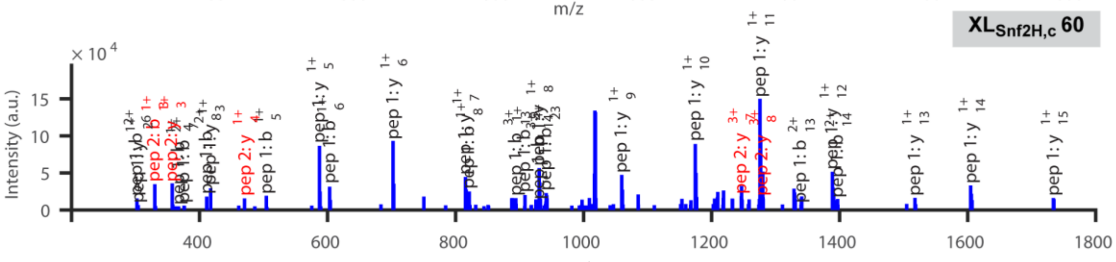
XL$_{Snf2H,c}$ 60

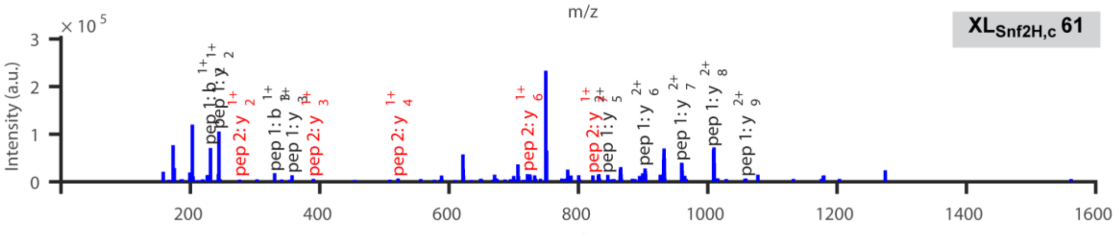
XL$_{Snf2H,c}$ 61

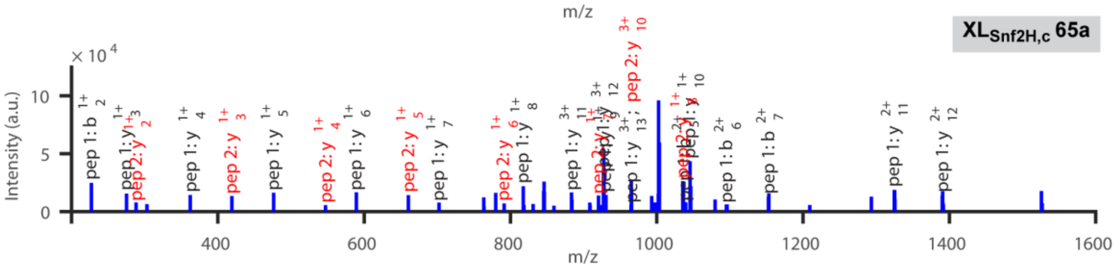
XL$_{Snf2H,c}$ 65a

* continues next page *

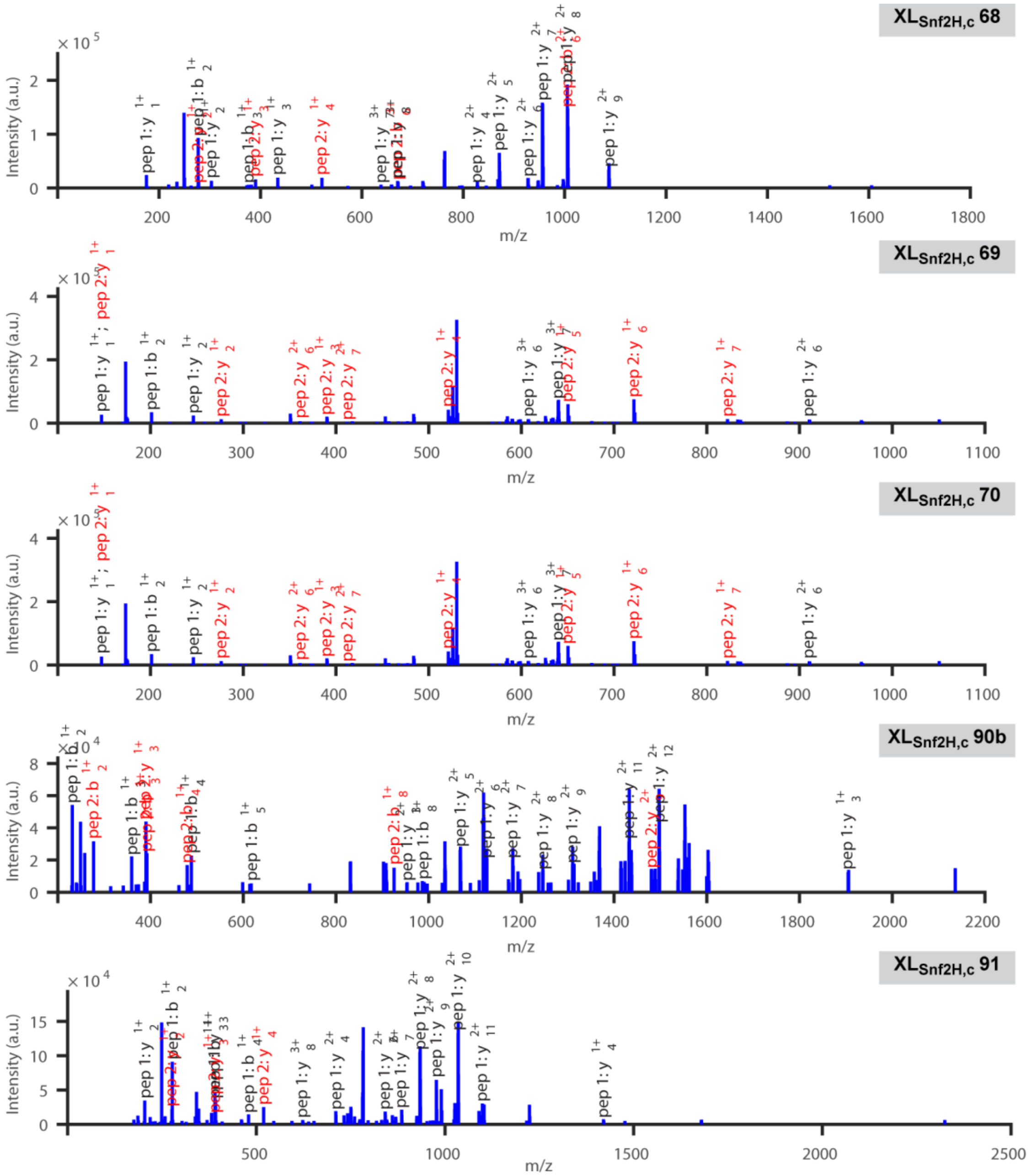

SFigure 10: MS/MS spectra of nucleosome-dependent inter-domain cross-links for the Snf2H enzyme listed in Table 5. Cross-links for the Snf2H enzyme in the **(A)** apo and **(B)** nucleosome state are denoted according to their XL identification number provided in STable 3 and STable 5, respectively.

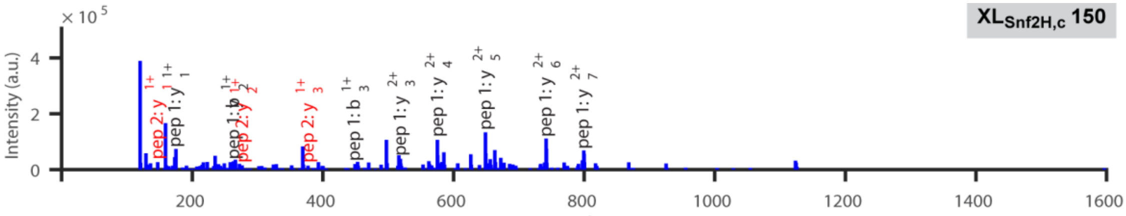

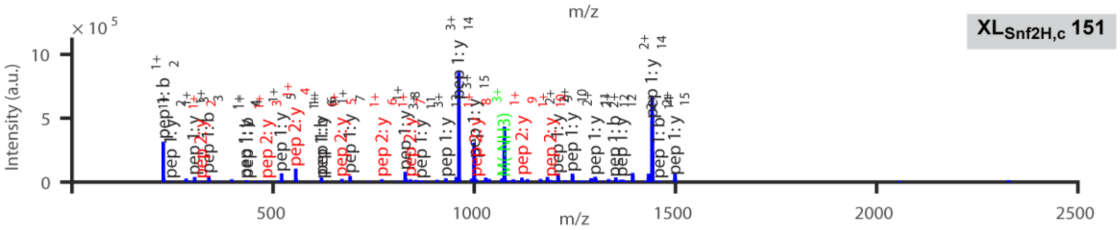

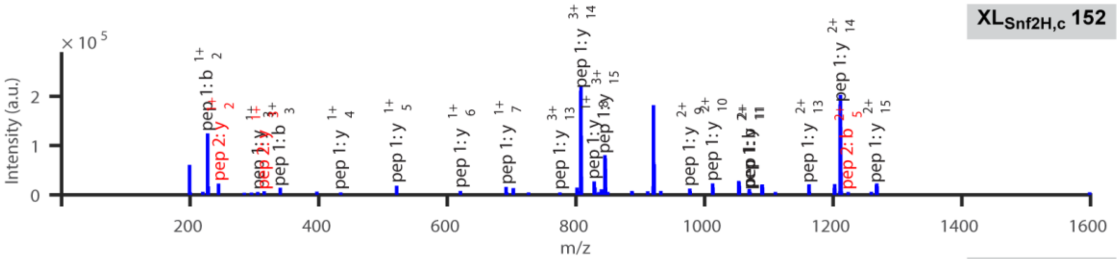

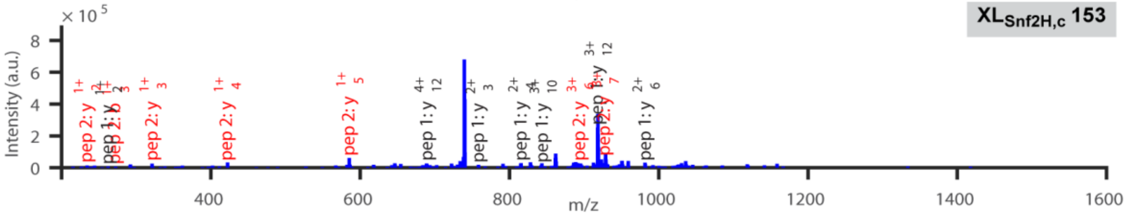

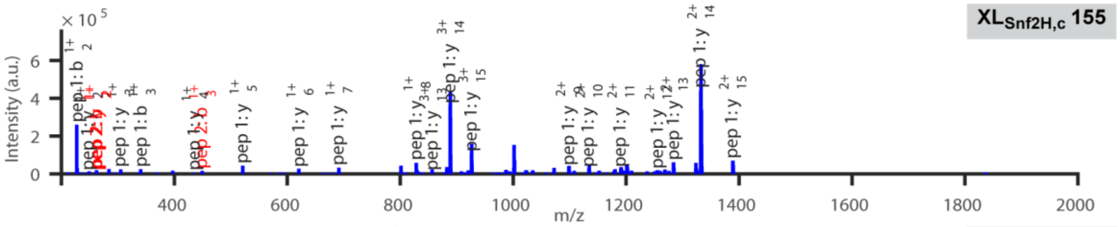

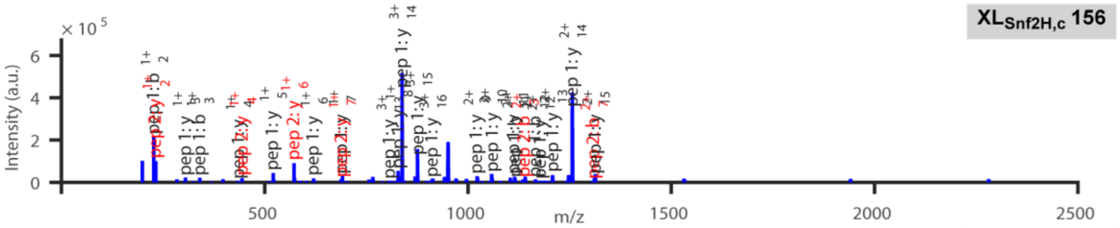

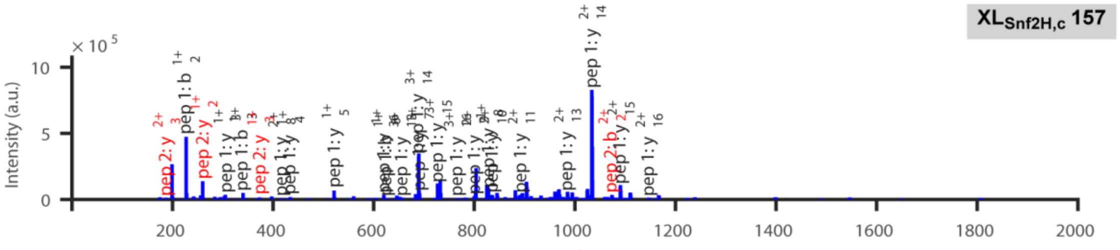

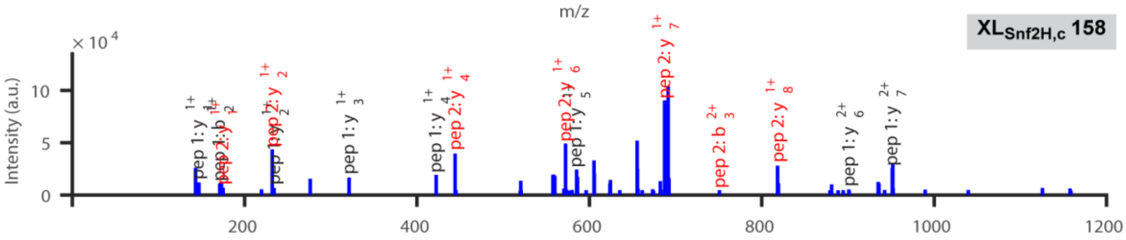

* continues next page *

XL$_{\text{Snf2H,c}}$ 159

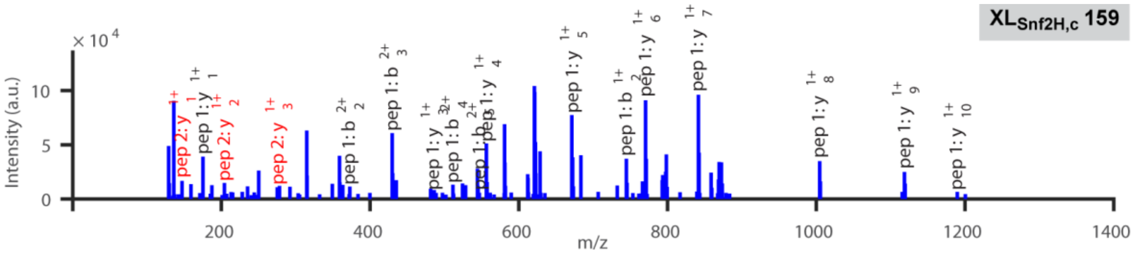

XL$_{\text{Snf2H,c}}$ 160

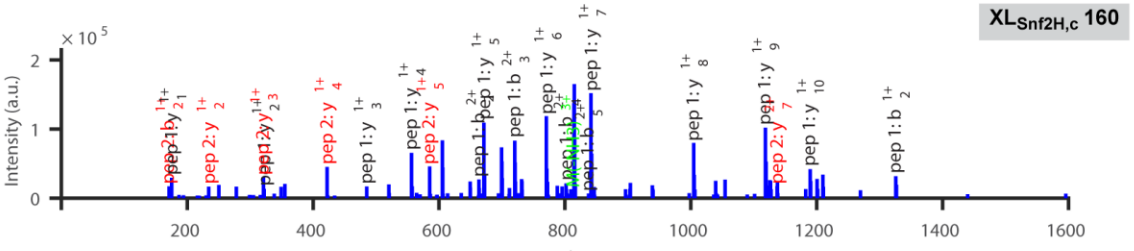

XL$_{\text{Snf2H,c}}$ 161

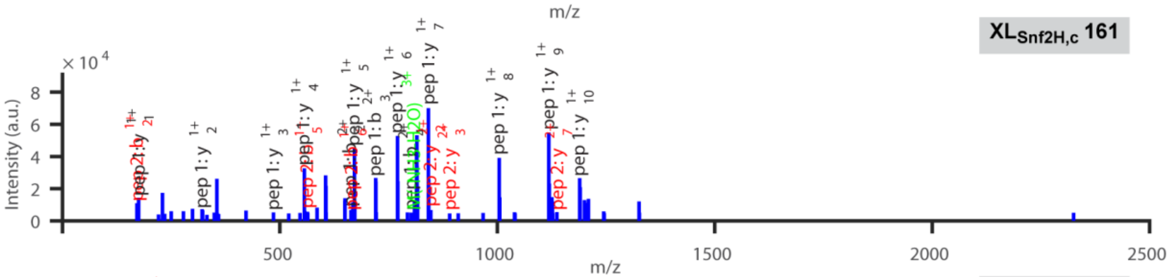

XL$_{\text{Snf2H,c}}$ 162

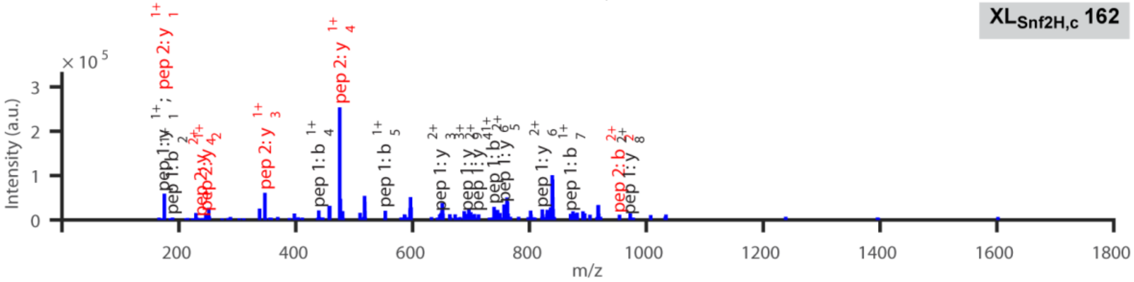

XL$_{\text{Snf2H,c}}$ 163

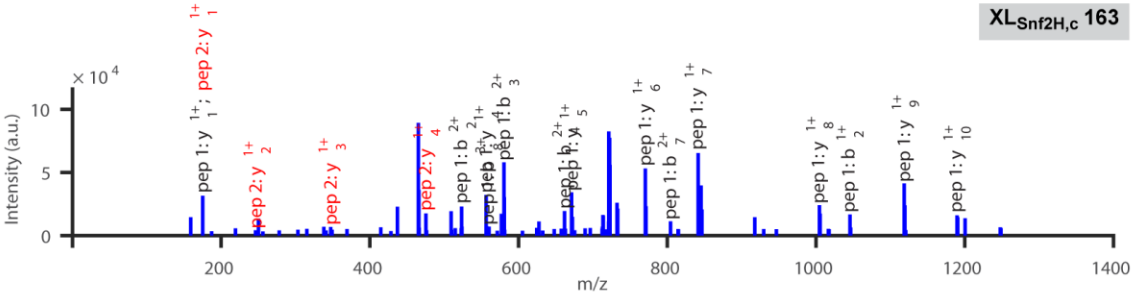

XL$_{\text{Snf2H,c}}$ 164

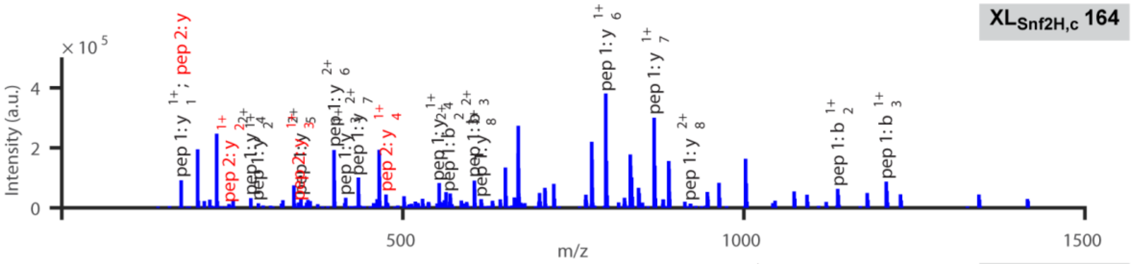

XL$_{\text{Snf2H,c}}$ 165a

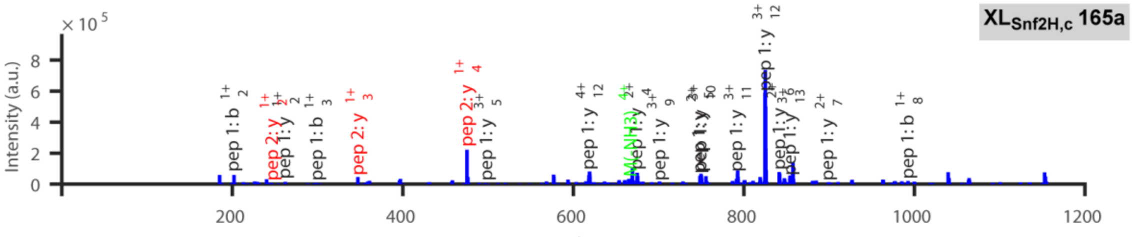

* continues next page *

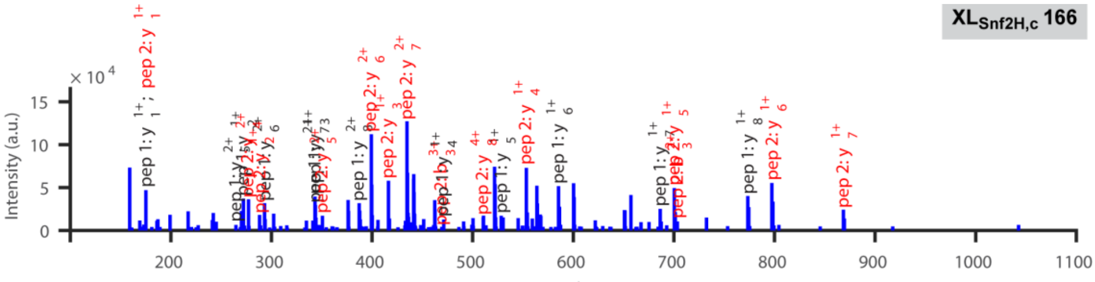

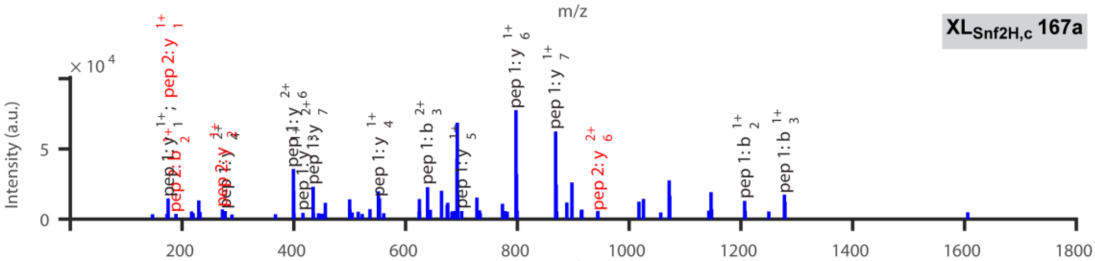

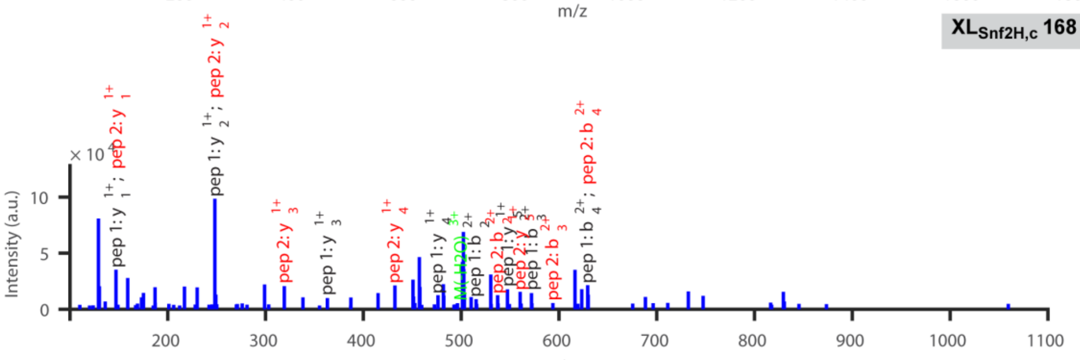

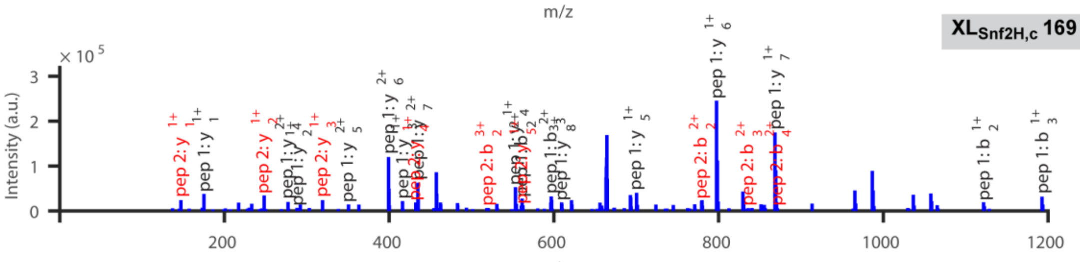

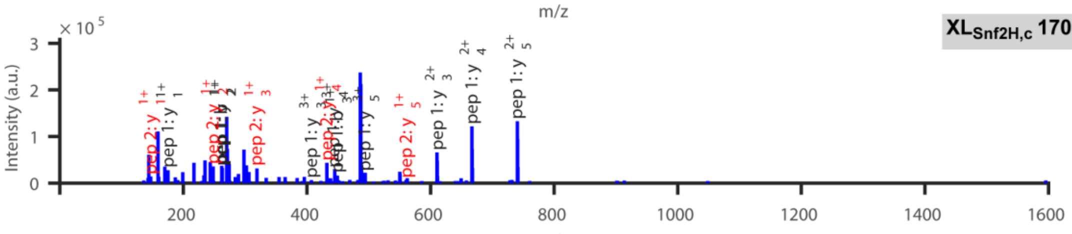

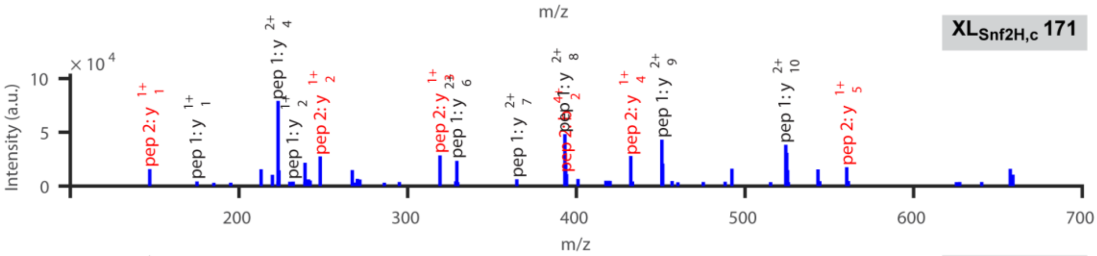

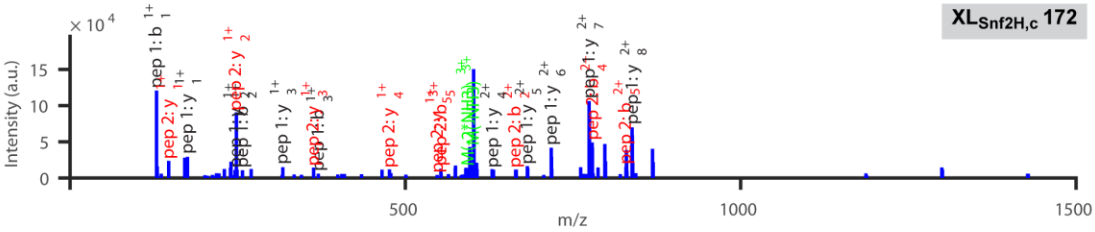

* continues next page *

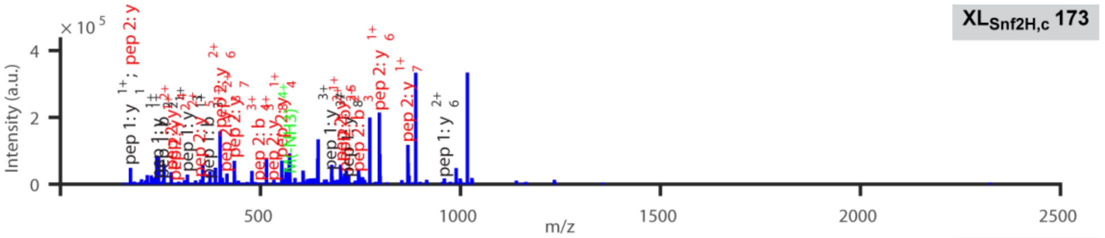
XL$_{\text{Snf2H,c}}$ 173

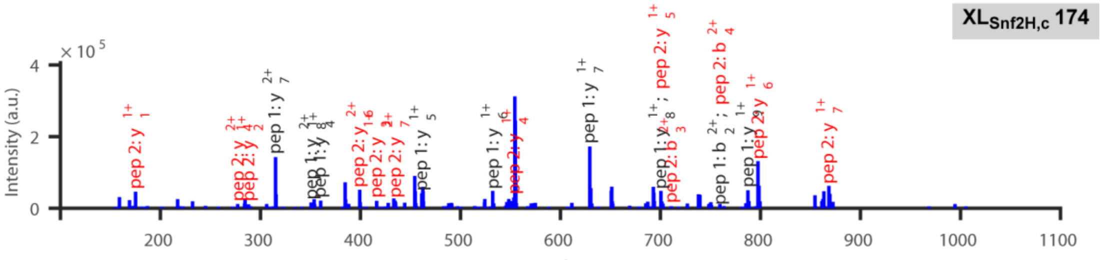
XL$_{\text{Snf2H,c}}$ 174

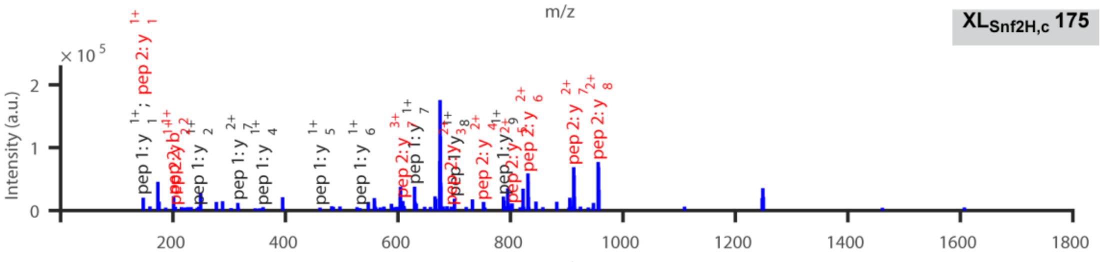
XL$_{\text{Snf2H,c}}$ 175

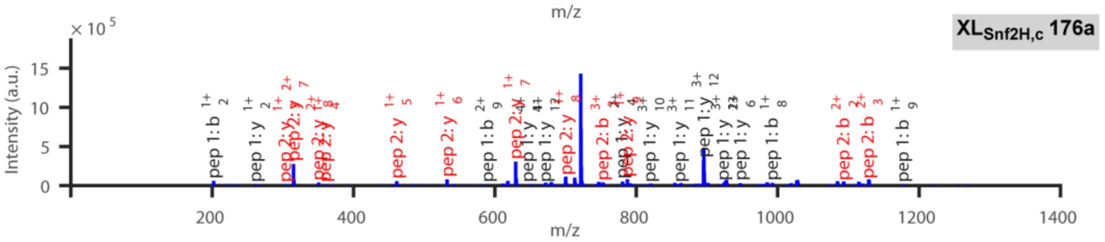
XL$_{\text{Snf2H,c}}$ 176a

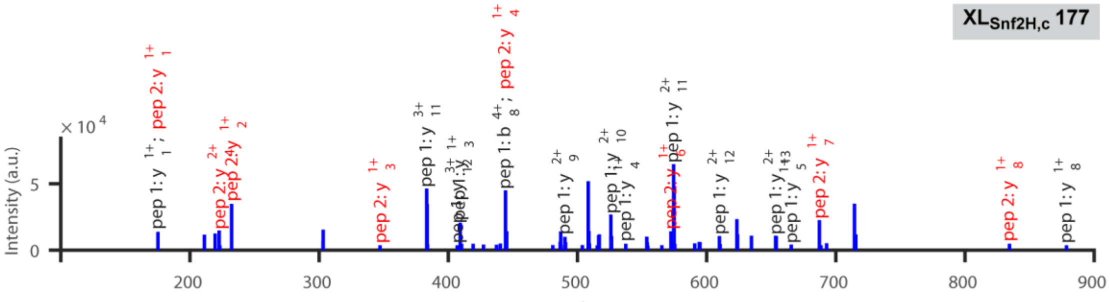
XL$_{\text{Snf2H,c}}$ 177

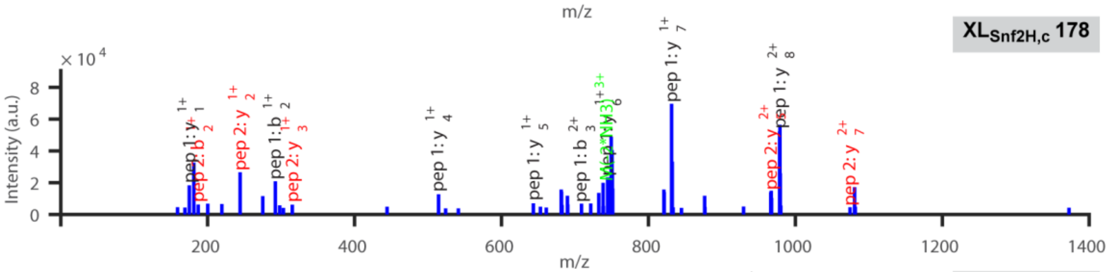
XL$_{\text{Snf2H,c}}$ 178

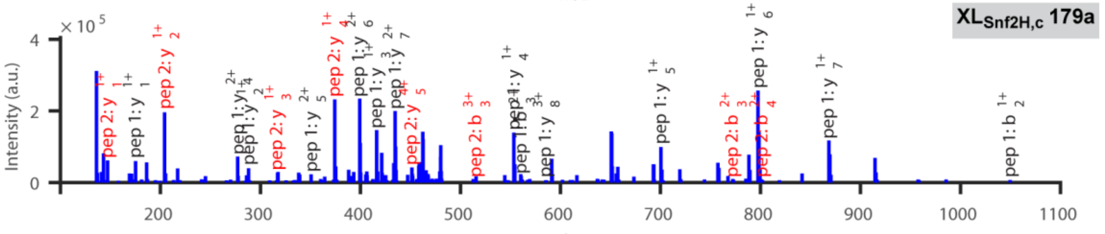
XL$_{\text{Snf2H,c}}$ 179a

* continues next page *

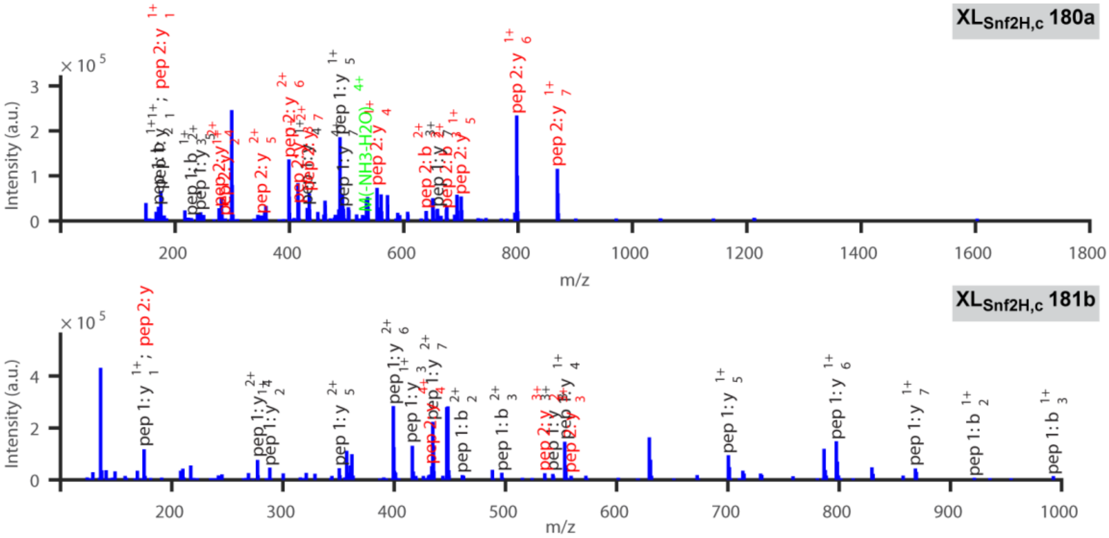

SFigure 11: Additional MS/MS spectra of inter-molecular cross-links between the Snf2H enzyme and the histone octamer. Cross-links are denoted according to their $XL_{Snf2H,c}$ identification number provided in STable 5.

7. Acknowledgements

First of all, I would like to thank Dr. Felix Müller-Planitz for providing me the opportunity to join his laboratory. I have been deeply grateful for your continuous support, guidance, and your inspiring ideas. I appreciated that your door was always open for questions and discussions. Thank you for being my mentor in professional aspects.

I am grateful to my ‘Doktorvater’ Prof. Peter Becker for providing an environment of outstanding scientific quality as well as for creating a pleasant working atmosphere at the institute. Thank you very much for your support and your valuable input during discussions.

I would like to thank additional members of my thesis advisory committee, Dr. Ignasi Forné and Dr. Franz Herzog, for their time and helpful comments.
Special thanks go to Ignasi for MS analysis of uncountable samples, sharing his expertise on data analysis, and for being a supportive collaborator throughout the time of my PhD project.

I would like to acknowledge Prof. Martin Zacharias and Dr. Christina Schindler for their efforts in computational modeling as well as Prof. Jan Lipfert and Dr. Linda Brützel for their efforts in SAXS analysis. Thank you for sharing your expertise and for many fruitful discussions.

I am grateful to have benefited from the IRTG Graduate Program. In addition, I would like to thank Dr. Elizabeth Schroeder-Reiter for the great coordination of research courses, retreats, and many more, but also being someone who really cares for her students.

I furthermore would like to acknowledge all members of the Becker lab as well as all participants of our ‘Remodeler Meetings’ for their interest in my project and their supportive input during joint group meetings.

In addition, I am grateful to all members of the ‘Zentrallabor für Proteinanalytik’ for sharing reagents and expertise. I also would like to thank all past and present members of the Molecular Biology Unit at the Biomedical Center of the LMU Munich for creating a pleasant working atmosphere.

I would like to thank all former and present members of the Müller-Planitz lab. Special thanks go to Johanna, Sabrina, Ashish, and Petra for fruitful discussions, constant support, and all the fun times during and after work.

I also would like to thank the ‘CC group’ for numerous lunch and/or coffee breaks. We had great moments inside and outside the lab.

Finally, I would like to express myself in my native language.
Mein tiefster Dank gilt meiner Muadda, Dad, Schwesterherz und der gesamten Familie für eure bedingungslose Unterstützung. Zusammen habt ihr einen unermesslichen Beitrag zu dieser Arbeit beigetragen, wofür ich euch immer dankbar sein werde.
Patrick, ich kann dir nicht genug danken für dein Verständnis, deine Liebe die du mir auch in schwierigen Zeiten entgegengebracht hast und die viiiieelen gesammelten Flugmeilen. Danke, dass du immer an mich geglaubt hast!